Air-Void Characteristics and Permeability of Fibre Reinforced Repair Mortar for Conservation

by

Md Toihidul Islam

A thesis submitted in partial fulfillment of the requirements for the degree of

Doctor of Philosophy

in

Structural Engineering

Department of Civil and Environmental Engineering
University of Alberta

ABSTRACT

Masonry is among the oldest and widespread construction materials, used to build structures traditionally, both in North America, and worldwide as well. Most of the historical buildings have been built with pre-Portland cement mortar. A large number of existing masonry buildings in Canada have been constructed in the last 200 years and most of them were built with lime mortar. These mortars exhibit good workability and high water retentivity in the plastic state and develop strength slowly over time. Over the years, the integrity of these old masonry buildings has constantly declined. One of the main reasons for this deterioration is the mortar's inherent permeability.

The addition of polypropylene micro-fibres in cement-based systems was found to be effective in improving permeability properties. However, the effect of polymeric fibre on the permeability of Hydraulic Lime Mortar (HLM) is unknown. In addition, it is hypothesized that applying nano-lime onto HLM shall suitably modify its water permeability. Therefore, a part of this thesis focuses on determining the permeability of the HLM, Type N mortar, and Type O mortar, along with the effects of micro-fibre and nano-lime.

In this study, the permeability test setup was used to monitor the onset of the steady state condition in fluid flow. The permeability apparatus consisted of five major sections: a cylindrical concrete specimen with a hollow core; a permeability cell that houses the concrete specimen; a pressurized water supply unit; an outflow measurement device (with an accuracy of 0.01g); and a Materials Testing System (MTS). In addition, this permeability cell was further

instrumented with a computer and programmed to measure and record the mass of water flow in real time, thereby enabling detection of the onset of equilibrium in flow. Hollow cylindrical specimens were prepared with HLM, Type N mortar, and Type O mortar. Specimens were cast and tested to investigate the influence of fibres and nano-lime upon permeability. The results show that the addition of fibres lowers the permeability coefficient significantly across all binder types, without unduly altering the mortar strength. On the other hand, applying nano-lime was most beneficial in limiting water permeability in the natural Hydraulic Lime Mortars.

The microstructure of cementitious materials has great influence on their engineering properties such as permeability, strength, and durability. The pore structure is important for understanding and modeling the transport phenomena through this material, which in turn decide the material's durability. In order to understand the physics of fluid flow and transport processes through porous media such as cement-lime mortar and HLM, one must have a detailed knowledge about the pore space geometry and their arrangement in three-dimensional space. Transport properties such as permeability depend on the porosity. In addition, the size, shape, and connectivity of the porous path strongly influence the transport properties. It is well known that the microstructure within cement and lime-based systems is very complex in nature. Fluid passes through this porous medium taking a path that is often very tortuous.

X-ray micro computed tomography is a powerful tool to investigate the 3D microstructure of cementitious materials. It is an image-based non-destructive 3D radiographic technique. In this method, a high-energy X-ray source is used to acquire 2D radiographic projections of each specimen by rotating it at certain angular intervals. Then a 3D computed reconstruction of the

sample is performed from those 2D images by applying suitable algorithms of mathematical tomography. In this study, the microstructure and water permeability of the mortars, with various dosage of fibre reinforcement, were evaluated using X-ray micro CT. Besides, the effect of polypropylene micro-fibre on water permeability and other microstructural properties was also examined. Here, the permeability values as predicted by analysis of images captured by X-ray microcomputed tomography are compared with experimental results. A Mathematica® based program was used to calculate microstructural parameters including the porosity, pore connectivity, tortuosity, formation factor, and the specific surface area. Thereafter, the water permeability was predicted by using the well-known Kozeny-Carman equation. The results show that the predicted permeability coefficients of both plain and fibre reinforced mortars are in agreement with the experimental values. In addition, there is an optimum fibre dosage, found to be 0.15% by volume, to achieve a favourable microstructure and the minimum water permeability.

DEDICATION

TO MY PARENTS,

MY WIFE ISHRAT JAHAN LUNA AND MY DAUGHTER TASMIA ISLAM

ACKNOWLEDGEMENTS

First of all, I am grateful to Almighty Allah, the most Gracious and most Merciful; for the strengths, wisdom, and blessings in completing this thesis.

This study was funded in part by the Canada-India Research Centres of Excellence (a Network of Centres of Excellence), known as the India-Canada Centre for Innovative Multidisciplinary Partnerships to Accelerate Community Transformation and Sustainability (IC-IMPACTS) under the auspices of the Natural Sciences and Engineering Research Council (NSERC), Canada. The author also thanks the Masonry Contractors Association of Alberta (Northern Region) and Scorpio Masonry Inc., Edmonton for the supply of materials and technician time.

I am highly grateful to my esteemed supervisor Dr. Vivek Bindiganavile for his continuous support and invaluable guidance during this time period. Without his knowledge, perceptiveness, constructive comments and suggestions, I would have never completed this thesis. Outside research, I have learnt from him the different aspects of life, which make my journey, smother along the path of my family life.

I would like to express my sincere gratitude to Dr. Roger Cheng who supervised and mentored me throughout the course of this research. I also extend my gratitude to the other members of my committee: Dr. Tayfun Babadagli, Dr. Mohamed Al-Hussein, Dr. Carlos Cruz Noguez for providing valuable comments toward this research.

I also like to express my sincere appreciation towards Dr. Narayana Suresh at the Department of Civil Engineering and Director, Building Fire Research Centre, at the National Institute of Engineering (NIE), Mysore, India for conducting pilot studies on site using nano-lime. This collaboration was made possible through the IC-IMPACTS (the India-Canada Centre for Innovative Multidisciplinary Partnerships to Accelerate Community Transformation and Sustainability).

I would like to thank the Civil and Environmental Engineering Department for financial support as well as providing necessary laboratory equipment, which was necessary to carry out this research work. My thanks go to the following civil engineering laboratory technicians, Mr. Rizadly Mariano, Mr. Greg Miller, and Mr. Cameron West for their continuous support from time to time during this research program. I also would like to express my sincere gratitude for their support during different stages of this research: Dr. Nancy Zhang - nanoFAB Fabrication and Characterization Centre at the University of Alberta, Ms. Diane Caird - X-Ray Diffraction (XRD) facility - Department of Earth & Atmospheric Sciences at the University of Alberta, Mr. Mark Labbe and Mr. Martin Von Dollen - The Thin Section Laboratory - Department of Earth & Atmospheric Sciences at the University of Alberta, and Mr. Nathan Gerein – Scanning Electron Microscopy (SEM) Laboratory - Department of Earth & Atmospheric Sciences at the University of Alberta.

I would also like to express my gratitude for Mr. Arlene Figley, Graduate Program Advisor, Faculty of Engineering - Civil and Environmental Engineering Dept. at the University of Alberta for her support throughout this course program. Special thanks to Dr. Murray Gingras, Department of Earth & Atmospheric Sciences at the University of Alberta for allowing to use his high-resolution X-ray micro CT facility.

I also would like to express my heartful gratitude to my friend and colleague, Muhammad Mamun for his encouragement and continuous support throughout this thesis.

Finally, and most importantly, I would like to thank my lovely wife Ishrat Jahan Luna for her understanding and love. Without her unconditional love, support, and encouragement, I would not have finished this thesis. Also, thanks to my daughter, Tasmia Islam who has made every moment of my life joyful and hopeful to progress.

TABLE OF CONTENTS

LIST OF TABLES

LIST OF FIGURES

LIST OF SYMBOLS

A	=	the area of the porous media normal to the flow
A_a	=	the mass of oven-dried sample in air
A_{archie}	=	a constant used in Archie's equation
C	=	the mass of surface-dry sample in air after immersion and boiling
c	=	a constant that depends on the cross-section of the tubes, usually taken to be equal to 2 for porous materials
c_1	=	a constant which is equal to $^1/_{226}$
C_f	=	A coefficient related to the fractal dimension
C_0	=	a parameter similar to the Kozeny-Carman coefficient
D	=	the diffusion coefficient of a porous material like concrete or mortar
d	=	the equivalent pore diameter
D_a	=	the apparent mass of sample in water after immersion and boiling
d_E	=	Euclidian dimension for two- and three-dimensional microstructure
D_f	=	pore area fractal dimension
D_T	=	tortuosity fractal dimension
D_o	=	the pure gas diffusion coefficient
F	=	the formation factor
$f(x)$	=	A characteristic function
g	=	acceleration due to gravity
g_1	=	the bulk density
g_2	=	the absolute density
h	=	the specimen's length (m)
k	=	the coefficient of water permeability (m/s)
k'	=	intrinsic permeability (unit length^2)
L	=	the specimen thickness or the length of flow path
l_c	=	the characteristic length of the pore space
L_e	=	the actual flow path

$l_{max}{}^{e}$	=	the pore throat diameter at which electrical conductance is maximum, which is equal to $0.34l_c$
$l_{max}{}^{h}$	=	the pore throat diameter at which hydraulic conductance is maximum, which is equal to $0.61l_c$
m	=	the Archie's exponent or an exponent used in Archie's equation
n	=	n^{th} pore
P	=	the applied mercury pressure
P	=	the equilibrium vapour pressure
P_0	=	the saturated vapour pressure of the adsorbate
P/P_0	=	The relative pressure of nitrogen
Q	=	the volumetric flowrate
R	=	The gas constant (8.314 x 10^7ergs/deg/mol)
r	=	the length of line segment
r^2	=	the mean-square displacement of the walker in porous space
r_{free}^2	=	the mean-square displacement of the walker in free space
r_g	=	the grain radius
R_o	=	the electrical resistivity of the porous media saturated with the electrically conductive fluid
R_w	=	the electrical resistivity of the electrically conductive fluid saturating the porous medium
r_p	=	The actual pore radius
s	=	the specific surface area
$\left(\frac{S}{V}\right)_{pore}$	=	the specific surface area of pores
$S_2(r)$	=	the two-point correlation function
t	=	The thickness of the adsorbed layer
t_r	=	the thickness of the observed layer at the corresponding relative pressure
T	=	The boiling point of nitrogen (77 K)
V_m	=	The molar volume of liquid nitrogen (34.7 cm^3/mol)

V_p	=	the actual pore volume
γ	=	The surface tension of nitrogen at its boiling point (8.85 ergs/cm^2 at 77 K)
Δt	=	the change of thickness of the adsorbed layer
ΔV	=	the observed volume of gas desorbed
μ	=	the viscosity of the pore fluid
ΔP	=	Differential Pressure
Δh	=	the pressure head (unit in length)
μ	=	dynamic viscosity of the fluid (N-s/m^2)
ρ	=	density of the fluid (kg/m^3)
τ	=	the Tortuosity, also called as geometric tortuosity
ϕ	=	the porosity
τ_g	=	geometric tortuosity
ρ_w	=	the density of water
θ	=	the contact angle between mercury and porous materials
γ	=	the surface tension between mercury and pore surface
γ'	=	empirical constant
β'	=	empirical constant
σ	=	the conductivity of the medium saturated with a brine solution having a conductivity of σ_0
σ_0	=	Conductivity of brine solution
λ_{max}	=	the maximum pore diameter
λ_{min}	=	the minimum pore diameter
Γ	=	the interconnectivity parameter
τ_d	=	the diffusive tortuosity
ϕ	=	porosity
ϕ_{eff}	=	the effective porosity

LIST OF ABBREVIATIONS

2D	=	Two Dimensional
3D	=	Three Dimensional
ACI	=	American Concrete Institution
ASTM	=	American Society for Testing and Materials
BEI	=	Backscattered Electron Imaging
BJH	=	Barrett, Joyner, and Halenda
BSE	=	Backscattered Electrons
BSEM	=	Backscattered Scanning Electron Microscopy
CSA	=	Canadian Standard Association
DIF	=	Dynamic Impact Factor
DSC	=	Differential Scanning Calorimetry
EN	=	European Standard
FD	=	Fractal Dimension
HLM	=	Hydraulic Lime Mortar
ITZ	=	Interfacial Transition Zone
Micro x-ray CT	=	Micro x-ray Computed Tomography
MIP	=	Mercury Intrusion Porosimetry
NHL	=	Natural Hydraulic Lime
NMR	=	Nuclear Magnetic Resonance
PSD	=	Pore Size Distribution
PVA	=	Polyvinyl Acetate
SE	=	Secondary Electrons
SEM	=	Scanning Electron Microscope
TPC	=	Two Point Correlation
X-ray CT	=	X-ray Computed Tomography

CHAPTER 1. INTRODUCTION

1.1 Introduction

Masonry is among the oldest and widespread construction materials, used to build structures traditionally, both in North America, and worldwide as well. Most historical buildings were built preceding the advent of Portland cement. A large number of existing masonry buildings in Canada were constructed in the last 200 years and most of them were built with lime mortar. These mortars exhibit good workability and high water retentivity in their plastic state and develop strength slowly over time. Over the years, the integrity of these old masonry buildings has constantly declined. One of the main reasons for this deterioration is their lack of water tightness, measured through permeability. Defined as the movement of fluid under a pressure gradient, permeability is one of the most important properties of mortar and governs its long-term durability. The parameters that define the internal pore structure (i.e. the number, size, distribution, and interconnectivity of the pores and cracks within the mortar) are assumed to play a major role on water flow. Therefore, the effective design of masonry buildings requires a sound understanding of the mortar's permeability and the underlying mechanisms.

Masonry used in water-retaining structures, exposed to severe weather or exposed to an aggressive environment must be watertight. This applies also to masonry structures in cold climate areas where frequent freeze-thaw cycles will affect their performance. Water permeability is primarily related to the porosity or air-void network in the mortar used in the masonry systems. Water generally percolates into the masonry systems through the inherent pores leading to the long-term degradation of the structure. Hence, a quantitative investigation of the inherent microstructure is the first step towards understanding the transport properties for masonry mortars.

The addition of polypropylene micro-fibre to cement-based systems is well known to improve their water tightness. But the effect of polymeric fibres on the permeability of traditional materials such as Hydraulic Lime Mortar (HLM) is unknown. Also, with the recent development of nano-lime, it is expected to benefit the carbonation process, leading to better

structural performance and microstructural properties. Explaining the underlying mechanisms requires a detailed study of pore connectivity in the air-void network, also known as percolation. There are several methods available to examine percolation. These include the Mercury Intrusion Porosimetry (MIP), cryoporometry and X-ray microcomputed tomography (X-ray micro CT). Among them, the MIP method is highly criticized due to certain inherent limitations (i) high stress causing damage to smaller pores and (ii) shift in the distribution towards smaller pores. With regard to air-void network, no direct measurements were made and also no predictive model has yet been found in the literature that describes the permeability parameters of controlled low strength mortars like HLM. Therefore, this research project focused on characterizing the air-void network of HLM and certain masonry mortars that contain Portland cement. Alongside, the effect of micro-fibres and nano-lime has been examined in each case.

1.2 Motivation and Goal

The stone masonry dam at the Krishna Raja Sagara in India, as shown in Figure 1.1, is about 90 years old. The dam was completed in 1924 by employing many novel construction techniques of that time and serves as the primary source of drinking water and irrigation for the Mysore region in India. In the century since its construction, there has been significant deterioration in this structure (shown in Figure 1.2), particularly with regard to the mortar joints, which severely threatens the primary function of this water-retaining structure. It is imperative therefore that a concerted investigation be made to develop and characterize innovative repair materials towards conserving this economically significant structure. Based on the studies on repointing mortars made with hydraulic lime (Islam and Bindiganavile 2014), a mix design was proposed to repair this dam. This mix was originally designed to suit the Canadian climate and has proven suitable for use in stone masonry conservation, most notably in the buildings on Parliament Hill, Ottawa. It has been demonstrated that adding polypropylene micro-fibres significantly improves the water tightness in cement-based mortars by effecting considerable reduction in the connected porosity (Hoseini 2013) as well as improving the fracture toughness of the stone-mortar bond (Chan and Bindiganavile 2010a). It was confirmed that identical fibres were available in Mysore, India. It was suggested to use

fibre reinforced Hydraulic Lime Mortar with nano-lime to repair the dam. This option was found to reduce water permeability by two orders of magnitude (Islam et al. 2014) but reasons behind this reduction were not apparent at that time. At the same time, nano-lime has emerged as a recent innovation towards improving stone masonry. Consequently, this thesis was focused on quantifying the effects of adding micro-fibres and nano-lime on the air-void characteristics and permeability of Hydraulic Lime Mortar. Alongside, two other CSA (A179-2014) (2014) specified low-strength mortars have also been examined.

a) b)

Figure 1.1 a) Location of Mysore, India; b) Krishna Raja Sagara Dam

Figure 1.2 Seepage through Body of the Dam in the form of Sweating

1.3 Objectives

The primary goal of this program is to determine the permeability of low strength mortars used in masonry and examine how it is affected by specific micro and nano additives. Specifically, HLM, Type N mortar, and Type O mortars are examined experimentally for water permeability and their internal air-void network is quantified. Using the experimental data, existing analytical models are applied to predict the water tightness of these masonry systems. The expected outcomes of this research project are as follows:

- Characterization of controlled low strength mortars
- Analysis and characterization of the inherent air-void network in these mortars
- Application of nano-lime for the enhancement of durability properties including breathability and permeability
- Role of micro-fibre in improving the transport properties of mortars and relating them to pore connectivity and refinement of pore size distribution
- Employ and verify existing analytical models to predict the water permeability of mortars
- Quantify the microstructure using X-ray micro CT and experimentally evaluate the water permeability of these mortars
- Determine the morphological characteristics of the mortars through XRD and XRF analysis
- Measure the compressive response of the plain and fibre reinforced mortars and correlate them with permeability

1.4 Scope

In order to confine the number of parameters associated with the microstructure and durability related aspects of repair mortar to a manageable level, it was decided to study the air-void characteristics and permeability of controlled low strength Hydraulic Lime Mortar, Type N mortar, and Type O mortar (Type N mortar and Type O mortar were prepared with slaked lime per CSA A179-2014 (2014). Note that these mortar are classified as repair mortars per CSA

A179 (2014)). It is worth mentioning that the mix proportions, mechanical and physical properties of these mortars are intended for standalone study. Appropriate modification to the mixture proportions must be made when using these mortars in masonry construction or repair. Since the properties of lime-based mortars evolve over time through carbonation and continued hydration, the outcome of this investigation may be used for practical purposes with suitable modification following the guidelines of applicable standards such as CSA A179 (2014). It is to be noted that the permeability (which is also termed as absolute permeability) was determined using a single-phase fluid namely, water, incorporating Darcy's Law where a steady-state flow condition was achieved. The effect of fibre reinforcement was evaluated by incorporating a hydrophobic polypropylene micro-fibre. Note that hydrophilic fibres were not studied in this research. Although the fibre geometry plays an important role when investigating the behaviour of cement-lime mortars, the current study was limited to a most commonly employed polypropylene fibre having a length of 20 mm and a diameter of 22 μm. The addition of micro-fibres is known to create a wall-effect at the fibre/matrix interface. The influence of this wall-effect on the permeability was not considered in this thesis. Furthermore, the three-dimensional air-void characteristics were determined through X-ray micro CT with a spatial resolution of 4 μm, which was deemed adequate for the purpose of this study. There were many attempts in the literature to establish simplified correlations between permeability and convenient parameters such as strength. No such correlation is able to successfully predict water permeability be it from the tensile strength or from the compressive strength (Alexander et al. 2017). However, the compressive strength of the mortars tested here was evaluated as a routine task.

1.5 Research Significance

The expected outputs of this research program will provide invaluable information that helps in understanding the transport of fluid through a porous cementitious medium. Very limited information can be found in the literature regarding the water permeability of controlled low strength mortars. Further, the influence of micro-fibres upon permeability in such low strength mortars will significantly help develop more durable masonry systems. Application of nano-lime is expected to reveal clear insights into its possible usage for enhanced durability.

1.6 Organization

As discussed in Section 1.4, the key objective of this research project is to characterize the mortars and determine their permeability characteristics. Bearing that in mind, the key aspects that were addressed in this thesis are: (i) microstructural evaluation, (ii) experimental measurement of water permeability and comparison with available analytical methods to predict same, (iii) quantification of the microstructure through X-ray micro CT, and (iv) to evaluate effects of micro-fibres and nano-lime upon the morphology, mechanical properties, microstructure and permeability of mortars.

To this end, this thesis consists of seven chapters starting with an introductory chapter and closing with a chapter that concludes the current findings. The present Chapter 1 introduces the subject, defines the problem and research objectives, and lists the scope as well as the significance of this research project. A comprehensive literature review is presented in Chapter 2. The various mortars along with their microstructure and evaluation procedures are presented there in. Different parameters related to permeability and their possible influence are also discussed. As well, specific micro-fibres and nanomaterials are introduced. The findings are separately discussed in Chapters 3 through 6. The parameters defining the microstructure and their corresponding evaluation procedure are detailed in Chapter 3. This includes porosity measurement and evaluating the pore size distribution through back-scattered electron micrography. This chapter describes image analysis leading to quantifying the fractal geometry and various air-void parameters through two-point correlation functions. The experimental technique to measure water permeability is presented in Chapter 4. Microstructural parameters obtained in Chapter 3 are used in this chapter for analytical prediction. The results from both laboratory experiments and analytical methods are compared. Alongside, the influence of fibre addition is also discussed.

Chapter 5 describes the use of X-ray micro CT in this study, for quantifying the microstructural properties and later, evaluating the permeability. The pore connectivity, tortuosity and 3D fractal behaviour are also presented in this chapter. The morphology and mechanical properties of the different types of mortars under investigation are presented in Chapter 6. The

morphological parameters and the mechanical properties are correlated with the microstructural parameters herein. A pilot study on the effect of nano-lime upon water permeability is presented at the end of this chapter. Finally, Chapter 7 relates the findings of the research to its goals and also provides recommendations for future studies.

CHAPTER 2. LITERATURE REVIEW

2.1 Introduction

In order to successfully accomplish the research objectives, the necessary information has been reviewed. The important background knowledge and major developments in the relevant area have been summarized here.

2.2 Background

2.2.1 Types of Mortar

2.2.1.1 Hydraulic Lime Mortar

Lime-sand mortars were used widely in Canada and elsewhere in the world until the late 1800s. In Canada, three types of mortar are currently being used to repoint historic masonry projects: lime mortars, Hydraulic Lime Mortars, and Portland cement/masonry cement-lime mortars. Mortar used for historic structures must comply with sound conservation principles and be compatible with the historic fabric as far as feasible; it must also be appropriate for the material to be bonded and remain durable under service conditions. Good conservation principles dictate that the mortar be somewhat flexible so that it can act as the sacrificial material saving the masonry unit. The three current types of mortar differ in their properties significantly. Hydraulic Lime Mortar (HLM) was the most common binder in Canadian masonry until late in the 19th century. As a material for repair, its performance when used in the conservation of Canadian heritage structures in the present century, was found to be satisfactory (Suter et al. 2001). With time, natural Hydraulic Lime Mortars were superseded by cement-based mortars due to their rapid and superior strength development. For the restoration and rehabilitation of historic structures, however, Hydraulic Lime Mortar is still preferable due to good adhesion, ductility, and reasonably high values of porosity and permeability that aid in transpiration. Hydraulic Lime Mortar also resembles the original mortar of the rehabilitated structures. In the framework of the restoration and rehabilitation process, the compatibility of the new repair mortars and original components of the structures are emphasized. The key considerations for

restoration and rehabilitation of historic masonry structures, like compressive strength, wetting and drying potential, bond, appearance, resistance to frost action and resistance to salts (e.g., chlorides, sulphates) make the richer cement-lime mortar preferable for this purpose (Cowper et al. 1998; Holmes and Wingate 1997; Vicat 2014).

Natural hydraulic lime (NHL) is a family of hydraulic lime binders that is derived after slaking argillaceous limestone. Hydraulic lime binders can be feebly, moderately, or eminently hydraulic, and the European Standard EN 459 (2001) classifies them by strength as listed in Table 2.1. Natural hydraulic lime is classified as NHL2, NHL3.5 and NHL5 with compressive strengths of 2 MPa, 3.5 MPa, and 5 MPa respectively (Maurenbrecher et al. 2007). The physical properties of hydraulic lime are described in Table 2.2, and the chemical composition of NHL2 is addressed in Table 2.3. As per EN 459 (2001), the initial flow of NHL should be 185 for the best workability, whereas as per ASTM C1437 (2007), the flow should be 100 to 115. The discrepancy is due to the fact that the two test methods are different. The EN 459 (2001) specifies the dropping at a rate of once per second for 15 s. On the other hand, ASTM C1437 (2007) recommends a drop of 25 times in 15 s. Hanley and Pavia (2008) conducted extensive research on the workability of natural Hydraulic Lime Mortars and its influence on strength. Figure 2.1 and 2.2 illustrate the outcome of the research where the compressive strength and flexural strength variations are shown with time for various natural hydraulic lime binders. It is suggested that a different flow value be met for different NHL mortars as opposed to a fixed flow value. Hydraulic lime binders still contain a high proportion of non-hydraulic lime, which gains strength by carbonation. The strength gain by hydration is much slower than for Portland cement; after a year the mortar strength could be three times the 28-day strength. Testing for compressive strength at 28 days is therefore not appropriate for non-hydraulic and Hydraulic Lime Mortars. Portland cement-lime mortars also continue to increase in strength, but the proportionate increase is much less (Maurenbrecher 2004).

Most recently, Chan and Bindiganavile (2010a; b) carried out research on Hydraulic Lime Mortar with and without fibre reinforcement. NHL2 was used for this purpose. The results showed that the addition of polymeric micro fibres to Hydraulic Lime Mortar improved the compressive, flexural, and shear strength, and the fibre efficiency was most evident for flexural

toughness factors. In addition, there was an optimum dosage of fibre-reinforcement beyond which the fibres did not improve mortar efficiency.

Table 2.1 Compressive strength of hydraulic limes

Type of hydraulic lime	Compressive strength (MPa)	
	7 day	28 day
HL 2	-	1.5-10
HL 3.5	≥ 1.5	2.7-14
HL 5	≥ 2	4.0-20

Table 2.2 Physical properties of hydraulic lime (EN 459-2 2001)

Type of hydraulic lime	Bulk density	Fineness (%)		Sound-ness	Free water content	Penetration	Air content	Setting time
	(kg/m^3)	0.09 mm	0.2 mm	(mm)	(%)	(mm)	(%)	(hour)
HL 2	400 - 800	≤ 15	≤ 5	≤ 20	≤ 2	20 and < 50	≤ 20	1 and ≤ 15
HL 3.5	400 - 800							
HL 5	400 - 800				≤ 1			

Table 2.3 Chemical composition of NHL2 (percentages related to original dry lime) (Lanas et al. 2004)

Compound	CaO	LOI	SiO_2	MgO	Al_2O_3	SO_3	K_2O	Fe_2O_3	Na_2O
% by mass	54.26	15	12.57	7.65	5.42	2.13	1.35	1.16	0.34

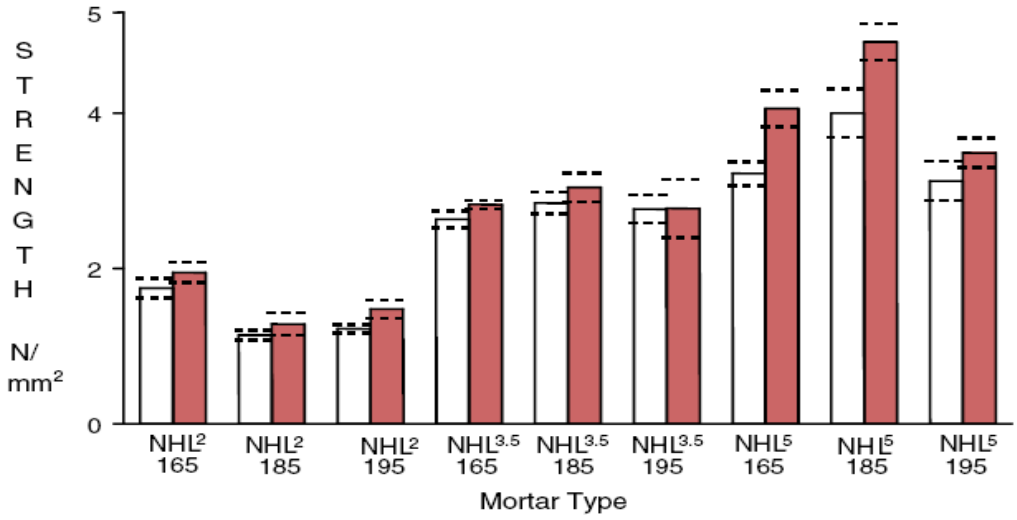

Figure 2.1 Compressive strength of NHL mortars with different values of initial Flow (Hanley and Pavía 2008)

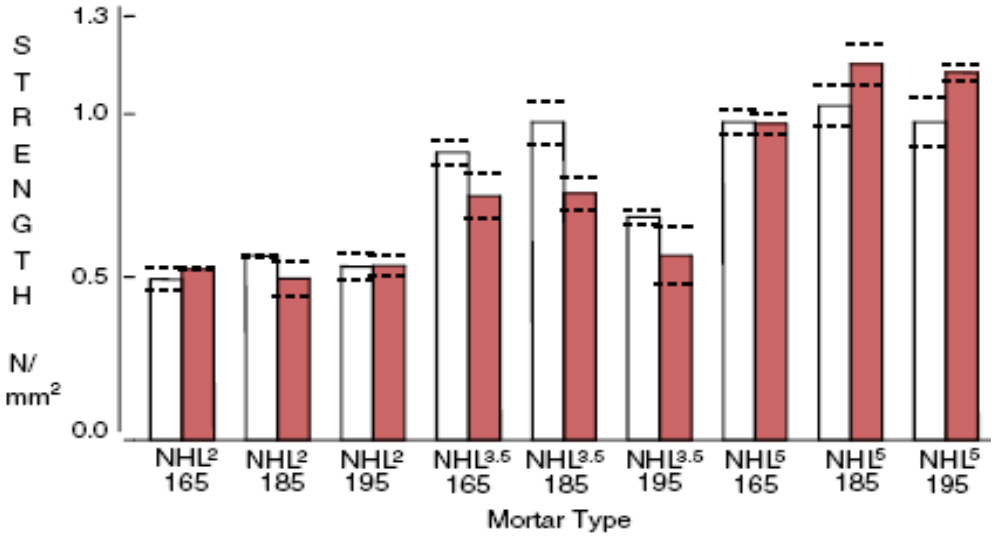

Figure 2.2 Flexural strength of NHL mortars with different values of initial Flow (Hanley and Pavía 2008)

2.2.1.2 Type N Mortar and Type O Mortar

Five mortar types namely, M, S, N, O and K were initially included in the first edition of CSA A 179-94 (1994) but later, Types M, O and K were excluded in the CSA A 179-04 (2004) edition. Only Type N mortar and Type S mortar are now specified in this Standard and recognized in CSA S304.1 (2004). As per CSA, Type N mortar has a moderate-strength, making it a mortar suitable for general use in exposed masonry above grade and recommended particularly when high compressive and/or lateral masonry strength are not required. Type O mortar is a low-strength, high-lime mortar, not recommended for severe exposure conditions. It can be noted that Type O mortar is moved to Annexs A and D in current version of CSA standard (CSA A179 2014) which is often used for restoring older, traditional masonry but is not recognized by CSA S304 (2014). As per CSA A 179-04 (2004), the mix design and strength requirements for Type N mortar and Type O mortar are described in Table 2.4 and 2.5 below. It is important to note that high-strength mortar, having a minimum cube compressive strength of 17.5 MPa at 28 days, is normally used for load-bearing structural components. This type of mortar is usually proportioned with higher fraction of cement content. On the other hand, low-strength mortar, having a minimum cube compressive strength of 0.5 MPa at 28 days, is normally used with low strength masonry block for non-structural applications. This mortar contains relatively high proportions of lime.

Table 2.4 Proportion specifications: mortar proportions by volume

Mortar type	Portland cement	Lime	Sand measured in damp, loose state
Type N	1	1	4-1/2 to 6
Type O	1	2	9

Table 2.5 Property specifications: compressive strength of mortar cubes

Preparation	Mortar Type	Minimum compressive strength, MPa	
		7 d test	28 d test
Job prepared or manufactured off-site in a batching plant, mixed to a flow suitable for use in laying masonry units	Type N	2	3.5
	Type O	1	2
Laboratory prepared, mixed to a flow of 110 to 115%	Type N	3	5
	Type O	0.5	2.5

2.2.2 Role of Fibre in Mortar Composites

The role of fibres in improving the mechanical properties of concrete is well-known (ACI 544.R1 1996). Fibres impart significant improvement to the tensile strength and post-crack residual strength in mortars under impact loading (Bharatkumar and Shah 2004; Glinicki 1994). Fibres improve the energy absorption capacity of concrete by enhancing its post-peak stress-transfer capability and hence their incorporation is an effective way of improving concrete's resistance to impact load. However, the choice of fibre type, length, and shape greatly influences the composite's performance. Fibres maybe metallic, mineral, polymeric, or natural. Short, discrete, polymeric fibres increase the energy dissipated by concrete under impact loading (Mindess and Vondran 1988) sometimes exceeding in dynamic impact factor over steel fibres (Bindiganavile and Banthia 2001). However, very little is known about their performance in mortars used for masonry. By using, Polyvinyl Acetate (PVA) fibres, Armwood et al. (2008) found that although the post-peak response in mortars improves with an increase in the fibre content, the strain at failure in a masonry unit was smaller, so that the flexural bond failed sooner and the benefits from the post-peak response of fibre reinforcement in mortars were not seen in the flexural response of the masonry unit. Their study concluded that the total fibre content should be restricted to an upper limit of 0.6% volume fraction. Chan and Bindiganavile (Chan and Bindiganavile 2010a) studied the effect of polypropylene micro-fibres on the behavior of Hydraulic Lime Mortar up to 0.5% volume fraction. Clearly, while micro-fibres may enhance the aggregate-paste interface in a stone masonry joint (Bentur and Alexander 2000), it is not just the strength but also the possible changes to the failure mechanism that define the composite response.

In general, fibres bridge cracks. Clearly, since the permeability is affected by crack widths, bridging the micro-cracks will definitely restrict the permeability. By using Type S mortar, Hoseini (2013) observed that the inclusion of polymeric fibres in mortar reduces its water permeability. Since permeability depends largely on the interconnected pore network within the mortar, it is important to examine and quantify the change of pore connectivity of that material.

2.2.3 Microstructure of Mortar

It is widely accepted that permeability is determined by the microstructure. Microstructure in this context is defined in terms of pores and the pore network. For cementitious materials, porosity and pore size distribution has a greater influence on fluid permeability (Goto and Goto 1981; Hughes 1985; Mehta and Manmohan, 1980; Nyame and Illston 1980) and only such pores with a diameter higher than a certain value contribute significantly to permeability (Goto and Goto 1981; Mehta and Manmohan, 1980; Nyame and Illston 1980). When determining permeability, only the liquid, which flows through the network of connected pores, is measured. Therefore, it is the structure and distribution of the connected pore network, and not the total porosity, which controls permeability.

Figure 2.3 describes a general scenario of the pore structure in porous media. Closed pores as in region '**a'** of Figure 2.3, do not contribute towards fluid permeability. Such closed pores are inaccessible to any external fluid and are totally isolated from their neighbours, and influence the macroscopic properties such as bulk density, elasticity, mechanical strength. On the other hand, pores that have a navigable channel of communication with the external surface of the body (like **b**, **c**, **d**, **e**, and **f**) are described as open pores. Open pores are further classified into "through pores" and "blind pores". Through pores have an open channel that begins at one location on the surface, extends into the particle, and re-emerges on the surface at a different location (like the pore channels c-e-c and c-e-d). Blind pores (also called dead-end or saccate pores) are open to the surface only at one end (like b and f).

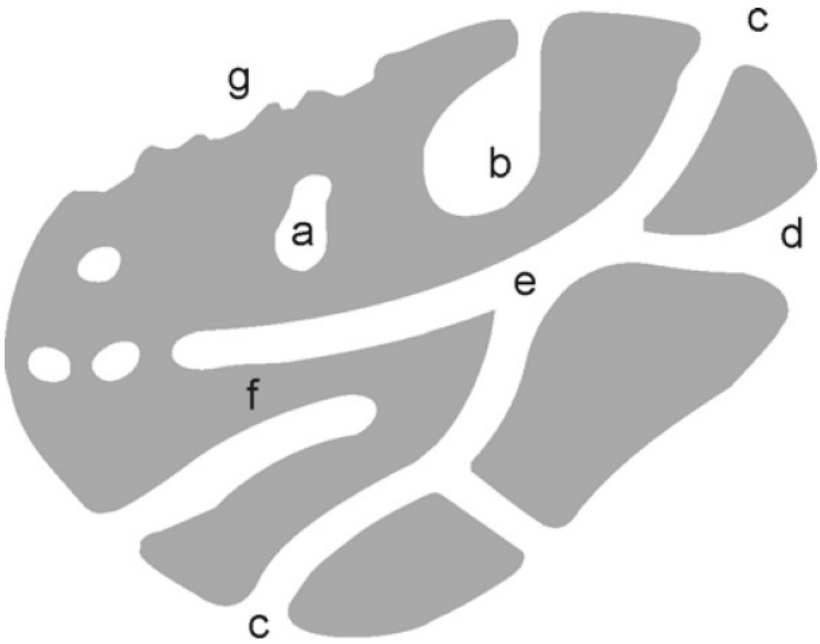

Figure 2.3 Schematic cross section of a porous solid (Rouquerol et al. 1999).

2.2.4 Methods to Evaluate Microstructure

The microstructure of cementitious materials has a significant influence on their physical and mechanical properties and on their durability. Over the past decades, researchers have tried to develop methods to determine the microstructure of these materials, to cover the entire range of pore size. Figure 2.4 describes several methods that are available for such an evaluation of porous material. It is worth noting that these methods are based on different physical principles and have their own limitations. Often it is necessary to use more than one method to cover the desired pore size range.

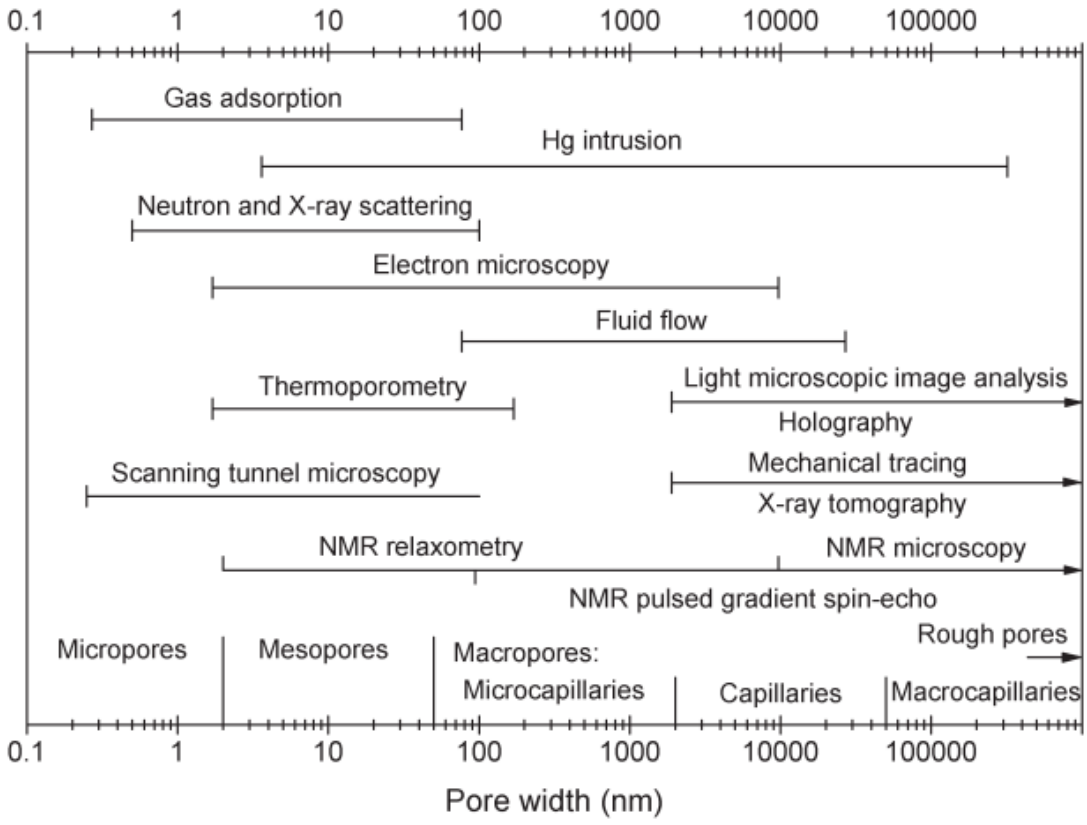

Figure 2.4 Measuring ranges of methods for pore size determination (*after*(Meyer et al. 1997)

2.2.4.1 Image analysis –Scanning Electron Microscope

Image analysis is a relatively new way to determine the pore structure of hardened concrete giving valuable information in this field. Both manual and automated methods of analyses can be used to assess the pore distribution of concrete paste. Standard ASTM C457 (2012) is one of the accepted methods, which measures the chords intercepted in the air voids along a series of regularly spaced lines of traverse (Hover and Phares 1996). Manual analysis is tedious and constitutes a limitation for a reproducible outcome. In addition, the results post analysis may be biased into a binary result by the operator who often has to run many images in a single session. Operator-fatigue might lead to erroneous results too. In the automated methods, images captured through a scanning electron microscope (SEM), optical microscope, or micro-

tomography device are analyzed by a suitable image analysis software. The air-void percentage, the spacing factor, shape factor, and surface area can be obtained when the automated technique is employed. Figure 2.5 shows an apparatus developed for the image analysis technique.

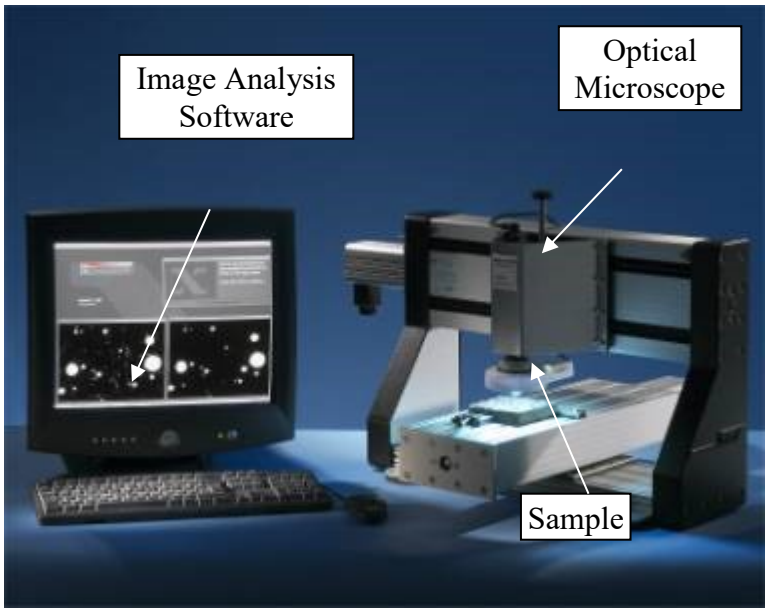

Figure 2.5 Image analysis technique employed for determining the structure of concrete ((CXI Corporate 2014) as of May 20th 2014)

Ever since pioneering work by Scrivener and Pratt (1984), Backscattered Scanning Electron Microscopy (BSEM) has been used more often as a method of microstructural evaluation for cement based materials. The SEM consists of an electric gun that emits electrons and the interaction of a beam of electrons and the specimen being investigated are the key feature to gather details of the specimen. Secondary electrons (SE) are produced throughout the interacting volume as a result of inelastic scattering whereas Backscattered Electrons (BSE) are the result of elastic scattering. This change from SE to BSE imaging is necessary as secondary electrons provide only topographical data whereas BSE provide atomic number contrast.

Secondary electrons are those electrons emitted from a sample with an energy less than 50 eV (Goldstein et al. 1981a). Most of the secondary electrons do not escape from the sample material because of their low energy. Only those secondary electrons, which are generated

very close to the surface, can emerge and be detected. Thus, secondary electrons have a very shallow sampling depth as shown in Figure 2.6. This is why, the secondary electron signals carry only topographic information and do not provide atomic number contrast. On the other hand, backscattered electrons are the result of elastic scattering. When the electron beams impinge on a target, some of the electrons penetrate into the target, expending all of their energy within the interacting volume. These electrons are absorbed by the target material. There is, however, a significant fraction of the beam of electrons, which strike the target and are then scattered back out of the specimen. These re-emergent electrons are known as backscattered electrons. The sampling volume for backscattered electrons is illustrated in Figure 2.6.

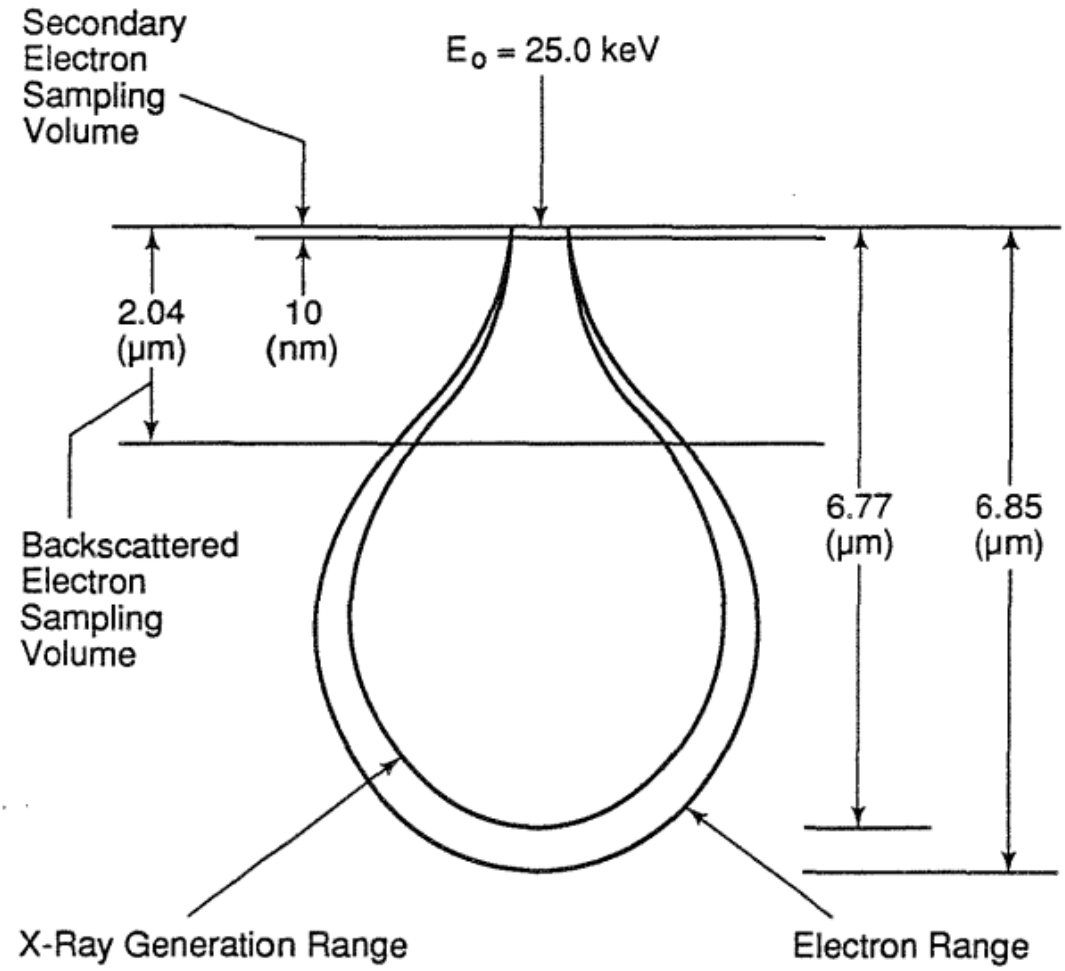

Figure 2.6 The schematic diagram of SEM comparing SE and BSE (adapted from (Zhao and Darwin 1990))

As BSE has higher energy than SE and so can penetrate greater depths, this is the prime favorable feature for the BSE. This feature is also responsible for the lower resolution of the BSE images compared to SE images. The intensity of the BSE signal is mainly a function of the average atomic number of the sample area under investigation. Analysis of flat polished sections, which can be prepared to be representative and reproducible, allows the quantification by image analysis of the different microstructural constituents.

In case of cementitious samples, they need to be properly polished to examine using BSE scanning. When preparing a polished section of such a porous material for examination by scanning electron microscope (SEM), it is often necessary to impregnate first with epoxy, to provide physical support during sectioning and polishing. Epoxy also facilitates the identification of voids and pores using SEM with backscattered electron (BSE) imaging, since the low atomic number of epoxy provides a contrast with the other constituents of hydrated cement products. Note that the epoxy impregnation can highlight more porous areas of cement paste, but it is not effective in distinguishing cracks (Soroushian et al. 2003).

As the intensity of the BSE signal is primarily a function of the average atomic number of the local sample area, this characteristic feature can be used to identify various microstructural features of the specimen surface with the help of morphological image processing techniques. Based on the contrast in atomic numbers, various phases like the unhydrated cement paste, CH, C-S-H and so forth can be identified.

Several researchers used the BSE technique to investigate the pore structure and to evaluate the air void network of cement based systems (Lange et al. 1994; Peterson et al. 2009; Yun et al. 2007; Zalocha and Kasperkiewicz 2005; Zhang et al. 2016). In most cases, the BSE method gives superior results in comparison with mercury intrusion porosimetry.

2.2.4.2 Image analysis – micro CT

X-ray Computed Tomography, also known as X-ray CT, is a novel non-destructive technique that has been used by a number of researchers to evaluate specific features of cement-based materials (Landis et al. 1999, 2003, 2007; Naik et al. 2006; Stock et al. 2002). Figure 2.7 describes the underlining principle of this process. In this method, an X-ray beam is sent to the specimen and the transmitted beam is recorded on a detector. The resulting image (or radiographs) is a superimposed information or projection of a volume in a 2D plane. A series of images, also called slices, are taken at many angles or projection views and then mathematically, a 3D map of X-ray attenuation is possible to reconstruct (Landis et al. 2007). Visualization and quantification of the microstructure of cementitious materials in 2D and 3D without physically cutting the specimen into thin sections are made possible using X-ray CT. It allows us to characterize the cracks that are formed inside a sample. Moreover, the information obtained from the analysis of digitized images allows us to measure 3D parameters such as the connectivity and tortuosity of voids, cracks or the pore space. Recently, researchers have developed algorithms that can be used to determine the degree of connectivity and tortuosity in cement-based systems such as mortar and concrete (Bentz et al. 2000; Hoshen and Kopelman 1976; Nakashima and Kamiya 2007; Watanabe and Nakashima 2001). However, this method requires high energy source and high resolution when studying cement-based systems (Diamond and Landis 2007). This method can also be used to calculate fracture parameters such as the fracture energy for mortar specimens (Landis et al. 2007; Landis and Nagy 2000).

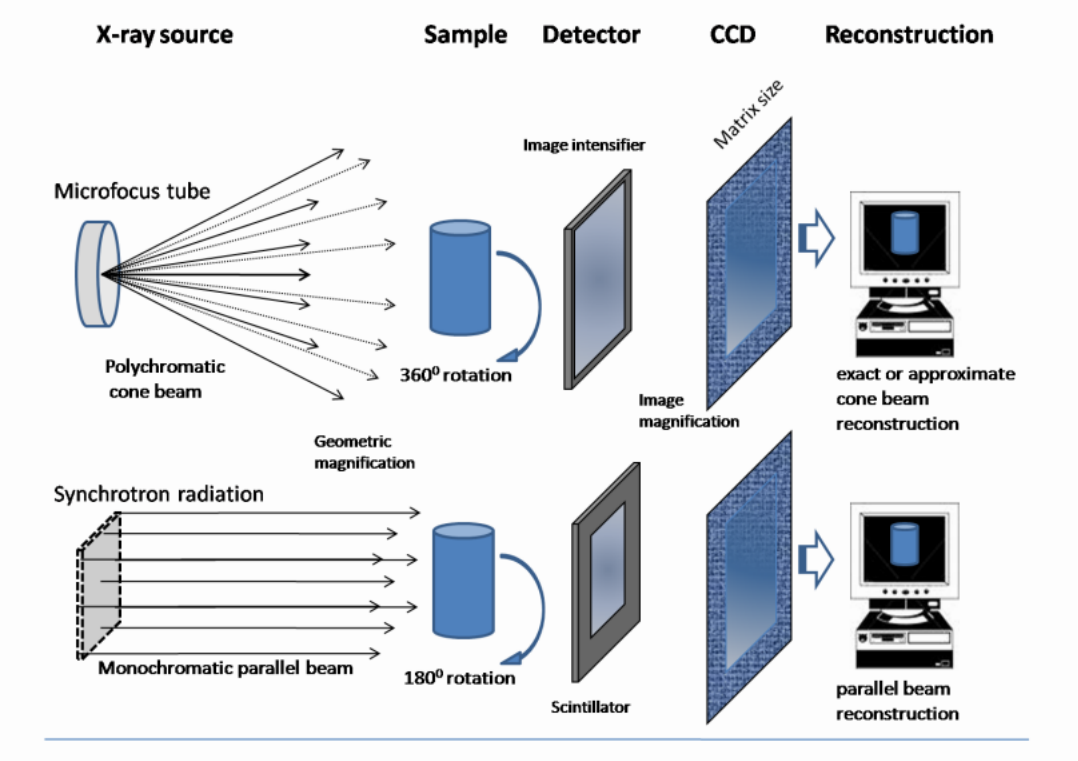

Figure 2.7 The schematic diagram of X-ray CT

2.2.4.3 Mercury Intrusion Porosimetry

Mercury Intrusion Porosimetry (MIP) is a widely used method for the evaluation of the pore structure in cement-based systems (Cnudde et al. 2009; Kumar and Bhattacharjee 2003; Laskar et al. 1997). The principle of MIP technique is well described in Figure 2.8. It is based on the principle that a non-wetting liquid (one having a contact angle greater than 90°) will only intrude capillaries under pressure. The relationship between the pressure and capillary diameter is described by Washburn (1921) as shown in Figure 2.8. Mercury intrusion measurements are extremely simple in principle and ease to apply, although a number of experimental complications need to be considered. In the MIP procedure, first a small specimen is dried to remove any existing fluid from the pores. The sample is then weighed, transferred to a chamber, which is then evacuated, and mercury is introduced to surround the specimen. In order to force mercury into the empty pores, pressure is applied, as mercury will not fill the pores on its own. This pressure is applied to the mercury progressively, and the intrusion of

mercury at each step is monitored. Then the pore size distribution will be calculated based on the set of pressure steps and corresponding mercury volume intruded into pores.

The two-basic assumptions of the Washburn model namely, 1) that pores are cylindrical and 2) that the pores are accessible from the outer surface of the specimens, are both, highly criticized (Diamond 2000; Ilavsky et al. 1997). The pore structure of the cementitious composites is not perfectly cylindrical (Nokken and Hooton 2007). Besides, only a small portion of the specimen is directly open to the outside of the specimen and hence influences the results (Diamond 2000). In addition, in MIP, larger pores are filled first with mercury under low pressure while the smaller pores are filled only later with an increase in the pressure. Hence, a pore size distribution calculated from the Washburn equation provides no measure of the proportion of pore space constituted by the large pores, or indeed, of its very existence. The MIP technique misrepresents the size of these pores due to the "ink-bottle" effect (Abell et al. 1999). This "ink-bottle" effect may also affect the contact angle of the mercury for cement-based systems. Further, the contact angle may change depending upon the roughness of the surface. It was also observed that the mercury intrusion might damage and alter the pore structure (Cook and Hover 1999; Shi and Winslow 1985). MIP results are also affected by other experimental factors such as sample preparation, forms and types of sample, sample drying technique and rate of pressure application (Bourdette et al. 1995; Feldman and Beaudoin 1991; Hearn and Hooton 1992; Laskar et al. 1997).

Though Diamond (2000) advised to discard the MIP technique of measuring pore size distribution in hydrated cement systems, knowledge of the critical pore radius and total porosity as derived through MIP may yet constitute useful comparative indices of the cement paste or the concrete pore (Mindess et al. 2003; Roy 1988).

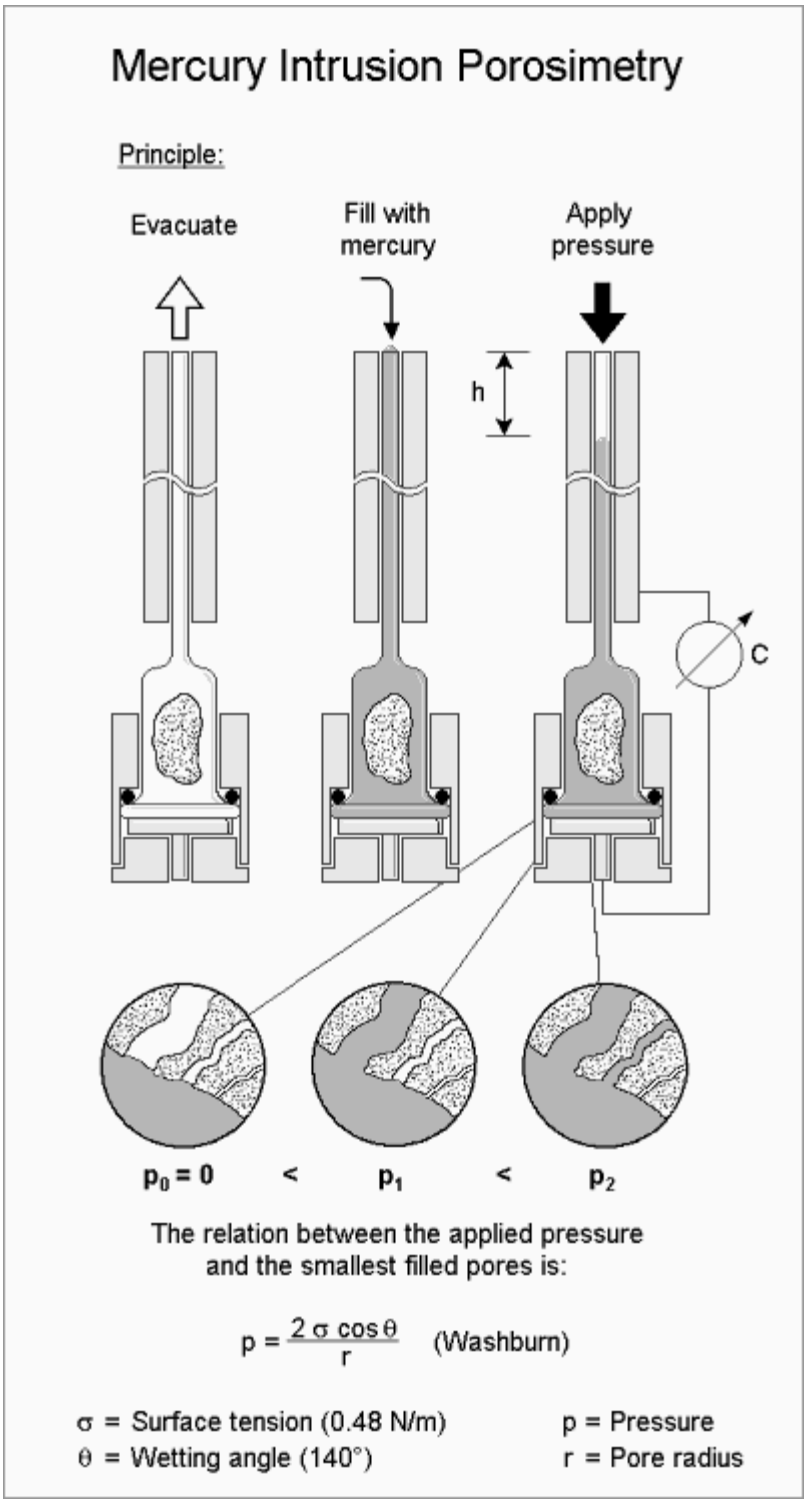

Figure 2.8 Principles of the MIP technique ((Fraunhofer 2014) as of May 19th 2014)

2.2.4.4 Cryoporometry

Cryoporometry (also known as Thermoporometry) is a method to measure porosity and pore size distribution based on the melting point depression or the crystallization point depression of a liquid confined in a pore (Brun et al. 1977). The main reason of this shifting of the melting or freezing points is due to the surface tension of the solid-liquid interface and the radius of curvature (Defay and Prigogine 1966). Water as well as several organic liquids such as chlorobenzene, cyclohexane, and 1,4-dioxane can be used as the probing liquid to create a solid-liquid interface for this study. By far, water is the most widely used among them.

The detection of the melting or freezing point can be accurately measured by a) sensing the transient heat flows during phase transitions using differential scanning calorimetry – DSC Thermoporometry (Brun et al. 1977), b) measuring the quantity of mobile liquid using nuclear magnetic resonance – NMR Cryoporometry(NMRC) (Mitchell et al. 2008; Petrov and Furó 2009) or c) measuring the amplitude of neutron scattering from the imbibed crystalline or liquid phases – ND Cryoporometry (NDC) (Webber and Dore 2008). Various researchers developed several methods to calculate the pore size and the change in pore volume from DSC thermogram (Brun et al. 1977; Ishikiriyama and Todoki 1995; Landry 2005). Ishikiriyama et al. (1996) verified the Cryoporometry method with DSC using composites of known pore characteristics.

The primary disadvantage of the method is that it is nontraditional, and its use is not as widespread as Mercury Intrusion Porosimetry (MIP). The effect of specific interactions between the probing liquid and the porous solid are largely unknown and may lead to uncertain interpretation of calorimetric signals (Landry 2005). This method is also applicable at the meso-level. However, is throws up superior results for cellulose-based fibre reinforced composites (Banthia et al. 2012) and also this method is preferable when other methods such as MIP may provide inaccurate pore properties due to damage to the micro-structure and over-estimation of smaller pore sizes (Iza et al. 2000).

2.2.4.5 Gas adsorption

Gas adsorption is one of the most widely established methods for pore size determination of porous materials. Pores ranging from 0.3 nm to 300 nm can be identified by gas adsorption method. Among other readily available gases and vapours that can be used as adsorptive for this method, nitrogen has remained universally pre-eminent and most commonly used adsorbate. The porosity of porous solids can be conveniently characterized by gas adsorption studies. The gas molecules adsorb on the solid surface when a porous solid is exposed to a gas. The solid sample is first cleaned from contaminants, cooled under vacuum to 77 K and then exposed to several doses of nitrogen. As pressure increases with every new nitrogen dose, nitrogen molecules occupy the surface and fill the pores. Depending upon the adsorbed gas quantity as related to the relative pressure at constant temperature produces an isotherm curve. An understanding of the surface area and porosity of an adsorbent can be achieved by the construction of an isotherm. A typical isotherm is shown in Figure 2.9 for porous materials. Adsorption or desorption isotherm are generated by recording the amount of gases removed from the system or returned to the system during the whole process. It is generally accepted that the desorption isotherm is more appropriate than the adsorption isotherm for evaluating the pore size distribution of an adsorbent. The desorption branch of the isotherm, for the same volume of gas, exhibits a lower relative pressure, resulting in a lower free energy state. Thus, the desorption isotherm is closer to the true thermodynamic stability. Conner et. al. (1986) found the similarity between the pore size distribution determined from nitrogen desorption data and the distribution obtained from the intrusion phase of mercury intrusion porosimetry. Finally, pore size distribution can be calculated from the isotherm and by choosing an appropriate model.

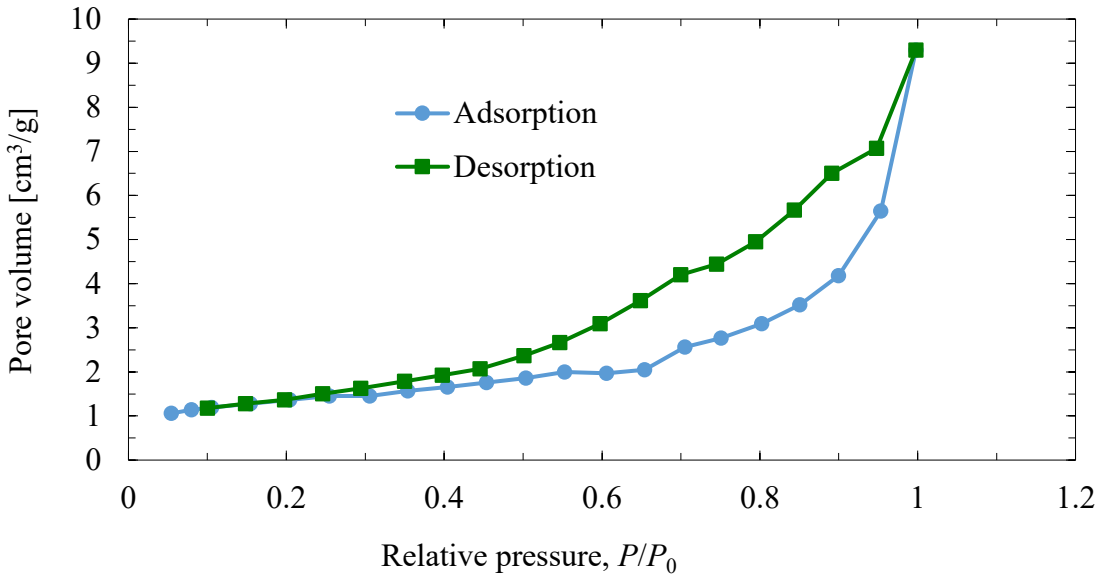

Figure 2.9 Isotherm of porous material generated by Nitrogen adsorption method

The pore radius can be determined from the following equation (Allen 2013):

$$r_p = r_k + t \tag{2.1}$$

where r_p is the actual pore radius, r_k is the Kelvin radius at which condensation occurs, t is the thickness of the adsorbed layer. r_k can be calculated by assuming cylindrical pore geometry using the Kelvin equation (16) in the form:

$$r_k = \frac{-2\gamma V_m}{RT \ln\left(P/P_0\right)} \tag{2.2}$$

Where γ is the surface tension of nitrogen at its boiling point (8.85 ergs/cm^2 at 77 K), V_m is the molar volume of liquid nitrogen (34.7 cm^3/mol), R is the gas constant (8.314 x 10^{7}ergs/deg/mol), T is the boiling point of nitrogen (77 K), and P/P_0 is the relative pressure of nitrogen.

A more convenient method for estimating t was proposed by de Boer (de Boer et al. 1966) in the following expression:

$$t(\text{Å}) = \left[\frac{13.99}{\log\left(P/P_0\right) + 0.034}\right]^{1/2} \tag{2.3}$$

Assuming that the initial relative pressure $\left(P/P_0\right)$ is close to unity, all pores are filled with the liquid. Then the volume of each pore can be calculated by using the BJH (Barrett et al. 1951) method:

$$V_{pn} = \left(\frac{r_{pn}}{r_{kn} + \Delta t_n/2}\right)^2 \left(\Delta V_n - \Delta t_n \sum_{j=1}^{n-1} c_j A_{pj}\right) \tag{2.4}$$

where n represents n^{th} pore, V_p is the actual pore volume, Δt is the change of thickness of the adsorbed layer, ΔV is the observed volume of gas desorbed, $c = \left(r_p - t_r\right)/r_p$, $A_p = \frac{2V_p}{r_p}$ and t_r is the thickness of the observed layer at the corresponding relative pressure.

As mentioned earlier, this method can only determine pores in the range of 0.3 nm to 300 nm. Other methods need to be used to evaluate larger pore sizes. One setback is that the time used for a single analysis can be hours. However, measurements can be done automatically for example during the night. With nitrogen adsorption, only open pores are determined, and the cylindrical pore model is assumed in pore size distribution measurements. The desorption isotherm in the characterisation of pore size distribution is affected by the pore network; i.e. when pressure is reduced, liquid will evaporate from large open pores, but pores of the same size that are connected to the surface with narrower channels remain filled (Allen 2013). This changes the shape of the pore size distribution. The samples come into contact with the temperature of liquid nitrogen (-196 ° C) during analysis, which may destroy them.

2.2.5 Permeability

Permeability is a transport property where fluid flow occurs through a medium and as per Darcy (1856), the rate of flow is directly proportional to the pressure gradient. Consider a porous, permeable medium such as a porous rock, filled with a fluid such as water. Whenever there exists a spatial gradient in the hydraulic potential of the pore fluid, the fluid will flow

through the rock in response to this gradient. The precise relationship between the potential gradient and the flowrate is given by Darcy's law, which states that the flow rate is given by:

$$Q = -\frac{kA}{\mu}\frac{\Delta P}{L} \tag{2.5}$$

where Q is the volumetric flowrate, A is the area of the porous media normal to the flow, μ is the viscosity of the pore fluid, ΔP is the pressure gradient, L is the specimen thickness or the length of flow path, and k is the permeability. In equation 2.5, k has the dimensions of (length)^2. By rearranging equation 2.5 and introducing a new term, k', called the intrinsic permeability, which is independent of the fluid involved (unit length^2), we get:

$$k' = -Q\frac{1}{A}\frac{\mu}{\rho g}\frac{L}{\Delta P} \tag{2.6}$$

Here, ρ is the density of the fluid (kg/m^3) and g is acceleration due to gravity. The coefficient of permeability, k (unit length/sec) and intrinsic permeably is related as:

$$k = k'\frac{\rho g}{\mu} \tag{2.7}$$

Hence, for a constant-head permeability set up as shown in Figure 2.10, the coefficient of permeability k can be expressed as:

$$k = -\frac{QL}{A\Delta h} \tag{2.8}$$

where Δh is the pressure head (unit in length).

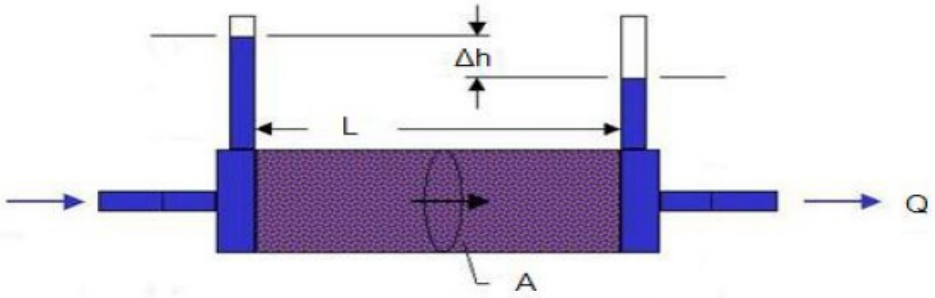

Figure 2.10 Schematic Illustration of Darcy's law

In SI units, the parameters described in equation 2.5 and 2.7 will have the following units:

k' = intrinsic permeability, which is independent of the fluid involved (m^2)

k = the coefficient of permeability (m/sec)

Q = rate of water flow (m^3/s)

A = permeation area (m^2)

Δh = pressure head (m)

L = specimen thickness or the length of flow path (m)

μ = dynamic viscosity of the fluid (N s/m^2)

ρ = density of the fluid (kg/m^3)

g = acceleration due to gravity

For water, $\rho = 1000\ {}^{kg}/_{m^3}$, $\mu = 1\ centipoises\ (= 10^{-3}\ {}^{kg}/_{m.s})$ and $g = 9.81\ {}^{m}/_{s^2}$, and hence,

$$k = 9.8 \times 10^6\ k' \qquad (2.9)$$

Therefore, for water at 20°C, the Darcy permeability coefficient (m/s) is approximately 9.8×10^6 times the intrinsic permeability coefficient (m^2). It is very common to express intrinsic permeability in term of darcy and millidarcy units: 1 darcy is equivalent to 9.869233×10^{-13} m^2 or 0.9869233 $(\mu m)^2$ (Society of Petroleum Engineers 1984). A medium with a permeability of 1 darcy permits a flow of 1 cm^3/s of a fluid with viscosity 1 cP (1 mPa·s) under a pressure

gradient of 1 atm/cm acting across an area of 1 cm². Darcy's law is only valid for low flowrates (Bear 1972). At higher flowrates, defined as those for which the Reynolds number is greater than unity, the pressure gradient is generally found to be a quadratic rather than a linear function of the flowrate. However, such high flowrates are the exception, and non-Darcy effects will not be considered in the present study.

2.2.6 Tortuosity and Formation Factor

Tortuosity is generally defined as the ratio of the length of the actual flow path to the length of the porous medium in the direction of the flow as shown in equation 2.10.

$$\tau = \frac{L_e}{L} \tag{2.10}$$

Where τ is the Tortuosity, L_e is the actual flow path and L is the length of the porous media.
The formation factor, F is another important parameter for determination of fluid permeability of porous media. Here, F refers to the electrical resistivity of porous media saturated with a conductive fluid, normalized by that of the bulk fluid (Guéguen and Palciauskas 1994). As shown in equation 2.11, the Formation factor can be expressed as follows:

$$F = \frac{\tau^2}{\phi} = \frac{D_o}{\phi D} = \frac{R_o}{R_w} \tag{2.11}$$

where F is the formation factor, τ is the tortuosity, ϕ is the porosity, D_o is the pure gas diffusion coefficient, D is the diffusion coefficient of a porous material like concrete or mortar, R_o is the electrical resistivity of the porous media saturated with the electrically conductive fluid and R_w is the electrical resistivity of the electrically conductive fluid saturating the porous medium.
However, the definition of tortuosity available in literature is not unique. While $\tau = \frac{L_e}{L}$ is called the geometric tortuosity or hydraulic tortuosity. Whereas, diffusive tortuosity is defined as the square of the geometric tortuosity (Promentilla et al. 2016b).

$$\tau_g = \frac{L_e}{L} = \sqrt{\frac{D_o}{D}} \tag{2.12}$$

where τ_g is the geometric tortuosity and $\frac{D_o}{D}$ is the diffusive tortuosity.

Tortuosity and Formation Factor are two important parameters for the determination of fluid permeability. Porosity and pore geometry are the two most important parameters for fluid flow through porous media. Though porosity can be easily determined, pore geometry is complicated and often not revealed. The importance of pore geometry on fluid permeability is described in Figure 2.11. Determining the tortuosity and formation factor therefore provides a better understanding of the fluid flow mechanism and void space complexity in porous media.

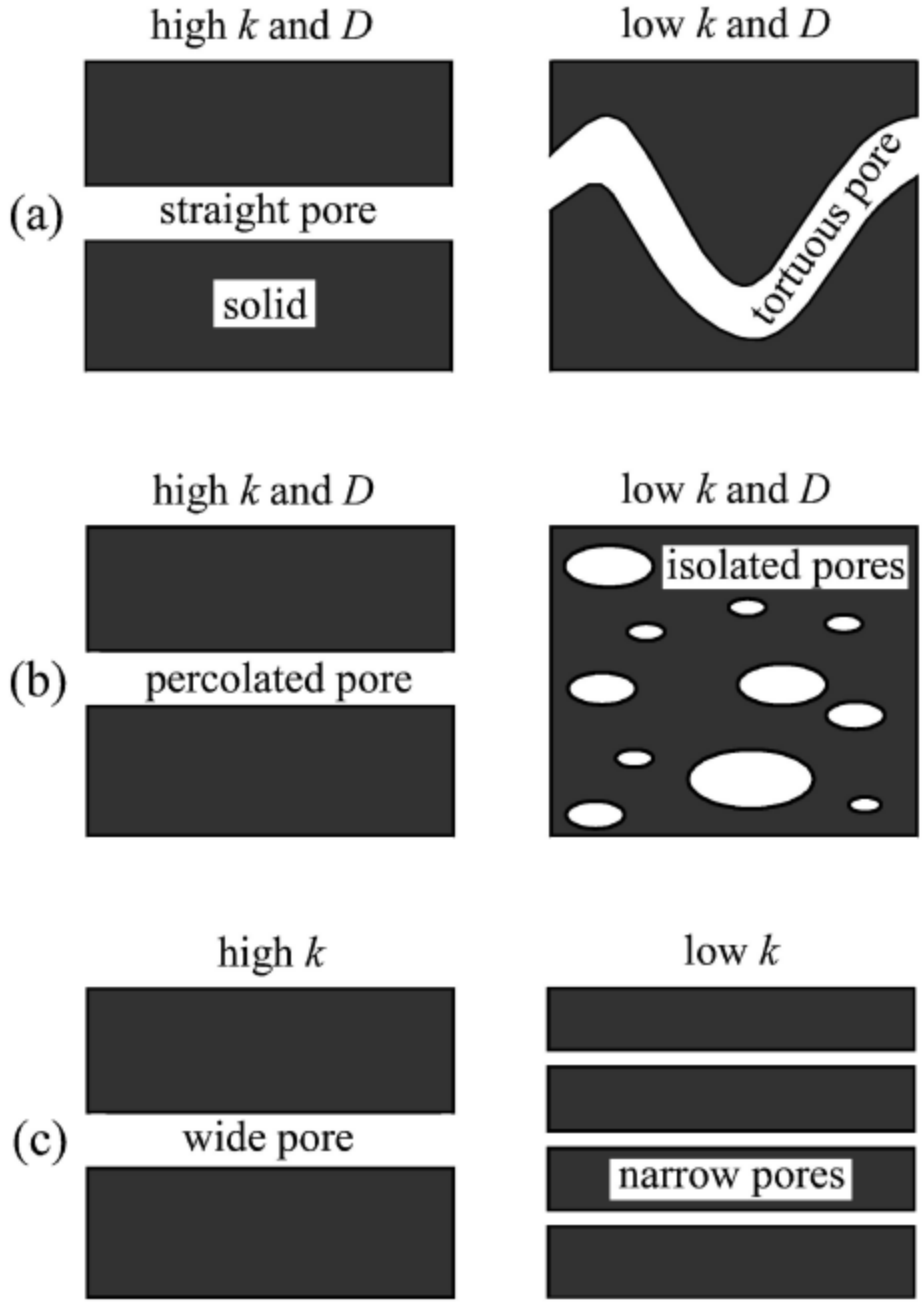

Figure 2.11 The effects of pore geometry on the permeability (k) and pore fluid diffusivity (D) in porous media, (a) Same pore diameter but with different tortuosity: The straight or less tortuous pipe yields higher permeability, (b) Percolated pore crossing the whole system compared with isolated pores: The former gives higher permeability, and (c) Same porosity but with different pore diameter: The former yields higher permeability. (Adopted from (Nakashima and Kamiya 2007)).

2.2.7 Permeability measurement techniques

Measuring permeability involves a time-consuming test, with attendant concerns about system equilibrium and load control. Therefore, a quick, simple and preferably in-situ test method for investigating the permeability of structures with mortar in service is favorable. This method has been used to evaluate cement-based composites since 1940s. There are very few examples available to use this method for mortars but there is none for controlled low strength materials like HLM (Lafhaj et al. 2006). Relating permeability with ultrasonic pulse velocity offers tremendous potential, especially in condition assessment of existing structures wherein a rapid and non-destructive test method is needed for durability evaluation of masonry structures.

The permeability test setup as used in this study was adapted from the apparatus developed by Biparva (2005) and was modified and used by Hoseini (2013) here to monitor the onset of the steady state condition in fluid flow. A schematic view of the permeability apparatus developed for the present study and a photo of the test setup at the Civil Engineering Materials Laboratory at the University of Alberta, are shown in Figures 2.12 and 2.13, respectively. The apparatus originally consisted of five major sections: a cylindrical concrete specimen with a hollow core; a permeability cell that houses the concrete specimen; a pressurized water supply unit; an outflow measurement device (with an accuracy of 0.01g); and a Materials Testing System (MTS) with capacity of 1000 kN, which is capable of applying stress in compression under load control. In addition, this permeability cell was further instrumented with a computer and programmed to measure and record the mass of water flow in real time, thereby enabling detection of the onset of equilibrium in flow. The flask used to collect the water are completely sealed to significantly minimize the water evaporation during the test and thus negligible evaporation will be assumed.

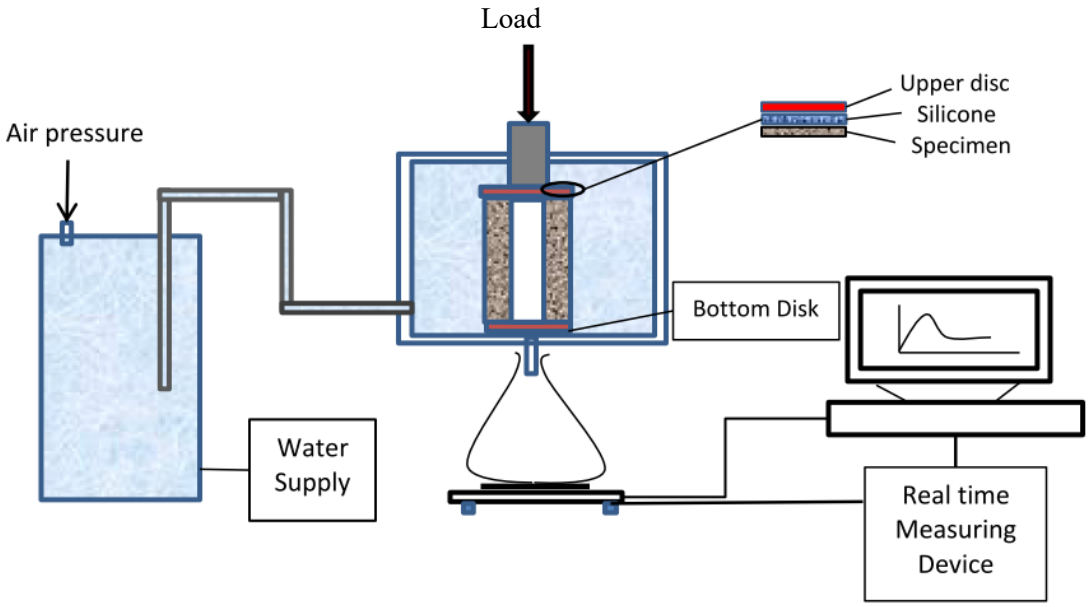

Figure 2.12 Schematic view of the test setup for permeability measurement under compressive stress (adapted from Biparva (2005)and used by Hoseini (2013)) (Source: (Hoseini 2013))

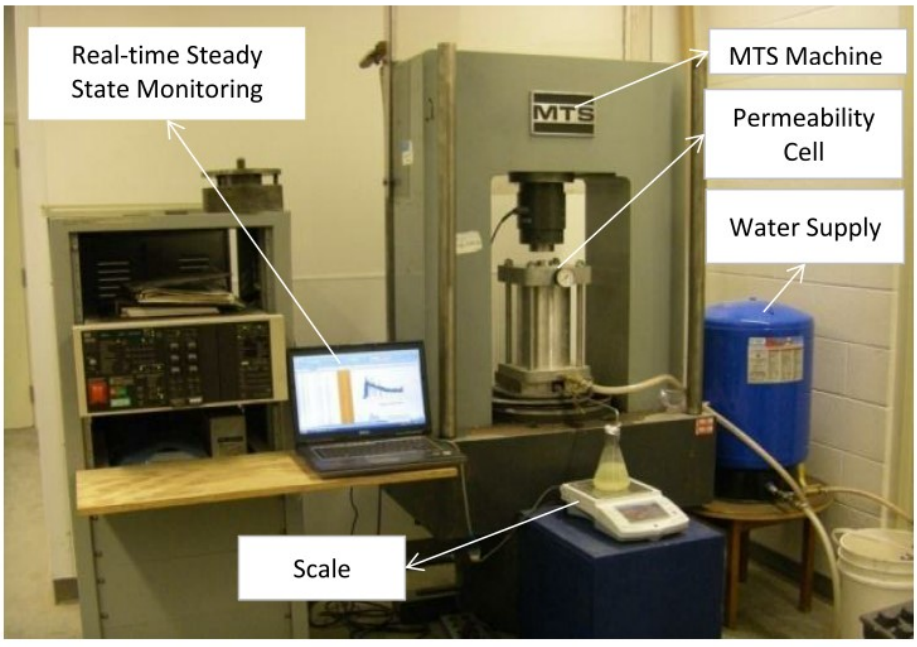

Figure 2.13 Measuring the water permeability under Stress (Source: (Hoseini 2013))

2.2.8 Application of Nano-lime

The use of nano-materials offers promise within construction in general and, the conservation of heritage structures, in particular. Two recent types of nano-products are nano-lime and nano-silica and both of them have been employed towards improving the performance of repointing mortar. Nano-lime consists of very small particles of calcium hydroxide suspended in alcohol; the average diameter is quoted as 150 nm with a range of 50-300 nm. Nano-lime particles are much smaller than the conventional particles of calcium hydroxide present in fresh lime putties (8,000 nm). The smaller particle size of nano-lime has the advantage of achieving greater penetration into the pores, while the higher surface area/volume ratio allows for greater reactivity (Musacchi 2014).

The main theoretical advantages of nano-limes are: (1) they can carry much greater quantities of lime because they are suspensions of lime (rather than solutions); (2) no water is involved in the application, since the nano-lime is suspended in alcohol.

When a substrate is treated with nano-lime, calcium hydroxide is precipitated in the pores of calcareous materials as the alcohol disperses and/ or evaporates. As calcium hydroxide carbonates to calcium carbonate, it replaces the lost binder or matrix in natural stone and plasters, thereby knitting together fine cracks and deteriorated stone, increasing the strength and imparting integrity. The overall carbonation process is represented by the following reaction:

$Ca(OH)_2 + (H_2O + CO_2) \rightarrow CaCO_3 + 2H_2O$

2.2.9 Durability of Mortar

The durability of mortar rests in its ability to endure exposure conditions. Durability is the most important property of masonry and consequently consideration must be given to those factors, which contribute to a lack of durability. In masonry, two prime requisites for durability are a dimensionally stable unit and a mortar that forms a permanent and complete bond, thereby making the structure watertight. Although aggressive environments and the use of unsound materials may contribute to the deterioration of mortar joints, the major destruction is from

water entering the masonry. Damage to mortar joints and to mortar bond by frost action in colder climates is of greatest importance in exposed applications such as parapet walls or exterior pavers. Air-entrained mortar will withstand hundreds of freeze- thaw cycles, and its use provides good protection against localized freeze-thaw damage. Masonry cement mortars generally have greater resistance to freeze-thaw deterioration than non-air- entrained mortars. This superior performance can be attributed to the controlled air content of masonry cement mortars.

A mortar of lesser durability may be suitable for internal walls but could weather very badly on exposed chimney stacks, for example. Where a mortar of lower strength than the masonry units is used, any water flow will tend to take place preferentially through the mortar joint. If any degradation occurs due to freezing and thawing, the mortar joint may be replaced relatively easily. In contrast, if a relatively dense and impermeable mortar is used with more permeable masonry, any flow of water that takes place will tend to pass preferentially through the masonry unit rather than through the mortar joint. This may lead to salt crystallization (efflorescence) on the surface of the masonry and/or degradation of the masonry unit due to freezing and thawing. There is often a requirement to test mortar for durability, but satisfactory tests are difficult to develop in practice and most suggested regimes are either too lengthy and complicated or do not relate sufficiently well to site practice.

2.3 Concluding Remarks

Based on the review of the relevant literature on the behaviour of plain and fibre reinforced lime mortar and cement-lime mortar, it was found that several aspects of microstructural and macro-mechanical characterization have received scarce attention. Evaluating the pore structure and permeability have not received adequate attention either. Furthermore, the experimental methods in some cases were found to be inappropriate. For example, the use of MIP technique to assess the pore structure does not reveal the true nature pore characteristics.

CHAPTER 3. EVALUATION OF MICROSTRUCTURE IN FIBRE REINFORCED REPAIR MORTARS

3.1 Introduction

Any cementitious material is essentially porous and so is permeable, allowing fluid flow through it. The disposition of the internal air-voids, their distribution, connectivity and size determine the water permeability of the system. Therefore, it is necessary to study first the parameters that constitute the microstructure and their quantum of influence on the overall permeability.

Materials prepared with binders such as lime and cement, can be regarded as chemically bonded ceramics. Upon mixing with water, the hydration reaction of these binders results in a solid product consisting a pore system. These pores, formed due to the desiccation of water added during mixing, are inherent to the cementitious systems. Apart from having a direct bearing on the permeability, the air-void system ultimately decides the hardened properties of the system, including its strength and durability (Därr and Ludwig 1973; Rostásy et al. 1980).

3.2 Objectives

The objectives of this chapter are firstly, to identify and evaluate the extent to which each of the various microstructural features affects the permeability and mechanical properties. The role of fibre reinforcement on the microstructure in such controlled low strength mixtures will be investigated using a polymeric micro-fibre. First, the porosity is evaluated using three different methods and the results are discussed along with the effect of adding fibres. Second, the pore size distribution of the plain and fibre reinforced mortars are determined by MIP method, nitrogen adsorption method, and image analysis method. Third, comparative studies are conducted for pore size distribution of plain and fibre reinforced mortar as recorded by MIP method and image analysis method. Fourth, microstructural features such as specific surface area and characterization of pore structure and their variation with fibre addition as determined by a spatial correlation called the two-point correlation function are discussed.

Finally, the fractal dimension for plain and fibre reinforced mortars, as determined from SEM images, is described using the dilation method and the box-counting method.

3.3 Experimental Details

3.3.1 Materials and Sample Preparation

Mortar samples were prepared using a drum mixer. The mixing sequence, crucial to achieving the desired workability, was as follows: First, 2/3 of the mix water was added to the mixer along with half the design amount of the fine aggregates and the entire binder. After 2-3 minutes of mixing, the remaining half of the sand and the balance amount of water were added with an additional 8-10 minutes of mixing. At this point, for the fibre reinforced mixtures, polypropylene micro-fibres was added to the mixer. These fibres needed to be fluffed through an air-jet to ensure maximum dispersion in the mix. After 2-3 minutes of further blending, the workability of the fresh mortar was determined by using a flow table as per ASTM C1437 (2007), and shown in Figure 3.1. Three different binders were used namely, one based on the natural hydraulic lime, and two others that were lime-Portland cement blends and correspond to Type N mortar and Type O mortar, respectively.

The natural hydraulic lime (NHL 2) with a targeted compressive strength of 2 MPa (at 180 days) was sourced from France. The mix design was prepared for specified 7-day and 28-day compressive strength and flow values as per CSA specification for Type N mortar and Type O mortar. Note that Type N mortar and Type O mortar were prepared by combining slaked lime with a specified fraction of Portland cement (as described in CSA A179-2044 (2004) . The reason for selection of such binder combination is: (a) to impart a certain degree of hydraulicity and (b) to promote faster gain in strength. Polypropylene micro-fibres, a hydrophobic fibre (Bentur and Mindess 2007), as shown in Figure 3.2, with properties as listed in Table 3.1, were introduced as the discrete reinforcement at dosage rates of 0.10%, 0.15%, 0.20%, 0.25%, and 0.50% by volume fraction (V_f). Since polypropylene fibre having a length of 20 mm and a diameter of 22 μm is the most commonly used fire for non-structural application (Bentur and Mindess 2007), it was utilized in this study to evaluate the effect of synthetic micro-fibres on

the permeability of repair mortar. The plain mortar was prepared as per CSA A179-04 (2004) and the mixture design with the three binder types are shown in Tables 3.2, 3.3 and 3.4. For the plain mortar, the water-to-binder ratio was suitably adjusted by trial-and-error, to achieve a flow between 100-115% in order to meet the workability criterion per CSA A179-04 (2004). The mixture proportions were kept the same for all samples of a particular mortar type, regardless of fibre content, even it resulted in a flow value different from that for the plain mortar. A blended sand was used as the fine aggregate conforming to the bounds as shown in Figure 3.3. This gradation is particularly designed to ensure superior durability in the context of historic masonry structures (Maurenbrecher et al. 2007).

Hollow-core cylinders as shown in Figures 3.4 and 3.5, having an outer diameter of 100 mm, an inner diameter of 50 mm, and a height of 200 mm were cast with all three types of mortar. The hollow core was created using a solid shaft of Teflon inserted at the time of casting. For Type N and O mortar, the hollow-core cylinders were cured in their moulds for 3 days to ensure a strength gain, sufficient to withstand the removal of the Teflon shaft. The Teflon shafts were removed using a hydraulic extrusion jack. After demolding, the cylinders were stored in a humidity and temperature-controlled room at 95±5% humidity and 23±2 °C for at least 28 days and thereafter, they were left in the ambient laboratory environment (18-24 ºC and 30-50% relative humidity) until they were tested. The specimens made from Hydraulic Lime Mortar were left in their moulds after casting at room temperature and humidity to be demoulded after 7 days, whereupon they were stored under ambient temperature and humidity (18-24ºC and 30-50% relative humidity) for another 180 days before conducting experiments.

After curing, a random representative hollow cylinder was sawn without using water for different microstructural tests. In order to prevent possible microstructural damage caused by drying and shrinkage cracks, water was avoided during the saw cut. Representative specimens were then prepared for each method of microstructural quantification.

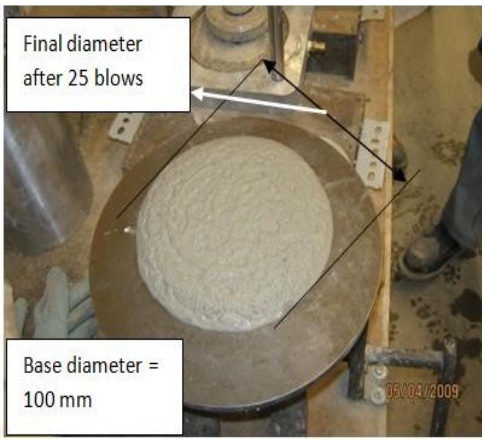

Figure 3.1 Workability of mortar mixes as determined by a flow table

Figure 3.2 Polypropylene micro-fibres used in this study

Table 3.1 Properties of polypropylene micro-fibres

Specific Gravity	0.91
Fibre Length (mm)	20
Density (kg/m^3)	910
Tensile Strength (MPa)	450
Modulus of Elasticity (MPa)	3450
Denier	3 (equiv. diameter = 22 μm)

Table 3.2 Mix design of Hydraulic Lime Mortar

Mix & Designation	Fibre Content (% V_f)	NHL-2 (kg/m^3)	Sand (kg/m^3)	Water (kg/m^3)	Slump Flow (%)	Compressive Strength (MPa)
0.00% V_f Fibre (F0.00)	0	400	1200	400	103	2.49
0.10% V_f Fibre (F0.10)	0.10	400	1200	400	97	2.47
0.15% V_f Fibre (F0.15)	0.15	400	1200	400	90	2.43
0.20% V_f Fibre (F0.20)	0.20	400	1200	400	65	2.39
0.25% V_f Fibre (F0.25)	0.25	400	1200	400	48	2.30
0.5% V_f Fibre (F0.50)	0.5	400	1200	400	39	1.99

Table 3.3 Mix design of Type N mortar

Mix & Designation	Water (kg/m^3)	Fibre Content (% V_f)	Cement (kg/m^3)	Slaked Lime (kg/m^3)	Sand (kg/m^3)	Slump Flow (%)	Compressive Strength at 28 days (MPa)
0.00% V_f Fibre (NF0.00)	425	0	215	914	183	107	7.87
0.10% V_f Fibre (NF0.10)	425	0.10	215	914	183	101	7.82
0.15% V_f Fibre (NF0.15)	425	0.15	215	914	183	95	7.62
0.20% V_f Fibre (NF0.20)	425	0.20	215	914	183	82	7.22
0.25% V_f Fibre (NF0.25)	425	0.25	215	914	183	68	6.81
0.50% V_f Fibre (NF0.50)	425	0.50	215	914	183	45	5.78

Table 3.4 Mix design of Type O mortar

Mix & Designation	Water (kg/m^3)	Fibre Content (% V_f)	Cement (kg/m^3)	Slaked Lime (kg/m^3)	Sand (kg/m^3)	Slump Flow (%)	Compressive Strength at 28 days (MPa)
0.00% V_f Fibre (OF0.00)	405	0	125	960	213	106	2.95
0.10% V_f Fibre ()F0.10)	405	0.10	125	960	213	98	2.89
0.15% V_f Fibre (0F0.15)	405	0.15	125	960	213	92	2.80
0.20% V_f Fibre (0F0.20)	405	0.20	125	960	213	75	2.63
0.25% V_f Fibre (0F0.25)	405	0.25	125	960	213	62	2.47
0.50% V_f Fibre (0F0.50)	405	0.50	125	960	213	34	2.09

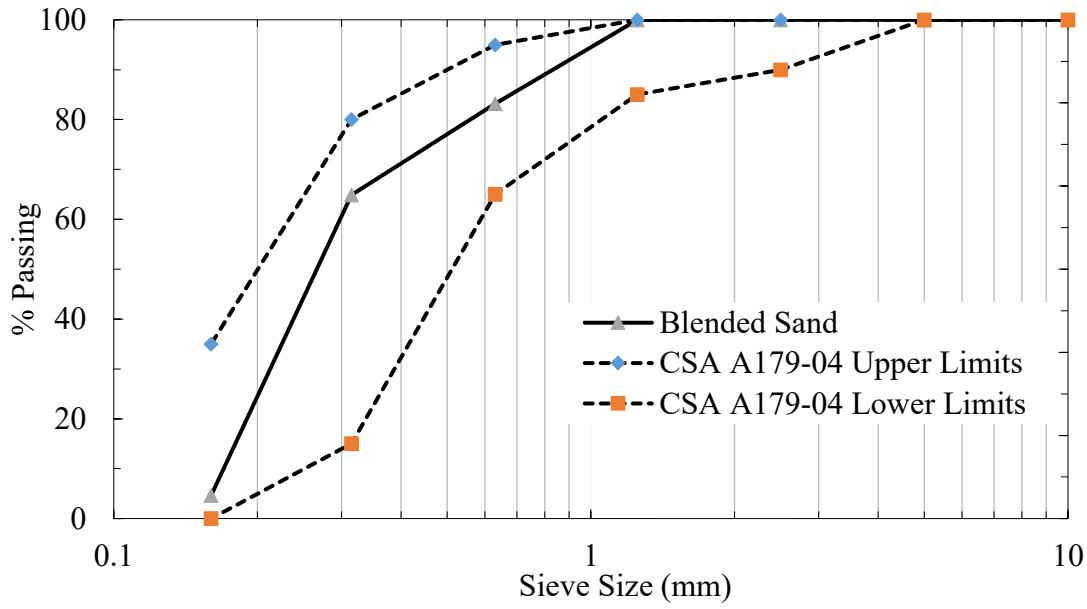

Figure 3.3 Grain size distribution of the fine aggregate in mortar

Figure 3.4 Preparation of hollow cylindrical specimen

Figure 3.5 Extracted hollow cylinder for permeability tests

3.3.2 Porosity and Density Measurement Using ASTM C642 (Displacement Method)

ASTM C642 (2006) is a suitable method to determine the porosity and density of the hardened cementitious materials. This method requires several pieces of cylinders, cores or beams of any desired shape for which each individual portion shall not be less than 350 cm^3 or 800 g for normal weight concrete that is free from observable cracks, fissures or shattered edges. For this method, at least eight solid cylinders were selected from each mortar category where each cylinder weighed more than 1000 gm. First, the specimens were dried in an oven at a temperature of 110 ℃ for 24 hours. Then the specimens were removed from the oven and their weights were recorded after letting the specimens cool down to 24 ℃. Next, the specimens were immersed into water at 21 ℃ for 48 hours, which allowed saturation of the water penetrable pores. Subsequently, the samples in water were boiled for 5 hours to remove entrapped air. This allowed water to enter into those pore spaces. Finally, specimens were weighed again at the ambient 24 ℃ after cooling through a natural loss of heat for a period of time no less than 14 hours. The volume of permeable pores and density were then calculated by using the procedure described in ASTM C642 (2006):

$$Bulk\ density, dry = g_1 = \frac{A_a}{(C - D_a)} \cdot \rho_w \tag{3.1}$$

$$Total\ pore\ volume, \% = \phi = \frac{(g_2 - g_2)}{g_2} \cdot 100 \tag{3.2}$$

where $g_1$is the bulk density, $g_2$is the absolute density, ϕ is the porosity, A_a is the mass of oven-dried sample in air, C is the mass of surface-dry sample in air after immersion and boiling, D_a is the apparent mass of sample in water after immersion and boiling, and ρ_w is the density of water.

3.3.3 Pore Size Measurement Using the Mercury Intrusion Porosimetry (MIP) Method

Mercury Intrusion Porosimetry (MIP) is a widely used technique to identify and characterize the pore size distribution of porous materials. As stated in Chapter 2, it is relatively convenient

and less time consuming, so that the MIP technique remains a popular technique to evaluate pore size distribution. Also, it is notable that MIP is the only method that covers the range of pore sizes relevant for studying the behaviour related to the pore structure in cementitious systems, such as water permeability (Scrivener et al. 2016). In this study, MIP was conducted by using the AutoPore IV 9500. The sample is first immersed in a bath of mercury and further, the mercury is injected under various levels of pressure. The pressure required to force mercury into the sample's pores is inversely proportional to the size of the pores. The assumption is made that the pores are cylindrical in shape and are entirely and equally accessible to mercury. Accordingly, the pore diameter can then be calculated by using the Washburn equation (Washburn 1921):

$$d = \frac{-4\gamma cos\theta}{P} \tag{3.3}$$

where, d is the equivalent pore diameter, P is the applied mercury pressure, γ is the surface tension between mercury and pore surface, θ is the contact angle between mercury and porous materials.

AutoPore IV 9500 can measure pore diameters ranging from 0.003 to 360 µm. The experimental details are as follows. First, the sample was degassed to remove the moisture inside the sample. Usually it is done by drying the specimen at high temperature but drying, above 25 °C, may alter the pore structures. Therefore, in order to avoid any alteration in the pore structure, the specimen was degassed at ambient temperature itself but for an extended time period with a vacuum source. After measuring their mass, the samples were placed in a cell which comes attached with a vacuum chamber. The chamber was evacuated to remove air and subsequently filled up with mercury. Mercury is a non-wetting liquid, having a contact angle greater than 90°, and enters into the sample when external pressure is applied. As the applied pressure was increased gradually in a step-by-step procedure, mercury was forced to intrude the specimen's pores. Using the volume intruded by mercury and the associated pressure in each step, a cumulative pore size distribution could be generated.

3.3.4 Pore Size Measurement Using Nitrogen Adsorption Method

Gas adsorption method is a good technique for knowing the disposition of micro-pores and meso-pores. Though pores having a radius below 60 nm do not contribute to water permeability (Neville 2011), this method was chosen to observe the influence of fibres on the mortar, specifically how fibres alter the pore structure in the above mentioned range. Nitrogen was chosen as the adsorbent for this method and the porosity and pore size distribution were determined by generating isotherms at different relative pressures.

An Autosorb Quantachrome 1MP equipment was used, which enables identifying pores between 0.35 – 500 nm. This evaluation is based on the B.E.T Theory (Brunauer et al. 1938). For this method, a small piece of fractured mortar specimen was taken from a separate hollow cylinder that was cast for water permeability test and set aside for pore structure investigation. While using this equipment, there is an optimal mass of sample, obtained from the following formula:

$$gram\ of\ sample = \frac{Total\ surface\ area\ (X)\ \ (m^2)}{Specific\ surface\ area\ (SA)\ \left(m^2/_{gm}\right)} \tag{3.4}$$

X = 10-15 m^2 is the optimal range for this equipment when Nitrogen is used as adsorbent. The total sample analysis process may take 18 to 24 hours or even more depending upon the pore size of the sample even with this optimal amount of sample weight. First, the mass of desired amount of sample was recorded. The sample was then transferred into the cell, which was then attached to a degassing station. The specimen needs to be degassed to remove unnecessary gas molecules or any other surface contaminants, including surface water that may interfere with nitrogen adsorption and pore volume measurements. The degassing station is equipped with a vacuum source and a heating element, which is capable of heating the specimen up to a temperature of 400 ºC. With heat and vacuum source, degassing can be performed within 2-3 hours. However, the use of high temperature, above 25 °C, is likely to alter the pore structure of the mortar. Therefore, in order to prevent any such possible distortion in this study, the degassing was performed by using a vacuum source at ambient temperature. As a result, the degassing period lasted from 12 to 15 hours. At the end of this period, the sample must pass an initial degas test for necessary degassing otherwise the procedure has to be conducted again.

Second, the specimen was weighed after successful degassing and then the sample cell was attached to the sample-loading valve. At this point, physisorption analysis parameters were selected from the analysis software menu. For pore size distribution, 20 points adsorption and 20 points desorption followed by 7 point BET were chosen. The relative pressure, P/P_0, was chosen in the range of 1.0 to 0.05. Choosing a relative pressure P/P_0 below 0.05 will again have impact on the total processing time since a special dosing procedure will be required at this relative pressure level. Note that P is the equilibrium vapour pressure and P_0 is the saturated vapour pressure of the adsorbate.

From this point forward, the test was run via the software. First, an initial leak test is done before going onto the next step. It involves checking the adequacy of the requirements associated with degassing of the specimen. If a specimen fails the initial leak test, then this process cannot proceed to the next stage. Note that the initial leak test may fail even if the specimen passed a degassing test previously. After passing initial leak test, the sample cell is placed in a nitrogen bath at a temperature of 77 K to promote the adsorption process. The whole procedure begins by applying a relative pressure, P/P_0 of 1.0 with a gradual reduction in increments of 0.05. The total procedure of adsorption and desorption were completed in about 6 to 9 hours depending on the nature of the specimen. The pore size distribution was then obtained from the recorded isotherms by using BJH (Barrett, Joyner, and Halenda) (Barrett et al. 1951) model.

3.3.5 Pore Size Measurement Using Backscattered Scanning Electron (BSEM) Method

Image-based analysis methods can be used to characterize the microstructure of cementitious materials and to provide a quantitative means for describing the dependence of the physical properties on the pore structure. Image analysis technique, using Scanning Electron Microscope (SEM), has often been employed for characterizing the microstructure. As stated in Chapter 2, the BSEM technique has higher potential as backscattered electrons has higher energy than Secondary Electrons (SE) and so can penetrate deeper layers of the specimen and

hence can be detected from greater depths. It is worth mentioning here that proper specimen preparation and imaging technique are prerequisites to carry out BSEM. The details of these steps involved are described below.

A flat piece of the specimen is required (Goldstein et al. 1981b) to take advantage of the analytical capabilities of the BSEM. Improper preparation method of extracting a flat and polished specimen for SEM may result in severe artifacts (Crumbie 2001; Stutzman and Clifton 1999). Therefore, the specimens was prepared by a skilled technician at the Thin Section Laboratory of Earth and Atmospheric Science department at the University of Alberta. First, a flat piece of specimen having a cross-section of 10 mm by 10 mm and a length of 20 mm was sawn from an intact hollow-core cylinder that was prepared along with other specimens for a companion test series. Second, before polishing, the specimen was impregnated with a low viscosity epoxy resin. The impregnation of the epoxy resin into the specimen was done under vacuum and at a temperature of 21 ^{o}C for 24 hours. Its purpose is to fill the pores with epoxy as hardened epoxy strengthens the microstructure preventing thereby any damage such as shrinkage cracking that may occur during the polishing process. In addition, the contrast between the pores and the solids becomes substantially distinct. Third, the surface of the specimen to be examined was exposed by grinding using mono-ethylene glycol. Lastly, the exposed surface was polished using a diamond disc having a diameter up to 3 μm. The specimens were ground successively using diamond discs of 1 and 0.25 μm in diameter. At the end, the prepared flat specimen was stored in a glass container for image acquisition.

The BSE images were obtained at an accelerating voltage of 25 KV by using the Zeiss Sigma 300 VP-FESEM, as shown in Figure 3.6. This machine, at the Earth and Atmospheric Science department of the University of Alberta was operated by a single technician for this study, and hence a certain degree of uniformity across all the BSEM images here, was ensured. For each specimen, 10 to 12 high resolution, 1024 x 768 pixel, images were captured. The working distance was set to 6 mm for all the captured images. For each specimen, images were taken at a magnification of 50x, 400x and 800x which resulted a spatial resolution of 2.1354 μm/pixel, 0.2636 μm/pixel and 0.1358 μm/pixel respectively.

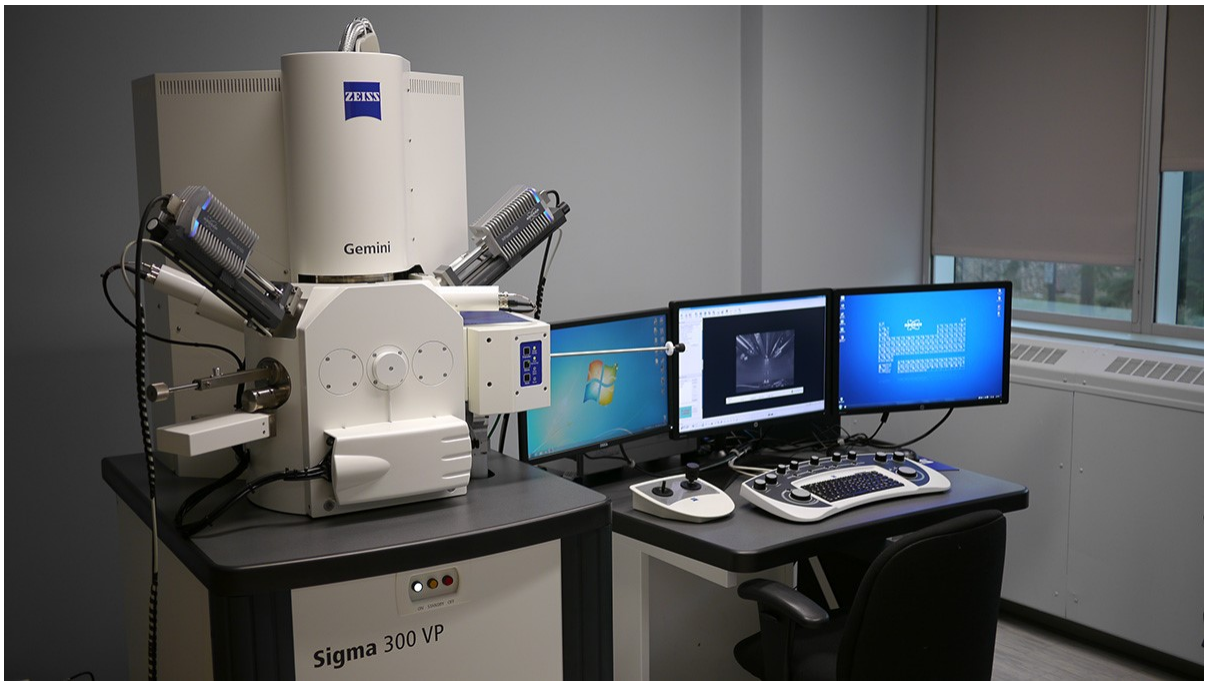

Figure 3.6 Zeiss Sigma 300 VP-FESEM used to capture BSEM images

3.3.6 Image Analysis

Image processing methods can be used for microstructure evaluation of cementitious materials. It provides a quantitative means for understanding the dependence of physical properties on the pore structure (Blair et al. 1996). Backscattered Scanning Electron Imaging (BSEM) has become well established as a method for the study of cementitious material and their microstructure. Analysis of images taken by the BSE method has many advantages including the visualization over a wide range of magnifications and reproducibility of contrast dependent on atomic number. Different phases of the mortar can be distinguished from BSEM image taken from properly prepared epoxy impregnated flat specimens as per their intensity or gray value. The pore space filled with epoxy resin appear as dark pixels compared to that of the solid portion. Also, gray value of the images is mainly a function of the mean atomic number of the local area of the sample. Therefore, solid components in compounds with higher molecular weight produce brighter pixels. By distinguishing between pixel intensities of solid component and pore space filled with epoxy resin, it is therefore possible to determine all the associated microstructural parameters namely, the porosity, the pore size distribution, the

specific surface area, and the fractal dimension of cementitious materials from the analysis of BSEM image.

Reproducibility of contrast makes BSEM imaging a convenient technique to identify different phases and hence, it is very important to maintain the same level of brightness for all the captured images. It was ensured during the entire period of study that the captured SEM images were properly focused and have same brightness level. These images were then analyzed to evaluate the pore structural parameters by selecting proper thresholding algorithm. It is possible to select the threshold value manually to distinguish the pores from the solid components. However, the output of manual thresholding is subjected to human error and fatigue. In order to get meaningful quantitative data, the pore-segmentation—through appropriate thresholding—needs to be precise and reproducible (Wong et al. 2006). There are several pore-thresholding methods available on literature ranging from simple manual thresholding to complex one. For this study, a pore-segmentation method suggested by Wong et. al. (2006) was adopted since this technique was found to be more consistent and reliable than other methods. In this method, the threshold is determined based on estimation of the critical overflow point. The critical overflow point corresponds to the inflection of the histogram, which can be estimated from the intersection of tangents drawn along the two linear segments as shown in the Figure 3.7. More details of this algorithm can be found at Wong et. al. (2006).

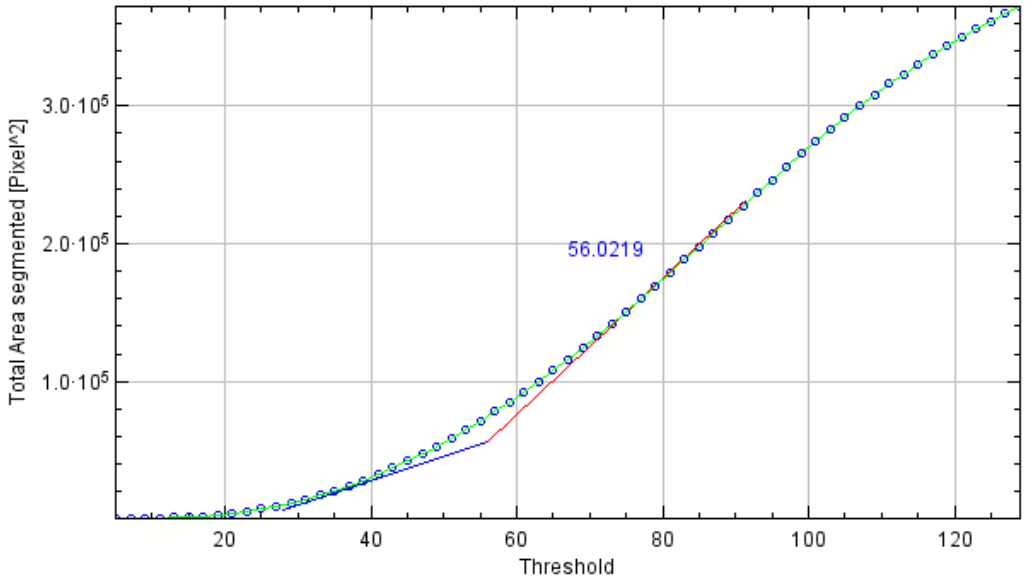

Figure 3.7 Pore-segmentation method for BSEM images (Wong et al. 2006)

3.3.6.1 Porosity

Porosity can be determined from the BSEM micrographs through pore-segmentation and subsequently converting them into binary images. The procedure to evaluate the porosity from the raw images is described in Figure 3.8. First, BSEM images were cropped in such a way to remove undesired regions of the images. These high-resolution images have a dimension of 1024x768 pixels. Second, a threshold algorithm was applied to distinguish between pores and solids using the method described in the previous section, 3.3.6. Third, 8-bit gray-scale images were converted to binary format having an intensity value of 0 and 1, representing the solid and pore pixels, respectively. Finally, the porosity was determined by dividing the number of recorded pore pixels with the total image area. Note that a noise filtration operation was applied prior to counting the pore pixels, to remove the isolated single pixels.

(a)

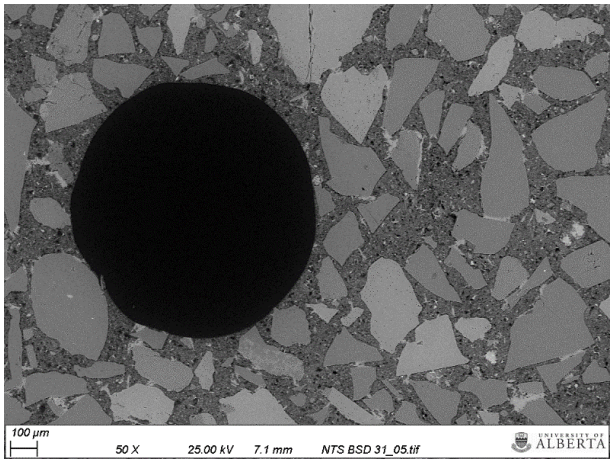

(b)

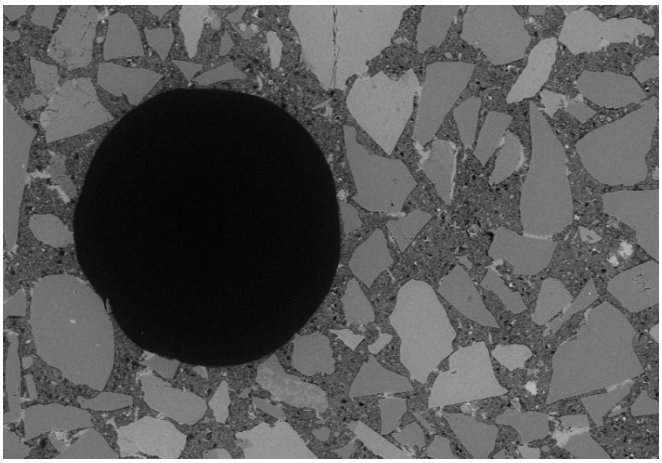

(c)

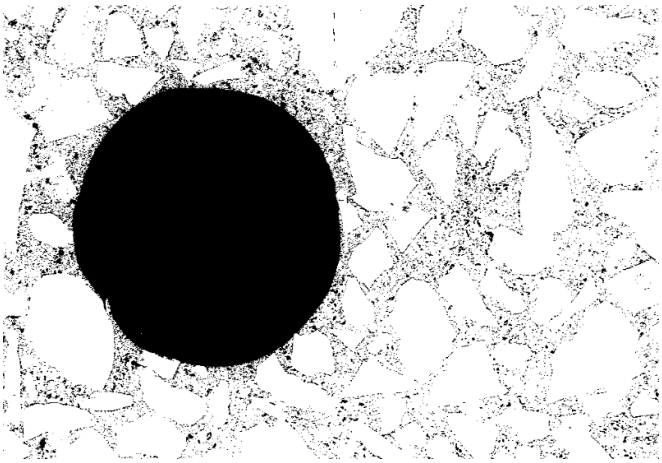

Figure 3.8 Image processing steps (a) original BSE image, (b) cropped image, and (c) binary image

When using a single magnification, an inherent limitation of image analysis is its inability to capture a wide range of pore sizes. Therefore, it is recommended that one utilize images captured at several different magnifications to cover a broader range of pore size. This procedure will incorporate the contribution of a wider range of pores to the intended physical properties that will be examined at a later stage. In this study, images from three different magnifications were processed to cover a reasonable pore size range. A typical set of images from all three magnifications are shown in Figure 3.9. By taking the combined effect of these three magnifications namely 50x, 400x, and 800x with a spatial resolution of 2.1354 μm/pixel, 0.2636 μm/pixel, and 0.1358 μm/pixel respectively, pores having a radius ranging from 0.13 μm to 214 μm were resolved.

(a)

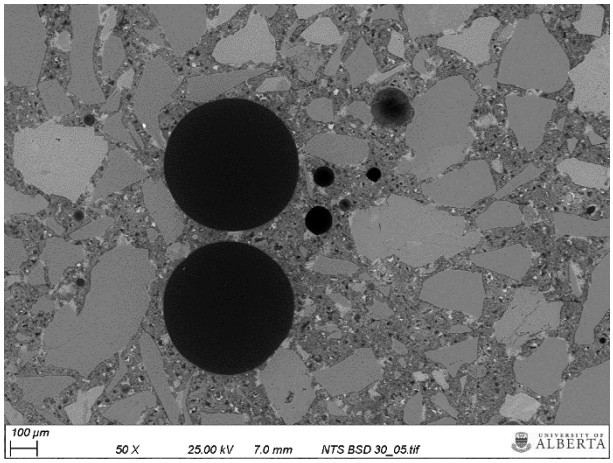

(b)

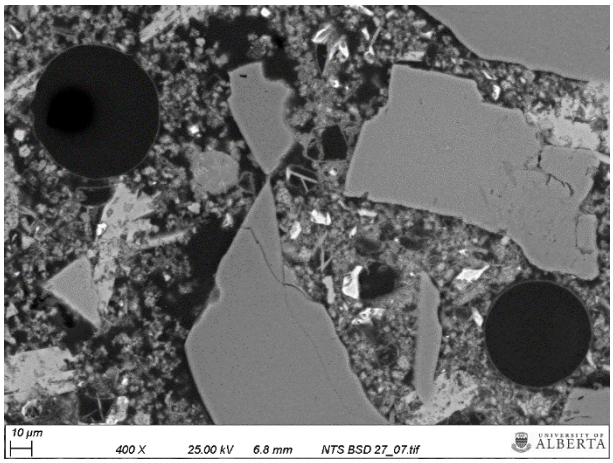

(c)

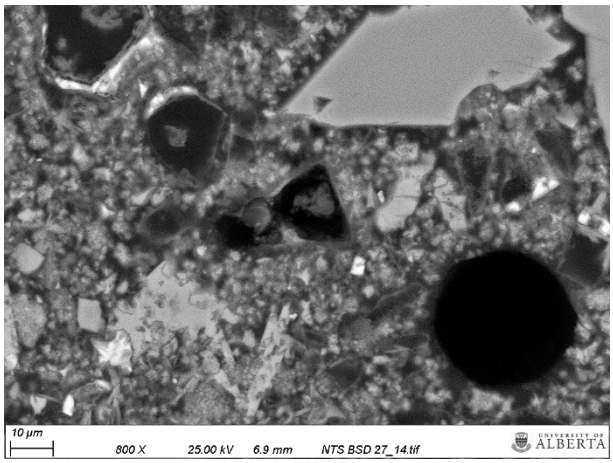

Figure 3.9 Image displaying taken at different magnifications (a) 50x (2.1354 µm/pixel), (b) 400x (0.2636 µm/pixel), and (c) 800x (0.1358 µm/pixel)

3.3.6.2 Pore Size Distribution by Opening Method

Based on BSEM imaging technique, pore size distribution (PSD) can be ascertained either by using the area-histogram based approach or by applying morphological operations (Lange et al. 1994; Scrivener 2004). One such method is the opening method. It is a combination of an erosion followed by a dilation process. In this method, a structure of interest, a set of pixels of specified configuration, is set to test the input image. The morphological dilation operation inspects each pixel to examine whether the structuring element centered on this pixel intersects the structure of interest. On the other hand, the principle of morphological erosion tests each pixel of the image as to whether the structuring element centered on this pixel is contained within the original set. Note that in the erosion process, a pixel in the original image will be retained if the structuring element is completely contained within the input image upon translation. For cementitious materials where the occurrence of complex interconnected structures like long cracks and connected pores are the common feature this method is suitable as features with smallest dimension less than the size of the structuring element is removed during the first step of this process. This process also eliminates any isolated features with overall size smaller than the structuring element. Thus, the size of the structuring element reflects the true measure of the pore size.

Any shape of the structuring element—such as a disk, square, octagon, diamond, or a straight line with angle of 0, 90, 45 or 135 degrees—can be chosen. In this study, a disk-shaped structuring element with increasing dimension was chosen to perform the morphological opening operation on the processed binary image. The size of the structuring element and the corresponding pixel count of the pore features were recorded for each step of the operation. The number of pore pixels for each step was normalized with respect to the total image area in order to get the relative fraction of the pore area. So that, the pore size distribution was obtained by plotting the size of the structuring element against the pore area fraction. Despite the limitation of this method regarding image resolution, Scrivener (1988) found a similar correlation between the pore size distribution obtained from this method and those obtained from gas adsorption or calorimetric method.

3.3.6.3 Two-Point Correlation Method

The two-point correlation (TPC) method is a morphological image processing technique that can be used to study the microstructural characterization of cement-based systems (Berryman 1985, 1987; Berryman and Blair 1986; Blair et al. 1993, 1996). It provides a quantitative measure of different parameters that are required to model various properties including the compressive strength and permeability (Torabi et al. 2008). It is based upon the statistical measure of the microstructure in porous materials that can be evaluated from high-resolution microscopic images. Various microstructural features such as the porosity, specific surface area, and the characteristic pore size can be quantified using the two-point correlation function.

A porous material can be idealized as a two-phase medium consisting of solids and pores. A characteristic function, $f(x)$ for such medium can be used for identifying pore structure in such a way that $f(x) = 1$ if x is in the pore space and $f(x) = 0$ if x lies in the sloid phase where x denotes any position in the medium. The two-point correlation (TPC) is the probability of finding a line segment of known length in the pore space when placed randomly in a porous medium. The spatial correlation function used in this study is shown below:

$$S_2(r) = \langle f(x) f(x+r) \rangle \tag{3.5}$$

$$S_2(0) = \phi \tag{3.6}$$

$$\lim_{r \to \infty} S_2(r) = \phi^2 \tag{3.7}$$

$$\lim_{r \to \infty} \frac{dS_2(r)}{dr} = -\frac{s}{4} \tag{3.8}$$

where $S_2(r)$ is the two-point correlation function, r is the length of line segment, s is the specific surface area, ϕ is the pore area fraction or porosity. The brackets $\langle\ \rangle$ indicate a volume average over the spatial coordinate x.

In this research, TPC functions were evaluated using a procedure as described by Berryman (1985) by using high resolution images that was taken by BSEM. In this method, TPC was evaluated by shifting (translation of a copy of the image with respect to the original) of a binary image with respect to its original image and counting the pixels in the overlapping portion of the images.

3.3.6.4 Fractal Behavior

Fractal analysis is a simple and powerful tool for quantifying the roughness and irregularities of cementitious materials. The main feature of fractal geometry is the fractal dimension of the object in question. Fractal dimension defines the level of details that can be observed with the changes in scale of observation. Among several methods of evaluating fractal dimension for cement-based materials, dilation method and box-counting method were used in this study. Box-counting is a sampling or data gathering process that systematically lays a series of grids of decreasing calibre (the boxes) over an image and record the count for each successive step. In order to enable box-counting, the images were first converted to a binary format and then covered with evenly spaced boxes of known size, which were subsequently reduced gradually in size. In order to eliminate the effect of image orientation, the images were rotated incrementally by an angle of 15 ° and the fractal dimension was taken as the average value of those estimated from each orientation. Figure 3.10 shows typical stages of the box-counting method. The fractal dimensions were determined from the slope of the plots of box count—required to cover the image area—against the size of the boxes. A typical plot arising from the box-counting method is shown in Figure 3.11.

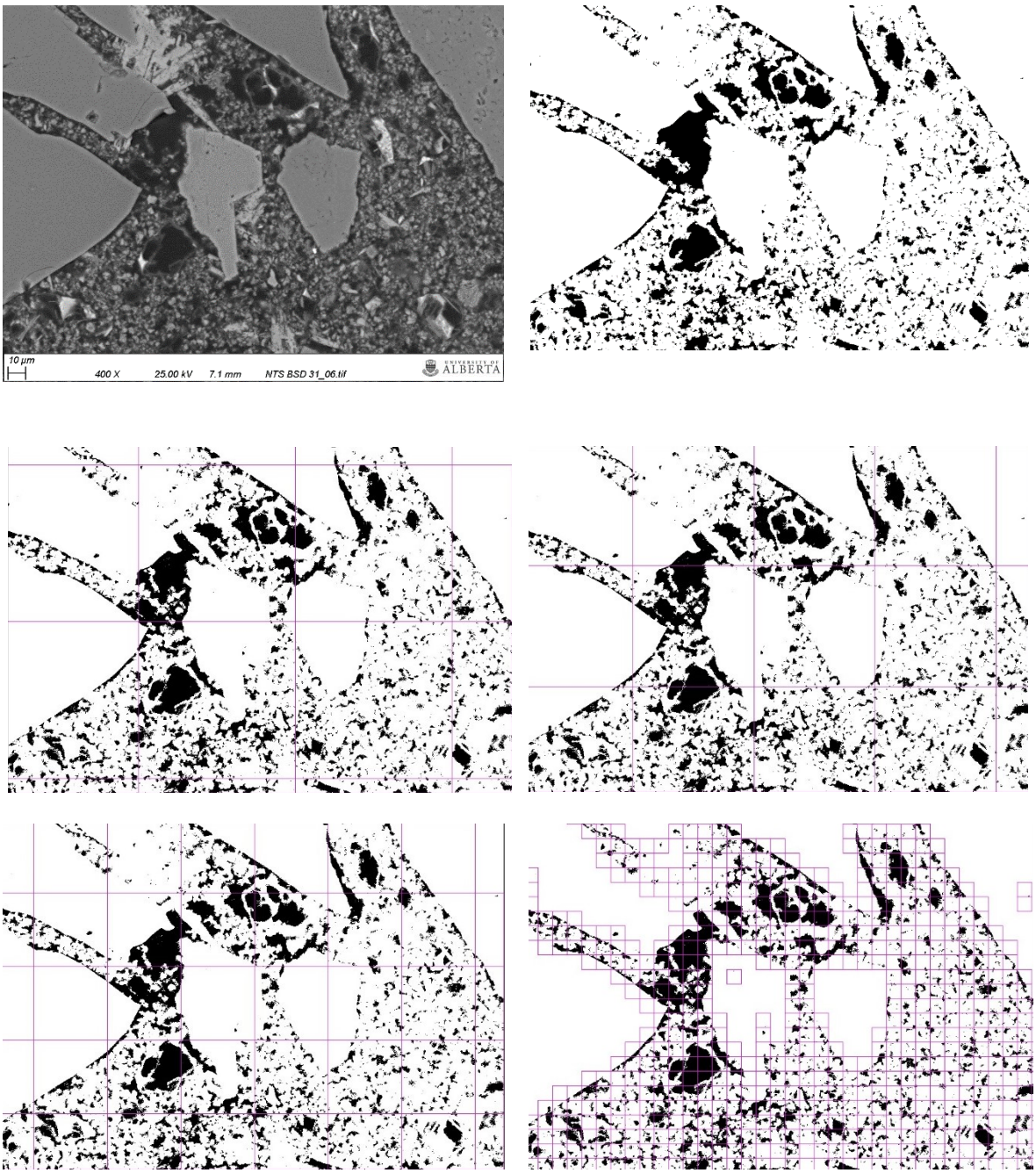

Figure 3.10 Box-counting process (a – top left) typical BSEM image, (b – top right) Binary image, (c – middle left) Image after 2nd iteration, (d – middle right) Image after 4th iteration, (e – bottom left) Image after 8th iteration, and (f – bottom right) Image after 12th iteration

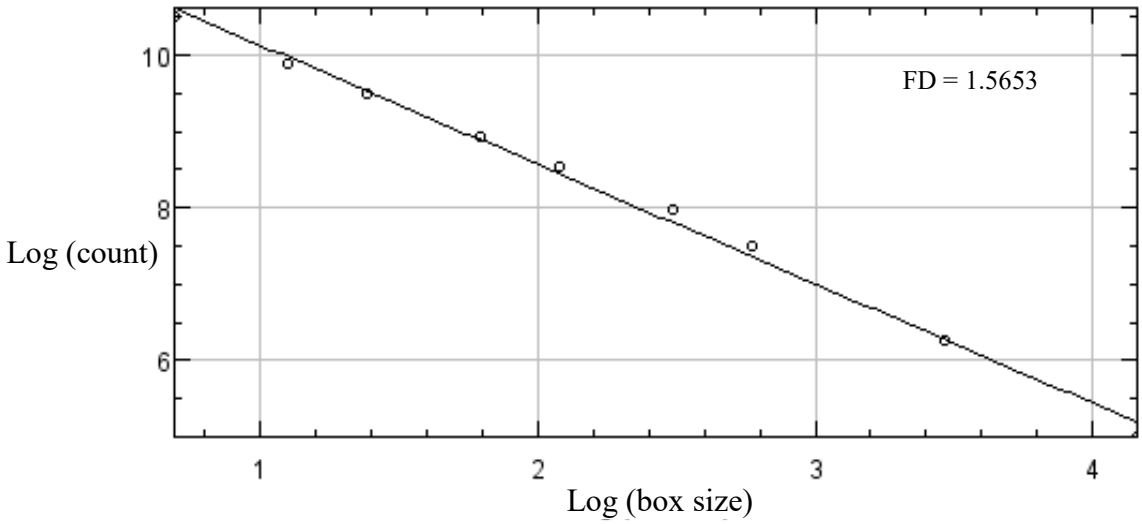

Figure 3.11 Fractal dimension as calculated by box-counting method where FD is equal to absolute value of slope

On the other hand, the dilation method is credited with giving accurate values of fractality in terms of computing (Eins 1996). In this method, each pore feature in the binarized image is converted to a single pixel outline and then each contour is dilated gradually by a specified number of pixels. The perimeter of each dilated outline is then measured. Note that each dilation operation is a simulation of the pore feature observed at a reduced level of resolution (Lange et al. 1994). Finally, after 60 iterations, the fractal dimension is obtained by calculating the slope of the graph generated by plotting the measured perimeter of the profile at each stage of dilation against the magnitude (thickness) of the dilation. Typical stages of the dilation process and determination of fractal dimension are presented in Figures 3.12 and 3.13 * MERGEFORMAT * MERGEFORMAT . Eins (1996) states that this method when used with images containing lineal objects i.e., features with open ends, as opposed to closed contours, tends to dilate them resulting in erroneous evaluation of the fractal dimension. However, noting this and making provisions to minimise (or eliminate) this error, the dilation method was found in the current study to provide valuable information on fractal dimension, allowing for comparison across data in the published literature.

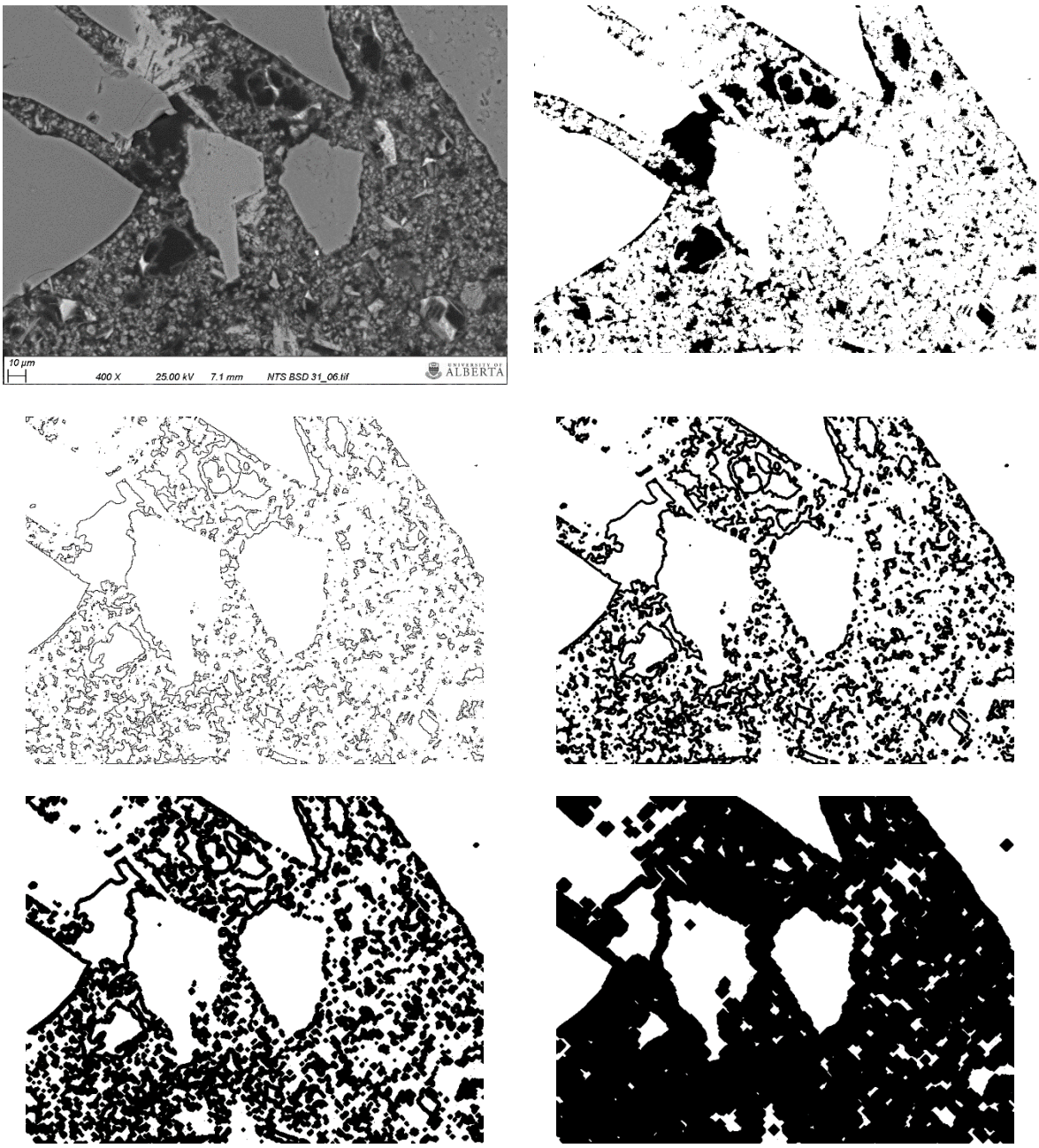

Figure 3.12 Dilation process (a – top left) typical BSEM image, (b – top right) Binary image, (c – middle left) Image after outline, (d – middle right) Image after 1st dilation process, (e – bottom left) Image after 3rd dilation process, and (f – bottom right) Image after 10th dilation process

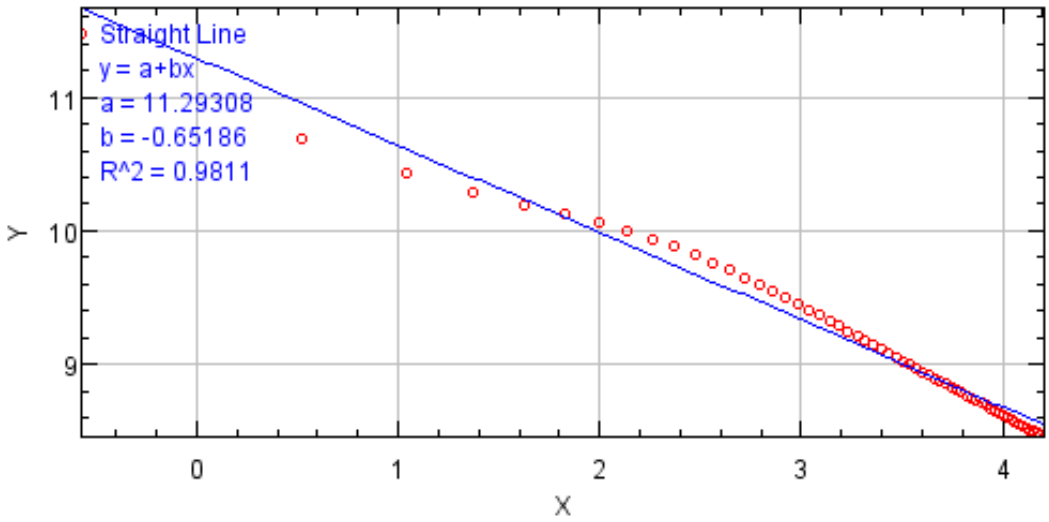

Figure 3.13 Fractal dimension as calculated by dilation method where X and Y denotes respectively, the contour thickness in pixel and estimated perimeter in pixel and FD is equal to 1+ absolute value of slope

3.4 Results and Discussion

3.4.1 Porosity

For a cement-based system, porosity is an important parameter that influences the macro-mechanical properties. It has a direct bearing on the transport properties and in turn, the durability of cementitious materials. The parameters of the pore system and its connectivity can provide the means to understanding the mechanisms by which aggressive species can penetrate the material. This is because the pore structure defines the paths along which liquid or vapour preferentially moves. This, in turn, underscores the importance of exploring the effect of pore structure on durability considerations including the transport of freezable water and electrolytes, such as chlorides, through cementitious materials.

The porosity of the Hydraulic Lime Mortar, Type N mortar, and Type O mortar are shown in Figures 3.14, 3.15, and 3.16 respectively. It was determined by three different methods: 1) Using the procedure according to ASTM C642 (2006) also known as displacement method which is described in section 3.4.2, 2) Mercury Intrusion Porosimetry method as described in section 3.4.3, and 3) Image analysis method using image captured from BSEM as described in section 3.4.5. It can be observed that the porosities of all three mortars follow similar trend

when plotted against the fibre dosage. Notice further that mortars having a fibre dosage of 0.15% show the lowest porosity. As the fibre dosage increase beyond 0.15%, the measured porosity of the mortars increases. The same trend in the porosity was observed across all three different types of measurement techniques, namely ASTM C642, MIP, and SEM.

Variation in porosity for fibre reinforced Hydraulic Lime Mortar is shown in Figure 3.14. It is noticeable that ASTM C642 (2006) method yielded the highest value of porosity for plain and fibre reinforced mortar while the SEM method gave the lowest amount of porosity and those measured using the MIP method lie between the two. The observed variation related to the measurement techniques may be attributed to the limitation associated with the respective experimental method. For instance, the porosity measured by SEM method depends on the resolution of the image especially when they are taken by detecting the backscattered electrons rather than the secondary electrons. Further, the minimum diameter of the pores that can be detected with maximum resolution of images is restricted to 0.272 μm. Hence, the porosity contribution of pores with a diameter smaller than the aforementioned minimum value is not reflected in SEM method. In contrast, MIP is capable of detecting a larger range of pore diameter. It, however, does not include the pores smaller than 3 nm. Besides, the MIP method is unable to include the fraction of pores contributed by the entrapped air-voids which are relatively larger than MIP's maximum detectable size. Furthermore, the maximum pore that was detected by MIP method was 45 μm in radius whereas SEM method was able to include pores having a radius of more than 200 μm.

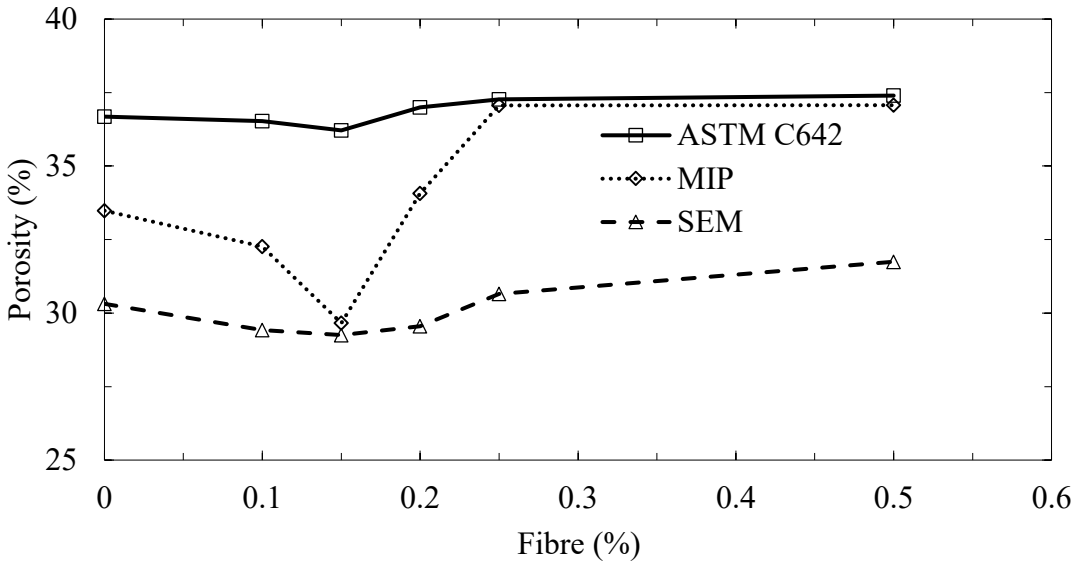

Figure 3.14 Porosity of Hydraulic Lime Mortar with and without fibre as determined by ASTM C642 method, MIP, and SEM images

As shown in Figure 3.14, the variation in porosity in Hydraulic Lime Mortar as measured by the ASTM C642 or SEM methods is hardly noticeable compared to the porosities measured by the MIP approach. Nonetheless, all three methods reveal a similar trend with fibre dosage. Porosity decreased with fibre addition up to a volume fraction of 0.15% fibre. The porosity increased again with more fibre addition and has the highest amount of porosity with volume fraction of 0.5% fibre, reaching a peak of 34 - 37% across the three methods. The maximum porosity decrement and increment was 1.27% and 1.96% upon the base plain mixture without fibres. For porosity measured with SEM, it followed the similar trend to ASTM C642 but saw more variation of lowest and highest porosity. For SEM, the porosity of the base mixture, and the lowest and highest porosity amounts were 30.31%, 29.25% and 31.75% respectively while maximum decrement and increment were 3.5% and 4.73% in comparison to the base mixture. Porosity measured by MIP method showed -11.41% and +10.73% change in porosity compared to the reference mix.

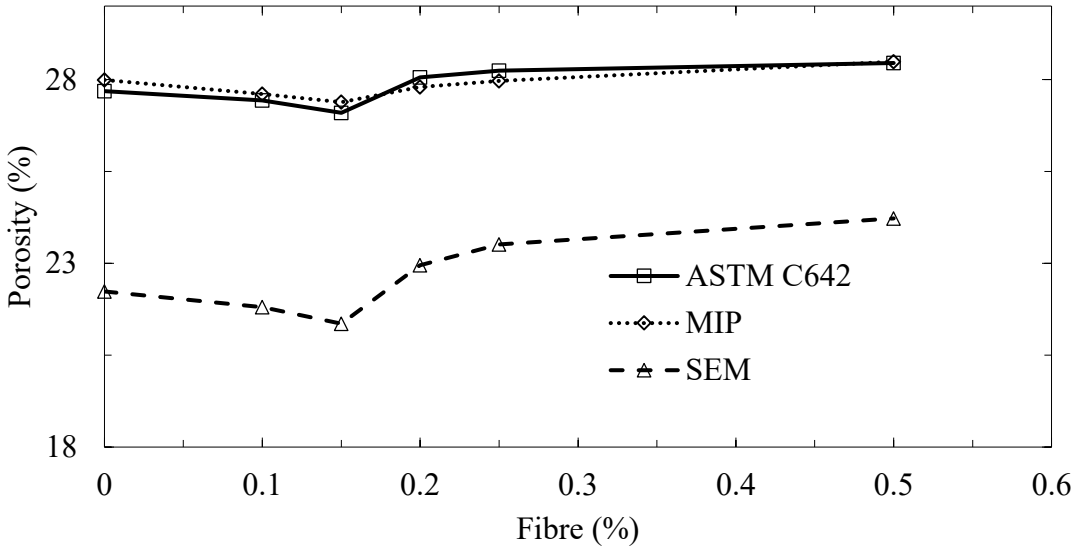

Figure 3.15 Porosity of Type N mortar with and without fibre as determined by ASTM C642 method, MIP, and SEM images

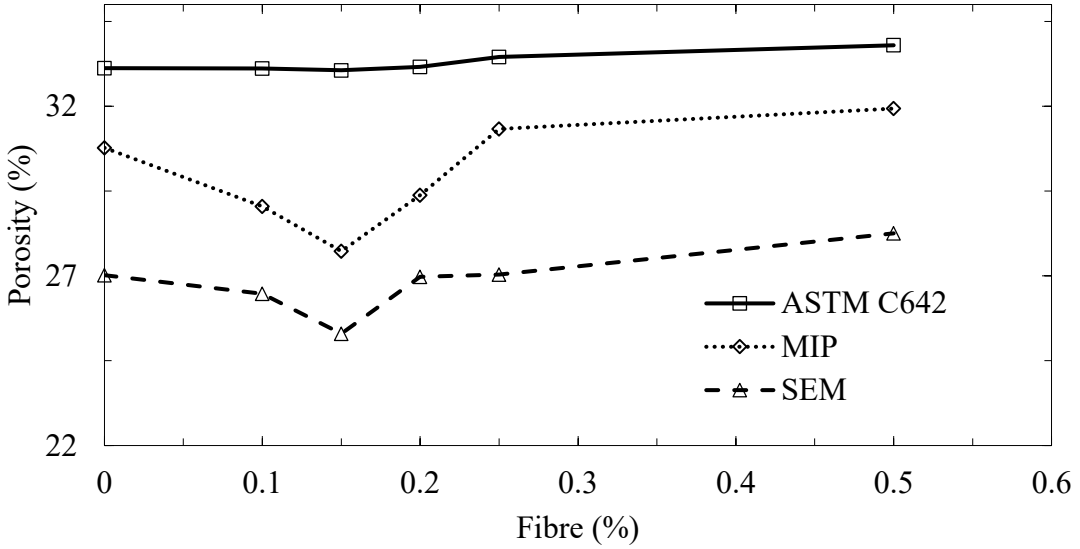

Figure 3.16 Porosity of Type O mortar with and without fibre as determined by ASTM C642 method, MIP, and SEM images

Porosity variation with fibre reinforcement for cement-lime mortar, Type N mortar and Type O mortar are shown in shown in Figures 3.15 and 3.16. It can be concluded that the porosity variation with fibre inclusion was almost identical irrespective of mortar types and porosity

measurements methods. For Type N mortar, porosity varied for all fibre regime in a similar manner way for MIP and ASTM C642 methods while SEM methods displayed lower porosity like other mortar types. A considerably different trend, especially for MIP, can be observed where porosity for the intermediated fibre dosage reduced. It can be attributed to the fact that the Type N mortar contains substantial amount Portland cement which, upon hydration, forms a much finer hydration products (Mehta and Monteiro 2006; Mosquera et al. 2006). Porosity for Type O mortar also showed a similar trend where porosity decreased as fibre added and amplified after 0.15% fibre amount.

The effect of polypropylene micro-fibre on porosity of HLM, Type N mortar and Type O mortar has been discussed in previous sections. It is noticeable that porosity varied in a similar manner for all types of mortar. The lowest amount of porosity was for a 0.15% fibre volume fraction and the highest porosity was for 0.5% fibre volume fraction. This change in porosity with fibre variation can be explained by the density variation as measured by ASTM C642 method as shown in Figure 3.17. The addition of polypropylene fibre led to a reduction in density of mortars for dosage up to 0.15% volume fraction of fibre and hence porosity decreased. This reduction in porosity may be as a result of lower amount of entrapped air contents due to fibre effect and capillary pore reduction in the vicinity of fibre-matrix interface (Balaguru and Ramakrishnan 1988; Bentur and Mindess 2007; Pereira de Oliveira and Castro-Gomes 2011). Izaguirre et. al. (2011) found a similar pattern of effect on material density with fibre addition for aerial lime based mortar. The higher amount of fibre addition led to an increase of porosity of all types of mortar. Higher fibre content of fibre made difficult to mix and compaction, which led more entrapped air, voids and increased larger pores substantially. While low fibre dosages led to pore refinement, addition of higher fibre dosages did the opposite, coarsening of the pores.

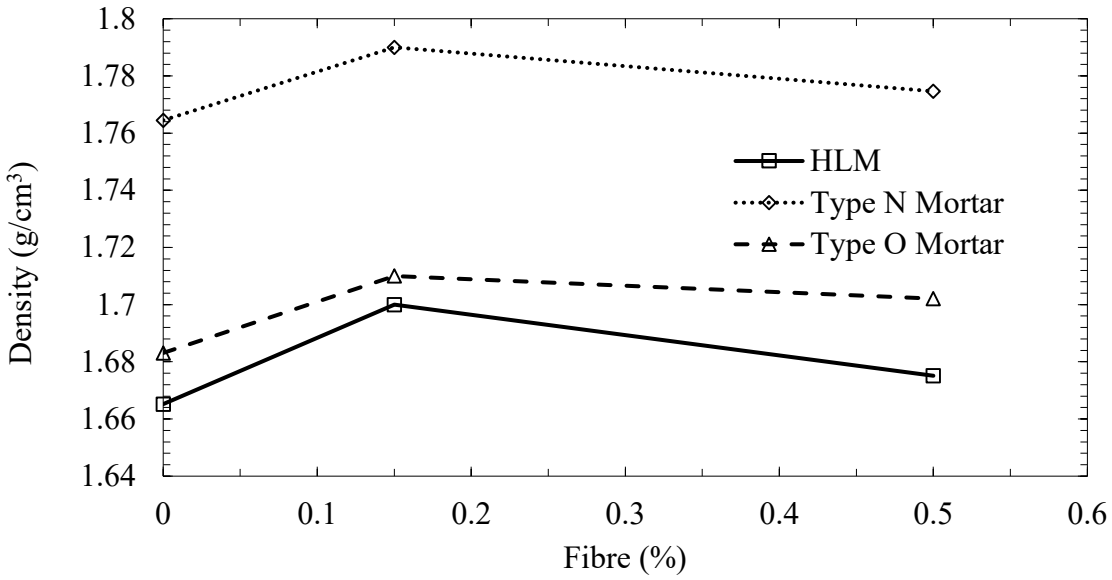

Figure 3.17 Density variation with fibre for Hydraulic Lime Mortar, Type N mortar, and Type O mortar as determined by ASTM C642 method

3.4.2 Pore Size Distribution by Mercury Intrusion Porosimetry (MIP) Method

As already mentioned, Mercury Intrusion Porosimetry (MIP) has certain limitations in its usage relating to the pore size characterization of cement-based systems. It is generally agreed that that this method cannot evaluate correctly for larger pore sizes (approximately 0.1–10 micron in diameter) (Diamond 2000). Despite its limitations, MIP is relatively quick, simple to conduct and captures a wide range of pore sizes.

Figures 3.18, 3.19, and 3.20 show respectively, the pore size distribution, frequency distribution, and differential pore size distribution, of pores in the Hydraulic Lime Mortar measured by employing the MIP method. Note that log differential pore size distribution was obtained by taking d(Volume)/d(logDiameter). It is noticeable that the addition of fibres contributed to a pore size alteration. At low dosage (0.15%), fibre addition resulted in a refinement in pore diameter where a fraction of the larger pores transformed into smaller ones. In contrast, higher fibre dosage resulted in a pore size coarsening. From Figures 3.19 and 3.20, it can be noticed that mortar containing high fibre dosage (0.5%) has more number of larger pores in the range of 1 μm to 100 μm whereas plain mortar has fewer pores in this range and

mortar with 0.15% fibre dosage has the lowest. Median pore size also shifted with the addition of fibre. At low dosage, fibres transform a fraction of the large (diameter ranging from 1 μm to 100 μm) air voids into finer ones implying a pore size refinement, while at high fibre dosage, a pore coarsening can be observed. Predominantly identical trend can be observed for Type N mortar and Type O mortar. Pore size distribution, frequency distribution of pores and differential pore size distribution of pores for Type N mortar are shown in Figures 3.21, 3.22and 3.23 while Figures 3.24, 3.25 and 3.26 displays those corresponding plots for Type O mortar.

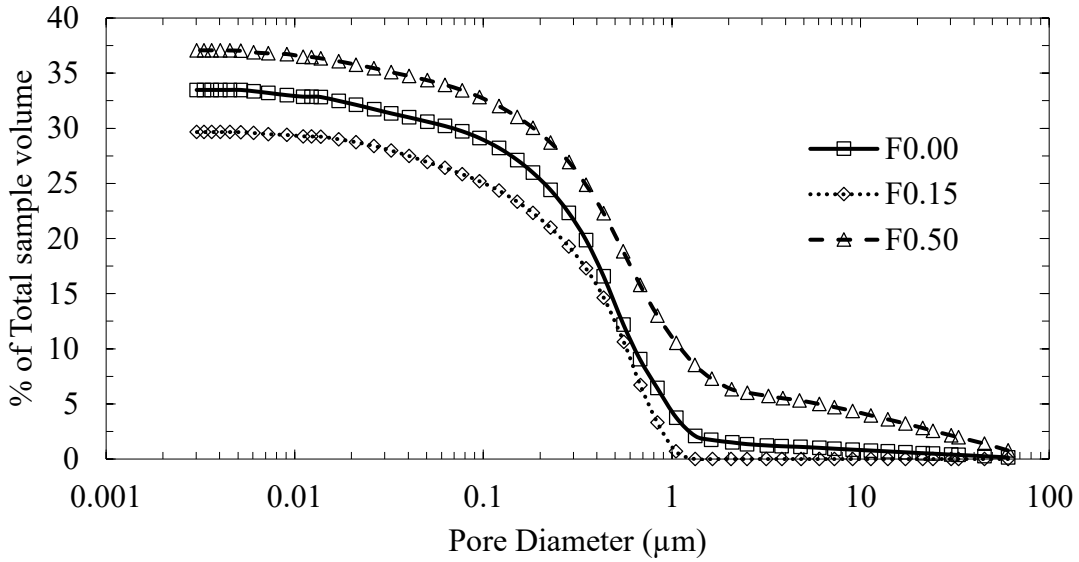

Figure 3.18 Pore size distribution of Hydraulic Lime Mortar by MIP method

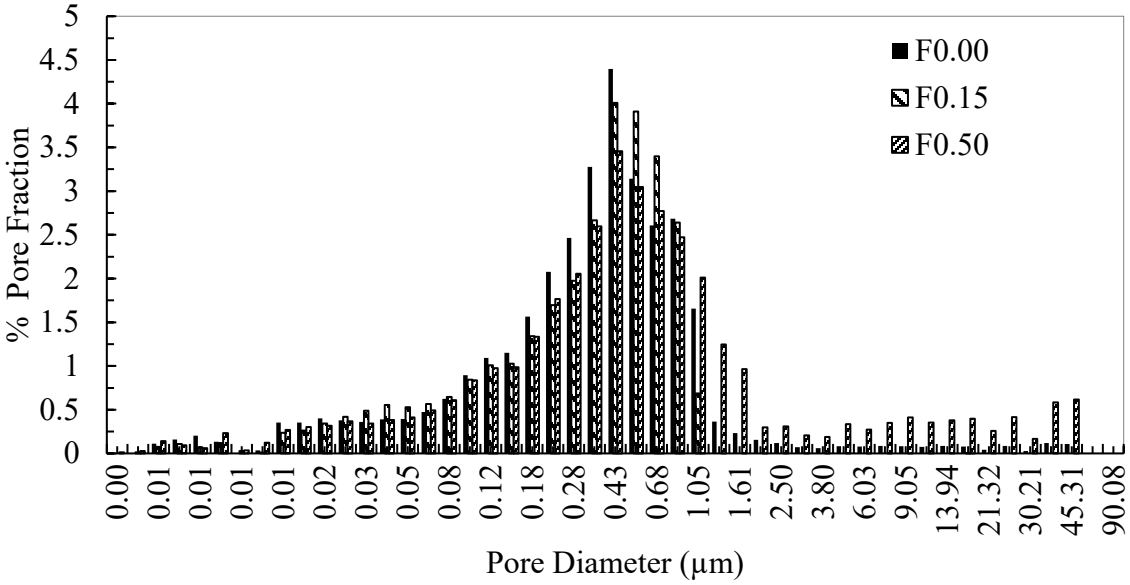

Figure 3.19 Frequency distribution of pores in Hydraulic Lime Mortar by MIP method

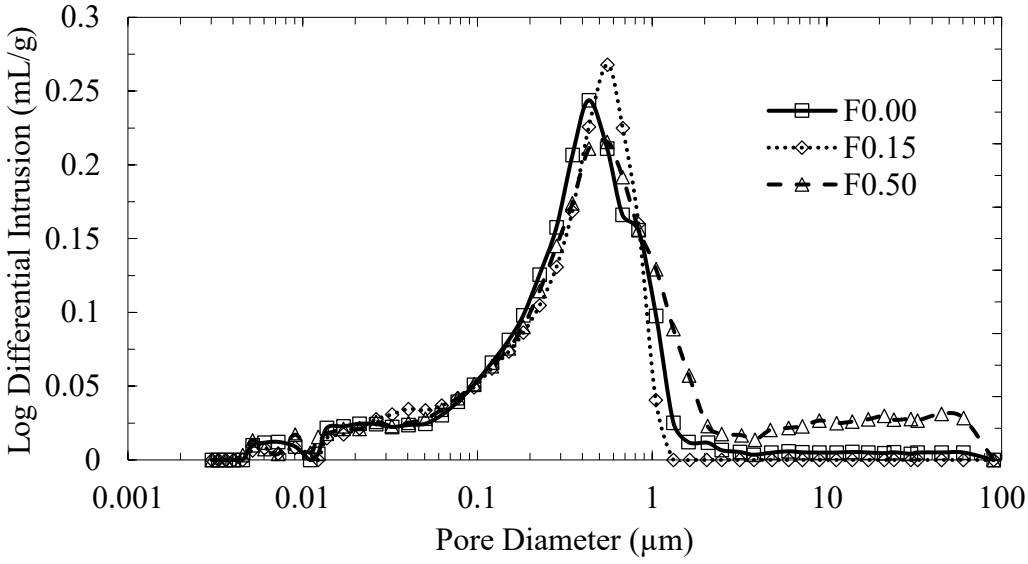

Figure 3.20 Differential pore size distribution of Hydraulic Lime Mortar by MIP method

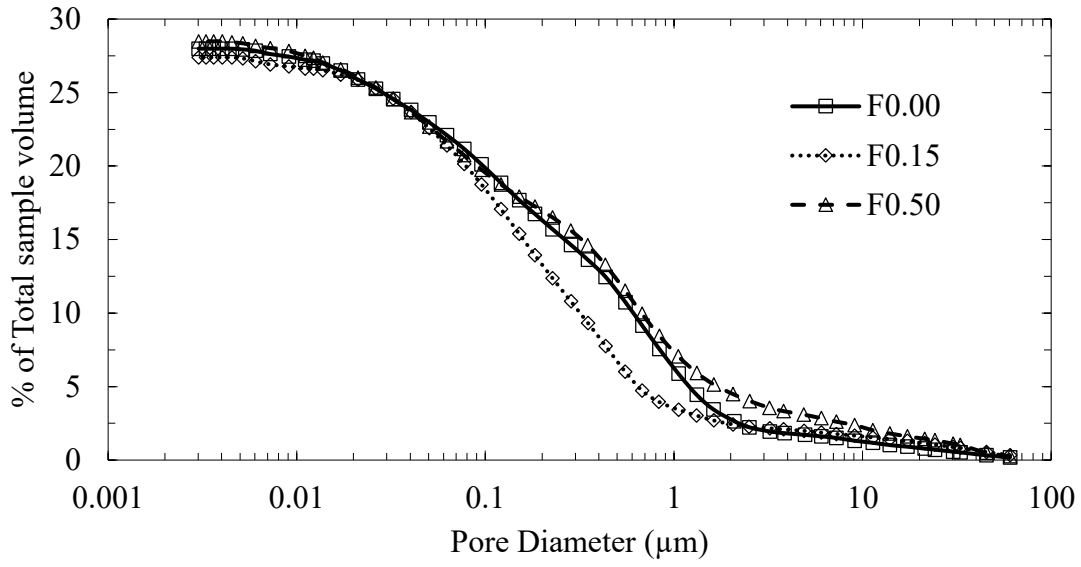

Figure 3.21 Pore size distribution of Type N mortar by MIP method

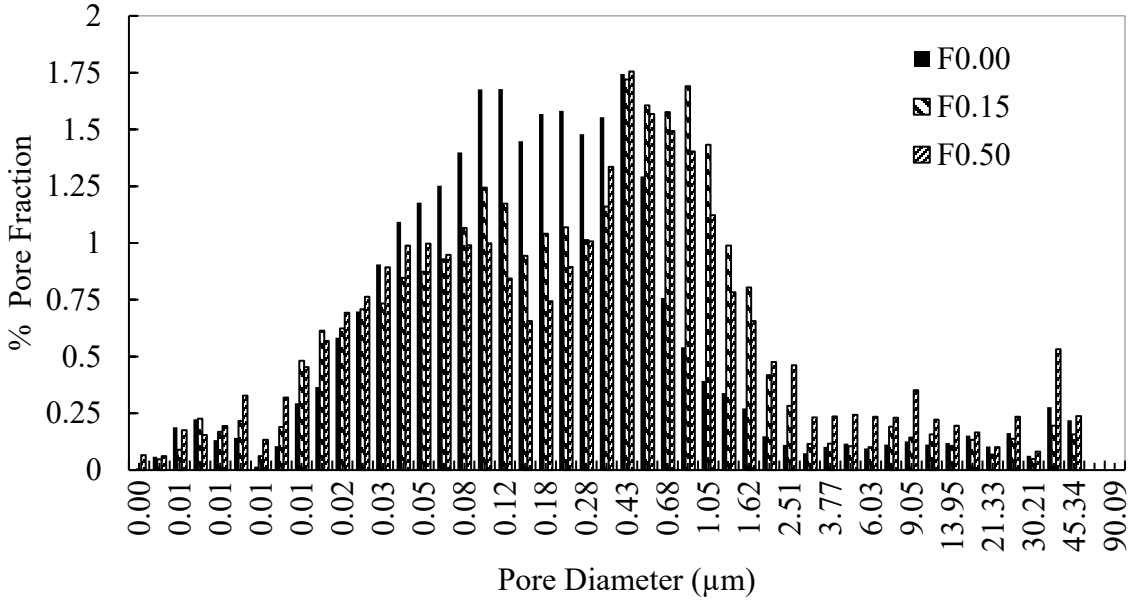

Figure 3.22 Frequency distribution of pores of Type N mortar by MIP method

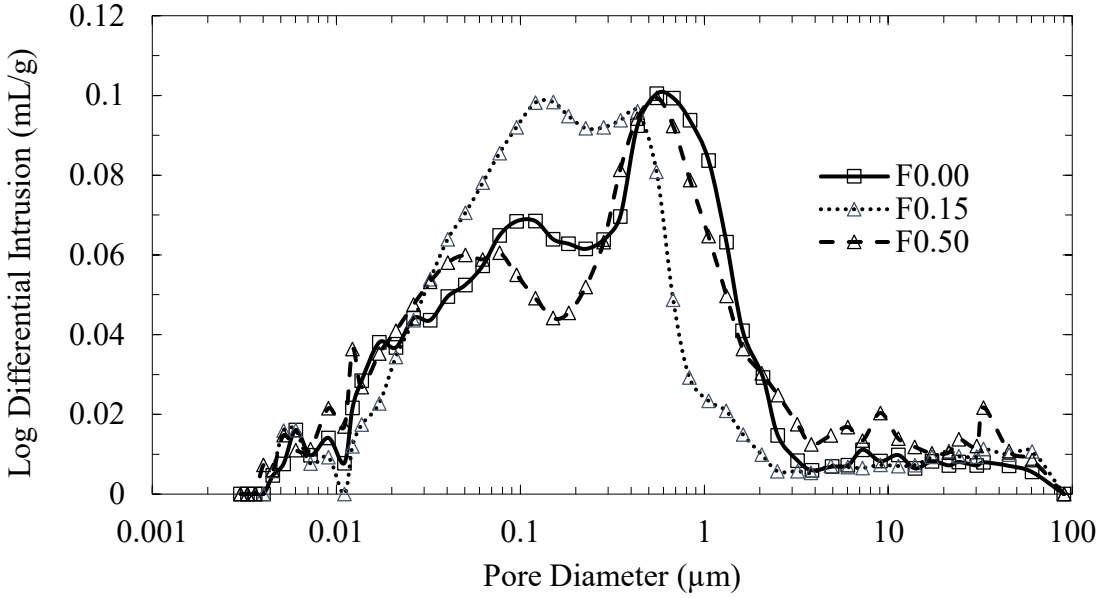

Figure 3.23 Differential pore size distribution of Type N mortar by MIP method

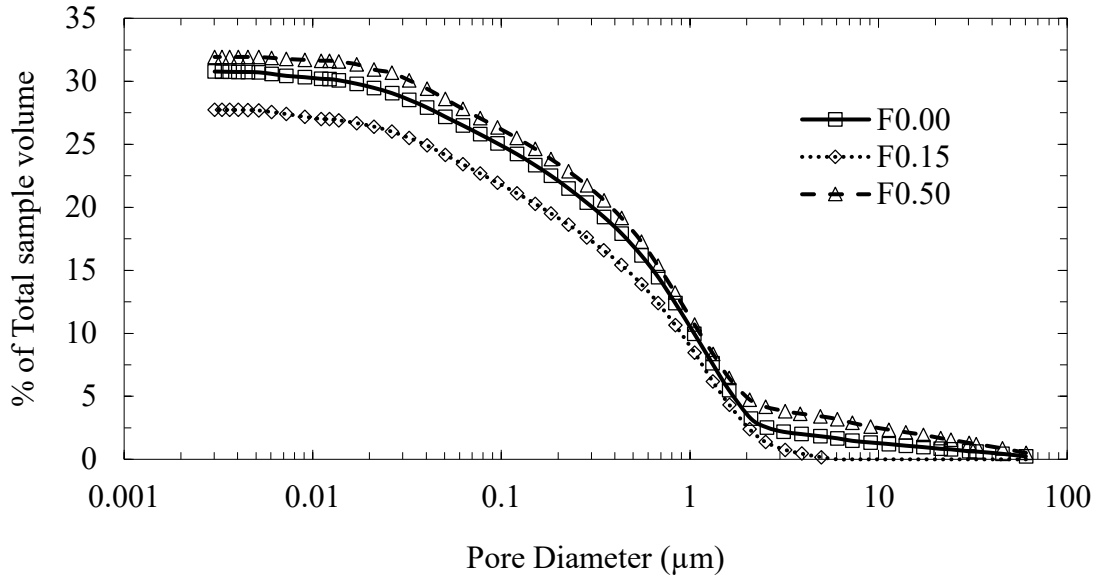

Figure 3.24 Pore size distribution of Type O mortar by MIP method

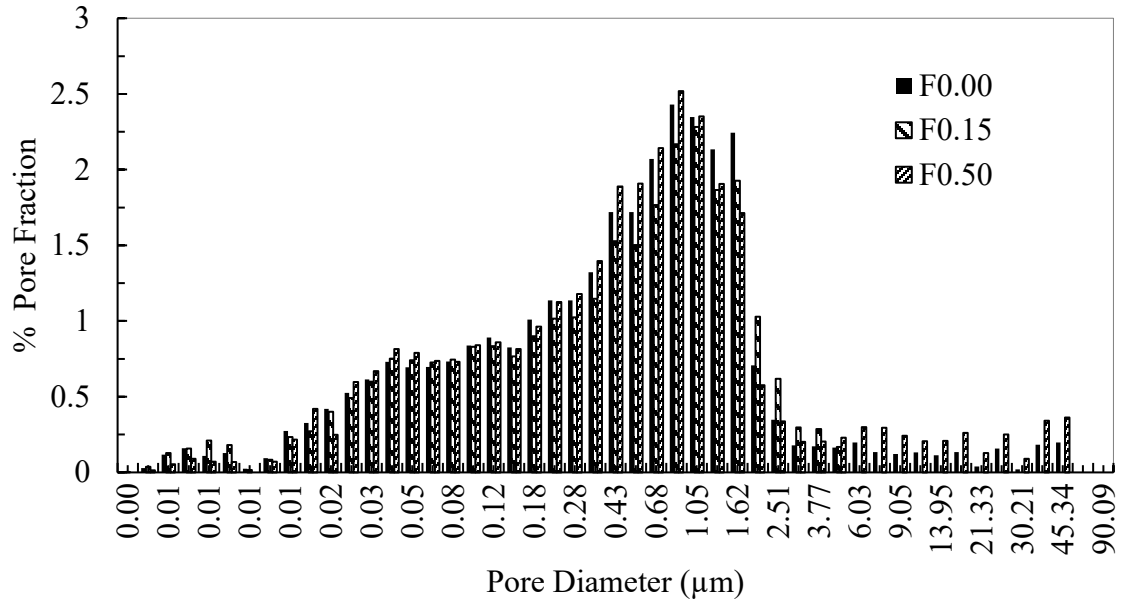

Figure 3.25 Frequency distribution of pores of Type O mortar by MIP method

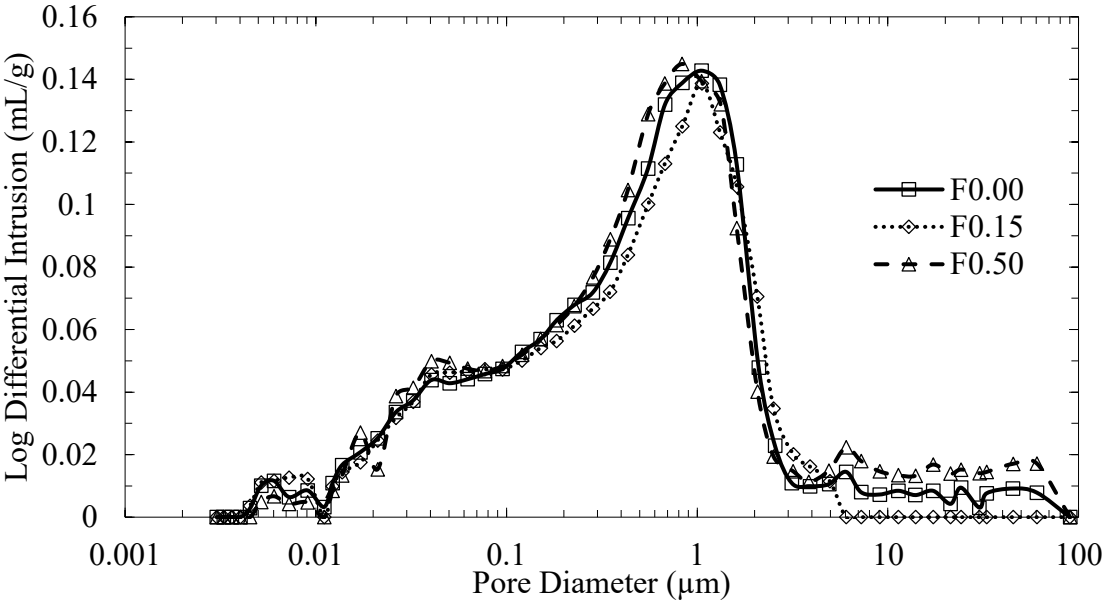

Figure 3.26 Differential pore size distribution of Type O mortar by MIP method

3.4.3 Pore Size Distribution by Nitrogen Adsorption

As stated previously, nitrogen adsorption is a common tool to determine the pore size distribution of nano-pores, and low porosity. It was adopted here to visualize how fibres alter pores in the sub-micron range-(1–300 nm). The size distribution of micro-pores along with

meso-pores (0.3–500 nm) offers a valuable guidance for better estimating the permeability in plain and fibre reinforced hydraulic lime and Portland cement-lime mortar. Recall that pores below 60 nm in radius do not contribute towards fluid transport (Neville 2011). As discussed in Section 3.3.4, isotherm that was obtained at 77 K, was estimated using the well-known BJH analysis method (Barrett et al. 1951). Note that an isotherm has both an adsorption and a desorption branch which can be analyzed for pore size distribution. However, here the pores size distribution was obtained by using the desorption isotherm and considering that it possesses a lower free energy state caused by lower relative pressure.

Pore size distribution as obtained by the BJH method is shown in Figures 3.27, 3.29, and 3.31, respectively for the Hydraulic Lime Mortar, Type N mortar, and Type O mortar. The pore size range that can be measured by nitrogen adsorption is 1 nm to 300 nm. Hence, the total detectable porosity as obtained by this method is the highest cumulative pore fraction. The total porosity for Hydraulic Lime Mortar within the stated size range was found to be between 2.4% and 2.5% (depending on fiber dosage). For the Type N mortar, the total porosity varied from 3.3% to 4.8% whereas for the Type O mortar it varied from 2.7% to 2.8%. It is seen that Hydraulic Lime Mortar has the lowest porosity (above mentioned size range) among these three mortars, Type N mortar has the highest porosity and Type O mortar porosity lies in the middle. As shown in Tables 3.2, 3.3, and 3.4, the compressive strength of Hydraulic Lime Mortar was the lowest, Type N mortar was the highest, and that of Type O mortar was between the other two. Hence, it can be concluded that a mortar will have higher meso-pores and micro-pores as compressive strength increases. As nano pores do not contribute towards fluid transport, it can be said that higher density implies lower fluid permeability. Further, the Figures 3.28, 3.30, and 3.32, once again reveal that the addition of fibre reinforcement generally results in a pore size refinement across all types of mortar whereby a fraction of large diameter pores transformed into smaller ones.

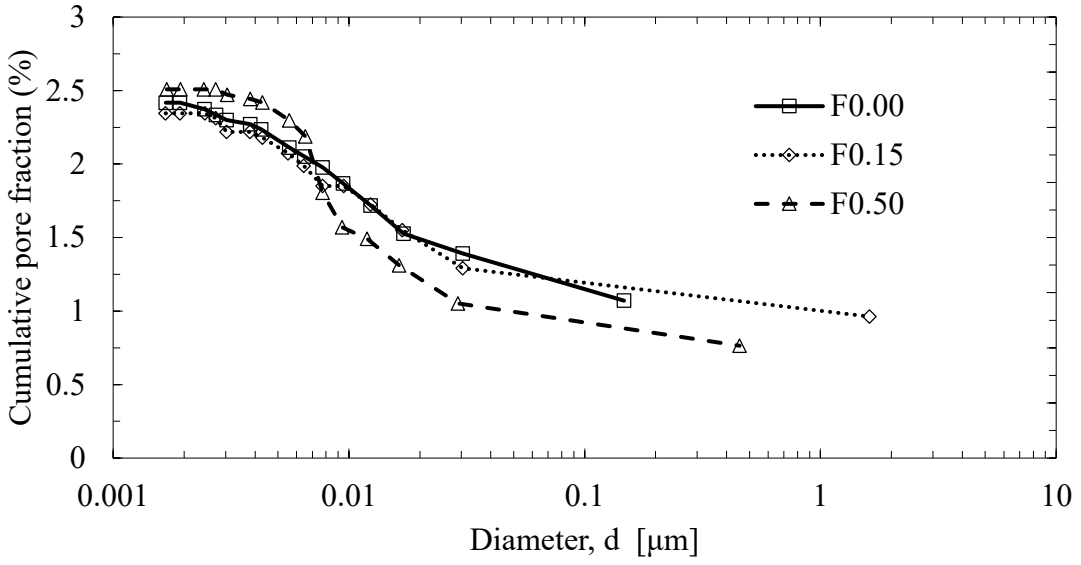

Figure 3.27 Pore size distribution of Hydraulic Lime Mortar by nitrogen adsorption method

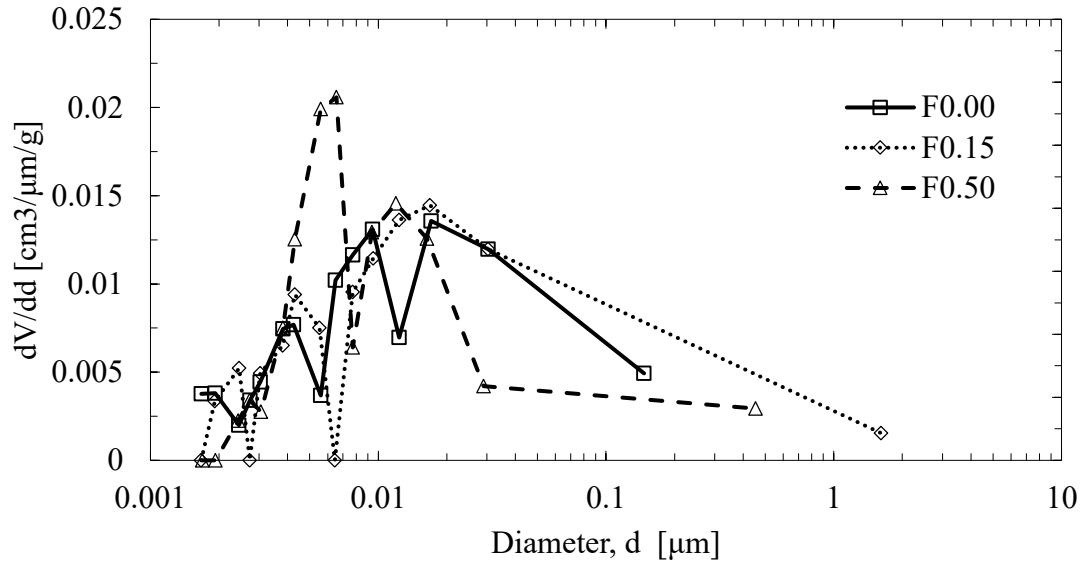

Figure 3.28 Differential pore size distribution of Hydraulic Lime Mortar by nitrogen adsorption method

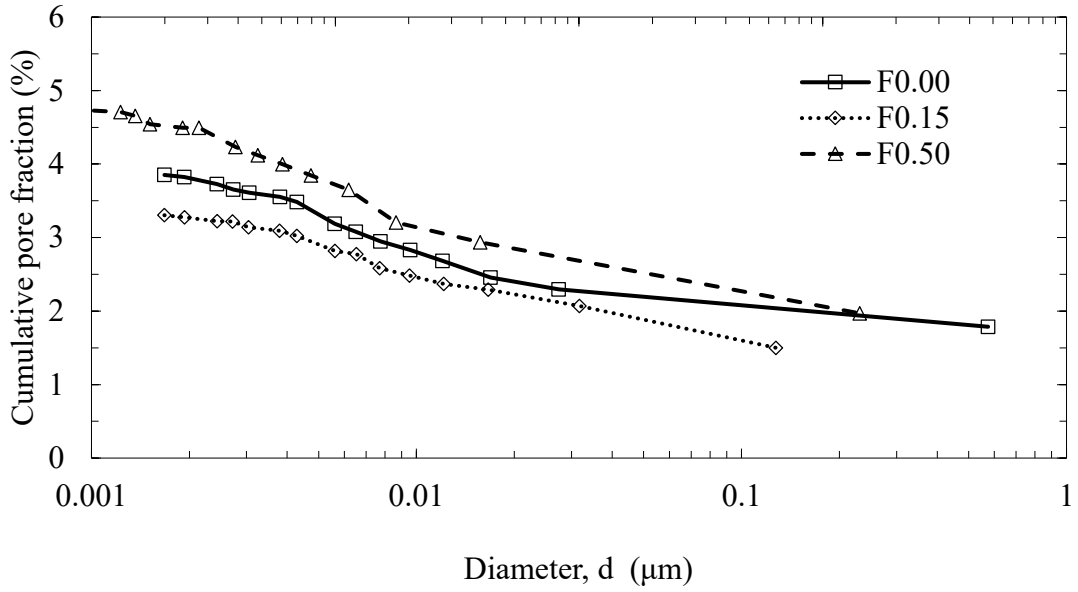

Figure 3.29 Pore size distribution of Type N mortar by nitrogen adsorption method

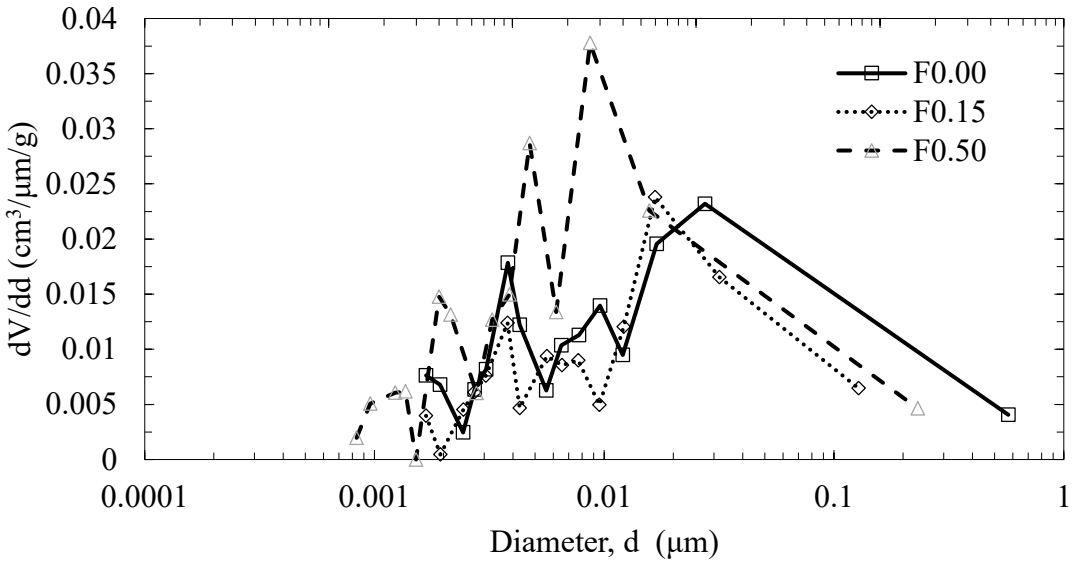

Figure 3.30 Differential pore size distribution of Type N mortar by nitrogen adsorption method

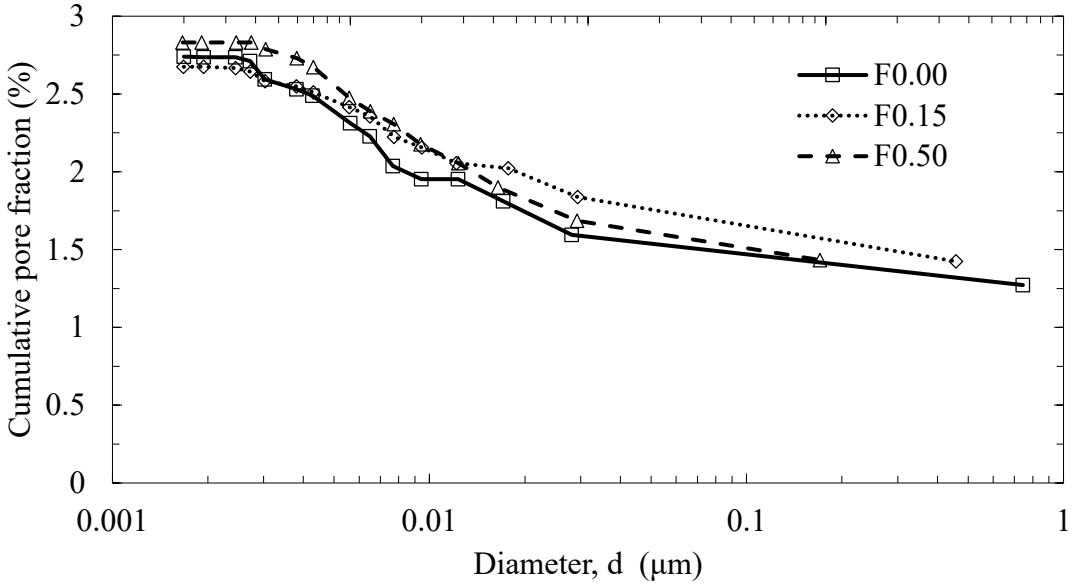

Figure 3.31 Pore size distribution of Type O mortar by nitrogen adsorption method

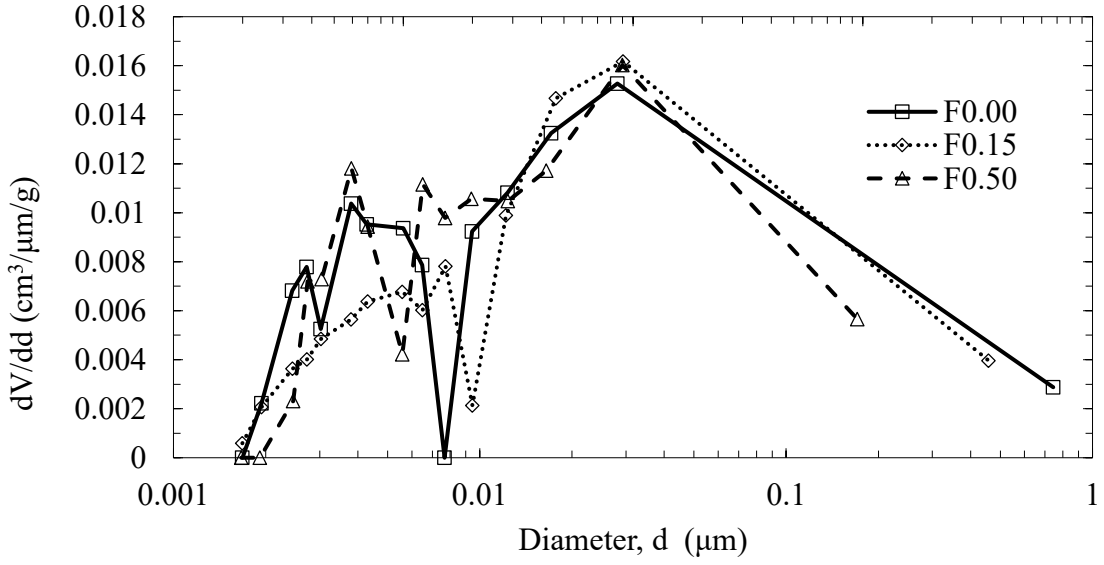

Figure 3.32 Differential pore size distribution of Type O mortar by nitrogen adsorption method

3.4.4 Pore Size Distribution by Image Analysis (Using Opening Method)

Image analysis is a very powerful tool to investigate the pore structure and relative pore size distribution for cement-based composites. As already discussed, the Opening Method is a

morphological image processing technique through which the pore size distribution of plain and fibre reinforced mortar can be determined. This process is a combination of two other morphological operations namely, erosion and dilation. Erosion and dilation operations (Gonzalez and Woods 2008) are run on a pre-processed binary image comprising only the pore phase. Pores smaller than the size of a chosen structuring element are removed from the image in each step of opening operation, and thus obtaining cumulative area fraction of pores having a size larger than the size of the structuring element. Note that the outcomes from opening method are in better agreement with that from strictly experimental method such as the Wood's Metal Intrusion Porosimetry, which is known to provide reliable pore size distribution (Abell et al. 1999; Scrivener et al. 2016; Willis et al. 1998).

Pore size distribution as obtained from images by opening method for plain and fibre reinforced Hydraulic Lime Mortar, Type N mortar, and Type O mortar are illustrated in Figures 3.33, 3.34 and 3.35 respectively. It is worth mentioning that the results were obtained by combined analyses of BSEM images having three different magnifications namely – 50X, 400X, and 800X with a spatial resolution of 2.1354 μm/pixel, 0.2636 μm/pixel, and 0.1358 μm/pixel. Due to wide variations of pores in cementitious materials, no single magnification can cover a representative range of pores. In fact, despite choosing three different magnifications, the smallest resolved pore size studied was 0.27 μm in diameter. The magnification for this study was chosen keeping in mind that pores having a diameter of 120 nm or larger are of interest as far as fluid transport phenomenon is concerned (Neville 2011). It is noteworthy that the higher energy of the backscattered electrons leads to lower resolution for the BSEM image compared with the regular SEM image. Images captured at 50X magnification and a spatial resolution of 2.1354 μm/pixel allowed detection of large capillary pores as well as air-voids, which are usually in the range of few μm to several hundred μm for cement-based systems.

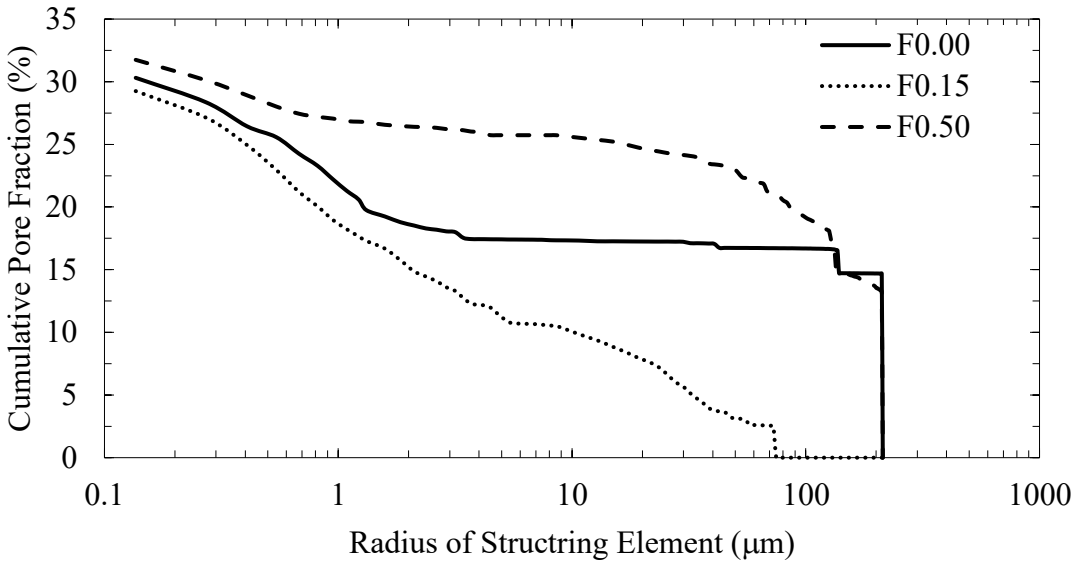

Figure 3.33 Pore size distribution of Hydraulic Lime Mortar by image analysis

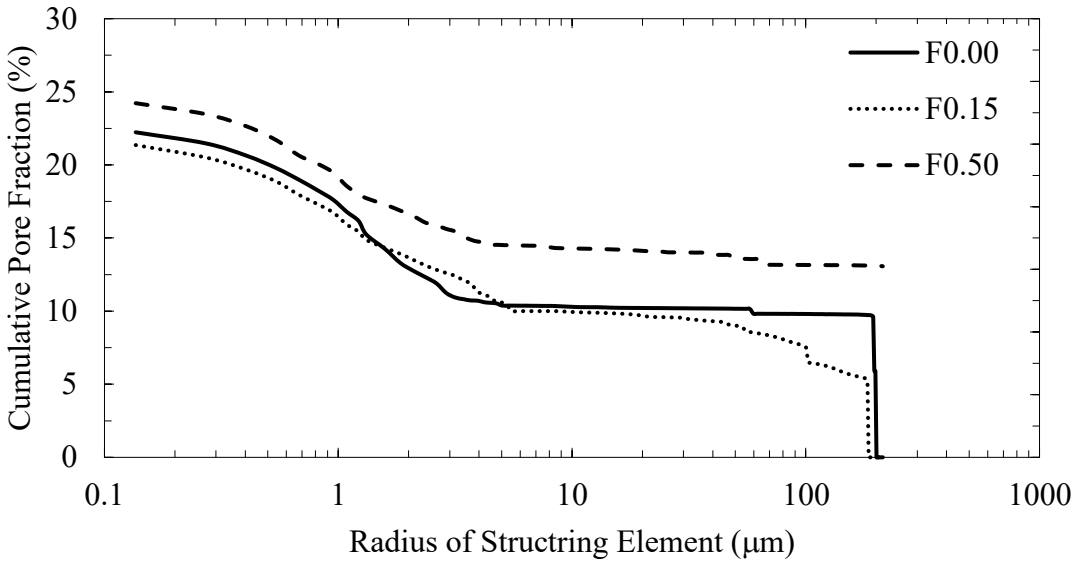

Figure 3.34 Pore size distribution of Type N mortar by image analysis

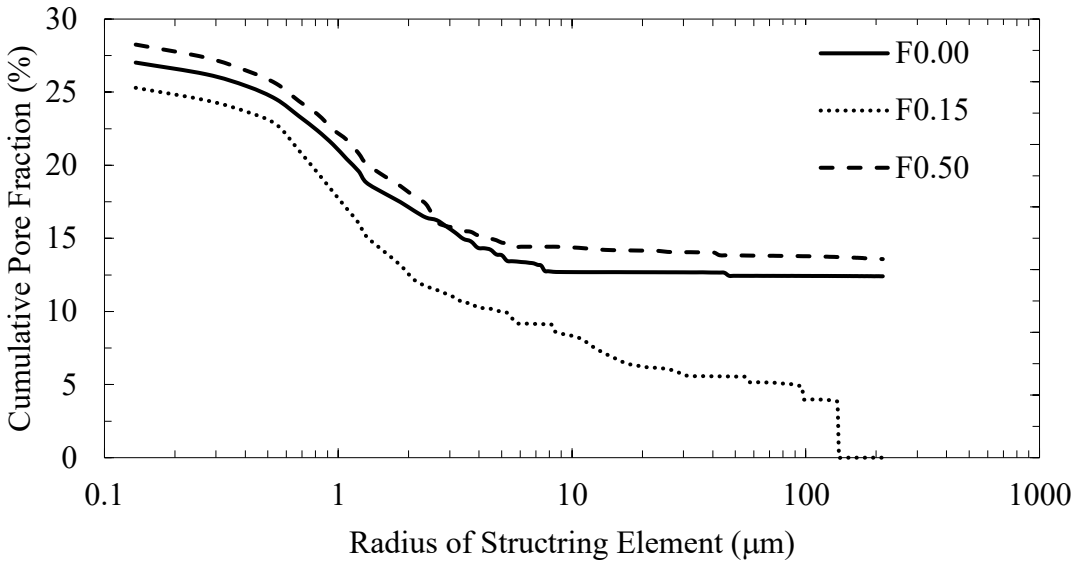

Figure 3.35 Pore size distribution of Type O mortar by image analysis

Figures 3.33, 3.34, and 3.35 show that large pores (radius larger than about 1 micron) are more prominent in mixtures with higher fibre dosage, in keeping with Bentur and Mindess, (2007) This is because a higher dosage of fibre makes it difficult to mix and properly compact the mortar, which leads to the presence of entrapped air-voids and an increase in the amount of larger pores. In other words, while low fibre dosages lead to a pore refinement, higher fibre dosages resulted in a coarsening of the pores. In addition, it can be observed that mean pore size generally decreased with low fibre addition. This phenomenon is more noticeable in Hydraulic Lime Mortar and Type O mortar, whereas it is not that significant for Type N mortar. This may be due to the fact that Hydraulic Lime Mortar and Type O mortar are low strength mortars having almost similar compressive strength whereas Type N mortar is of slightly higher strength.

3.4.5 A comparison between Results from Mercury Intrusion Porosimetry (MIP) and Image Analysis (Using the Opening Method)

A comparison of pore size distribution obtained from MIP and Image analysis are shown in Figures 3.36, 3.37, and 3.38 for plain and fibre reinforced Hydraulic Lime Mortar, Type N mortar, and Type O mortar respectively. It is clearly visible that the MIP method

underestimates pore sizes for all types of mortar. It should be emphasized that the range of pore sizes as identified by MIP method is not representative of actual pore sizes. As seen from a typical SEM image in Figure 3.8, the mortar has large air-voids having a pore size of about 400 μm. It is known for some time that cementitious materials have air-voids in the range of 10 μm to 500 μm which constitutes a substantial portion of the total pore volume (Song 2014). However, there is very small amount of such air-voids in any of the pore size distribution obtained through MIP. This scenario is true across all three types of mortar.

As stated earlier, MIP has been criticized as it overestimates finer pore sizes due to so called "ink-bottle effect" and accessibility issues which are well described here (Lange et al. 1994). Diamond (2000) suggested not to use MIP method to measure the actual pore sizes distribution. Despite this limitation, MIP was adopted in this study for a comparative study of the effect of different fibre contents on the pore size distribution of mortar. Note that the total detectable porosity by MIP instrument and threshold diameter are not affected by the abovementioned limitations and can be used as comparative indices for cement-based mortars. It is worth mentioning that there is very limited literature available for Hydraulic Lime Mortar and cement lime mortar. Hence, the outcome of this research can be a valuable guideline for similar types of mortars.

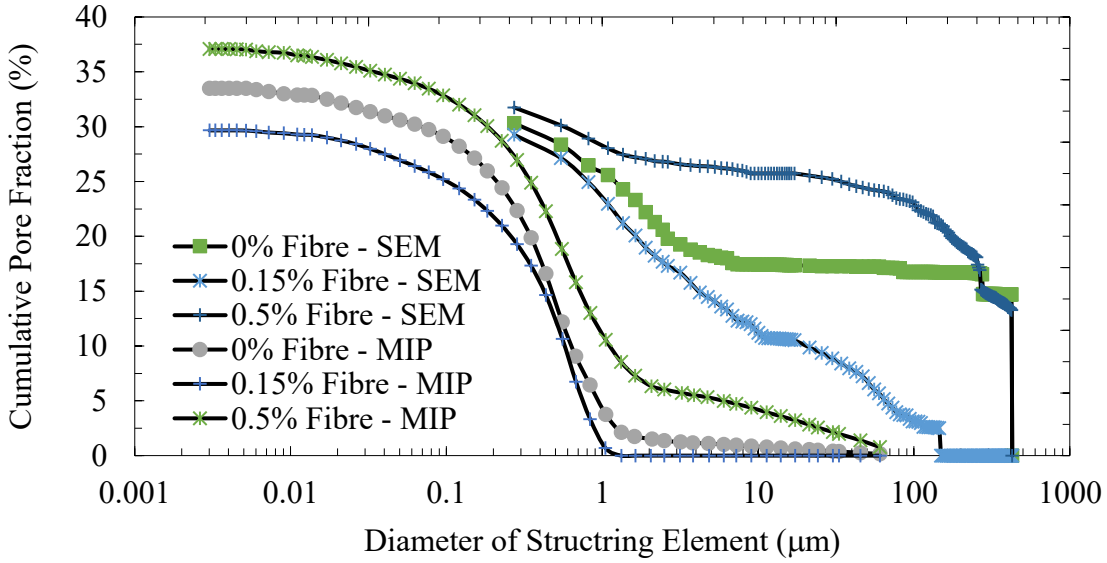

Figure 3.36 Comparison of pore size distribution of Hydraulic Lime Mortar

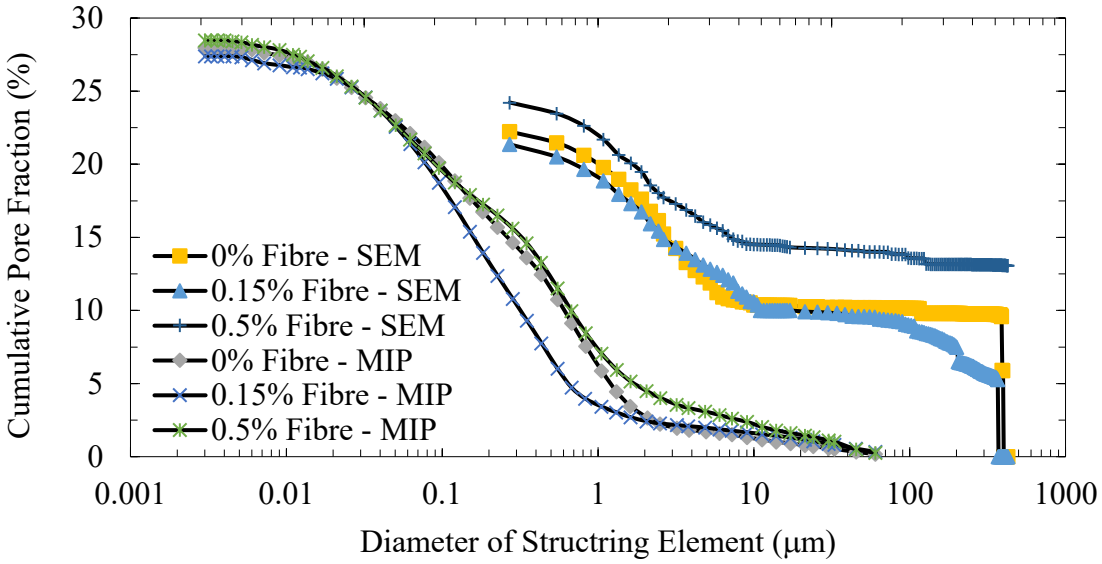

Figure 3.37 Comparison of pore size distribution of Type N mortar

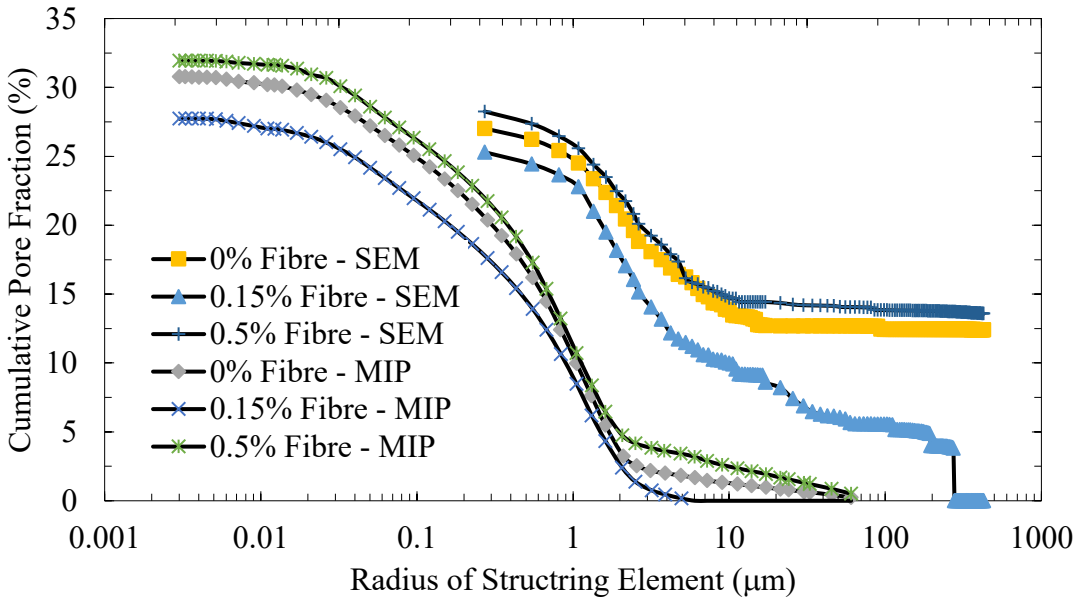

Figure 3.38 Comparison of pore size distribution of Type O mortar

These above results are compared in Figure 3.39. Notice that the MIP method covers a wider range at the lower size of pores than SEM. Lange et al. (1994) has presented the same trend

but with an off-set by 3 orders of magnitude where MIP failed to capture larger pores. . (Willis et al. 1998) came to the same conclusion based on a study of cement-based materials. Their data was recalculated by Diamond (2000) as shown in Figure 3.39(b). The image analysis was conducted by Wood's metal intrusion porosimetry – a method capable of producing a more reliable size distribution although it requires a complex experimental protocol (Hu 2004; Willis et al. 1998). From the graphs, it can be seen that MIP method was not able to detect the large air-voids for cement-based mortar.

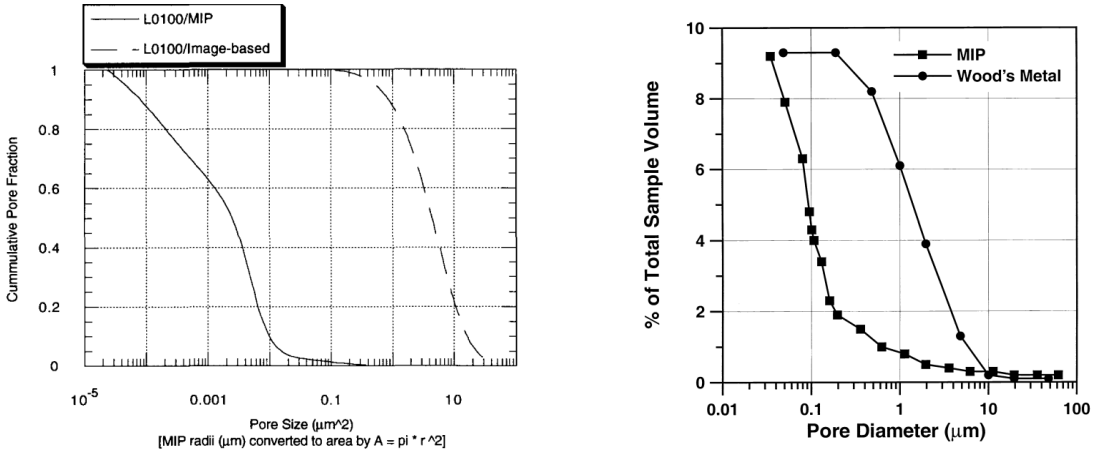

(a) (b)

Figure 3.39 Comparison of pore size distribution by MIP and image analysis by other authors (a) extracted from (Lange et al. 1994) (b) cited from (Diamond 2000) and data sourced from (Willis et al. 1998)

3.4.6 Two-Point Correlation Method

As mentioned in the foregoing paragraphs, the Two Point Correlation (TPC) function developed by Berryman and Blair, (1986), is a simple statistical function, which uses SEM images of cross sections of porous media to determine its microstructural features. Figure 3.40, shows how various parameters that define the pore structure such as the porosity (ϕ), the specific surface area (s), and the characteristic pore size (r_c) can all be directly determined from image processing. As described in Figure 3.40, the porosity (ϕ) is the maximum value

of TPC evaluated at $R = 0$, whereas the slope of the plot at that point provides a measure of specific surface area of the material. The details of TPC functions can be found in the literature (Berryman 1985, 1987; Berryman and Blair 1986; Blair et al. 1993, 1996).

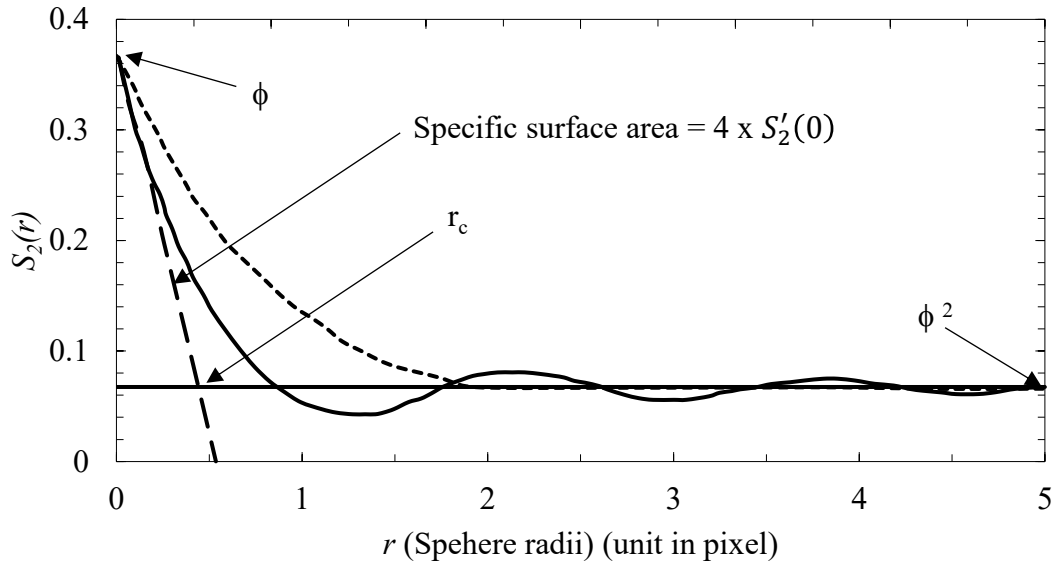

Figure 3.40 Pore structure parameters from two-point correlation function for fully penetrable (short dashes) and impenetrable (solid curve) sphere models (after Berryman and Blair (1986)) (adopted from (Blair et al. 1993))

The TPC functions of plain and fibre reinforced mortars are shown in Figures 3.41, 3.42, and 3.43 for Hydraulic Lime Mortar, Type N mortar, and Type O mortar respectively. High-resolution images with a resolution of 400x (0.263 μm/pixel) was used to develop the TPC functions. Berryman and Blair (1986) have suggested to use spatial resolution in the range of 500x when specific surface area of the materials are of special interest. They arrived at this conclusion by using this correlation method on sandstone. But, as can be seen from Figures 3.41, 3.42, and 3.43, the basic trend for variation in all types of mortars examined here are similar to the afore cited work. Thus, this correlation technique is deemed fit to apply on mortars as well, to get a reliable information on their pore structure. From these TPC plots, it can be observed that the peak value, which represents the porosity, (ϕ) is the lowest for the mix with 0.15% fibre, whereas 0.5% fibre mix has the highest value. Hence, it can be concluded that porosity measured at this resolution changes with fibre addition. When fibre is

added in small dosages, porosity decreases while it increases with the addition of higher doses of fibre. Further, it is noticed that all the TPC functions have a monotonic nature becoming asymptotic in the range of large *R* values. This shows the interconnected nature of pores in the mortar because TPC function captures the isolated pore features as the oscillating trail portion in the plot (Torquato 2013).

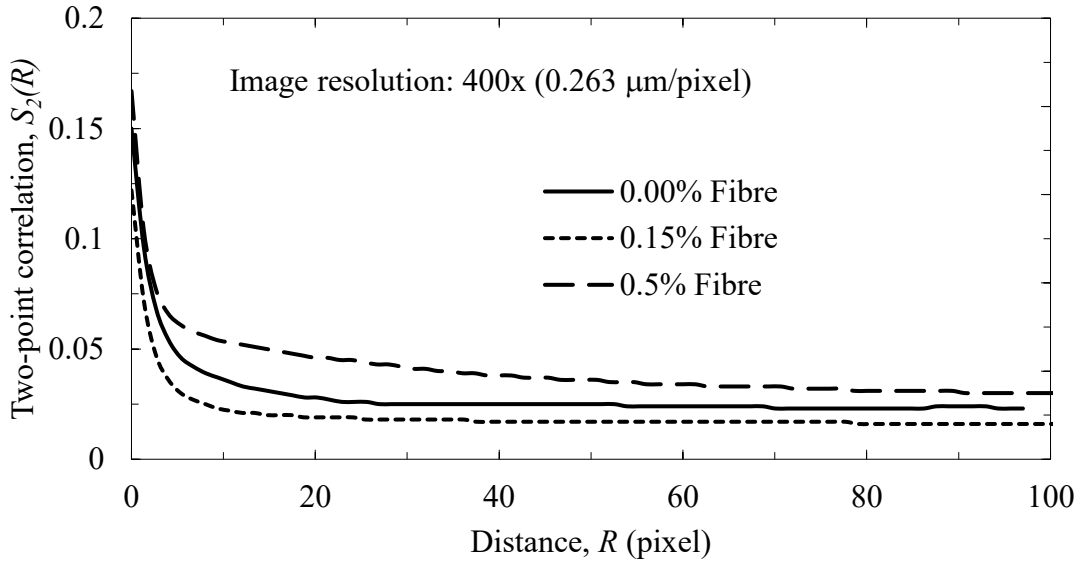

Figure 3.41 Two-point correlation function of plain and fibre reinforced Hydraulic Lime Mortar

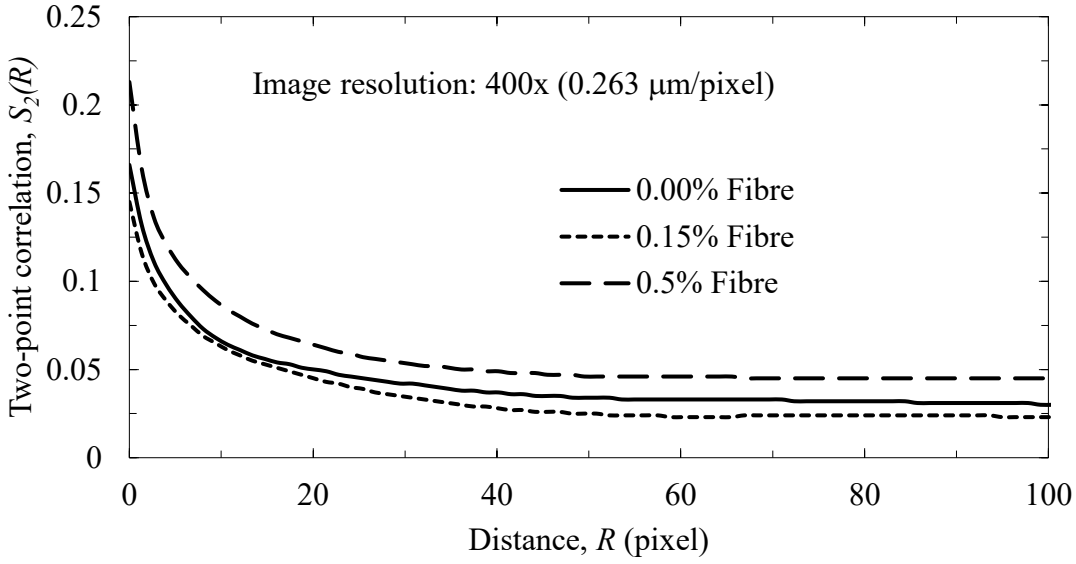

Figure 3.42 Two-point correlation function of plain and fibre reinforced Type N mortar

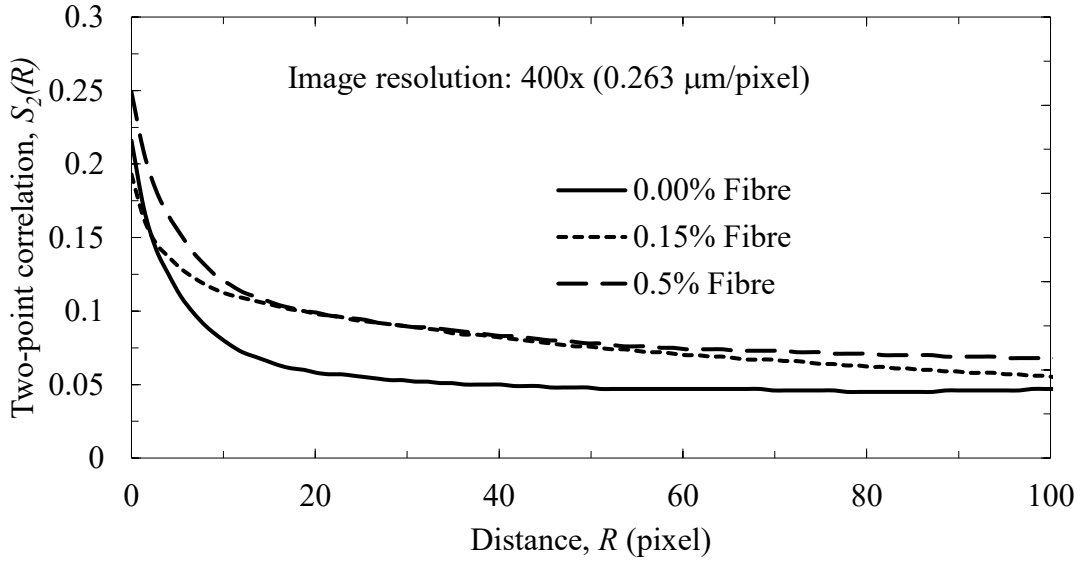

Figure 3.43 Two-point correlation function of plain and fibre reinforced Type O mortar

The image specific surface area (SSA) as obtained from TPC functions is illustrated in Figures 3.44, 3.45, and 3.46, respectively, for the Hydraulic Lime Mortar, Type N mortar, and Type O mortar. The plots include results on both plain and fibre reinforced mixtures. These estimated specific surface areas were seen to vary with the addition of fibres. Again, the variation is almost identical across all types of mortar. Low fibre dosage at 0.15% by volume fraction causes a drop in the SSA when compared with the plain mix i.e., without any fibre. On the other hand, the SSA increases with further addition of fibres. The value of SSA reaches the highest for the mixture with 0.5% fibre by volume. This decrease in SSA at low fibre content, but an increase at higher fibre content is principally due to the altered nature of pore structure of the mortar caused by the presence of fibre. The lower SSA value for mixes with low fibre dosage may be attributed to the pore refinement, while the increased SSA value is likely caused by the pore coarsening effect at higher fibre dosage, referred to earlier. This finding will further facilitate the prediction of transport properties of these materials.

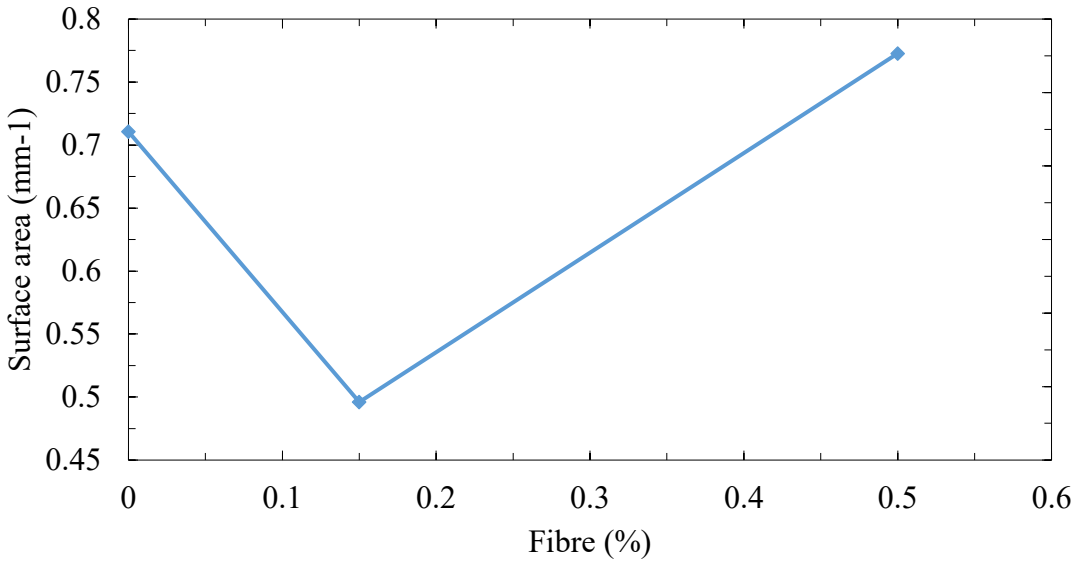

Figure 3.44 Specific surface area of plain and fibre reinforced Hydraulic Lime Mortar determined using two-point correlation method

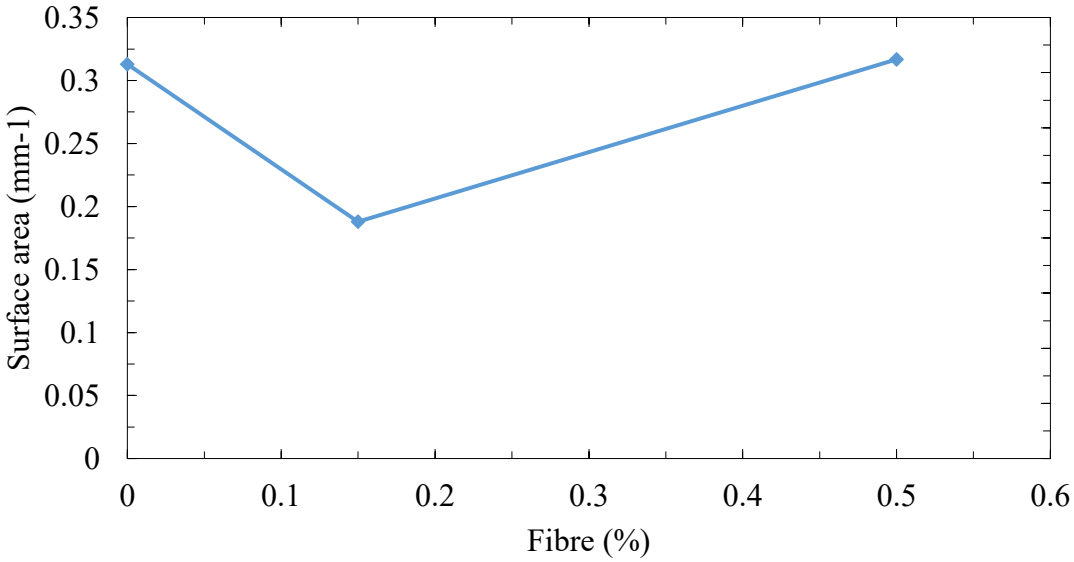

Figure 3.45 Specific surface area of plain and fibre reinforced Type N mortar determined using two-point correlation method

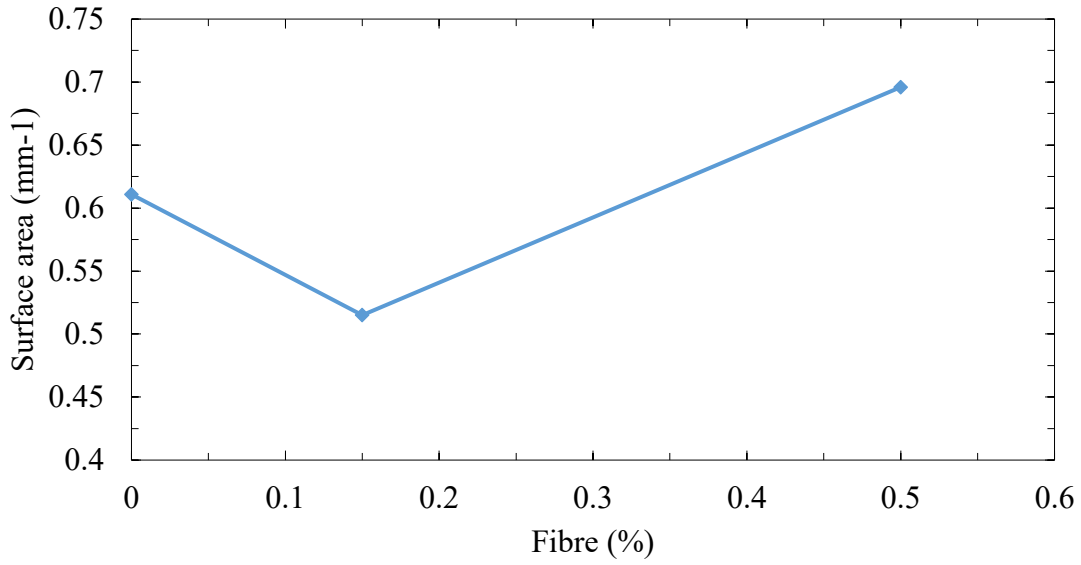

Figure 3.46 Specific surface area of plain and fibre reinforced Type O mortar determined using two-point correlation method

Another important microstructure parameter called characteristic pore size (r_c) which gives an estimate of mean pore size, can also be evaluated from TPC functions. It is defined as illustrated in Figure 3.40. The calculated values of the characteristic pore size (r_c) for plain and fibre reinforced mortars are plotted in Figure 3.47. It illustrates the characteristic pore size (r_c) as a function of fibre dosage for all three mortars namely, Hydraulic Lime Mortar, Type N mortar, and Type O mortar. Here again, the variations are similar across all types of mortar. The characteristic pore size (r_c) decreases for mixtures with low fibre dosage whereas it increases for higher dosage of fibre. Since the value of r_c can be regarded as the median pore radius in the mortar, it may therefore be considered as an indicator of the permeability itself.

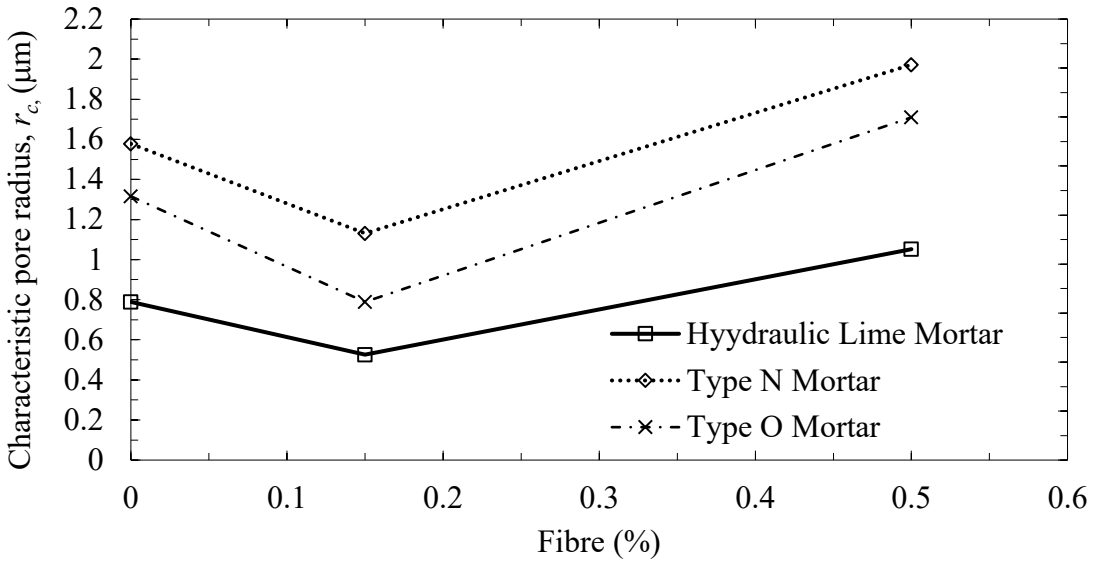

Figure 3.47 Characteristic pore radius determined using two-point correlation function for plain and fibre reinforced Hydraulic Lime Mortar, Type N mortar and Type O mortar

3.4.7 Fractal Dimension

Fractal dimensions (FD) of plain and fibre reinforced mortars made with hydraulic lime, Type N mortar, and Type O mortar are illustrated in Figures 3.48, 3.50, 3.52 as determined by the dilation method. In addition, in Figures 3.49, 3.51, 3.53, as determined by the box counting method. The variation in FD values follows a similar trend in all cases: FD decreases at low dosages of fibre and increases at higher fibre content, rather similar to the porosity variations at identical fibre dosage. It must be mentioned here that the literature on fractal behaviour of lime or cement mortars is scarce. Therefore, any available literature, from previous work has been taken as valuable guidance for this study.

In a study with polyester fibre reinforced cement based mortar, Mamun and Bindiganavile (2017) have made a detailed investigation on the fractal behaviour of mortars for different fibre contents and at different elevated temperature conditions. They also found that FD values increased as the porosity increased, both resulting from the addition of fibre reinforcement. SEM images were used in that study to calculate FD values for cement mortar. Castano et al.

(1990) found that the FD decreased with an increase in polymer content from a study on polymer modified cement paste. Though they did not measure porosity for polymer modified cement paste, since powdered polymer up to an optimal level decreases the porosity, this in other words would mean FD decreases with a decrease in porosity. (Ohama 1995) noticed that in polymer modified cement paste. The porosity decreased with an increase in polymer content. Thus, the conclusions drawn in this study are in agreement with those by Castano et al. (1990). From a study on concrete, Konkol and Prokopski (2011) concluded that the application of the fractal dimension to the description of porosity had proved to be an efficient, reliable method, and the results so obtained well suited to describing the water transport of concrete. The fractal dimension of pore space in cement paste was seen to increase with the water/cement ratio, which appears to be linearly dependent on the porosity for pores no smaller than 1 μm (Gao et al. 2014). On the other hand, Lange et al. (1994) could not find any variation in FD values measured by dilation method with different porosities for silica fume modified cement paste. They also suggested using a constant value of FD as a modeling parameter.

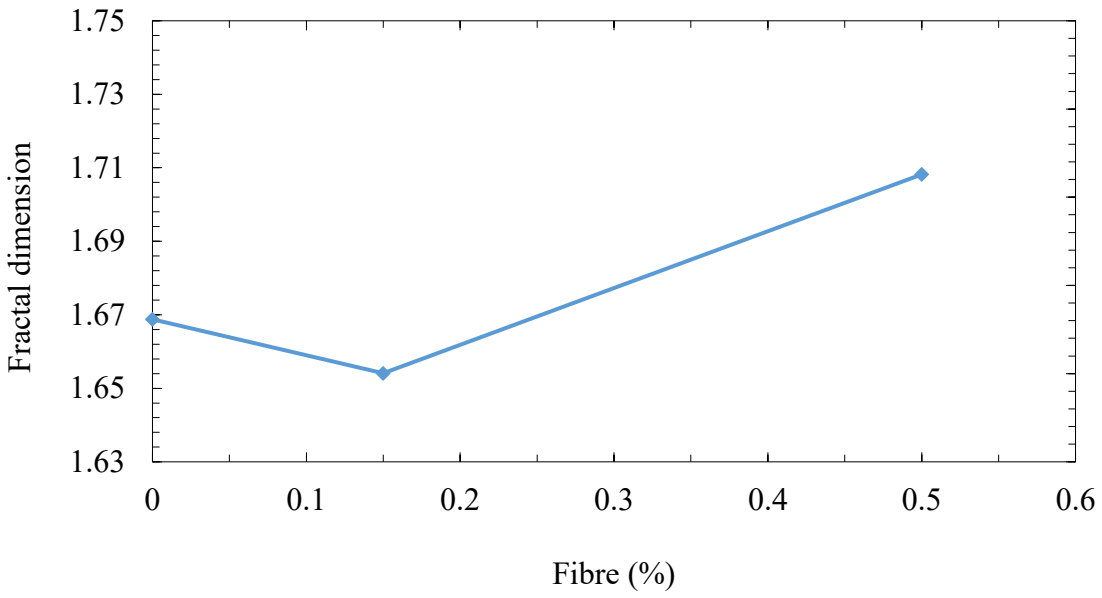

Figure 3.48 Fractal dimension of plain and fibre reinforced Hydraulic Lime Mortar determined using dilation method

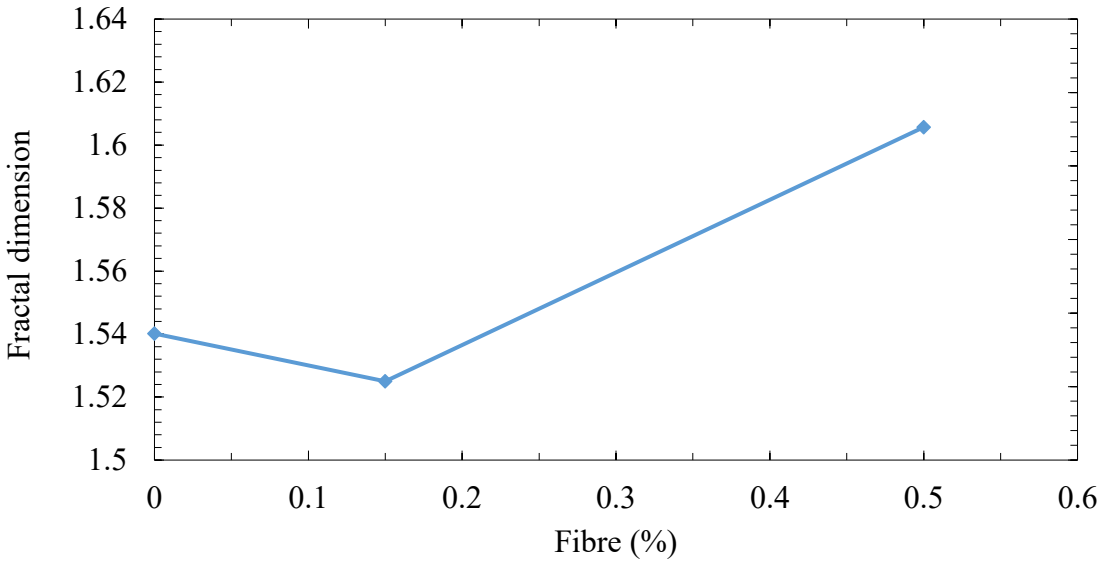

Figure 3.49 Fractal dimension of plain and fibre reinforced Hydraulic Lime Mortar determined using box-counting method

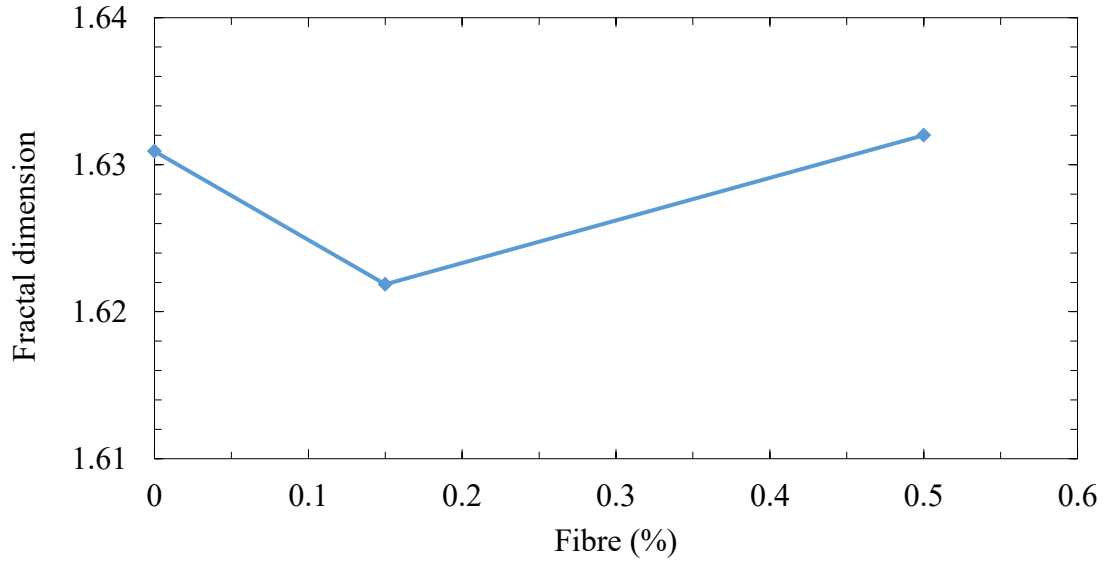

Figure 3.50 Fractal dimension of plain and fibre reinforced Type N mortar determined using dilation method

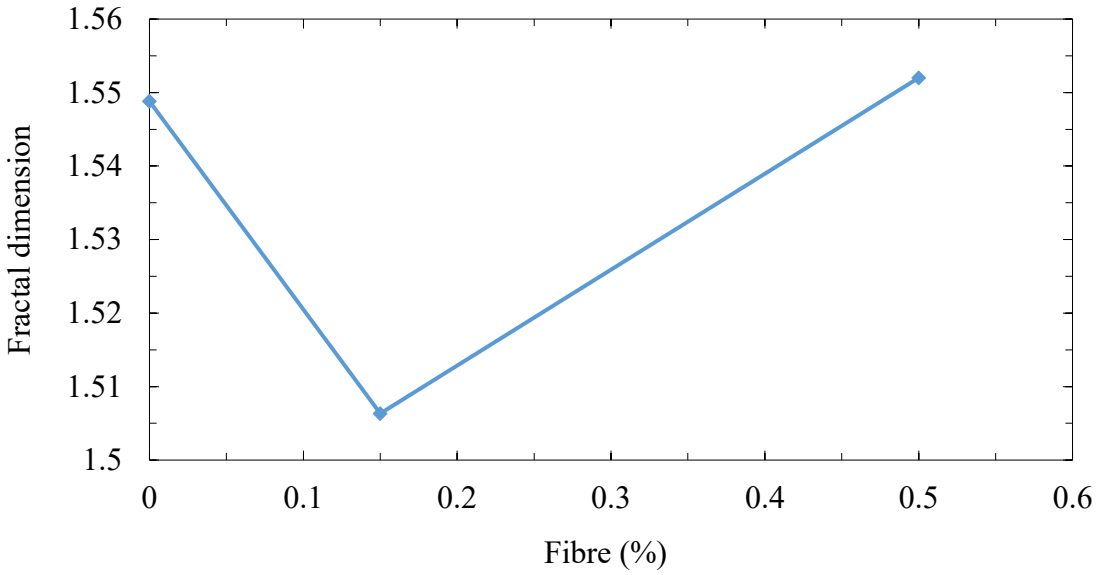

Figure 3.51 Fractal dimension of plain and fibre reinforced Type N mortar determined using box-counting method

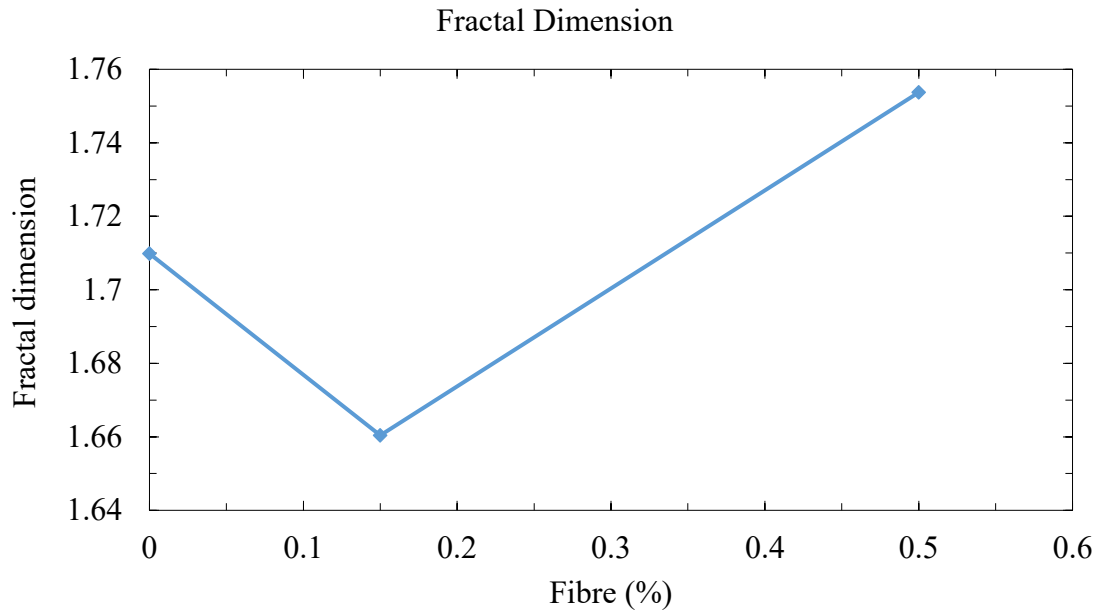

Figure 3.52 Fractal dimension of plain and fibre reinforced Type O mortar determined using dilation method

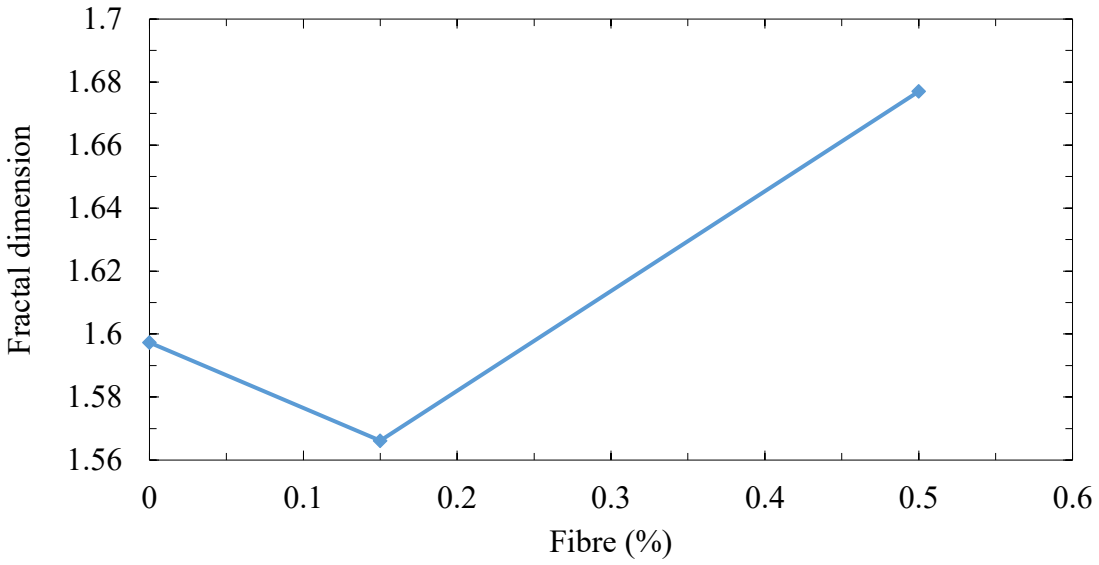

Figure 3.53 Fractal dimension of plain and fibre reinforced Type O mortar determined using box-counting method

3.5 Concluding Remarks

In this work, an effort has been made to evaluate and identify several microstructural features of cement-lime mortar and Hydraulic Lime Mortar. Influence of polymeric fibre on the microstructural properties of mortars is also determined. It is repeatedly made clear from the present findings that there is an optimum level of fibre dosage in repair mortars, which was 0.15% by volume. The key findings of this research through several methods to evaluate the pore structure for plain and fibre reinforced Hydraulic Lime Mortar, Type N mortar, and Type O mortar can be summarized as follows:

- Porosity decreases with fibre addition up to a volume fraction of 0.15% fibre. However, beyond this level, the porosity increases with a higher fibre dosage. This trend was found irrespective of mortar type or methods of evaluation.
- At low dosage (0.15%), the addition of fibre results in a refinement in pore size whereby a fraction of the larger pores transforms into smaller ones. In contrast, fibre reinforcement at levels beyond 0.15% by volume causes a pore size coarsening.

- MIP underestimates the macro pores for all three types of mortar, which is evident from the comparison of pore size distribution obtained through MIP method and image analysis.
- From two-point correlation function, the monotonic nature of the asymptotic region is visible in the range of large R values implying the interconnected nature of pores in the mortar.
- The specific surface area of all three types of mortar varies with fibre addition and the variation is almost identical for all mortar types. With the addition of low fibre dosage (0.15% by volume), the specific surface area decreases whereas it increases with the addition of higher dosage of fibre.
- The fractal dimension changes in a similar pattern across all types of mortar and methods of evaluation. It decreases with the addition of fibres up to a dosage of 0.15% by volume.

CHAPTER 4. EXPERIMENTAL AND ANALYTICAL EVALUATION OF PERMEABILITY IN FIBRE REINFORCED REPAIR MORTARS

4.1 Introduction

Permeability is one of the important properties governing the long-term durability of cementitious materials. Permeability depends not only on the porosity, but also on the pore size distribution, inter-connectivity and tortuosity of the pore channels. Permeability can be assessed to a reliable degree of accuracy through establishing its correlations with pore structure parameters such as porosity, pore connectivity, specific surface area, and tortuosity.

Permeability is defined as fluid flow through a medium under a pressure gradient. It can be estimated by direct measurement in the laboratory. But quite often, the permeability measurement through laboratory experiments requires expensive equipment and extensive time due to elaborate procedures. Water, air or other gases can be used as the flowing fluid for permeability measurements in the laboratory experiments. It is customary to utilize the well-established Darcy's law to determine the coefficient of water permeability in laboratory test method, assuming a steady-state unidirectional, laminar flow. It is generally assumed that the material is microscopically homogeneous. However, experimental outcomes must include the associated statistical variation of the measured properties.

Together with laboratory evaluation, it is attractive to obtain permeability information through analytical modeling. This requires a knowledge of microstructural properties of the material. There are several such parameters that need to be obtained experimentally as input when modelling the properties of heterogeneous porous materials. When employing a predictive model, it is equally important to justify the underlying assumptions of that particular model to estimate the permeability of porous materials such as cementitious systems. For instance, two materials having the same porosity but different tortuous path and connectivity will have different permeability properties.

Among several analytical methods, the Katz and Thomson (1986) model, which is based on percolation theory, relates permeability of a porous material to its pore structural parameters. As discussed in Section 3.3.3, MIP is a widely used technique for estimating the pore structure parameters such as formation factor and the size of critical flow path (Abell et al. 1999; Cook and Hover 1999; Giesche 2006; Zhou et al. 2010). However, one of the commonly cited drawbacks of this method is that it underestimates pore size distribution due to the so called "ink-bottle effect" and the associated difficulty with accessing those pores that are not continuously connected. MIP does not measure the true distribution of sizes for pore geometries found in cementitious materials. For these systems, large internal pores are accessible by very narrow throats. As a consequence, MIP technique misrepresents the size of these pores as having the diameter of their throats. This bias is referred to as the "ink-bottle" effect. The permeability equation proposed by Katz and Thomson (1986) is based on pore throat diameter (Figure 4.1) and the characteristic length determined through MIP test for rock samples. Application of this model for permeability prediction of porous material such as cementitious systems is limited due to the fact that MIP is unable to provide a reliable estimation of pore structure parameters (Abell et al. 1999; Diamond 2000; Willis et al. 1998) . Besides, the model does not reflect the tortuous nature of the flow path.

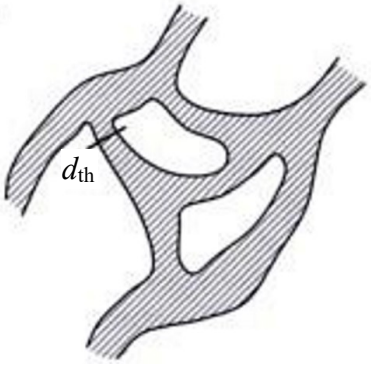

Figure 4.1 Schematic of pore throat diameter (Aligizaki 2005)

The pore microstructure as determined by image analysis are used often to predict the permeability of porous materials including Hydraulic Lime Mortar and cement-lime mortar. A spatial correlation method developed by Berryman and Blair (1986) is used here to determine the permeability coefficient. Originally, this method was developed to predict the permeability

of rocks. But it is found that this method can be applicable for cement-based materials as well (Neithalath et al. 2006; Wong et al. 2012). This method is based upon the statistical properties of the microstructure as observed in scanning electron micrograph (SEM) images of cross sections of porous materials. This method utilizes the spatial correlation function to evaluate the porosity and specific surface area. These two parameters along with the formation factor are incorporated into the well-known Kozeny-Carman relationship, as described in Section 4.5.1, to predict the permeability of porous materials.

Fractal nature is another well-known concept that can be used to predict the permeability of porous materials. The property of the fractal geometry satisfies the self-similarity at different scales by a single parameter called the fractal dimension. Note that in case of deterministic fractals, the fractal dimension refers to the self-similar characteristics of the geometry while for the natural fractals it describes the inherent statistical nature of self-similar behaviour. (Katz and Thompson 1986) Winslow (1985) has also shown that the irregular surface of cementitious materials may be considered a fractal. The porosity and roughness of the surfaces can be blended together to evaluate permeability properties of porous media. The Kozeny-Carman equation is probably the most used analytical method where the effect of these parameters can be demonstrated reliably (Henderson et al. 2010; Xu and Yu 2008). While porosity can be determined using any of the well-established experimental techniques, the roughness of the surface can be evaluated by using fractal concept. It is worth mentioning that most permeability models developed based on fractal geometry are essentially a modified version of Kozeny-Carman model where the tortuosity parameter is substituted by appropriate empirical constants (Atzeni et al. 2010; Berg 2014; Costa 2006; Pape et al. 1999; Xu and Yu 2008).

The presence of micro-fibres in cement-based systems is known to influence the microstructure. According to Banthia et. al. (2012), the fibres cause a refinement in the pore systems in cement-based composites. Consequently, the permeability of the material reduces due to the addition of fibre. This research investigates the effect of synthetic micro-fibre on the permeability of repair mortar.

4.2 Objectives

The investigation reported in this Chapter was performed to evaluate the permeability of three types of mortars namely, a Hydraulic Lime Mortar, Type N mortar and Type O mortar. Both plain and fibre reinforced mixtures were examined. First, a coefficient of permeability is determined experimentally by using water as the fluid medium. The influence of polypropylene micro fibre is also assessed. Secondly, permeability coefficients are predicted based on Katz-Thompson model, together with image analysis. Then, a relationship between the fractal dimension of the pore space and the permeability is developed to predict the permeability of both plain and fibre reinforced mortars.

4.3 Materials and Sample Preparation

Details of material properties, mixer proportions, specimen preparation is described in Section 3.3.1.

4.4 Permeability of Mortar: Laboratory Measurement

Historically, experimental measurements of permeability have been made with either water or various gases including oxygen, nitrogen, argon, and air. In order to describe the observed flow conditions, Darcy's Law is employed (Darcy 1856). It describes the precise relationship between the potential gradient and the flow rate through a porous medium for laminar flow, where fluid particles follow uniform and undisturbed paths at a very slow rate.

4.4.1 Test Setup and Experiment Details

Generally, measuring permeability involves a time-consuming experimental protocol, with attendant concerns about system equilibrium and load control. Therefore, a permeability test setup that could yield reproducible results was used in this study. It was adapted from a method developed by Biparva (2005) and later modified by Hoseini (2013) and notes the onset of the steady state condition in fluid flow. A schematic view of the permeability apparatus developed for the present study and a photograph of the test setup at the Civil Engineering Materials Laboratory at the University of Alberta, are shown in Figures 4.2 and 4.3, respectively. The apparatus originally consisted of five major sections: a cylindrical concrete specimen with a

hollow core; a permeability cell that houses the concrete specimen; a pressurized water supply unit; an outflow measurement device (with an accuracy of 0.01g); and a Materials Testing System (MTS) with capacity of 1000 kN, which is capable of applying compressive stress in with a load-controlled configuration. However, the current study was conducted on unstressed condition and hence, the MTS system was not utilized. In addition, this permeability cell was further instrumented with a computer, programmed to measure and record the mass of water flow in real-time, thereby enabling detection of the onset of equilibrium of fluid flow. Note that the flask used to collect the out-flow water is completely sealed thus ensuring that any moisture lost to evaporation during the test is strictly negligible.

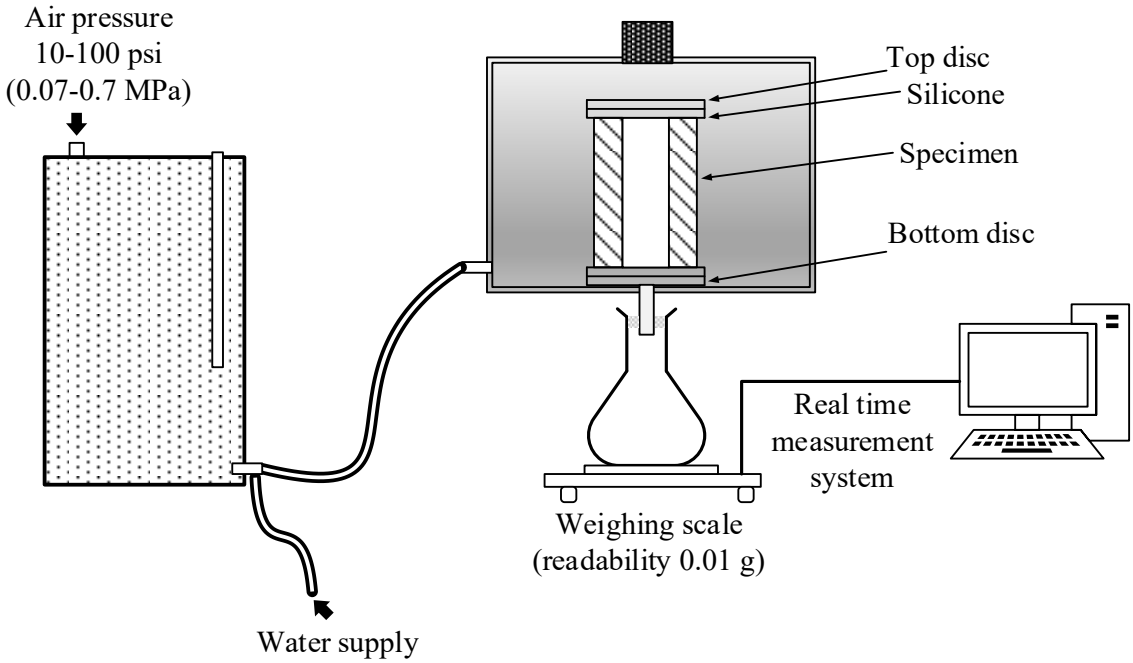

Figure 4.2 Schematic view of the test setup for permeability measurement

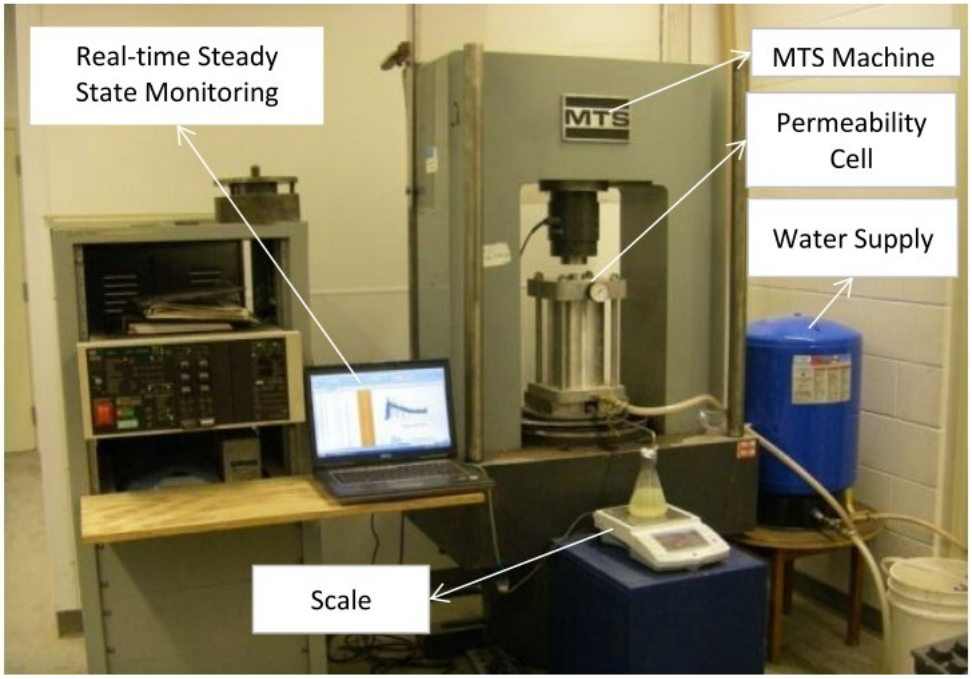

Figure 4.3 The water permeability measurement in progress

In this research program, permeability tests for the plain and fiber-reinforced mortar specimens were conducted at unstressed condition. For each category, at least four hollow-core cylindrical specimens were used to determine the water permeability. As shown in Figure 4.3, pressurized water was introduced around the outer wall of the hollow cylindrical specimen inside the permeability cell and allowed to permeate through to the inner core of the specimen. For Type N mortar and Type O mortar, a cell pressure of 100 psi was chosen whereas, for Hydraulic Lime Mortar, the cell pressure was reduced to 10 psi due to the fact that fact that HLM has low strength compared to the former two types of mortar. This constant water pressure was expected to have similar effect on all tested specimens. The outflow water was collected in a flask and measured on a highly sensitive weighing scale (precision = 0.01 g). In addition, the measured value of the outflow was continuously monitored as function of time in order to be able to observe the onset of fluid flow equilibrium. The experiment was continued until it reached the steady-state condition (further description is presented below). Finally, the water permeability of the mortar specimen was evaluated according to Darcy's law for laminar flow as follows (Ahmed 2006):

$$k = \frac{Q}{2\pi h \Delta P} \ln\left(\frac{r_2}{r_1}\right) \tag{4.1}$$

where k = the coefficient of water permeability (m/s), Q = the rate of water flow (m^3/s); h = the specimen's length (m); ΔP = the pressure head (m); r_2 and r_1 = the outer and inner diameter of the hollow cylinder (m).

As mentioned earlier, a crucial parameter for a steady-state flow system is the constant mass flow rate. In this study, this parameter was used to define the steady-state condition as follows: the test was carried out until the mass of the out-flow water in the flask was the same at any two consecutive time intervals. A representative time history of out-flow upon reaching the equilibrium condition is shown in Figure 4.4, wherein a tolerance in successive records of 5% or less, with respect to the previously recorded value, was considered acceptable. A typical experiment will take from half an hour to two hours for the flow to reach a steady-state condition. It was observed that this duration is dependent largely on the mix proportion of the specimen, with the stronger mortars taking longer.

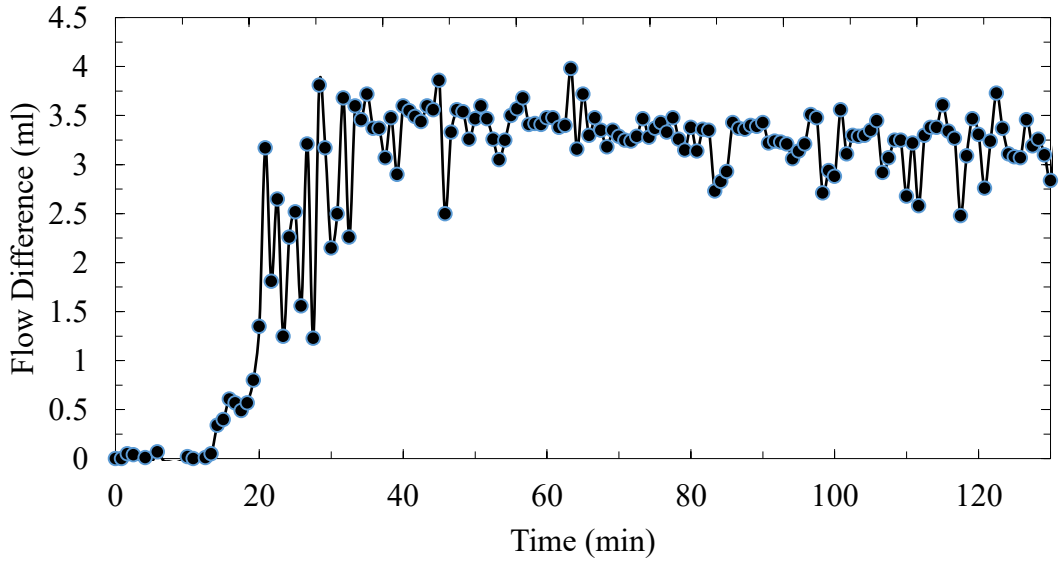

Figure 4.4 Time history of water flow showing the onset of steady-state for Type O mortar specimen with a fibre dosage of 0.15%

Since this study involves single fluid (water) movements through the porous media, the permeability determined using the experimental setup described in this Section, can be termed as "absolute permeability". It can be noticed that Darcy's Law employed to evaluate the permeability requires a steady state flow condition (Section 4.4.1, Figure 4.4) which was achieved in this study. The same experiment has also been used by several researchers to evaluate permeability of cement-based systems (Banthia et al. 2005; Bhargava 2006; Bhargava and Banthia 2008; Bindiganavile et al. 2017; Biparva 2005; Hoseini 2013). On the other hand, relative permeability involves the presence of more than one phase when fluid flows through the porous medium.

4.4.2 Results and Discussion

Permeability coefficient, *k*, as determined by laboratory experiments are shown in Figure 4.5, for the three types of mortar examined in this study. Across all binders, a similar trend is seen between the increase in fibre dosage and the permeability coefficient. Furthermore, the permeability coefficient dropped noticeably for an intermediate dosage of polypropylene micro-fibre, when compared with the plain mortars. As shown in the Figure 4.5, a fibre dosage of 0.15% (by volume) resulted in the lowest permeability coefficient. At dosage beyond 0.15%, the permeability coefficient increased monotonically across all mortar types.

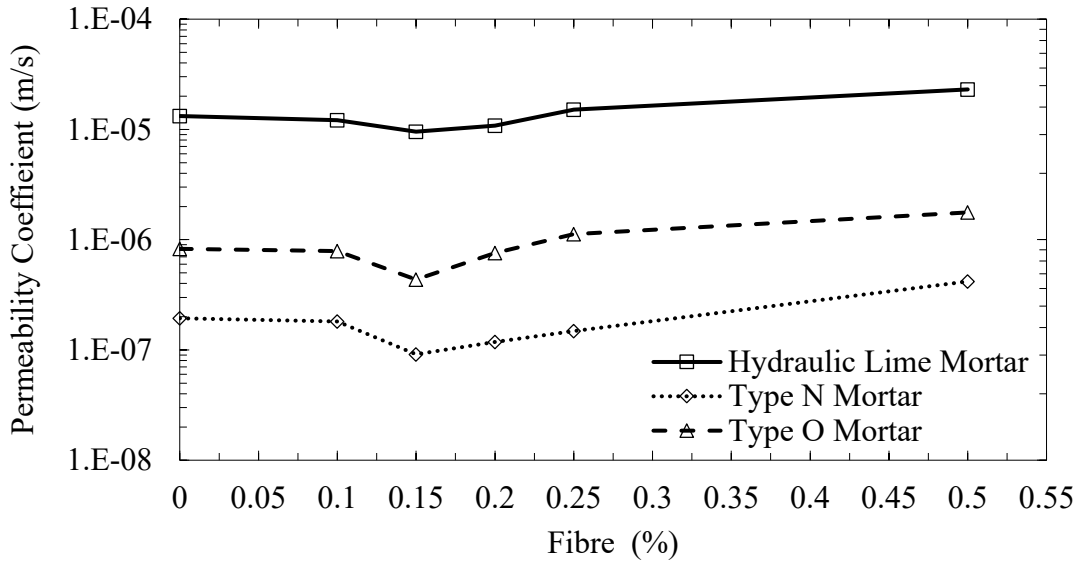

Figure 4.5 Effect of fibre on permeability coefficient for different types of mortar

It may be mentioned here that studies on the effect of fibres, particularly micro-fibres, upon the permeability of cement based systems is well documented (Banthia et al. 2012; Banthia and Bhargava 2007; Hoseini 2013). However, their effect on the water permeability for controlled low strength cementitious mixtures is not well explored. A study on the effect of polypropylene fibre, conducted by Izaguirre et al. (2011), on air lime-based mortar is the only relevant literature that can be found. They used two different fibre dosages, 0.06% by weight and 0.5% by weight, which are equivalent to approximately 0.13% by volume and 1.08% by volume. Their study reported that the permeability coefficient varies with the dosage of polypropylene fibres. Also, when a low dosage was incorporated, the permeability of water vapour decreased notably, whilst a higher dosage of fibre led to an increase the permeability. The outcome of the present study is in agreement with those findings by Izaguirre et al. (2011).

At low fibre dosage, the reduction in permeability coefficients for all mortar mixtures may be explained as follows. The fibre alters the pore structure of the mortar whereby a fraction of the large air-voids is transformed into a smaller one. Due to this pore size refinement, water permeability in the fibre reinforced composite decreases. Further, fluid flow path becomes more tortuous due to the addition of these fibres, which creates more hindrance to the flow of water through the mortars and thereby results in a drop in the permeability. On the other hand, as will be discussed in Section 5.4.3, a high fibre dosage makes the mortar less tortuous and increases the pore connectivity, which in turn increases the water permeability coefficients. Micro-fibres result in a significant number of larger air-voids, even as the mean void size becomes smaller (Izaguirre et al. 2011). Hence, the measured water permeability coefficient increases beyond an optimal fibre dosage. In this study, the amount of water was kept constant across the plain and fibre reinforced mixtures. On the other hand, Izaguirre et al. (2011) accommodated more water with fibre dosage to maintain a desired slump. Despite this difference in the mixture proportions, the findings of both studies are generally in agreement. According to the current study, an optimal dosage of fibre would be 0.15%, by volume, in order to reduce water permeability.

It appears that the nature of fibre, whether hydrophobic or hydrophilic, has an effect on the permeability of fibre reinforced mortar. Bhargava and Banthia (2008) studied the permeability of concrete containing cellulose fibre, a hydrophilic fibre, with a volume fraction ranging from 0.1–0.5%. They reported a monotonic reduction in permeability with the increase in fibre dosage. In contrast, the present study, which incorporates polypropylene fiber, a hydrophobic fibre, shows that up to a certain threshold value of the fibre dosage permeability of the mortars gradually decreases.

A typical fibre distribution of a hardened mortar is shown in Figure 4.6. It can be seen that the fibres are arranged in a well-distributed fashion. There is no visible lump or clumping of the fibres in the mortar. A satisfactory dispersion of fibres may be achieved to the "fluffing" of fibres before gradually adding them to the mixture. This procedure of fibre fluffing and gradual addition may not be feasible for large-scale projects or may not be practical for construction industry where other suitable fibre mixture procedure, found in the literature or standard guidelines, can be adopted. Although the equivalent number of fibres at a section relate to the fibre volume fraction was not evaluated in this research, it is possible to calculate that with the help of existing literature ((Zollo 1997). Equivalent number of fibres (FC) per unit volume of a matrix can be calculated by $FC = 1.27 \cdot V/(l \cdot d^2)$ where V = volume fraction in percentage, l = length and d = diameter. However, the fibre count at a section depends upon the randomness of the orientation of the fibre.

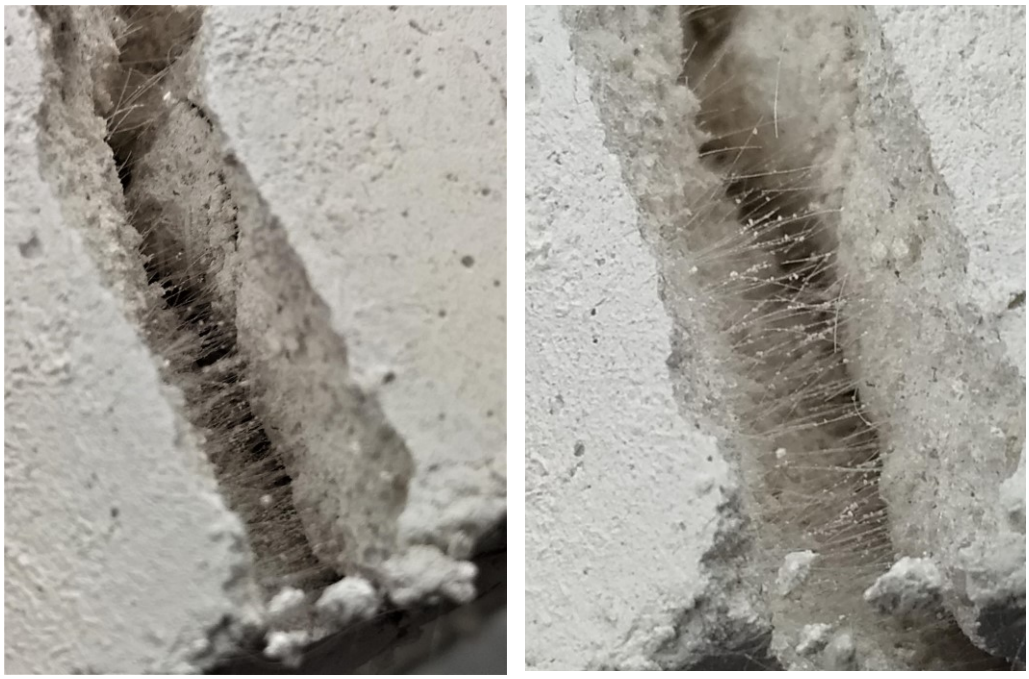

Figure 4.6 Fibres in mortar

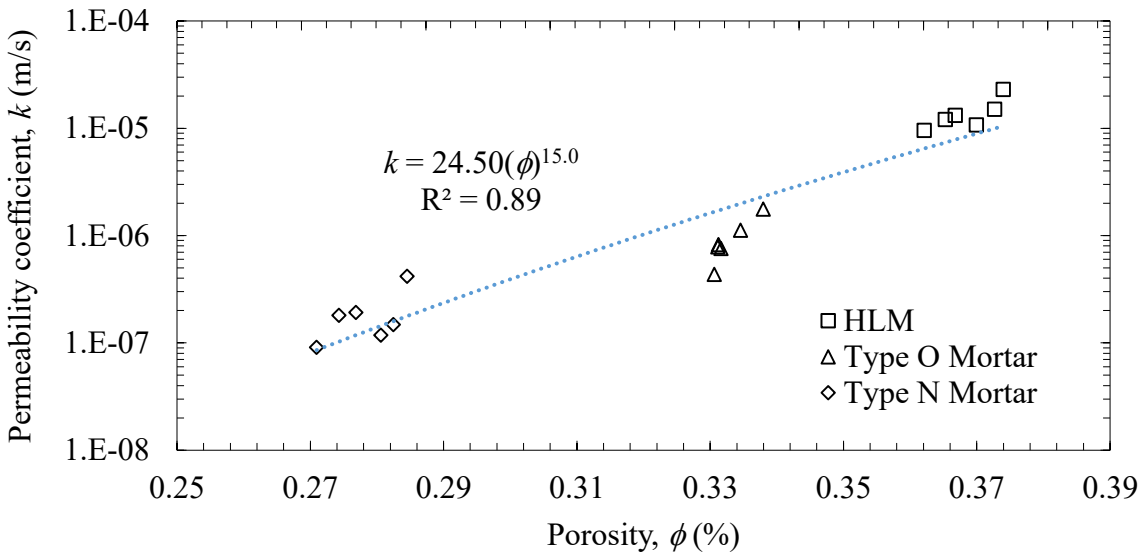

Figure 4.7 Relationship between porosity and water permeability coefficient for plain and fibre reinforced mortars

A correlation between the measured water permeability and the porosity of different types of mortars is illustrated in Figure 4.7. The effect of mortar porosity on its permeability is captured through the regression model. It can be seen that the due to the presence of Portland cement

binder, the reduced porosity of the mortar causes a substantial drop in the permeability in Types O and N mortar. It is evident that higher replacement of lime with cement, in Type N mortar imparts superior durability. The observed trend can be explained by employing the well-established Kozeny-Carman equation, $k = \phi^3/(c\tau S^2)$, (also shown in Section 4.5.2, Equation 4.2, where F is replaced with a function of τ and ϕ), which relates permeability with several microstructural parameters. If one assumes that all the parameters are constant except the porosity, an increase in permeability with an increase in porosity is justified.

As mentioned in the Section 1.4 (Scope), this thesis does not include the effect of stress on the permeability. According to literature, up to a certain threshold, an increase in stress results in a drop in the permeability of cementitious systems (Bhargava and Banthia 2008). As the applied sustained load increases, the permeability reduces due to the ensuing pore closure and the associated reduction in pore connectivity and simultaneous increase in pore tortuosity (Bhargava and Banthia 2008; Hoseini 2013).

4.4.3 Role of Fibres and Underlying Mechanism

Addition of micro-fibres in cement/lime-based composites alters the latter's physical properties either through modification of the microstructure or through alteration of the response when subjected to load. In the former case, micro-fibres render a composite having an improved air-void structure depending upon the volume fraction of the fibre, the fibre geometry, whether it is hydrophobic or hydrophilic, surface treatment, and the degree of dispersion in the matrix. A well dispersed and appropriately proportioned fibre-matrix system results in low porosity, reduced interconnectivity in air-voids, and increased tortuosity. Consequently, as discussed earlier in this thesis, polypropylene fibres cause an air-void structure having a favourable influence on the transport properties of cement/lime-based mortars when incorporated at a low dosage. However, the beneficial influence of fibres on the permeability of mortars examined in this study was found to disappear for an increase in fibre dosage beyond a critical value namely, 0.15% by volume. Besides having an impact on transport properties, fibres can be expected to improve mechanical properties such as post-peak stress-strain response and fracture toughness of the composite through crack bridging depending on the elastic modulus of the fibre added to the composite.

As discussed in the preceding paragraph, fibre dosage is an important factor when designing a fibre reinforced cement/lime-based composites for enhanced transport properties. This thesis reports that a fibre dosage around 0.15% by volume provides a substantial reduction in water permeability across all types of mortars. The underlying mechanism behind such outcome may be the size redistribution of air-voids, both macro and micro, of the mortars. Fibres are known to refine the macro-level air-voids (Banthia et al. 2012; Sappakittipakorn et al. 2010) of cement-based systems whereby the air-void size distribution curve shifts towards the smaller air-voids. The same phenomenon is also true for micro and nano-level air-voids as evidenced from cryoporometry study reported by Sappakittipakorn et al. (2010). The outcome of the refined pore structure along with slightly lower porosity is the significant drop in fluid permeability of the cement/lime-based mortars. On the other hand, specimens having a fibre dosage higher than the critical value, namely 0.15%, leads to an air-void network with much higher degree of interconnectivity, due to the increased amount of porous fibre-matrix interface, which inevitably results in an increase in permeability.

At low dosage, fibre decreases the porosity, interconnectivity, and permeability. On the other hand, the porosity, interconnectivity and permeability increases with higher fibre dosage. Due to a decrease in bleeding and internal shrinkage cracking associated with fiber reinforced mortars are likely to the reason of this reduction at low fibre dosage, which reduce the bleed channels and thus decrease the available flow paths (Hoseini 2013). In addition, permeability transforms from being a bulk phenomenon at lower dosages of fibre to a local one at higher fibre dosage (Hoseini 2013). At low fibre dosage, the lower number of cracks formed during shrinkage can lead lower permeability whereas higher fibre dosage leads higher permeability by leaving outstanding number of large pores due to requirement of high amount of kneading water or decreased workability which are associated with the addition of high amount of hydrophobic polypropylene micro-fibre (Izaguirre et al. 2011).

4.5 Permeability Predictions by Analytical Method

4.5.1 Two-Point Correlation Function

The Two-Point Correlation (TPC) function is a statistical measure of spatial correlation of features of the pore space, such as the specific surface area, pore size and distribution. Note that the term "pore" here includes both air-voids and cracks in the mortar. Using the procedure as discussed by Berryman and Blair (1986), the permeability coefficients of mortar can be predicted by using the TPC function. TPC functions embody statistical information about the arrangements of the constituents in a composite material. By using TPC functions, several pore structure parameters such as porosity (ϕ), specific surface area (s), and characteristic pore size (r_c) can be directly determined through image processing. These microstructural parameters can be utilized to estimate the fluid permeability by employing the well-known Kozeny-Carman equation. Berryman and Blair (1986) used a modified version of the well-known Kozeny-Carman equation that was first developed by Paterson (1983) and later, Walsh and Brace (1984) developed a modified version by modelling the fluid flow paths through porous media such as rocks in the form of a bundle of tube. The formula has the general form as shown below:

$$k = \frac{(\phi)^2}{cFs^2} \tag{4.2}$$

where k is the permeability coefficient, ϕ is the porosity, c is a constant that depends on the cross-section of the tubes, usually taken to be equal to 2 for porous materials, F is the formation factor, and s is the specific surface area.

This study was done using SEM images with two different magnifications namely, 50X and 400X, yielding spatial resolutions of 2.1354 μm/pixel and 0.2636 μm/pixel, respectively. Subsequently, the water permeability was computed by using the model presented in Equation 4.2, where the porosity and specific surface area evaluated as shown in Figure 4.8, through TPC, were utilized. Note that the formation factor required for Equation 4.2, was derived by analyzing X-ray micro tomography images. In order to compute the formation factor for Hydraulic Lime Mortar, Type N mortar, and Type O mortar, a random-walk simulation program (details of this program are discussed in Chapter 5.3.2) developed by Nakashima and

Kamiya (2007) was employed. The predicted permeability coefficients of plain and Hydraulic Lime Mortar, Type N mortar, and Type O mortar are shown in Figures 4.9, 4.10, and 4.11 respectively.

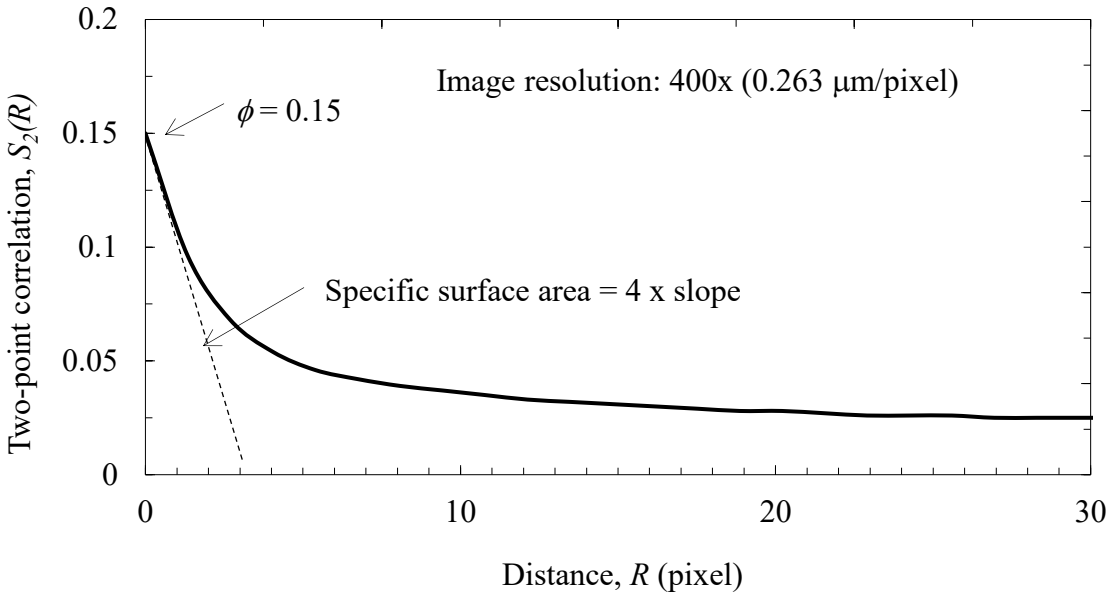

Figure 4.8 Parameters derived from TPC for permebility prediction

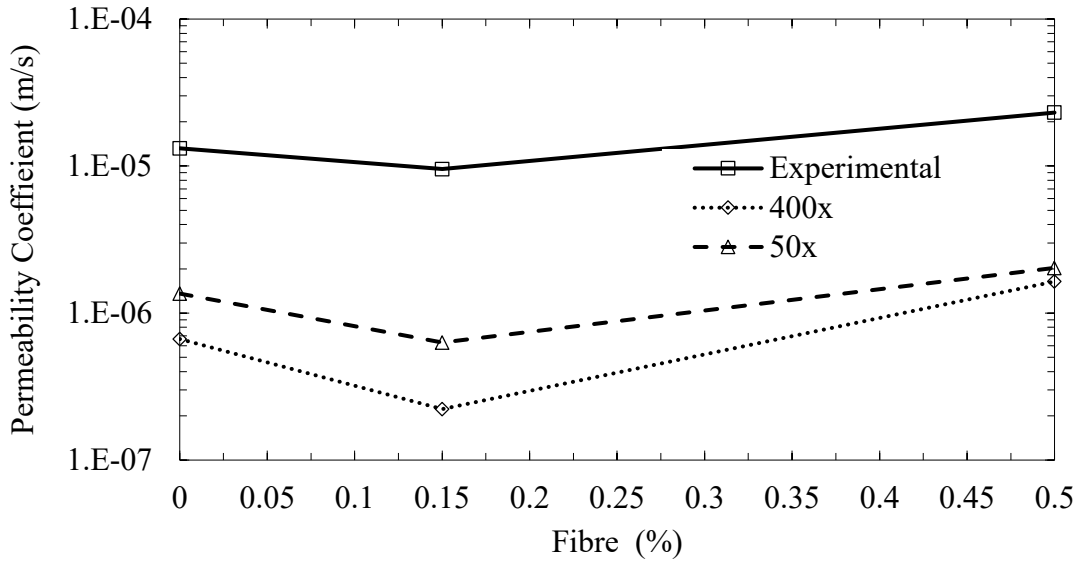

Figure 4.9 Permeability prediction by two-point correlation functions for Hydraulic Lime Mortar

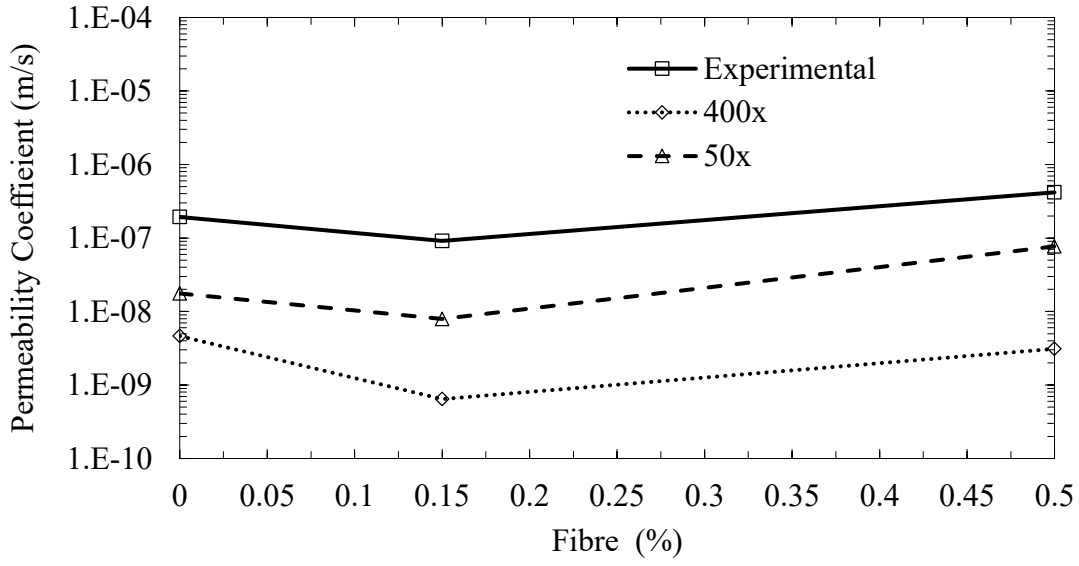

Figure 4.10 Permeability prediction by two-point correlation functions for Type N mortar

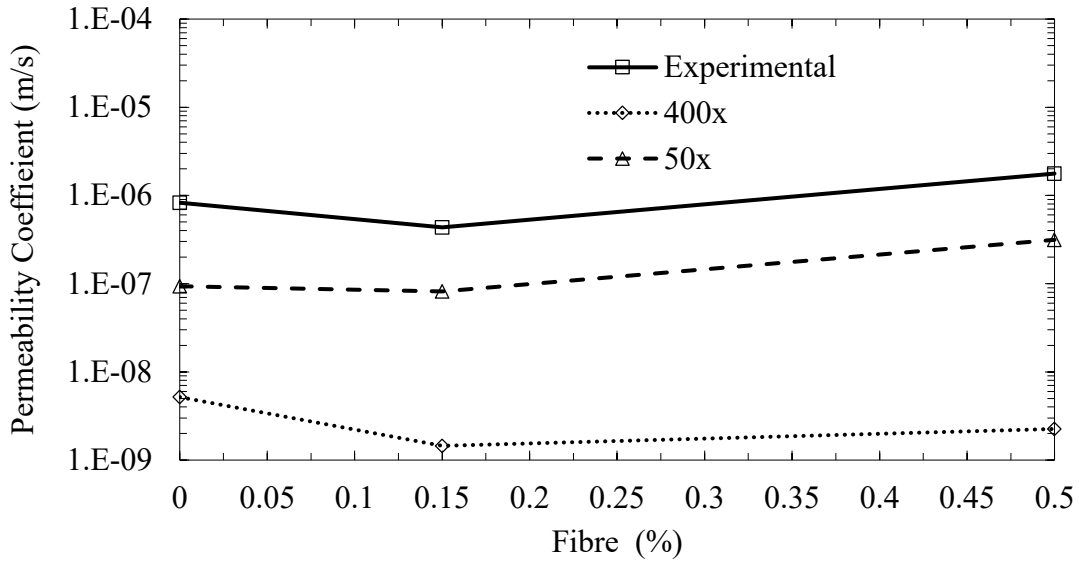

Figure 4.11 Permeability prediction by two-point correlation functions for Type O mortar

It can be noticed that the predicted permeability coefficients vary in a bi-linear fashion with an increase in the fibre dosage, across all types of mortar. It is also observed that the predicted values are largely in good agreement with the experimental values across all mortar mixtures. It is apparent that SEM images with 50x magnification (spatial resolution 2.1354 μm/pixel) show smaller deviation, from measured permeability coefficients, when compared with that from images having a magnification of 400x (spatial resolution 0.2636 μm/pixel). This may be due to fact that 400x magnification was not able to capture larger air voids. As shown in the aforementioned Figures, the predicted values for 50x (spatial resolution 2.1354 μm/pixel) magnification are within one order of magnitude of experimental results. Although two-point correlation function and SEM image analysis have been used extensively for fluid permeability prediction of rocks. There are very few studies that are available in literature where TPC is used for permeability prediction of cement-based systems. Hence, appropriate caution must be taken when employing these methods for cementitious materials, especially the variation associated with the determination of formation factor. Traditionally, the formation factor is estimated based on Archie's law (Archie 1942) which can be presented as $F = \phi^{-m}$. Note that it was developed for rocks (Berryman and Blair 1987; Blair et al. 1993; Torabi et al. 2008) and hence, its applicability in cement-based systems will be limited.

4.5.2 Katz-Thompson Equation

An accurate measurement or estimation of permeability has been a challenging and time-consuming task especially for material like Hydraulic Lime Mortar and cement-lime mortar. There are several empirical methods available in literature for permeability prediction to avoid those constraints related to permeability measurements. Katz and Thompson (1986) introduced the following equation to calculate permeability based on MIP data:

$$k' = c(l_c)^2\left(\sigma/\sigma_0\right) \tag{4.3}$$

where k' is the intrinsic permeability (m^2), l_c is the characteristic length of the pore space, σ is the conductivity of the medium saturated with a brine solution having a conductivity of σ_0, and c is a constant which is equal to $1/226$.

Here it is important to note that Equation 4.3 proposed by Katz and Thompson is for rocks and not for concrete or other cementitious materials where the characteristic length, l_c of the rock samples is determined by running MIP test as shown in Figure 4.12.

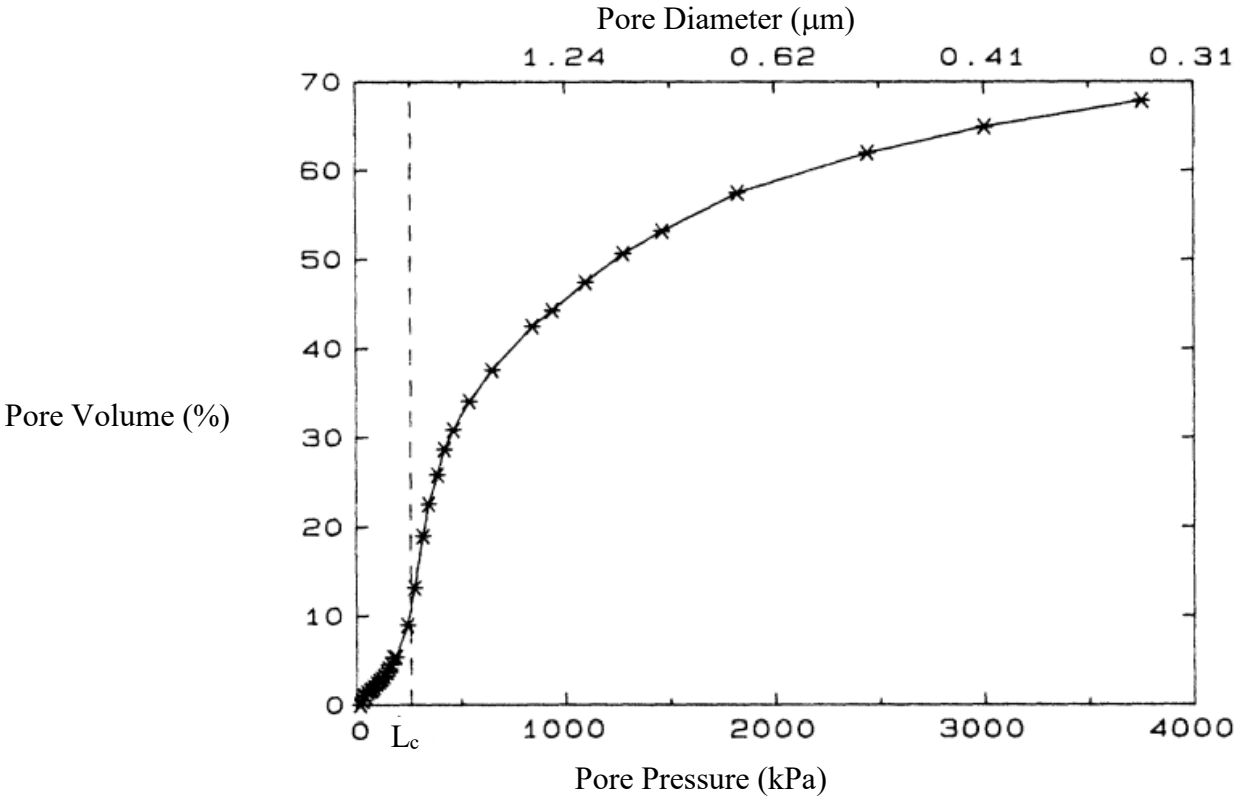

Figure 4.12 Characteristic length, l_c as defined by (Katz and Thompson 1986) from MIP test results (Source: (Katz and Thompson 1986))

Equation 4.3 can be rewritten as:

$$k' = \frac{c(l_c)^2}{F} \tag{4.4}$$

where F is the formation factor and equal to ${}^{\sigma_0}/_{\sigma}$.

Instead of measuring the formation factor, F directly, several researchers (Gao and Hu 2013; Nokken and Hooton 2007; Zhang et al. 2016) used the following equation for permeability prediction and formation factor as described by Katz and Thompson (1987):

$$k' = ({}^{1}/_{89})({l_{max}}^{h})^2 \left({{l_{max}}^{h}}/{l_c}\right) \phi S({l_{max}}^{h}) \tag{4.5}$$

$${}^{1}/_{F} = {}^{\sigma}/_{\sigma_0} = \left({{l_{max}}^{e}}/{l_c}\right) \phi S({l_{max}}^{e}) \tag{4.6}$$

where k' is the intrinsic permeability (m^2), l_c is the characteristic length of the pore space, σ is the conductivity of the medium saturated with a brine solution having a conductivity of σ_0 , F is the formation factor which is equal to σ_0/σ, $l_{max}{}^{h}$ is the pore throat diameter at which hydraulic conductance is maximum, which is equal to $0.61l_c$, and $l_{max}{}^{e}$ is the pore throat diameter at which electrical conductance is maximum, which is equal to $0.34l_c$.

The MIP method was used for all 3 types of mortar to evaluate the pore size distribution as shown Figures 4.13, 4.14, and 4.15. Due to its aforementioned limitation in regard to pore size sensitivity, the MIP method does not provide a true pore size distribution. It is accepted now that MIP misrepresents the actual pore size distribution for cementitious materials due to the well-known "ink bottle" effect and pore accessibility issue (Abell et al. 1999; Diamond 2000; Diamond and Landis 2007; Zhou et al. 2010). Even so, as mentioned earlier in Section 3.3.3, it leads to the pore radius using the well-known Washburn equation (Washburn (1921)) wherein the pore shape is assumed cylindrical.

For MIP, a small representative sample was cut from intact hollow cylinders cast for water permeability testing. For specimens with Hydraulic Lime Mortar, the sample was cured in ambient temperature for more than six months. On the other hand, samples taken from Type N and O mortar were cured in a humidity room for at least 28 days as per CSA A179 (2004) specification. In addition, the sample was degassed at a temperature of 24 ^{0}C, an extended time period deemed sufficient to remove the moisture.

Pore size distribution as obtained from the MIP test is shown for the Hydraulic Lime Mortar, Type N mortar, and Type O mortar in Figures 4.13, 4.14 and 4.15, respectively. It is used to predict the permeability of these three types of mortar by using Katz and Thompson (1987) equation as described earlier in Equations 4.4, 4.5, and 4.6. The predicted permeability for the three binder types are shown in Figures 4.16, 4.17, and 4.18. These plots capture the variation in the permeability for the three fibre dosages studies namely, between 0.00 - 0.15% by volume. As seen from these predicted trends, it is obvious that the Katz and Thompson (1987)

equation failed to predict correctly the permeability for Hydraulic Lime Mortar and cement-lime mortars including the fibre reinforced ones. The predictions deviate from experimental values by as much as three to four orders of magnitude. In addition, the Katz and Thompson (1987) model fails to differentiate among different type of mortar. The analytical prediction by Equations 4.2 and 4.5 are almost in the same range for plain and fibre reinforced Hydraulic Lime Mortar, Type N mortar, and Type O mortar. It is observed that the experimental values for Hydraulic Lime Mortar and Type N mortar are at least two orders of magnitude apart from each other while the Katz and Thompson (1987) equation fails to capture this phenomenon.

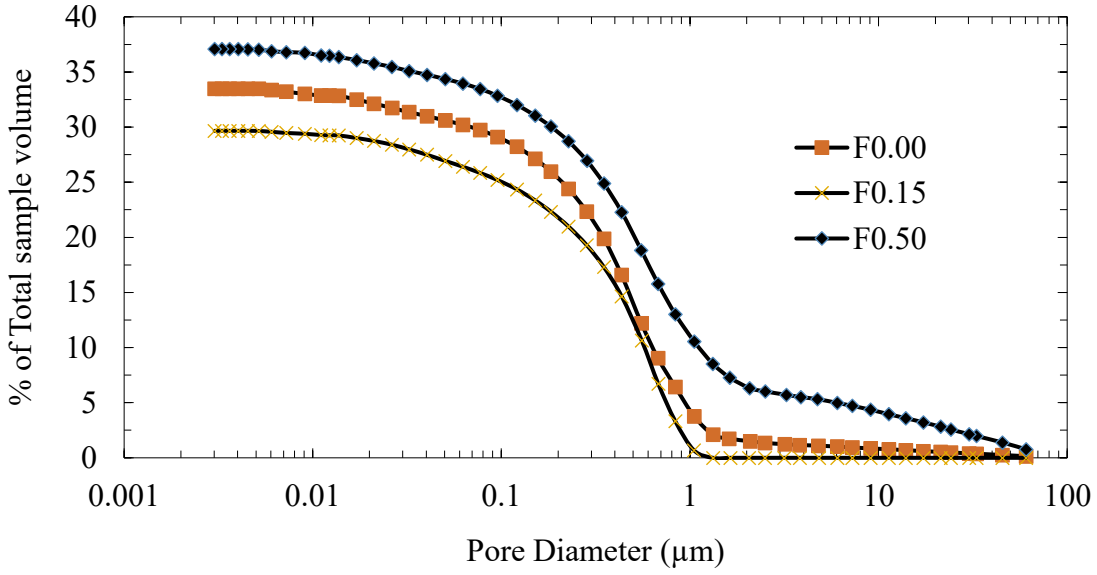

Figure 4.13 Pore size distribution of Hydraulic Lime Mortar by MIP method

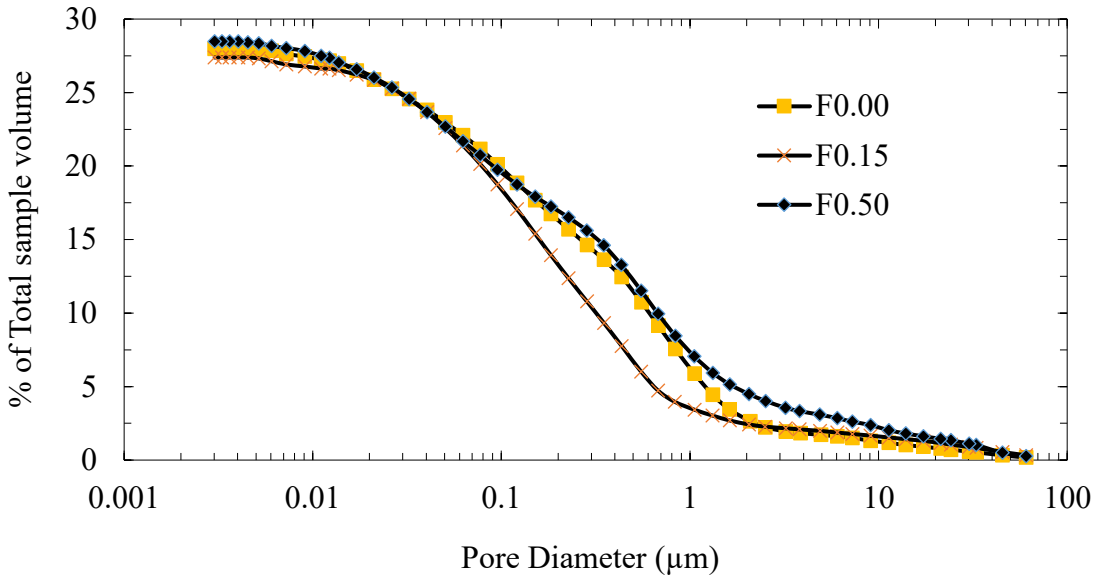

Figure 4.14 Pore size distribution of Type N mortar by MIP method

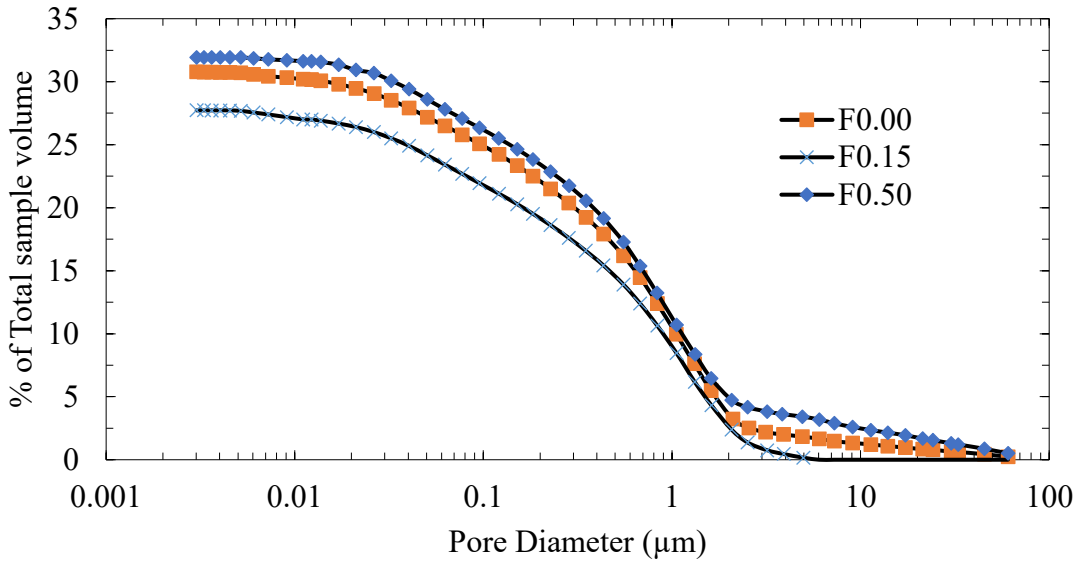

Figure 4.15 Pore size distribution of Type O mortar by MIP method

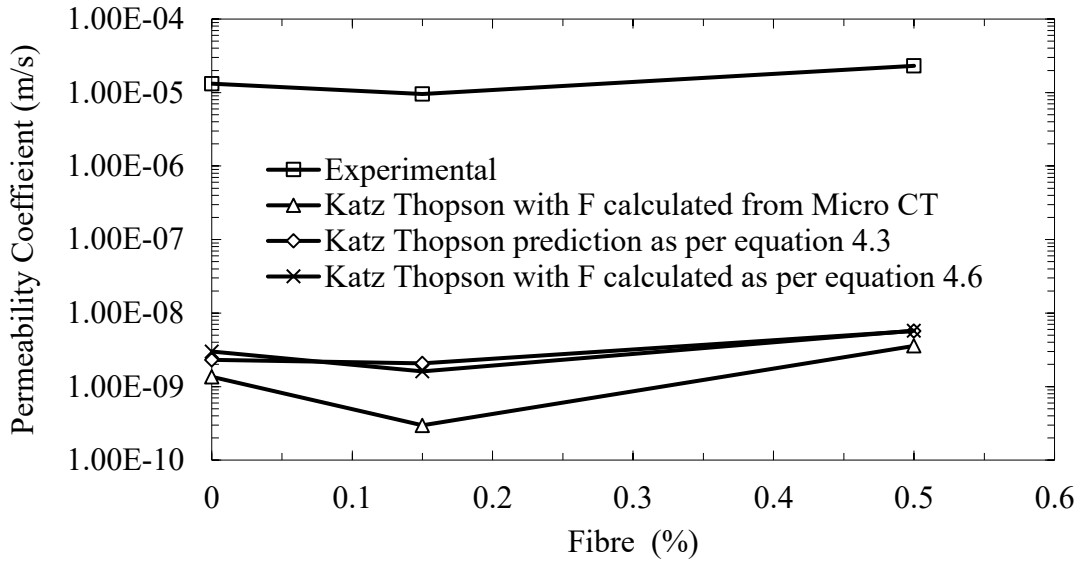

Figure 4.16 Permeability prediction by Katz and Thompson (1986, 1987) analytical model for Hydraulic Lime Mortar

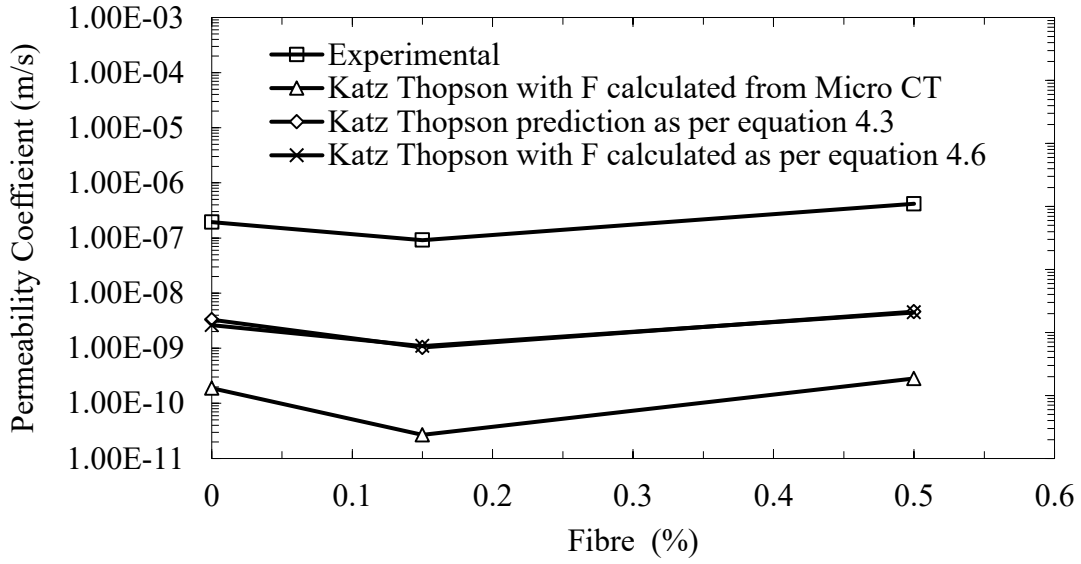

Figure 4.17 Permeability prediction by Katz and Thompson (1986, 1987) analytical model for Type N mortar

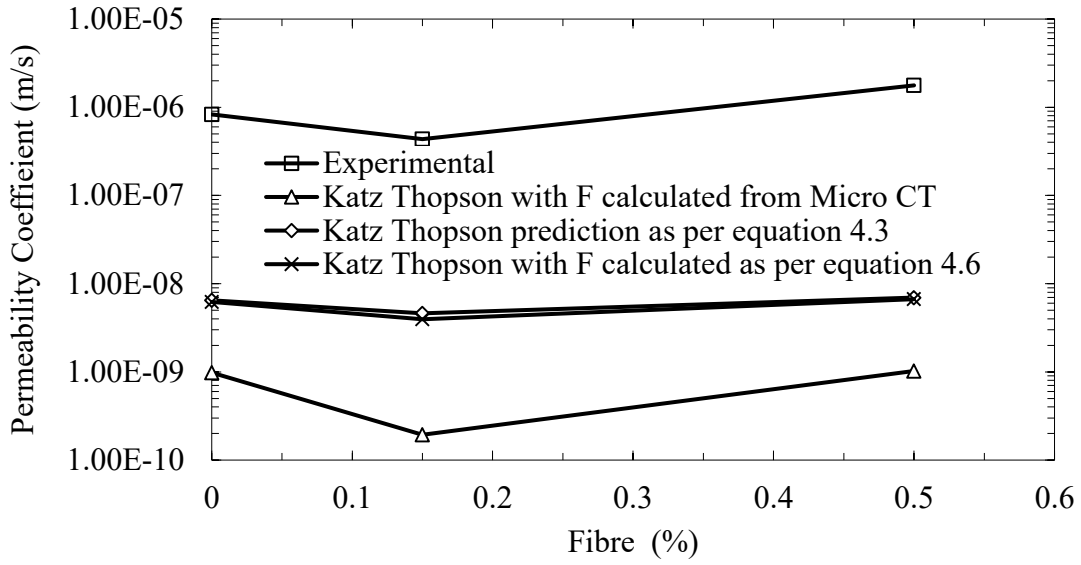

Figure 4.18 Permeability prediction by Katz and Thompson (1986, 1987) analytical model for Type O mortar

The failure of Katz and Thompson (1987) model to predict the permeability of cementitious materials may be attributed to the limitation of the MIP to identify the realistic pore size distribution. It is worth emphasizing here that Katz and Thompson (1987) model was developed mainly for rocks in which case the MIP method predicts the true pore size distribution. As observed in this study, also demonstrated by Lange et. al. (1994) and Diamond (2000), the shape of pore size distribution curves from MIP are identical to that of actual pore size distribution for cement-based materials, however, they are shifted by two to three orders of magnitude. Since MIP pushes the entire curve towards the smaller pore size, Katz and Thompson (1987) equations are likely to yield lower permeability coefficients. Katz and Thompson (1987) model, as shown in Equation 4.2 and 4.3, varies as the square of the term, l_c , which denotes the characteristic length of the pore space. This causes a further reduction in the predicted permeability values.

4.5.3 Fractality

Since the pioneering work of Winslow (1985) wherein it was demonstrated that the internal microstructure of cement paste is essentially a fractal, various studies have examined its

applicability to estimate the permeability of cementitious systems. The concept of fractality describes the self-similarity of the internal structure of a material at different scales characterized by a single parameter called the "fractal dimension". While estimating fluid permeability from fractal geometry is commonly used for rocks and sandstones (Berg 2014; Costa 2006; Henderson et al. 2010; Pape et al. 1999; Xu and Yu 2008), studies on its applicability to cement-based systems is rather limited. In most such cases, the permeability equations were developed from the well-known Kozeny-Carman equation are described below.

Xu and Yu (2008) proposed a model for porous media based on Kozeny-Carman equation and fractal geometry:

$$k = C_f \lambda_{max}^2 \left(\frac{\phi}{1-\phi}\right)^{\left(1+D_T/2\right)} \tag{4.7}$$

where the coefficients $C_f = \frac{(\pi D_f)^{\left(1-D_T/2\right)}[4(2-D_f)]^{\left(1+D_T/2\right)}}{128+(3+D_T-D_f)}$ is only related to the fractal dimension. Also, D_f and D_T denotes pore area fractal dimension and tortuosity fractal dimension, and λ_{max} is the maximum pore diameter. D_f, D_T and average tortuosity was expressed as:

$$D_f = d_E - \frac{\mathrm{In}\phi}{\mathrm{In}\frac{\lambda_{min}}{\lambda_{max}}} \tag{4.8}$$

$$D_T = 1 + \frac{\mathrm{In}\bar{\tau}}{\mathrm{In}\frac{L_0}{\bar{\lambda}}} \tag{4.9}$$

$$\frac{L_0}{\bar{\lambda}} = \frac{D_f - 1}{{D_f}^{1/2}}\left[\frac{1-\phi}{\phi}\frac{\pi}{4(2-D_f)}\right]^{1/2}\frac{\lambda_{max}}{\lambda_{min}} \tag{4.10}$$

$$\bar{\tau} = \frac{1}{2}\left[1 + \frac{1}{2}\sqrt{1-\phi} + \sqrt{1-\phi}\,\frac{\sqrt{\left(\frac{1}{\sqrt{1-\phi}} - 1\right)^2 + \frac{1}{4}}}{1-\sqrt{1-\phi}}\right] \tag{4.11}$$

Here, $d_E = 2$ or $d_E = 3$ Euclidian dimension for two and three-dimensional microstructure. Also, λ_{min} denotes the minimum pore diameter. They also assumed that tortuosity is a function of porosity as shown in Equation 4.11.

Costa (2006) has developed an equation for fractal porous media given by:

$$k = C_0 \frac{\phi^m}{(1-\phi)} \tag{4.12}$$

where C_0 is a parameter similar to the Kozeny-Carman coefficient and $1 < m < 4$ is the Archie's exponent. Here, tortuosity was expressed in terms of formation factor and porosity, and Archie's law $\left(F = {A_{archie}}/{\phi^m}\right)$ was used to relate them. Since Archie's law was developed for rocks, its application to cement-based systems may not produce accurate results.

Civan (2001) has given the following equation for permeability based on the porosity of the medium:

$$\sqrt{\frac{k}{\phi}} = \gamma\left(\frac{\phi}{1-\phi}\right)^{\beta} \tag{4.13}$$

where γ and β are empirical constants. Also, model proposed by Civan (2001) does not have any parameter that reflects tortuosity of the material.

Based on a study on sandstone, Pape et. al. (2000) proposed the following equation that captures on the porosity, pore connectivity and fractal dimension:

$$k = \frac{\phi r_g^2}{8\Gamma^2}\left(\frac{2\phi}{3\Gamma^2(1-\phi)}\right)^{2/(D-1)} \quad (4.14)$$

where r_g is the grain radius, D is fractal dimension, and Γ is the interconnectivity parameter. Here, tortuosity was expressed in terms of formation factor and porosity, and Archie's law ($F = A_{archie}\phi^{-m}$) where F is the formation factor, A_{archie} is a constant, ϕ is porosity, and m is an exponent, was used to relate them.

Predicted permeability coefficients from fractal geometry investigation of this study are illustrated in Figures 4.19, 4.20, and 4.21 for plain and fibre reinforced Hydraulic Lime Mortar, Type N mortar and Type O mortar respectively. The fractal model proposed by Xu and Yu (2008) was employed here for the prediction. This model was chosen because of its simplicity in predicting permeability coefficient by employing the results obtained through image processing technique. In this study, SEM images having two different magnifications—50x (spatial resolution 2.1354 μm/pixel) and 400x (spatial resolution 0.2636 μm/pixel)—were utilized for permeability prediction. The parameter required for this model such as porosity, fractal dimension, and the maximum pore size, λ_{max}, were determined through image analysis. The fractal dimension of the mortar microstructure was evaluated by the box-counting method. It can be noticed, illustrated in Figures 4.19, 4.20, and 4.21, that fractal model proposed by Xu and Yu (2008) does not predict the permeability of the mortars mixtures examined here. This is mainly because Xu and Yu (2008) did not consider the tortuosity of the voids inside the mortars. It can be seen that the predicted permeability coefficients lie almost in the same range irrespective of the type of mortar. In addition, the predictions based on SEM images having a magnification of 50x (spatial resolution 2.1354 μm/pixel) lie above the experimental values, which may be attributed to the fact that lower magnification can capture larger air voids. On the other hand, predictions based on 400x magnification (spatial resolution 0.2636 μm/pixel) underestimate the permeability coefficients because of its inability to capture large pores. In addition, mortars with different porosity may have identical maximum pore sizes but with different mix design. This model does not take the above fact into account. In this study, all three types of mortar contain almost identical value of maximum pore diameter and

therefore this model is not capable of producing the desired output for different types of cement and lime-based composites.

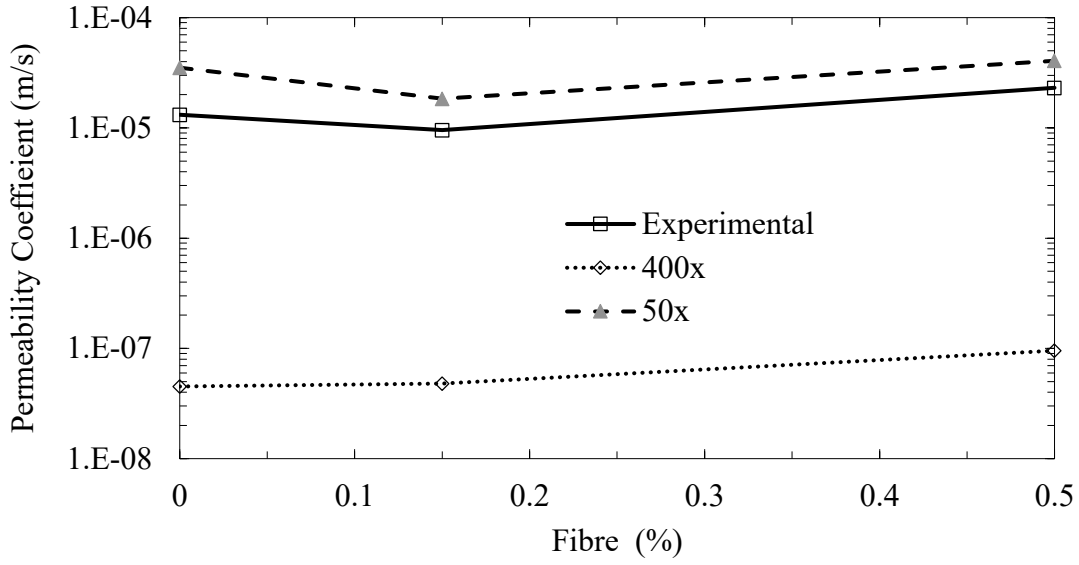

Figure 4.19 Permeability prediction by fractal model developed by Xu and Yu (2008) for Hydraulic Lime Mortar

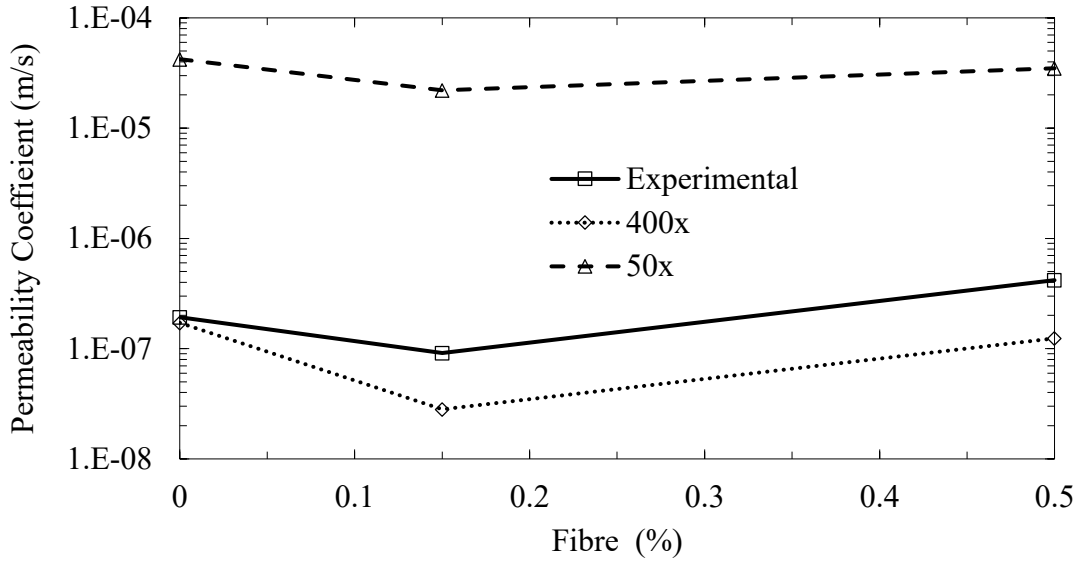

Figure 4.20 Permeability prediction by fractal model developed by Xu and Yu (2008) for Type N mortar

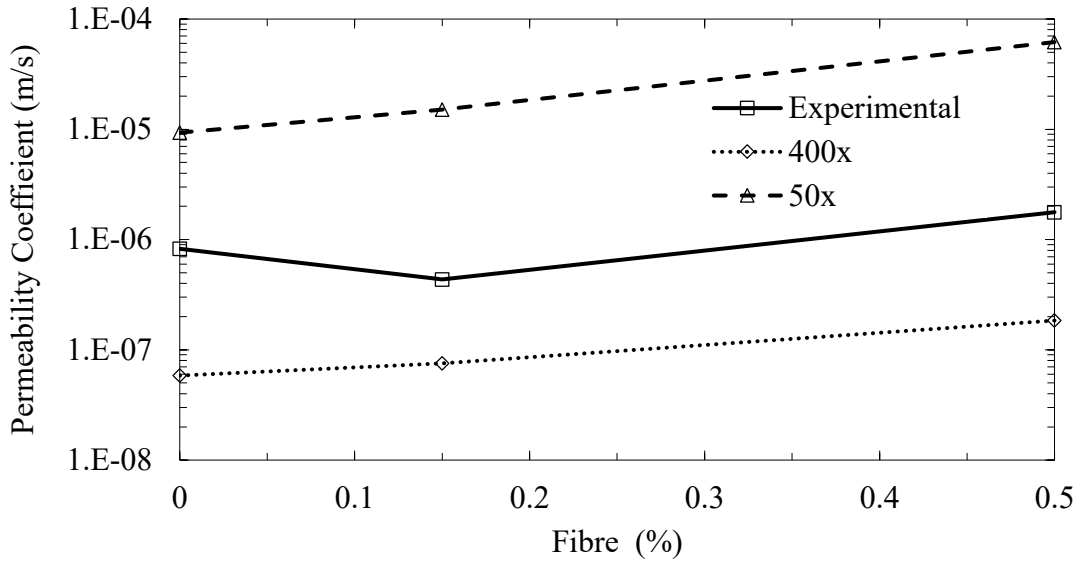

Figure 4.21 Permeability prediction by fractal model developed by Xu and Yu (2008) for Type O mortar

4.6 Concluding Remarks

Water permeability of plain and fibre reinforced Hydraulic Lime Mortar, Type N mortar, and Type O mortar were determined thorough laboratory experimental procedure. In addition, water permeability of these mortars is predicted by utilizing existing several analytical methods such as two-point correlation method, Katz-Thompson model, and fractal model. Based on the findings in this chapter, the following concluding remarks can be drawn:

- Water permeability is influenced significantly by the addition of polypropylene micro-fibres. This variation occurs in an identical manner for all three types of mortars.
- An optimum fibre dosage exists beyond which the water permeability registers an increase. This optimum fibre dosage is found here to be 0.15% (by volume) and is applicable for all three types of mortar.
- At low fibre dosage, the reduction in permeability coefficients is noticeable and this coefficient increases with further addition fibre. Due to pore size refinement, a more tortuous flow path, and the reduction in pore connectivity at low fibre dosage are the

main influencing factors for the observed reduction in water permeability. On the other hand, higher fibre dosage causes an increase in pore connectivity, thus making the flow path less tortuous, which in turn causes an increase in water permeability.

- Permeability prediction by two-point correlation function is largely in good agreement with the experimental values across all three types of mortar. In addition, predicted permeability values from SEM images, with 50x magnification, show smaller deviation from experimental permeability coefficients when compared with that from images having a magnification of 400x. Therefore, 50x would be the recommended magnification for predicting permeability of similar types of materials using image-based approach.
- The predicted permeability coefficients by Katz-Thompson model do not agree satisfactorily with experimental values for both plain and fibre reinforced mortars of all types. This disagreement may be attributed to the inability of the MIP method to identify the realistic pore size distribution of cementitious materials.
- The employed fractal model is not capable of predicting the permeability coefficients of plain and fibre reinforced mortars. The possible reason behind the apparent disagreement may be the absence of some critical parameters reflecting the pore tortuosity as well as connectivity effects. Further, the fractal model is unable to distinguish between mortars with different porosity having identical maximum pore size.

CHAPTER 5. CORRELATING WATER PERMEABILITY IN FIBRE REINFORCED REAPIR MORTARS WITH ITS AIR-VOID NETWORK USING X-RAY MICRO COMPUTED TOMOGRAPHY

5.1 Introduction

Microstructure of pores in cement-based mortars has a significant influence on their engineering properties such as permeability, strength, and durability. It is therefore important to know the quantum of influence that the pore microstructure has on the above properties, especially water transport, which in turn affects the durability of the said mortar. (Sugiyama et al. 2003, 2008). Water permeability through porous media depends upon the pore space geometry and their arrangement in three-dimensional space, specifically, the porosity, the size, shape, and connectivity of the porous path and its tortuosity. Notwithstanding the extensive literature that pertains to their quantification (Akhavan et al. 2012; Kaufmann 2010; Neville 2011; Roy et al. 1993) information is still very limited by way of pore connectivity and tortuosity, especially in three dimension.

X-ray micro computed tomography is a powerful tool to investigate the 3D microstructure of cement-based materials. It is an image-based non-destructive 3D radiographic technique. In this method, a high-energy X-ray source is used to acquire 2D radiographic projections of the specimen by rotating it at certain angular intervals. Then a 3D computed reconstruction of the sample is performed from those 2D images by applying suitable algorithms of mathematical tomography. In principle, this method is similar to medical CAT (Computed Axial Tomography) scan or industrial micro-focus CT. However, X-ray micro CT can achieve much higher spatial resolution as low as 0.5 μm by combining extremely bright, monochromatic synchrotron radiation with high quality optics and X-ray detection, where conventional X-ray CT can reach maximum of 1 mm (Landis et al. 2003; Promentilla et al. 2009).

As mentioned above, X-ray micro CT is a 3D visualization of a series of 2D images taken at different angles. One can observe the interior of a sample without physically damaging it,

which makes X-ray micro CT one of the most suitable methods for non-destructive 3D microstructural evaluation for cementitious materials. Note that an image captured through X-ray micro CT is a spatial distribution of the linear attenuation coefficients. Therefore, the microstructure of a material can be studied from the linear attenuation coefficients, obtained through micro CT, which vary across the images.

X-ray micro CT has been used by several researchers to evaluate different microstructural features of cementitious materials such as pore structure (De Boever et al. 2012; Nakashima and Kamiya 2007; Okabe and Blunt 2004; Shah et al. 2013; Wang et al. 2009), fracture properties (Landis et al. 1999, 2003, 2007), sulfate and chloride attack on concrete (Bentz et al. 1994; Naik et al. 2006; Stock et al. 2002; Sugiyama et al. 2003, 2008). Digitized images of microstructure of cement-based materials and rocks from X-ray micro CT has also been utilized to predict their permeability properties (Bentz and Martys 2007; Korvin 2016; Mostaghimi et al. 2013; Okabe and Blunt 2004; Shah et al. 2013) and tortuosity (Promentilla et al. 2009; Matyka et al. 2008; Nakashima and Kamiya 2007; Latour et al. 1995; Suman and Ruth 1993; Epstein 1989).

5.2 Objectives

The goals of imaging with the X-ray micro CT technique and subsequent analysis of the images are (1) to determine the total porosity and the effective porosity, (2) to quantify the pore connectivity, (3) to evaluate the specific surface area of the pores, (4) to estimate the tortuosity and formation factor, (5) to assess the permeability and the role of fibres, and (6) to determine the pore space fractal dimension.

5.3 Experimental Details

5.3.1 Sample Preparation, Image acquisition and processing

Cylindrical specimens having a diameter of 9 mm were cored from hollow-cylindrical samples that were cast to measure water permeability. A Skyscan 1172 system, a widely used scanning equipment, was employed to generate the 3D images. The system consists of an X-ray light source from the beam line, a double crystal monochromator, a high precision rotation stage,

and a high precision X-ray detector. A cone-beam type scanner with a micro-focus X-ray source was used to generate raw shadow image of the cylindrical specimens. Images were acquired using an X-ray source with 100 kV voltage and 100 μA tube current. The transmitted images were captured by using the X-ray detector, which consists of a thin scintillator and a 10 mega pixel camera capable of capturing high-resolution images. The scan was performed at an angular step of 0.3 º with a total rotation of 360 º. The total number of output images were 2096 with a width of 4000 pixels and a height of 4000 pixels. The effective size of the voxel (volume picture element, an analogous term of pixel which is used for 2D image) of the output images was 4.34 μm. In this study, a resolution of 4.34 μm/pixel was employed which provides a reasonable estimation of microstructural parameters and permeability estimation for the purpose of this research.

X-ray micro CT has some inherent problems as in any other analytical techniques that must be addressed properly in order to obtain optimum quality 3D images (Davis and Elliott 2006; Ketcham and Carlson 2001; Mees et al. 2003). Beam hardening and ring artifacts are among those problems, which need to be considered to achieve a reliable representation of 3D microstructure of the specimen. Beam hardening is a phenomenon that occurs during scanning the specimen due to the presence of low-energy X-rays. It manifests as a high relative density zone at the edge of the specimen, where a significant number of low energy X-rays are blocked or absorbed. This effect can be reduced by implementing several measures. For instance, filtering the X-ray cone beam before and after it passes through the specimen is one of the techniques to reduce beam-hardening effect. This is usually accomplished by placing a metallic filter between specimen and X-ray source. Another way to reduce this effect is by applying a beam hardening correction during the image reconstruction process. Since the scanning process is rotational, spherical or cylindrical specimens are a preferable choice as opposed to irregularly shaped specimens. In this study, all the preventive measures, described above, were taken to reduce beam-hardening effects. In addition, micro CT images can have ring artifact effect. Note that ring artifact is a distortion that occurs due to miscalibration of the scanning equipment. These artifacts were reduced by applying a correction factor during the reconstruction stage. Also, scanning at angular intervals of 0.3° for a total rotation of 360° minimizes the ring artifacts in the reconstructed images.

5.3.2 Image analysis

High resolution digital images captured by X-ray micro CT is a series of radiographic scan, known as shadow image or projection image at a certain angular interval. These two-dimensional images, which are a map of X-ray attenuation coefficients of the samples, were then mathematically reconstructed by using suitable algorithm called back-projection. 3D model of the specimen was subsequently rendered from these slices, which simulates the actual samples within the resolution of the X-ray micro CT images. A typical reconstruction sequence is shown in Figures 5.1, 5.2, and 5.3 for Hydraulic Lime Mortar, Type N mortar, and Type O mortar respectively.

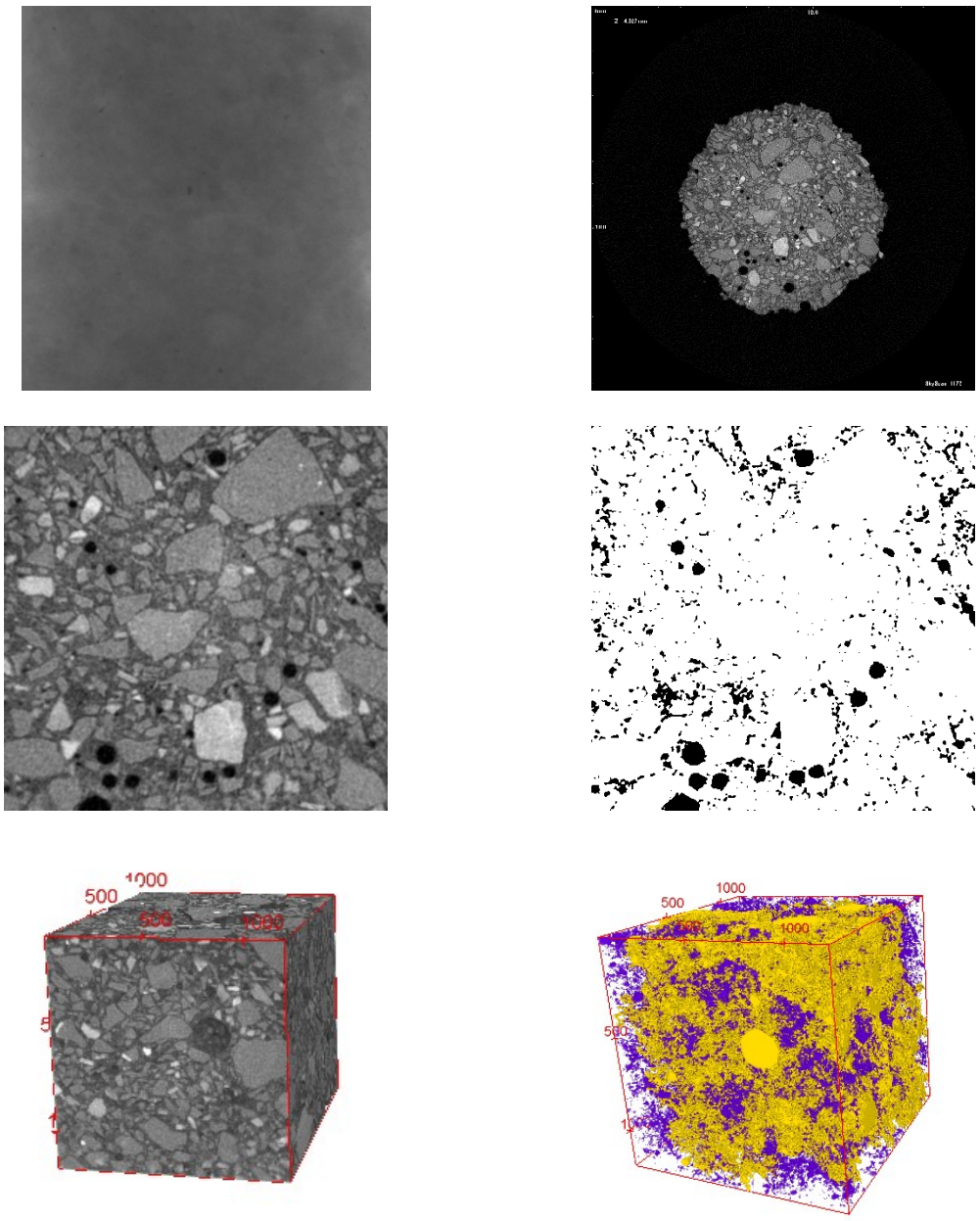

Figure 5.1 Typical X-ray micro CT images for Hydraulic Lime Mortar (a – top left) projection image, (b – top right) reconstructed image, (c – middle left) Cropped image, (d – middle right) Image after pore segmentation, (e – bottom left) 3D rendering of reconstructed image set, and (f – bottom right) Segmented view – showing pores, purple = largest connected cluster, yellow = the remaining clusters.

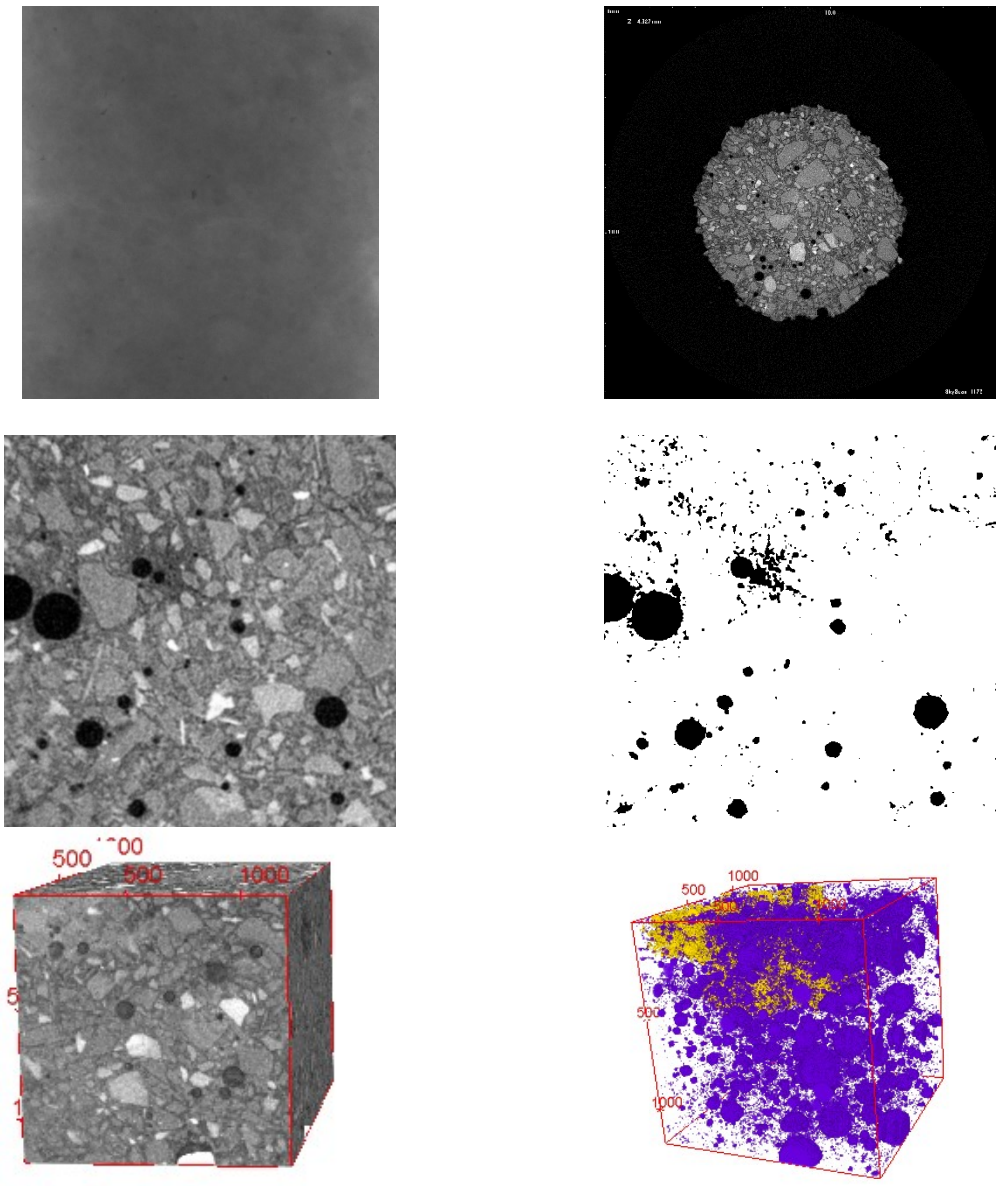

Figure 5.2 Typical X-ray micro CT images for Type N mortar (a – top left) projection image, (b – top right) reconstructed image, (c – middle left) Cropped image, (d – middle right) Image after pore segmentation, (e – bottom left) 3D rendering of reconstructed image set, and (f – bottom right) Segmented view – showing pores, purple = largest connected cluster, yellow = the remaining clusters.

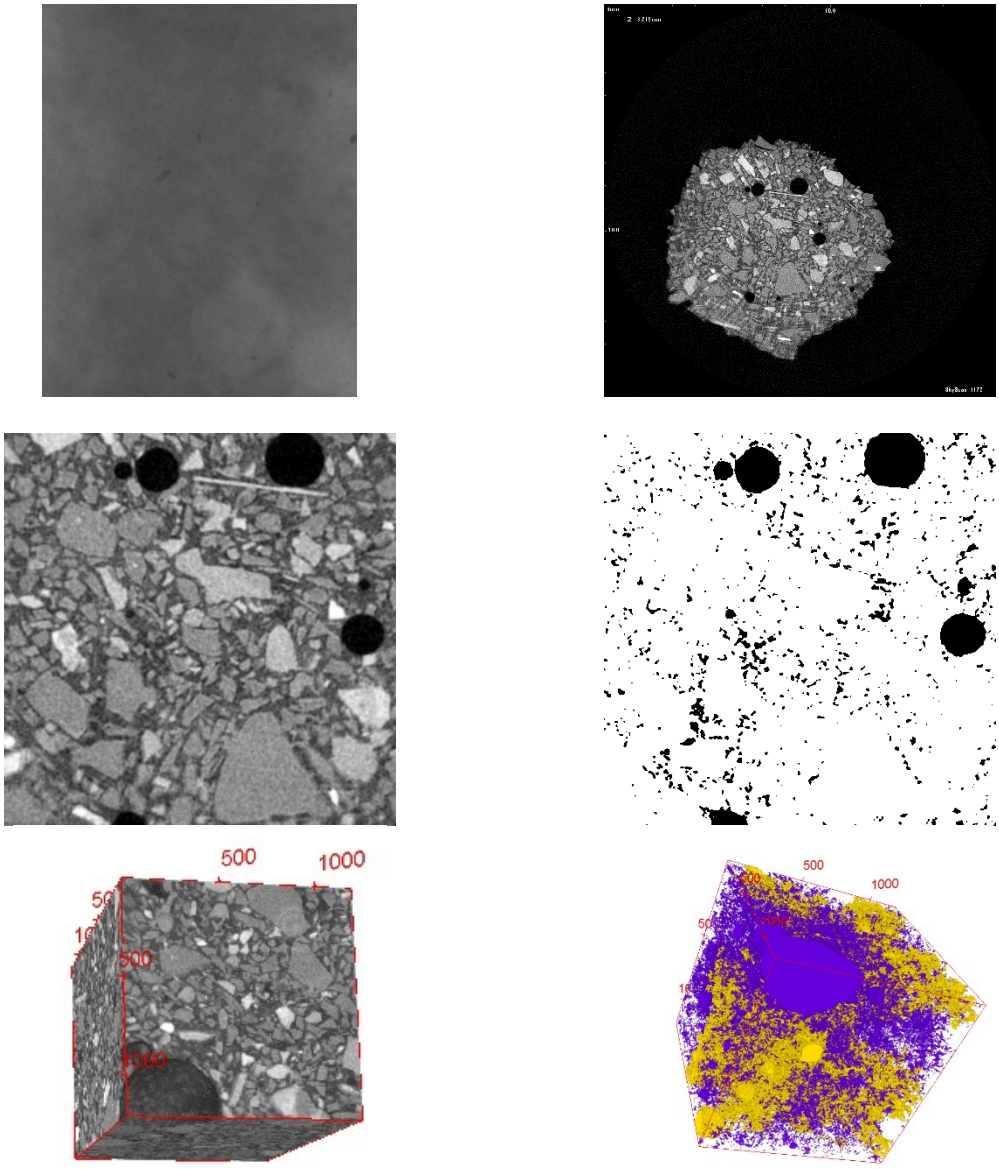

Figure 5.3 Typical X-ray Micro CT images for Type O mortar (a – top left) projection image, (b – top right) reconstructed image, (c – middle left) Cropped image, (d – middle right) Image after pore segmentation, (e – bottom left) 3D rendering of reconstructed image set, and (f – bottom right) Segmented view – showing pores, purple = largest connected cluster, yellow = the remaining clusters.

In order to evaluate the pore structure, —parameters such as porosity, pore connectivity, tortuosity, formation factor, specific surface area, and permeability— images reconstructed from X-ray micro CT raw images need some pre-processing like cropping, adjustment of

brightness and contrast, filtering and binary conversion. To that end, a cubic volume of 1200^3 voxel was cropped from the original image for micro CT analysis. The cropped images were then adjusted for brightness and contrast to enhance the intensity of the gray value to yield a sharper image. It is very common to have noise in high-resolution X-ray micro CT image; hence suitable noise filter process was utilized to minimize the impact of these noises. Note that the pre-processing parameters—Gaussian blur, despeckle, brightness and contrast—were kept in a consistent range to avoid artifacts that can be introduced due to excessive pre-processing which might yield artificial microstructural features that are otherwise non-existent. Finally, 8-bit gray scale images were converted to binary images by applying a suitable thresholding algorithm. Thresholding or pore segmentation is a process of converting the gray scale X-ray micro CT image to a binary image where pores and solid can be identified using the intensity of voxels. Among various thresholding algorithm, a more reliable and systematic thresholding method called critical overflow method (Promentilla et al. 2009; Wong et al. 2006) was adopted for this study.

After pore thresholding, a cluster-labeling program, developed by Nakashima and Kamiya (2007), was employed to label the pores and solids in images which enables the estimation of connected pore fraction along with quantification of specific surface area. Note that this cluster-labeling program originally developed by Hoshen and Kopelman (1976). Pore connectivity is determined based on how the voxels are connected to each other in 3D coordinate system. When analyzing the voxels for connectivity, two voxels are considered connected only if they share an adjacent face. If voxels are connected by edges or corners, they are considered not connected. In order to quantify the connectivity, a Mathematic®-based program developed by Nakashima and Kamiya (2007) was implemented. Furthermore, using this program the porosity, tortuosity, formation factor, and specific surface area were determined. Finally, the permeability of the mortar samples was predicted by utilizing these parameters with the following modified version of Kozeny-Carman equation developed by Walsh and Brace (1984):

$$k = \frac{(\phi)^2}{cFs^2} \tag{5.1}$$

where k is the permeability coefficient, ϕ is the porosity, c is a constant that depends on the cross-section of the tubes, usually taken to be equal to 2 for porous materials, and F is the formation factor, and s is the specific surface area.

5.4 Results and Discussion

5.4.1 Porosity and Pore Connectivity

Quantification of porosity and pore connectivity, which are two important parameters of porous microstructure, can reveal practically useful information about the transport properties of the mortars. The term 'pore' represents any microstructural voids including any capillary voids that can be identified with the chosen resolution of images. Porosity, which is a fraction of void space in the mortar, can further be divided as total porosity and effective porosity. Total porosity is the total segmented pores (pore voxels separated through thresholding), measured from the 3D reconstructed image, which includes all the connected and isolated pores. On the other hand, effective porosity is the largest connected percolating pore cluster in any orthogonal direction, normalized over the total volume. After pore thresholding and cluster labeling, total porosity, effective porosity, and pore connectivity can be measured from pore voxel count, total voxel count and the highest connecting cluster. Total porosity is the ratio of the pore voxel count and total voxel count and effective porosity is the ratio of connected pore voxel count and total voxel count.

Total segmented porosity is shown in Figures 5.4, 5.5, and 5.6 for the Hydraulic Lime Mortar, Type N mortar, and Type O mortar, respectively. Both plain and fibre reinforced mixtures are shown. The variation in porosity variations with the increase in fibre for all three mortar types are identical. Mortar with 0.15% fibre has the lowest amount of total segmented porosity compared to the plain mortar. The total porosity increases with further addition of fibre. Although effective porosity is a more relevant parameter when fluid transport phenomena is concerned, the total porosity can be good comparative index that can be used to study the mechanical properties too.

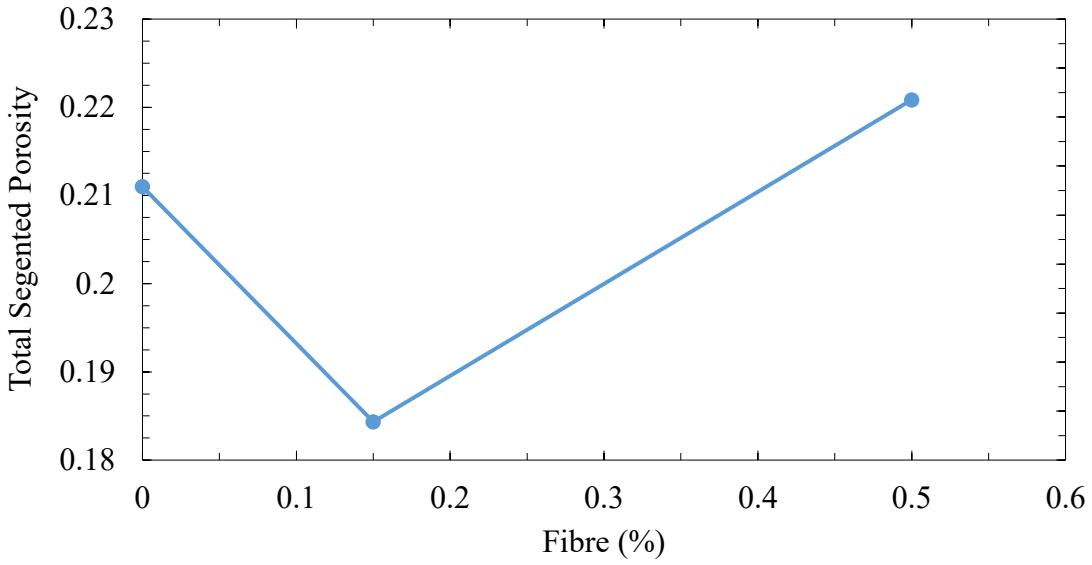

Figure 5.4 Segmented total porosity of plain and fibre reinforced Hydraulic Lime Mortar determined using X-ray micro CT method

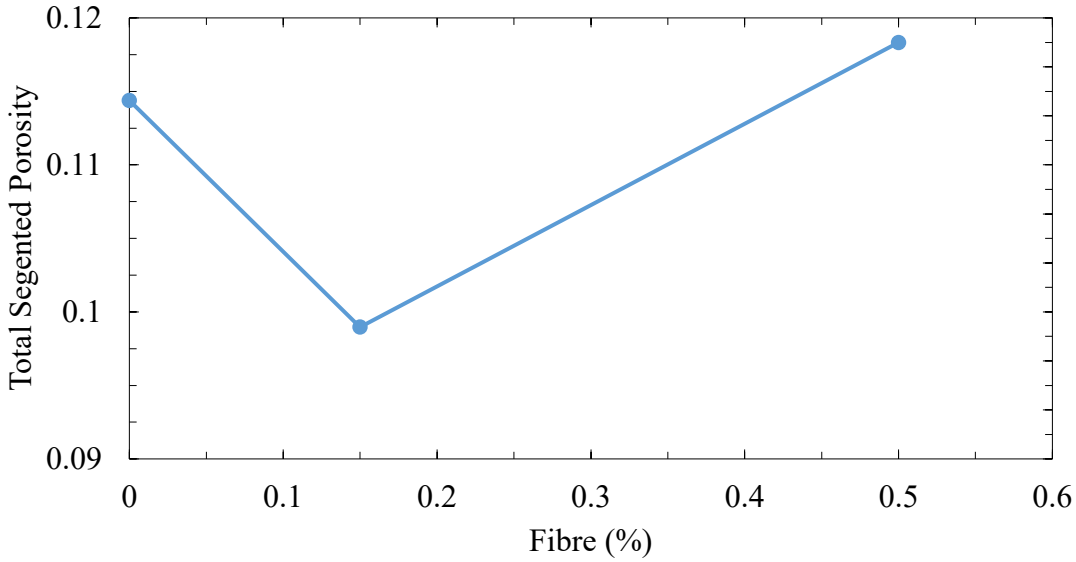

Figure 5.5 Segmented total porosity of plain and fibre reinforced Type N mortar determined using X-ray micro CT method

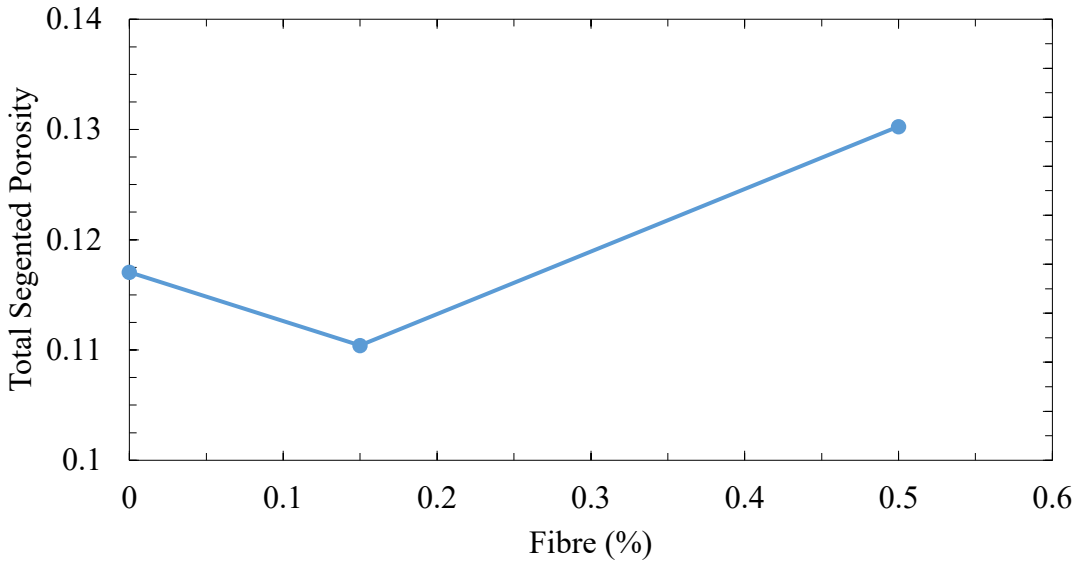

Figure 5.6 Segmented total porosity of plain and fibre reinforced Type O mortar determined using X-ray micro CT method

Effective porosity and pore connectivity for the Hydraulic Lime Mortar, Type N mortar, and Type O mortar are represented in Figures 5.7, 5.8, 5.9 and Figures 5.10, 5.11, 5.12, respectively. Both plain and reinforced mixtures are shown. Effective porosity is the largest connected pore cluster whereas pore connectivity is the ratio of the largest connected pore cluster and total pores. It can be observed that pore connectivity in HLM is highest and it decreases with the addition of cement. This trend is consistent across all fibre dosages. It is noticeable that the effective porosity and pore connectivity are the lowest for mortar with 0.15% fibre, whereas the higher dosage of fibre lead a reverse trend. An identical trend was observed for all three types of mortar. At low dosages, fibre reduces effective porosity due to pore refinement when compared with its plain counterpart. As the fibre dosage increases, the observed pore refinement diminishes and the fraction of large air-voids increases causing an increase in effective porosity and pore connectivity. This increased effective porosity and pore connectivity suggests a favourable condition for fluid transport through the mortar.

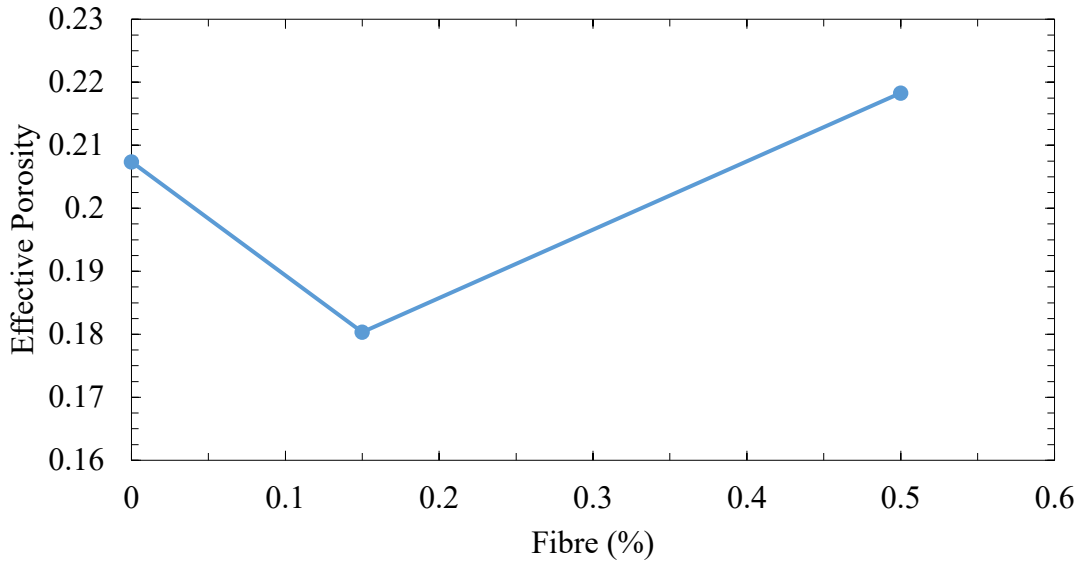

Figure 5.7 Effective porosity of plain and fibre reinforced Hydraulic Lime Mortar determined using X-ray micro CT method

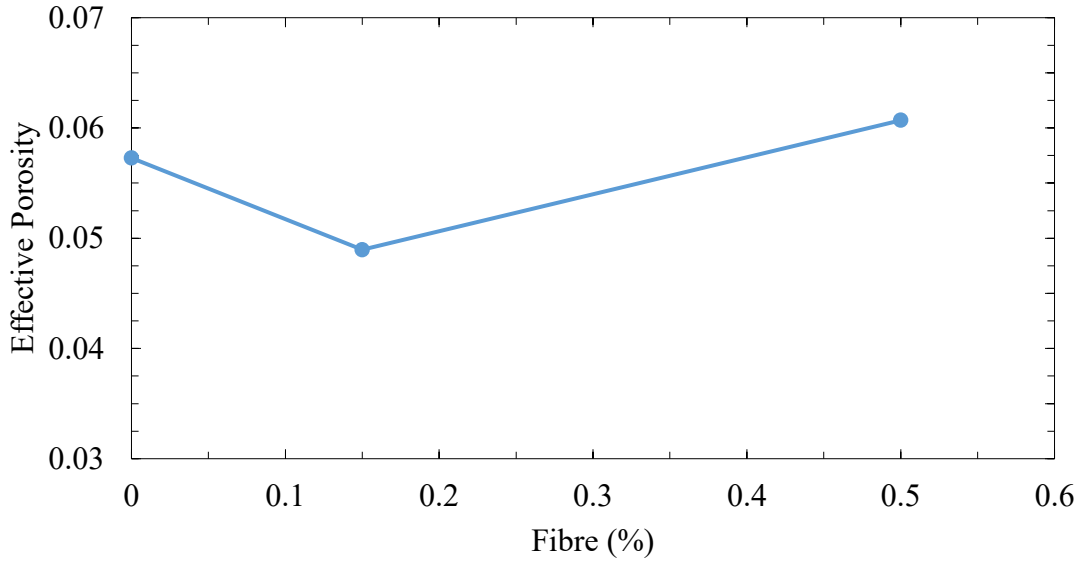

Figure 5.8 Effective porosity of plain and fibre reinforced Type N mortar determined using X-ray micro CT method

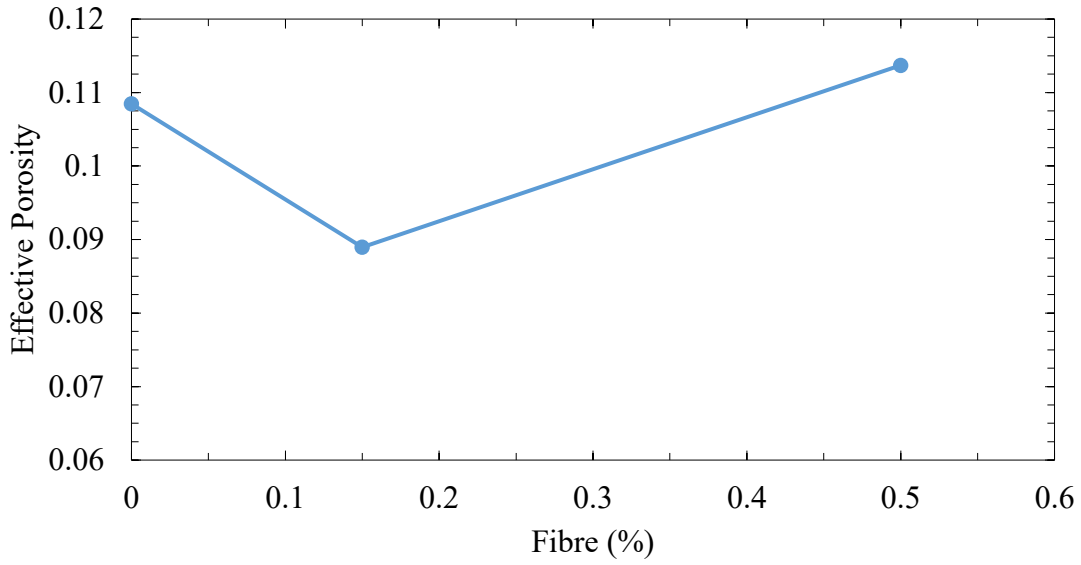

Figure 5.9 Effective porosity of plain and fibre reinforced Type O mortar determined using X-ray micro CT method

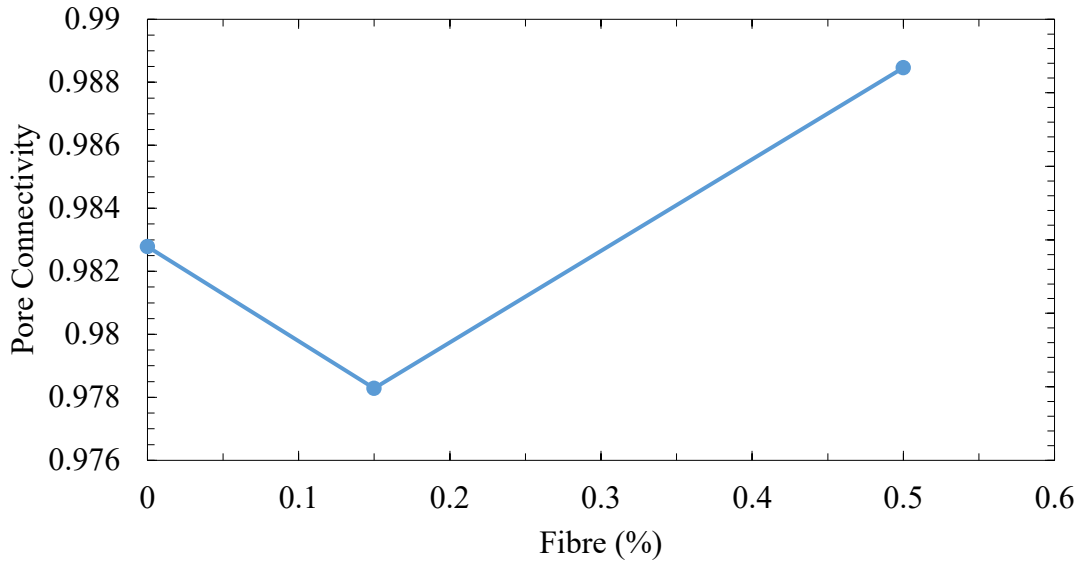

Figure 5.10 Pore connectivity of plain and fibre reinforced Hydraulic Lime Mortar determined using X-ray micro CT method

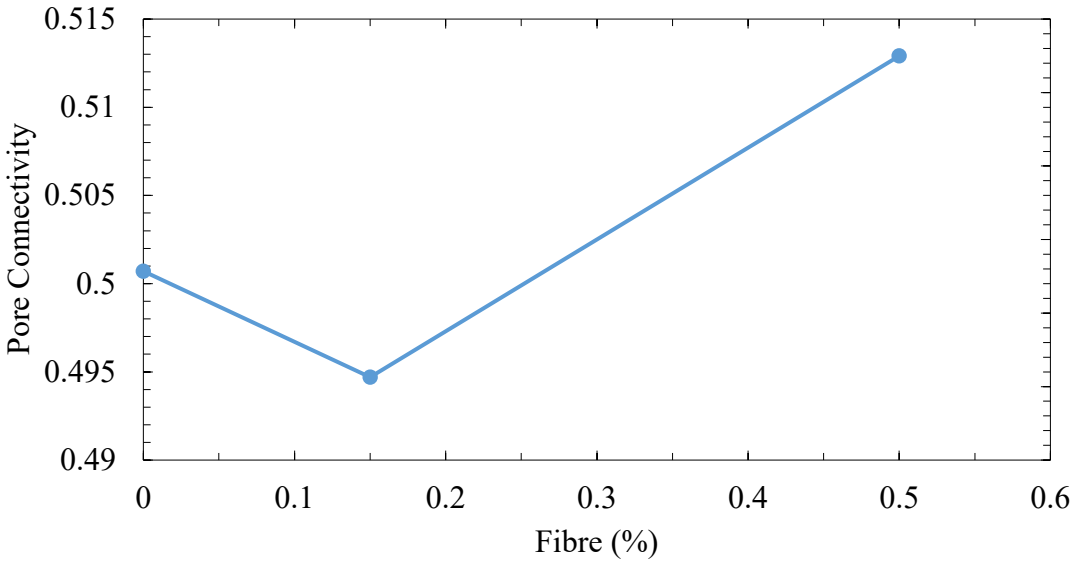

Figure 5.11 Pore connectivity of plain and fibre reinforced Type N mortar determined using X-ray micro CT method

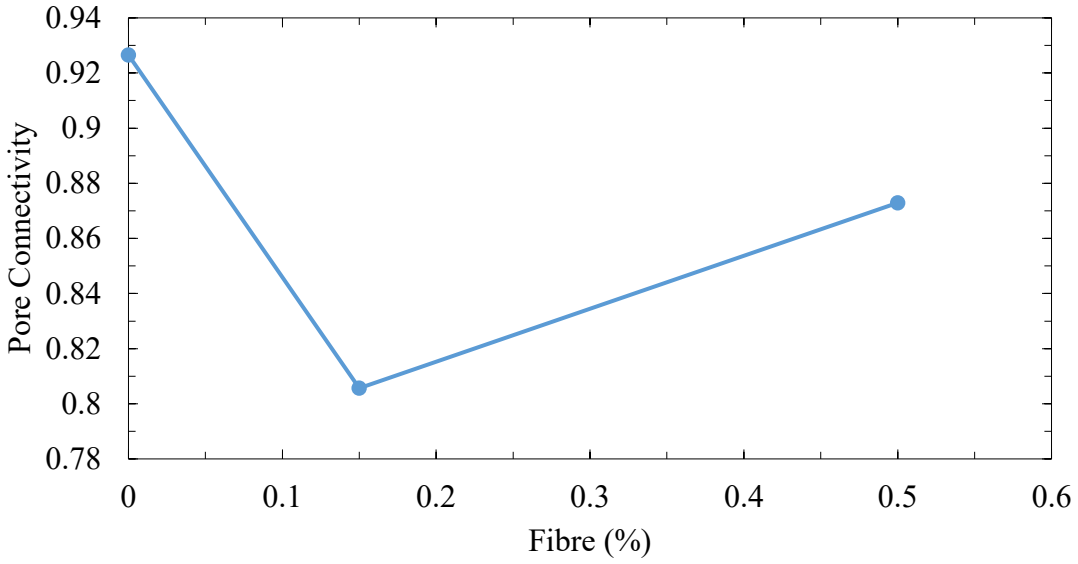

Figure 5.12 Pore connectivity of plain and fibre reinforced Type O mortar determined using X-ray micro CT method

5.4.2 Specific Surface Area

The surface to volume ratio or specific surface area of the plain and fibre reinforced Hydraulic Lime Mortar, Type N mortar, and Type O mortar was calculated from X-ray micro CT images. It was determined by normalizing the pore interface area with the bulk volume of the mortar specimen from processed micro CT images where pore-solid interface was identified by examining the interfaces with the surrounding voxels. In Figures 5.13, 5.14, and 5.15, specific surface area of plain and fibre reinforced mortars are illustrated. It can be seen that the change in specific surface area with fibre addition is very marginal, the trend of the change is quite similar for all types of mortar across all fibre regime. Specific surface area decreases slightly with the addition of 0.15% fibre compared to the plain mix, whereas the values increase as more fibres are added. Once again, this is because a low dosage of fibres causes a pore refinement as mentioned earlier in Section 5.4.1, whereas higher dosage causes a pore coarsening effect. The optimal fibre dosage was found to be 0.15% across all three mixtures in this study. This pattern can be explained with the phenomenon that the addition of low dosage fibre renders a refined pore structure whereas a coarsening of pores resulted with the addition of high fibre dosage. The lower specific surface area indicates lower microstructural flaws in pore structure of the materials, which will hinder any fluid flow through pore systems, and the opposite will happen for higher specific surface area.

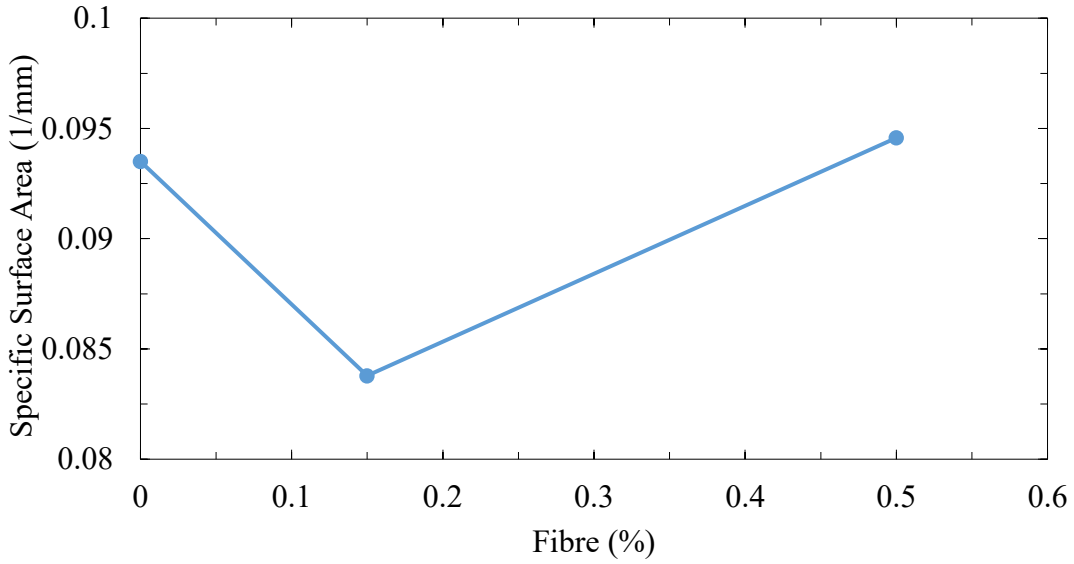

Figure 5.13 Specific surface area of plain and fibre reinforced Hydraulic Lime Mortar determined using X-ray micro CT method

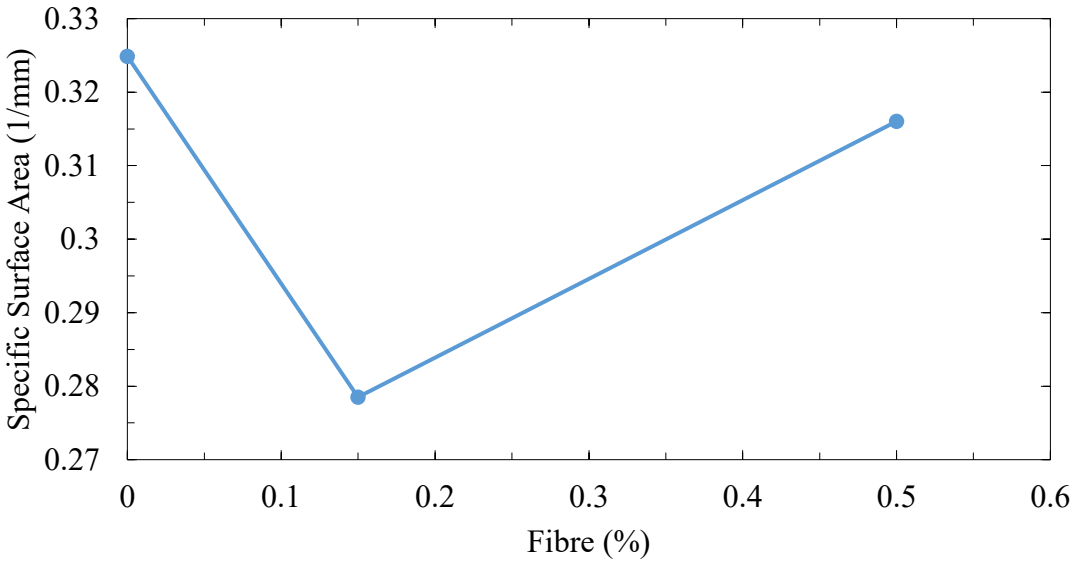

Figure 5.14 Specific surface area of plain and fibre reinforced Type N mortar determined using X-ray micro CT method

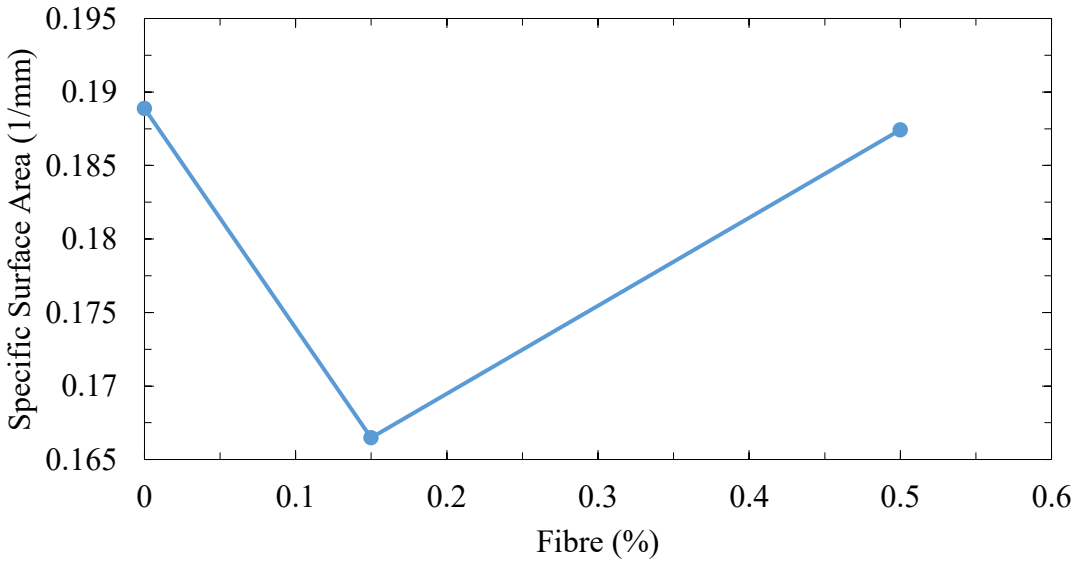

Figure 5.15 Specific surface area of plain and fibre reinforced Type O mortar determined using X-ray micro CT method

5.4.3 Tortuosity and Formation Factor

Tortuosity is a dimensionless parameter that describes the actual path of a fluid in the porous media. Geometrically, tortuosity is defined as the ratio of the actual flow path to the straight line or shortest distance along the direction of the flow. In the literature, tortuosity is defined variously, as detailed in Section 2.2.6. For instance, *diffusive tortuosity* is the ratio of the diffusion coefficient in free space to that in the particular porous media and is given by Equation 5.1.

$$\tau_d = \frac{D_o}{D} = F\phi_{eff} \tag{5.2}$$

where F is the formation factor, τ is the tortuosity, ϕ is the effective porosity, D_o is the pure gas diffusion coefficient, D is the diffusion coefficient of a porous material like concrete or mortar.

The formation factor is defined as the ratio of the electrical conductivity of the electrolyte in the bulk fluid to that of the electrolyte in the porous media. Both tortuosity and formation factor are very important parameters as they indicate fluid transport. Equally, they describe the mechanical properties of cement-based systems, as well (Awoyera et al. 2018).

In this study, both tortuosity and formation factor were estimated for across all binder systems by using 3D reconstructed images obtained from X-ray micro CT. The tortuosity was measured as diffusive tortuosity utilizing the "random-walk path" simulation (Watanabe and Nakashima 2002). The diffusive tortuosity is defined as the ratio of the diffusion coefficient in free space to that in the porous medium (Nakashima et al. 2004; Nakashima and Nakano 2011; Promentilla et al. 2016a; Watanabe and Nakashima 2002). It was obtained as per Equation 5.2.

$$F = \frac{\tau^2}{\phi} = \frac{\left(\frac{L_e}{L}\right)^2}{\phi} = \frac{D_o}{\phi D} = \frac{R_o}{R_w} \tag{5.3}$$

where τ_d is the diffusive tortuosity, D_o is the diffusion coefficient in free space, D is the diffusive coefficient in porous space, L_e is the actual flow path, and L is the length of the

porous media, F is the formation factor, ϕ_{eff} is the effective porosity, R_o is the electrical resistivity of the porous medium saturated with the electrically conductive fluid and R_w is the electrical resistivity of the electrically conductive fluid used to saturate the porous medium.

If the diffusion coefficient in three-dimensional space is defined using the time derivatives of the mean-square displacements, Equation 5.2 can be expressed as:

$$\tau_d = \frac{\left(\frac{1}{6}\frac{d\left(r_{free}^2\right)}{dt}\right)}{\left(\frac{1}{6}\frac{d(r^2)}{dt}\right)} = \frac{\frac{d\left(r_{free}^2\right)}{dt}}{\frac{d(r^2)}{dt}} \tag{5.4}$$

where t is the time, r_{free}^2 is the mean-square displacement of the walker (virtual agent that simulates fluid particle for the purpose of transport phenomena as adopted in the "random-walk" algorithm) in free space, and r^2 is the mean-square displacement of the walker in porous space.

In this research, the diffusive tortuosity as defined in Equation 5.3 was calculated using a random-walk simulation program developed by Nakashima and Kamiya (2007). In this Mathematica® based simulation program, diffusion coefficients are estimated from time-dependent mean-square displacement of virtual walkers in the 3D images. The non-sorbing random walk is a discrete lattice walk in a simple cubic lattice. The walkers choose a random pore voxel as a starting point of walk in the pore space and then attempt to move in 3D pore spaces depending on the conditions of the neighboring voxels. Walker will jump to neighboring voxel if that voxel is pore otherwise jump will not occur. Mirror image boundary conditions are applied on the original 3D X-ray micro CT images to ensure sufficiently long path for the walker so that walker can experience tortuous nature of the porous media path. The simulation was run by using 24 million time steps and 10,000 walkers in selected 3D images having a dimension of 1200 x 1200 x 1200 pixels. The effect of different number of walkers are illustrated in Figure 5.16. A typical output of the simulation is shown in Figures 5.17, 5.18, and 5.19 for the Hydraulic Lime Mortar, Type N mortar, and Type O mortar mixtures, respectively.

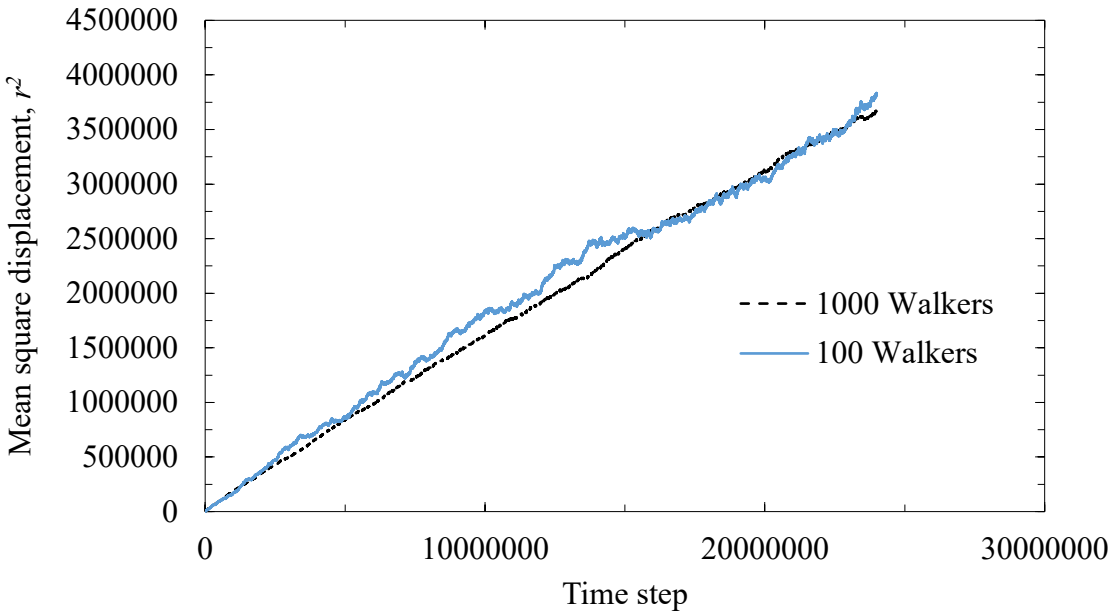

Figure 5.16 Time step vs mean square displacement as calculated by random-walk simulation for 24 million time steps

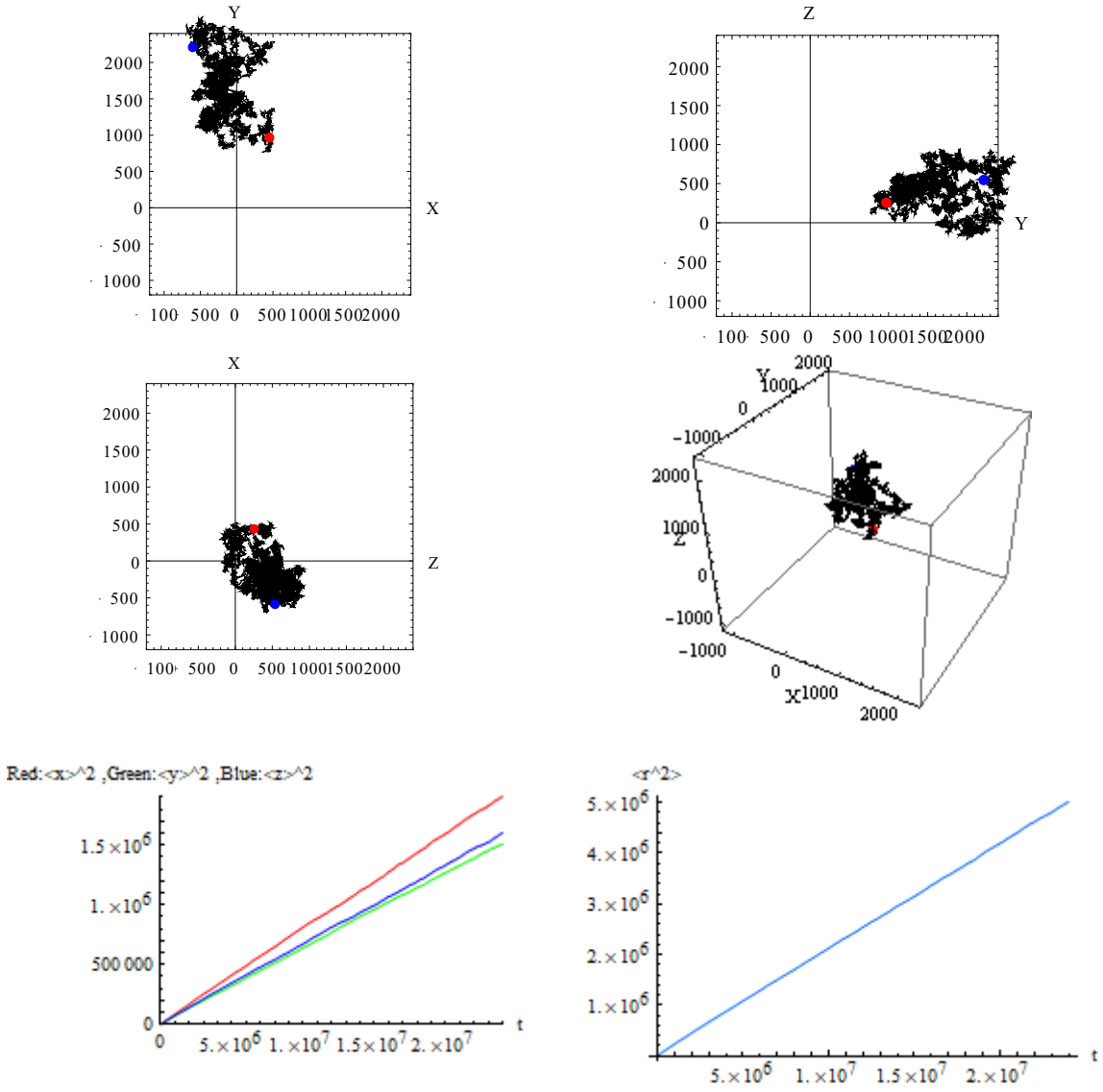

Figure 5.17 Typical example of output from the 3D random walk simulation in the percolating space of X-ray Micro CT images for Hydraulic Lime Mortar (a – top left) projected trajectory of a walker in the X-Y plane, (b – top right) projected trajectory of a walker in the Y-Z plane, (c – middle left) projected trajectory of a walker in the Z-X plane, (d – middle right) 3D view of the trajectory wherein the total time step is 24 million, (e – bottom left) plot of dimensionless mean square displacements ($\langle x^2 \rangle$, $\langle y^2 \rangle$, $\langle z^2 \rangle$) vs. time of 10,000 walkers for percolating pore space, and (f – bottom right) plot of dimensionless mean square displacement ($\langle r^2 \rangle$) vs. time of 10,000 walkers for percolating pore space

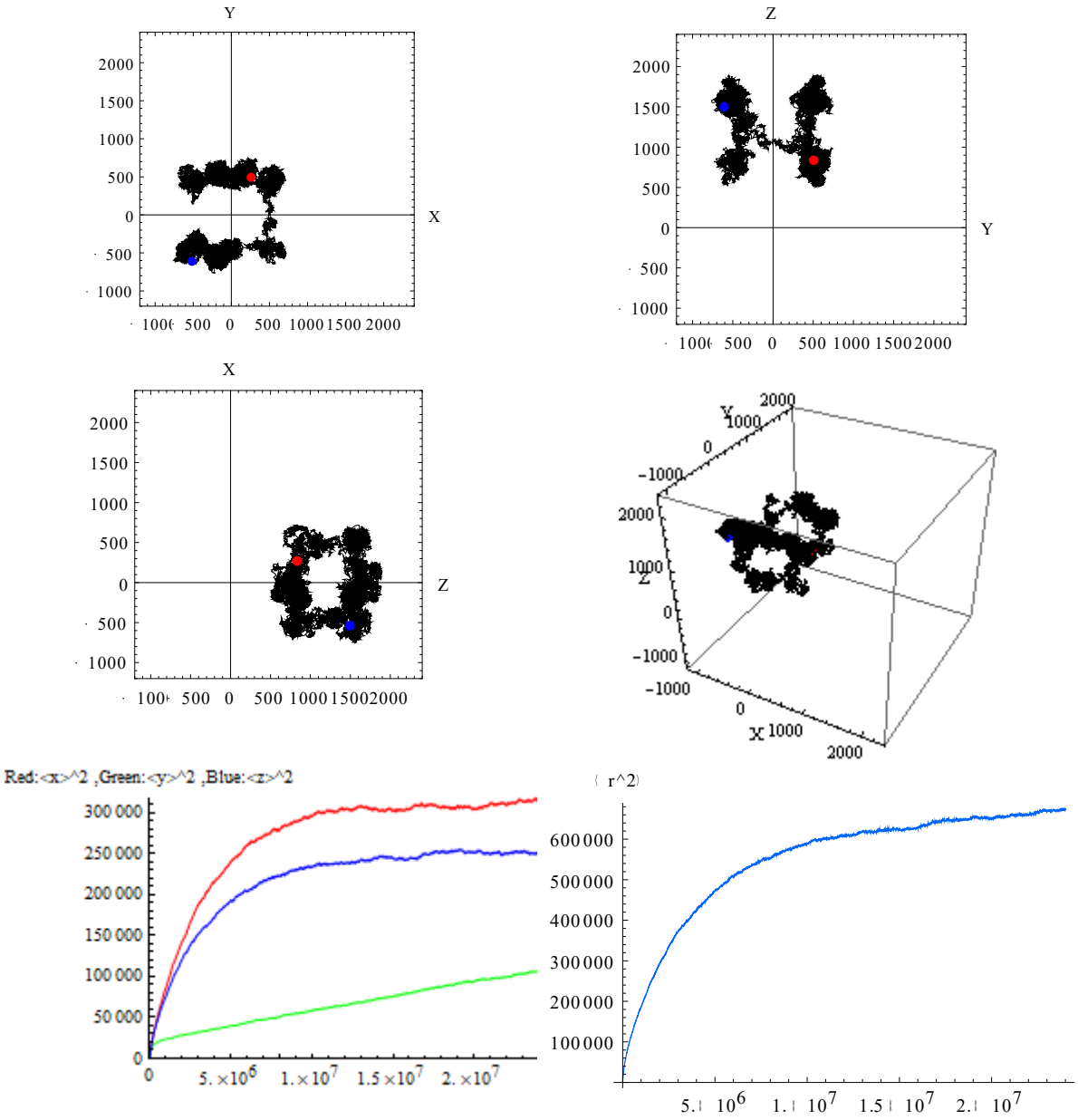

Figure 5.18 Typical example of output from the 3D random walk simulation in the percolating space of X-ray Micro CT images for Type N mortar (a – top left) projected trajectory of a walker in the X-Y plane, (b – top right) projected trajectory of a walker in the Y-Z plane, (c – middle left) projected trajectory of a walker in the Z-X plane, (d – middle right) 3D view of the trajectory wherein the total time step is 24 million, (e – bottom left) plot of dimensionless mean square displacements ($\langle x^2 \rangle$, $\langle y^2 \rangle$, $\langle z^2 \rangle$) vs. time of 10,000 walkers for percolating pore space, and (f – bottom right) plot of dimensionless mean square displacement ($\langle r^2 \rangle$) vs. time of 10,000 walkers for percolating pore space

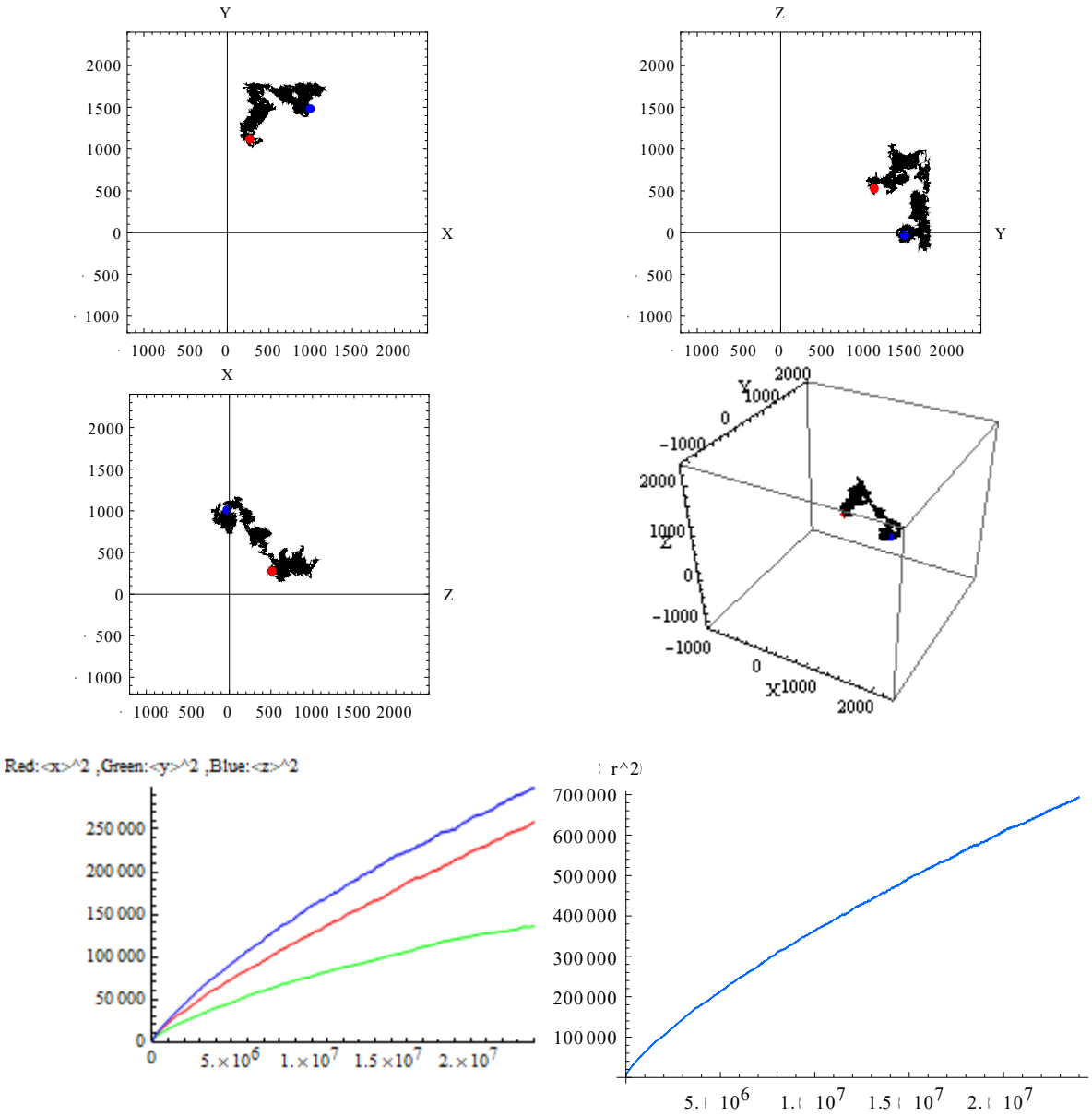

Figure 5.19 Typical example of output from the 3D random walk simulation in the percolating space of X-ray Micro CT images for Type O mortar (a – top left) projected trajectory of a walker in the X-Y plane (b – top right) projected trajectory of a walker in the Y-Z plane (c – middle left) projected trajectory of a walker in the Z-X plane (d – middle right) 3D view of the trajectory wherein the total time step is 24 million (e – bottom left) plot of dimensionless mean square displacements ($\langle x^2 \rangle$, $\langle y^2 \rangle$, $\langle z^2 \rangle$) vs. time of 10,000 walkers for percolating pore space (f – bottom right) plot of dimensionless mean square displacement ($\langle r^2 \rangle$) vs. time of 10,000 walkers for percolating pore space

Using the mean-square displacement determined through random-walk simulation, the tortuosity values were computed from Equation 5.4. Note that while calculating tortuosity, the diffusion coefficient in free space was taken as unity and diffusion coefficient in percolated space was determined by taking the inverse of the slope of mean-square displacement vs time step plot. On the other hand, formation factor was calculated by using Equation 5.3. Note that the slope of the mean square displacement vs time step was taken from the end segment of the plot. The diffusive tortuosity as measured for the Hydraulic Lime Mortar, Type N mortar and Type O mortar is shown in Figures 5.20, 5.22, and 5.24, respectively whereas formation factors are shown in Figures 5.21, 5.23, and 5.25 for plain and fibre reinforced Hydraulic Lime Mortar, Type N mortar, and Type O mortar respectively. The tortuosity and formation factor demonstrate identical trend with the fibre dosage. Both values increase at low fibre dosage, 0.15% volume fraction, compared to plain mix and then decrease when fibre dosage is increased to 0.5%. Fibre at low dosages affect microstructure of the mortar in such way that the effective porosity and pore connectivity drop due to pore refinement. Tortuosity as well as formation factor increase due to the reduction in effective porosity and pore connectivity. Consequently, the porous path becomes more tortuous which will provide more resistance to fluid flow. On the other hand, both tortuosity and formation factor decrease with higher volume fraction of the fibre. Note that higher fibre fraction results in an increase in effective porosity and pore connectivity due to pore coarsening, which in turn creates a less tortuous fluid flow path; in other words, greater permeability.

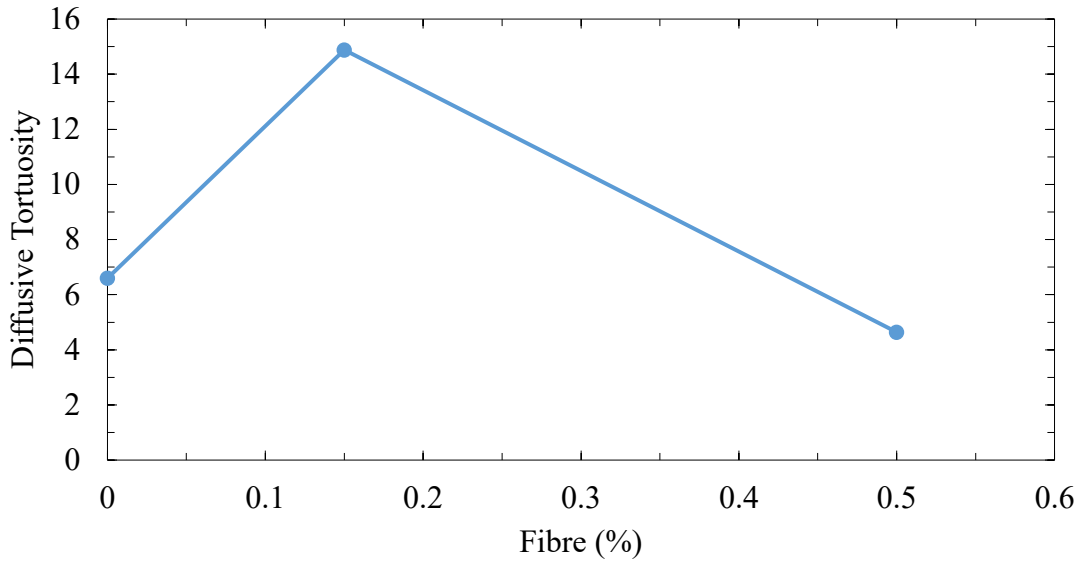

Figure 5.20 Diffusive tortuosity of plain and fibre reinforced Hydraulic Lime Mortar determined using X-ray micro CT method

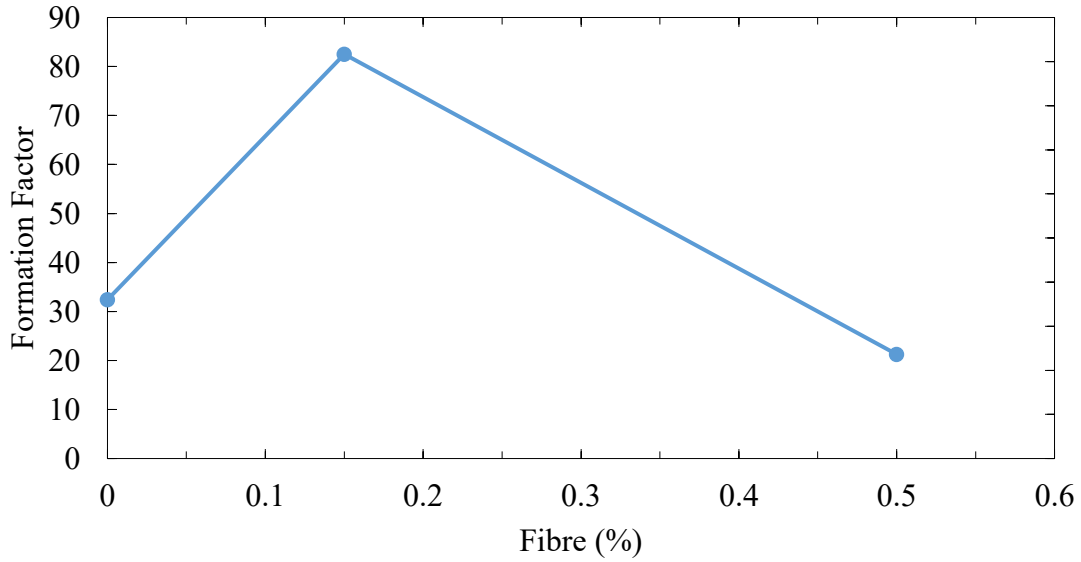

Figure 5.21 Formation factor of plain and fibre reinforced Hydraulic Lime Mortar determined using X-ray micro CT method

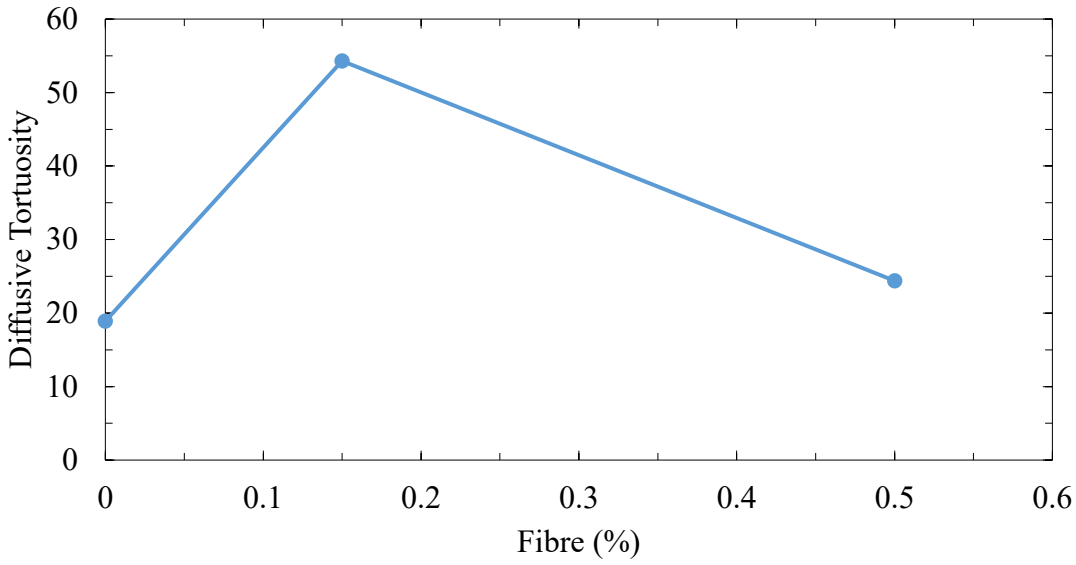

Figure 5.22 Diffusive tortuosity of plain and fibre reinforced Type N mortar determined using X-ray micro CT method

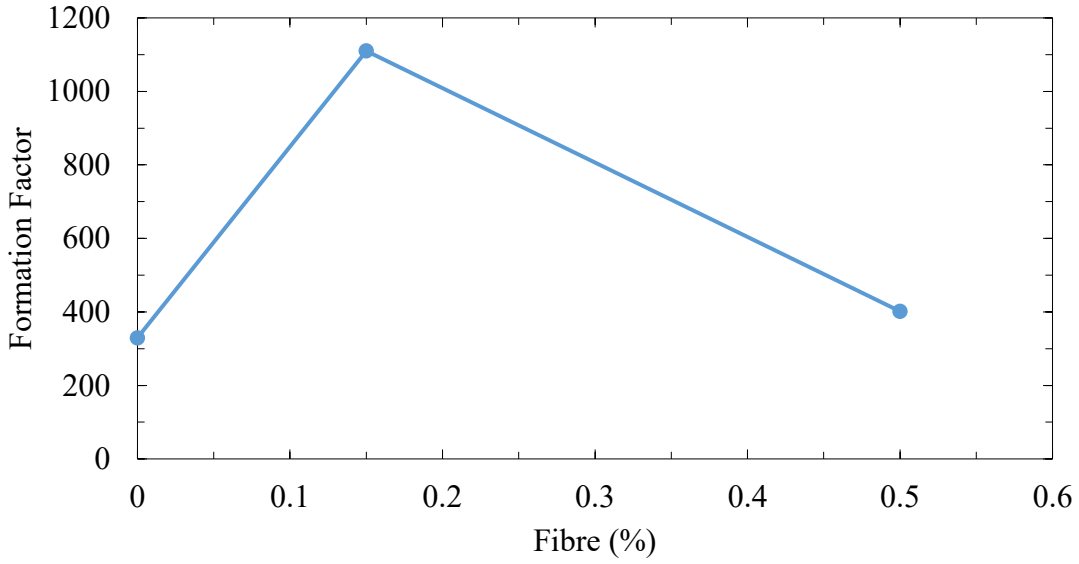

Figure 5.23 Formation factor of plain and fibre reinforced Type N mortar determined using X-ray micro CT method

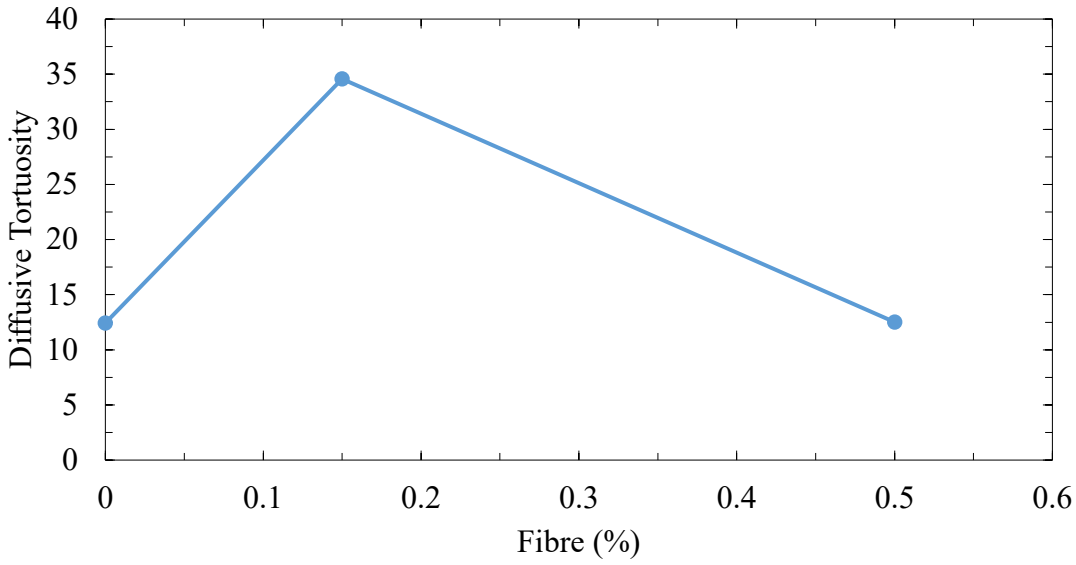

Figure 5.24 Diffusive tortuosity of plain and fibre reinforced Type N mortar determined using X-ray micro CT method

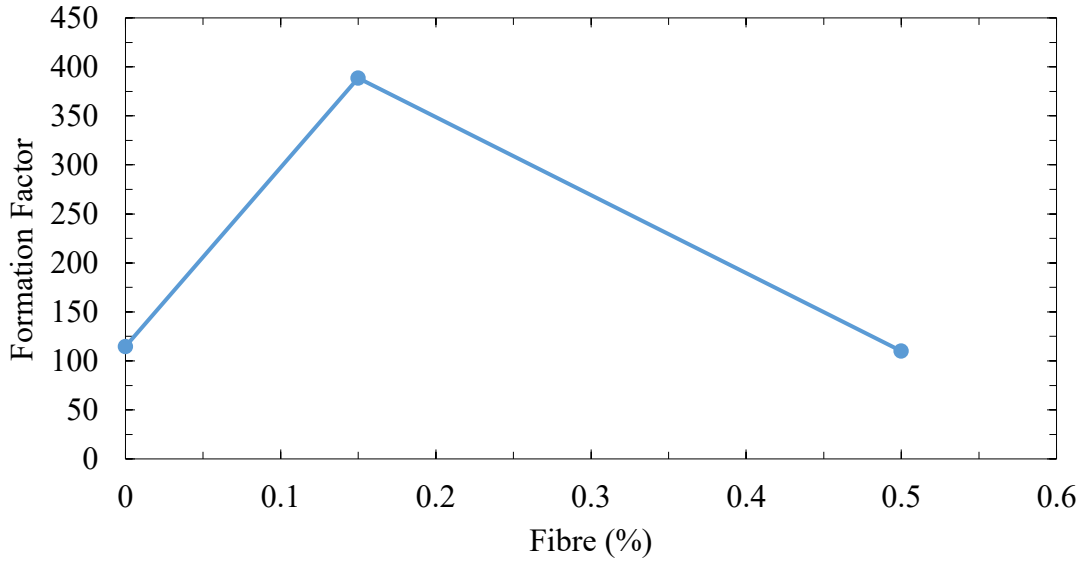

Figure 5.25 Formation factor of plain and fibre reinforced Type O mortar determined using X-ray micro CT method

5.4.4 Permeability evaluation

The images obtained through X-ray micro CT may be used with advantage to evaluate permeability, as this technique is non-destructive and less time-consuming.

In this study, permeability was evaluated for plain and fibre reinforced Hydraulic Lime Mortar, Type N mortar, and Type O mortar from 3D X-ray micro CT images. Using the results from random walk simulation, developed by Nakashima and Kamiya (2002; 2004), the permeability can be estimated by employing the Kozeny-Carman equation. This well-known model, developed for Poiseuille flow, can be expressed as:

$$k = \frac{\phi}{\alpha\, \tau^2 \left(\frac{S}{V}\right)^2_{pore}} \tag{5.5}$$

where k is the intrinsic permeability (m^2), ϕ is the porosity, α is a constant which is usually taken as 2.0 for porous media (Berryman and Blair 1987), τ is the geometric tortuosity, and $\left(\frac{S}{V}\right)_{pore}$ is the specific surface area of pores.

X-ray micro CT images were analyzed as per the procedure described by Nakashima and Kamiya (2002; 2004) to evaluate porosity, tortuosity, and specific surface area of pores for plain and fibre reinforced Hydraulic Lime Mortar, Type N mortar, and Type O mortar. For X-ray micro CT images, effective porosity as resolved by the chosen voxel size, was used in Equation 5.4 instead of total porosity since fluid flow only occurs through the connected pores. Furthermore, the largest connected pore cluster was used for permeability computation. In Equation 5.4, α was taken equal to 2.0 as suggested for porous media (Berryman and Blair 1986, 1987; Blair et al. 1996). It is worth mentioning that Nakashima (Nakashima et al. 2004; Nakashima and Watanabe 2002) used different α values for seemingly same type of porous medium. For instance, they computed transport properties using micro CT images by assuming α value as 1.0 (Nakashima and Watanabe 2002), whereas a value of 6.0 was used in another study involving the same material (Nakashima et al. 2004) assuming that 1/3 of the pipes are parallel to the flow (Nakashima and Yamaghuci 2004). However, subsequently they nullified

this assumption noting they had omitted a factor of 3 (Nakashima and Yamaguchi 2004) Thus, the value of α should have been 2.0 in their computations, all along.

Transport properties obtained by cluster labeling and random-walk simulation using X-ray micro CT data are compared with the results from the actual water permeability experiments. Figures 5.26, 5.27, and 5.28 depict this comparison for the Hydraulic Lime Mortar, Type N mortar, and Type O mortar, respectively. It can be noticed that the output from micro CT and experimental results follow the same trend. The difference between the permeability coefficients from these two methods does not vary more than one order of magnitude. Studies by (Nakashima et al. 2004) report identical trends with similar deviation (1 order of magnitude) between experimental and estimated coefficients of permeability. Also, the accuracy of this computational technique is of the same order as in the conventional NMR logging based on the T2-realxometry (Straley et al. 1997) It is likely that this deviation is due to the inherent limitation of X-ray micro CT method associated with spatial resolution since it cannot detect pores smaller than 4.34 μm. Which means that, in this present study, the contribution of pores smaller than those that can be resolved using the adopted resolution of 4.34 μm to the computed permeability, was neglected. One may observe that predicted permeability for Type N mortar at higher (> 0.15%) fibre dosages diverges compared to other two types (HLM and Type O) of mortar. This may be due to the fact that the pore size distribution altered by the presence of Portland cement where a pore size refinement occurs. The selected resolution of X-ray micro CT was unable to capture these refined pores that lead to a drop in predicted permeability.

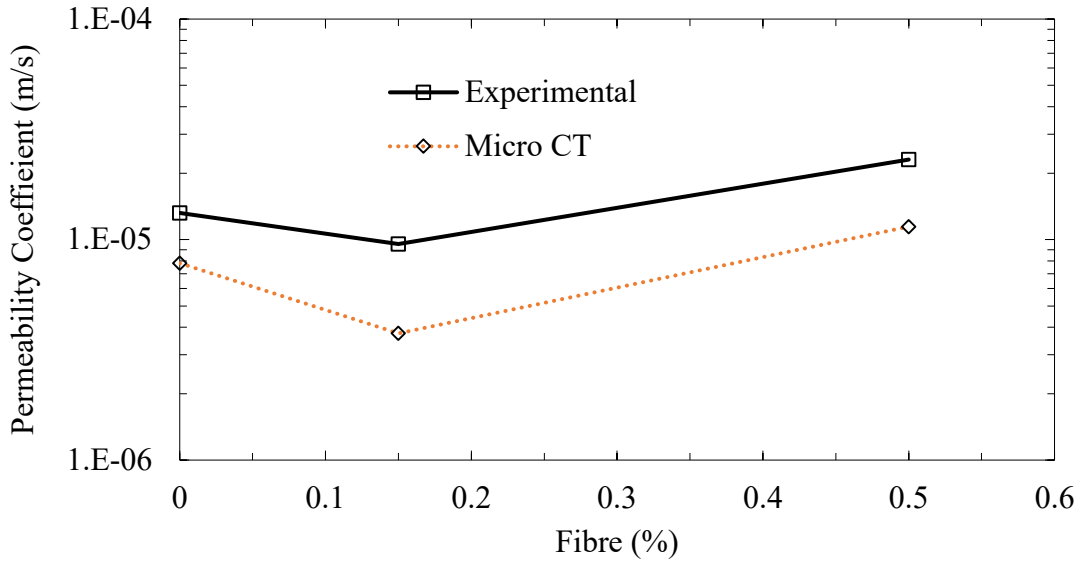

Figure 5.26 Permeability evaluation of plain and fibre reinforced Hydraulic Lime Mortar determined using X-ray micro CT method

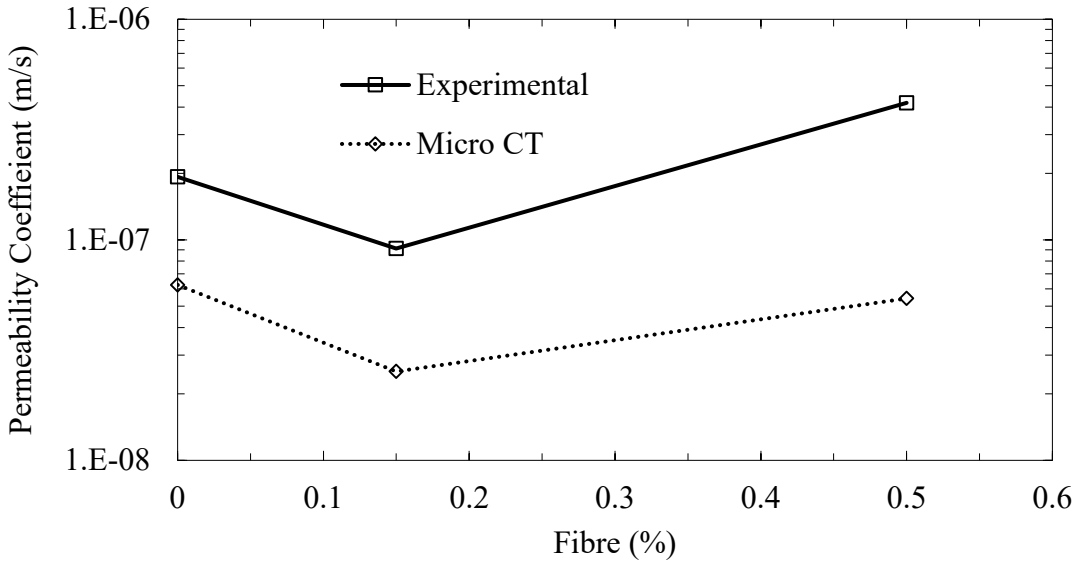

Figure 5.27 Permeability evaluation of plain and fibre reinforced Type N mortar determined using X-ray micro CT method

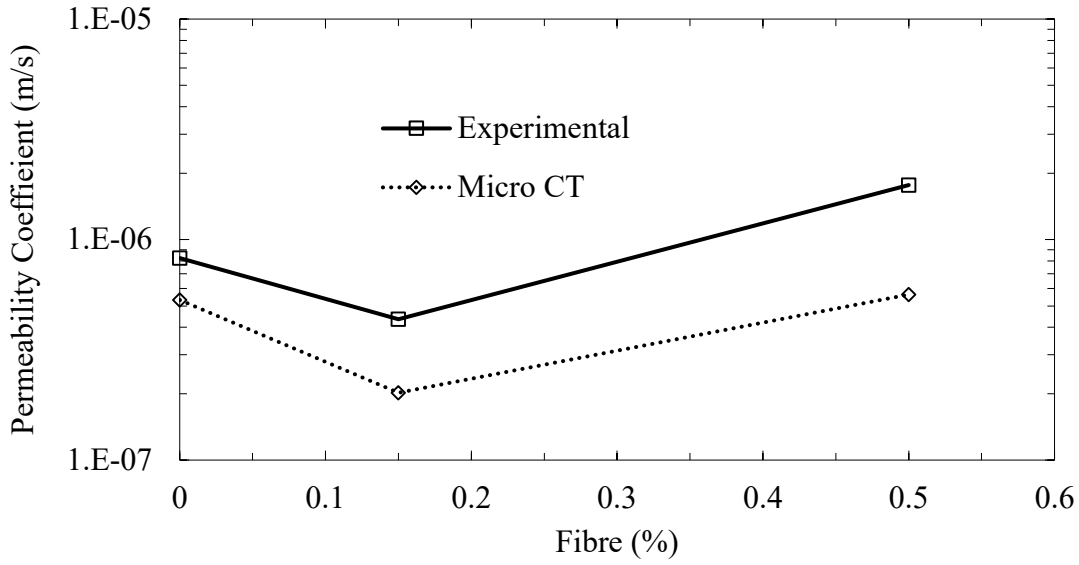

Figure 5.28 Permeability evaluation of plain and fibre reinforced Type O mortar determined using X-ray micro CT method

5.4.5 Fractal Dimension

The concept "fractality" is a convenient way to describe internal material structure that possess self-similarity. It is another way to describe the complexity of microstructure where rough pore surface and interfaces play an important role. The fractal dimension (FD) expresses the roughness of the texture, having repetitive pattern that appears in X-ray micro CT images. In this study, the fractal dimensions were evaluated from 3D micro CT model geometry to analyze the nature of pore structure that develops due to the addition of fibre in the cement/lime matrix. FD values were determined by using a software package called ImageJ together with its plug-in called BoneJ (Doube et al. 2010). ImageJ is an open source image processing program designed for scientific multidimensional images whereas BoneJ is a morphological analysis plug-in for ImageJ, where the box-counting method is adopted, where varying sized cubes were used instead of squares, to calculate FD from 3D X-ray micro CT images (Parkinson and Fazzalari 2000). Note that fractal dimension determined through X-ray micro CT is space filling in nature and thus varies from 2.00 to 3.00 whereas those described in Chapter 3 are area-filling nature i.e., ranging from 1.00 to 2.00.

FD in 3D for plain and fibre reinforced hydraulic mortar, Type N mortar, and Type O mortar is demonstrated in Figures 5.29, 5.30, and 5.31 respectively. It can be observed that the variation of FD with the increase in fibre fraction is identical for all three types of mortar. The FD values drop with an increase in fibre fraction up to a value of 0.15% followed by a rise in fractality with further increase fibre dosage. Due to pore refinement at 0.15% fibre dosage, FD value decreased as pore structures became more regular. With higher fibre fraction, an increased FD value indicates a complex nature of the pore structure. As discussed earlier, when fibre is added at a higher volume fraction, such as 0.5%, the observed increase in fractality, implying a more irregular pore structure, was resulted due to pore coarsening.

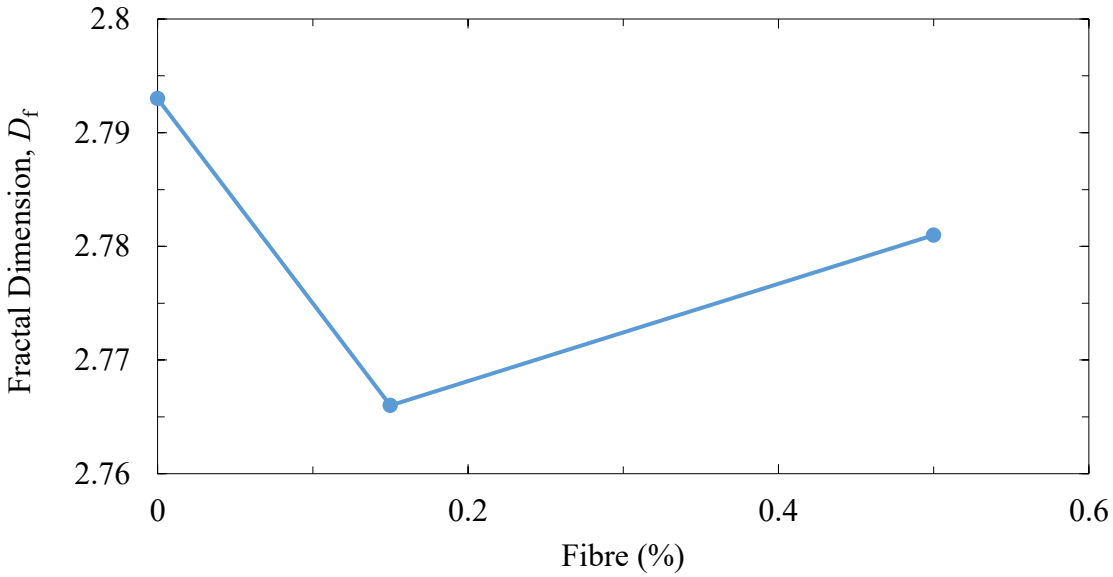

Figure 5.29 Pore space fractality of Hydraulic Lime Mortar with fibre variation

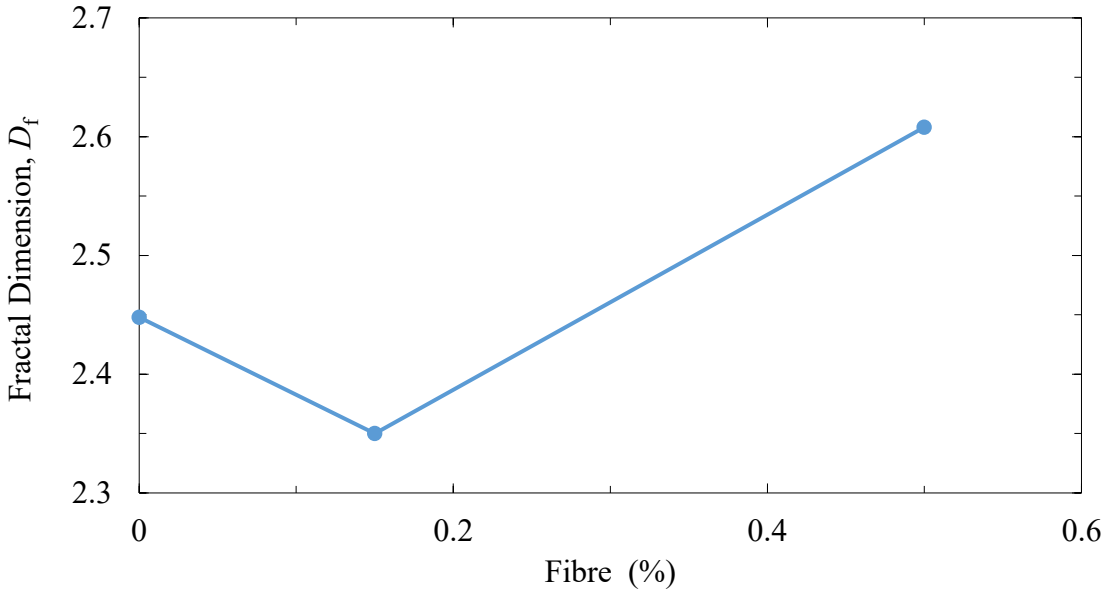

Figure 5.30 Pore space fractality of Type N Mortar with fibre variation

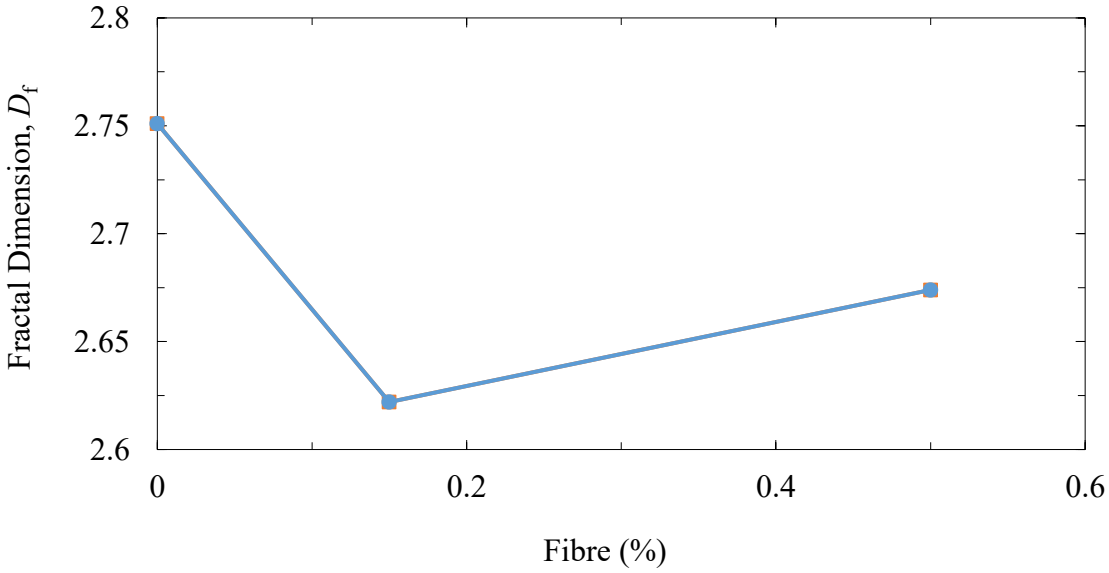

Figure 5.31 Pore space fractality of Type O Mortar with fibre variation

5.5 Concluding Remarks

In this chapter, permeability was evaluated by using the X-ray micro CT technique to capture images of the microstructure. This method allows for a non-destructive, 3D evaluation. From this study, it can be stated that an optimum fibre dosage of 0.15% by volume provides a microstructure that yields a durable mortar. Based on the findings of this chapter, the following specific conclusions can be made:

- Mortar with 0.15% fibre has the lowest amount of total segmented porosity compared to the plain mortar and the total porosity increases with further addition of fibre.
- The effective porosity and pore connectivity are the lowest for mortar with 0.15% fibre, whereas a higher fibre dosage reverses this trend.
- Specific surface area decreases slightly with the addition of 0.15% fibre compared to the plain mix, and increase as more fibres are added.
- The tortuosity and formation factor values increase at low fibre dosage, 0.15% volume fraction, compared to plain mix and then decrease when fibre dosage is increased to 0.5%.
- The predicted permeability coefficients of plain and fibre reinforced Hydraulic Lime Mortar; Type N mortar and Type O mortar by this X-ray micro CT method are in good agreement with experimental values.
- Fractal dimension in three dimensions for plain and fibre reinforced mortars decreases with low fibre dosages (0.15% by volume) in comparison to plain mortar and increases with more fibre addition.

CHAPTER 6. EFFECT OF POLYPROPYLENE MICRO-FIBRE AND NANO-LIME ON THE STRENGTH AND PERMEABILITY OF REPAIR MORTARS

6.1 Introduction

Cement-based materials being complex multiphase systems, their mechanical properties are considerably influenced by the properties of constituent components and the interface between them. Macroscopically, concrete is composed of mortar matrix with dispersed coarse aggregate phase which itself can be said to be a composite made of different minerals. The mortar in turn consists of hydrated cement paste and fine aggregates. It is essential to recognize therefore that the strength of these composites differs substantially from the properties of the individual components that it contains especially due to the condition at the interface between the matrix and aggregates.

The microstructure of lime-based composites evolves through the interaction with the environment, especially the well-known lime-cycle. For instance, carbonation is one such chemical reaction the lime undergoes. Carbonation of Hydraulic Lime Mortar is based on a complex reactive-transport mechanism governed by CO_2-diffusion within the porous network and the chemical reactions between CO_2 and the hydration compounds. It is well established that carbonation is generally responsible for significant microstructural changes (Lawrence et al. 2007). Carbonation changes the microstructure of the mortar, that will improve mechanical properties but carbonation can also affect the pore structure, and in turn, the water transport characteristics. In cement-lime mortar, both carbonation and hydration occur simultaneously but carbonation usually takes place slowly.

The recent development of nanoscience and nanotechnology has opened the way to new applications in many scientific fields, including that of the conservation of structural heritage. Over the last few decades, nano-lime, a compound having nanoscale particles of $Ca(OH)_2$ with potentially superior consolidation properties has been developed. Application of nano-lime on existing lime-based structures is similar to the limewater application technique, traditionally

used for its durability and high compatibility with the calcareous matrix but requiring a large number of applications and not always yielding effective consolidation. On the other hand, nano-lime can penetrate in greater depth and hence can reduce water ingress through materials.

6.2 Objectives

The objectives of this chapter are to determine morphological characteristics of the mortars used in this study through XRD and XRF analysis, evaluation of the compressive response of the plain and fibre reinforced mortars and its correlation with permeability and assess the extent to which nano-lime application would affect the permeability of NHL mortar.

6.3 Morphology

Lime mortars were used widely in Canada and elsewhere in the world until the late 1800s. In Canada, three types of mortar are currently being used for repointing historic masonry structures: lime mortars, Hydraulic Lime Mortars, and Portland cement/masonry cement-lime mortars. Mortar used for historic structures are expected to comply with good conservation principles and be compatible with the historic fabric as far as feasible; it must also be appropriate for the material to be bonded and remain durable under service conditions. Hydraulic Lime Mortar (HLM) was the most common binder in Canadian masonry until late in the 19th century. The performance of Hydraulic Lime Mortars used on major Canadian heritage structures over the past five years was monitored in a pilot of projects and its performance was satisfactory (Suter et al. 2001). With the rapid development in building materials, use of natural Hydraulic Lime Mortars gradually declined because of their variable performance, and cement-based mortars became popular due to their rapid strength development with time. For the restoration and rehabilitation of historic structures, however, Hydraulic Lime Mortar is still preferable due to good adhesion, ductility, and reasonably high values of porosity and permeability.

Natural hydraulic limes (NHL) are derived completely from argillaceous limestone after slaking. Hydraulic limes can be feebly, moderately, or eminently hydraulic, however, the new

European Standard EN 459 (2001) classifies them according to its compressive strength as listed in Table 6.1. Natural hydraulic lime is classified as NHL2, NHL3.5 and NHL5 with compressive strengths of 2 MPa, 3.5 MPa, and 5 MPa respectively (Maurenbrecher et al. 2007). The physical properties of hydraulic lime are described in Table 6.2, and the chemical composition of NHL2 is addressed in Table 6.3.

Table 6.1 Compressive Strength of Hydraulic Limes (From EN 459)

Type of hydraulic lime	Compressive strength (MPa)	
	7 day	28 day
HL 2	-	1.5-10
HL 3.5	≥ 1.5	2.7-14
HL 5	≥ 2	4.0-20

Table 6.2 Physical Properties of Hydraulic Lime (EN 459-2 2001)

Type of hydraulic lime	Bulk density	Fineness (%)		Sound-ness	Free water content	Penetration	Air content	Setting time
	(kg/m^3)	0.09 mm	0.2 mm	(mm)	(%)	(mm)	(%)	(hour)
HL 2	400 - 800	≤ 15	≤ 5	≤ 20	≤ 2	20 and < 50	≤ 20	1 and ≤ 15
HL 3.5	400 - 800							
HL 5	400 - 800				≤ 1			

Table 6.3 Chemical Composition of NHL2 (percentages related to original dry lime) (Lanas et al. 2004)

Compound	CaO	LOI	SiO_2	MgO	Al_2O_3	SO_3	K_2O	Fe_2O_3	Na_2O
% by mass	54.26	15	12.57	7.65	5.42	2.13	1.35	1.16	0.34

Cement-based mortars have replaced lime-based mortars because of their faster setting, higher mechanical strength, and advanced industrial development and affordable cost. However, in

spite of their widespread use in civil engineering, cement-based mortars have been found to present major disadvantages when used as repair mortars for restoring cultural heritage (Lanas and Alvarez-Galindo 2003). It presents a considerable incompatibility with existing stone masonry blocks, having a high salt content, which can damage the stone block by crystallization and/or hydration cycles and has also been found to possess low flexibility in contrast with lime-based mortars. The latter hinders any accommodation of movement resulting from creep or thermal effects (Hendry 2001; Mosquera et al. 2002). The use of cement-lime mortars could be interesting in this sense, because mortars prepared by adding a small fraction of Portland cement behave similar to hydraulic mortars, which are characterized by higher strengths than lime mortars (but not as high as cement mortars), as well as a faster setting time, which improves their application (Maurenbrecher 2004; Sébaïbi et al. 2004). In some countries, the availability of natural commercial hydraulic lime is very low; therefore, information regarding the behaviour of cement-lime mortars may be beneficial in developing a suitable replacement based on cement-lime mixtures.

The term hydraulic can be defined in relation to two specific properties: the capacity of hardening when water is added to the dry binder and the property to harden under water (Sabbioni 2001; Sabbioni et al. 2002). A hydraulic binder is obtained by adding different ingredients to the lime (air-hardening binder) that confer it the aforementioned properties. The contents of these ingredients, such as silica (SiO_2) and alumina (Al_2O_3) mainly, are the responsible for this effect (Sabbioni 2001; Sabbioni et al. 2002) . The reaction between the lime, SiO_2 and Al_2O_3 leads to the formation of calcium silicates and aluminates.

Hydration of these compounds provides consistency to the mortar matrix, which imparts strength gradually (Thomassin and Rassineux 1992). During production, the final burning temperature should be kept below 1250 ^oC, otherwise sintering may occur at higher temperatures. In the cement production, limestone and clay are calcined at temperatures exceeding 1400 ^oC: a clinker is formed due to the sintering process. Calcium silicates (mainly C_3S) and calcium aluminates (C_3A and C_4AF) are formed during sintering. In NHL, C_2S is the hydraulic phase. C_3S, C_3A, and C_4AF could also be detected in NHL, in small amounts, due to a local overheating in the limekiln.

Carbonation, as shown in the lime cycle in Figure 6.1, is a chemical process whereby slaked lime, or portlandite, ($Ca(OH)_2$) reacts in solution with atmospheric carbon dioxide (CO_2) to form calcium carbonate, or calcite ($CaCO_3$) which is significantly stronger and less soluble that the portlandite it replaces. The relevant chemical equations of the lime cycle are:

$$CaCO_3 \xrightarrow{\text{Heat}} CaO \text{ (Quick lime)} + CO_2 \quad (6.1)$$

$$CaO + H_2O \rightarrow Ca(OH)_2 \text{ (Slaked lime)} \quad (6.2)$$

$$Ca(OH)_2 + CO_2 \rightarrow CaCO_3 + H_2O \quad (6.3)$$

Therefore, for carbonation the presence of water is essential, since CO_2 reacts with $Ca(OH)_2$ in dissolved state (Thiéry et al. 2011). During carbonation reaction, there are five stages involved: 1. Diffusion of gaseous CO_2 through pores of mortar, 2. Dissolution of the CO_2 in the pore water, 3. Dissolution of $Ca(OH)_2$ in the pore water, 4. Solution reaction between $Ca(OH)_2$ and CO_2 , and 5. Precipitation of solid $CaCO_3$ (Lawrence et al. 2007). Carbonation changes the microstructure of the mortar, not only improving the mechanical properties but also affecting the pore structure, and hence water transport characteristics. Compared with cement-based mortars, this results in a much more extended setting time, lower compressive strength, higher porosity, deformability, and water transport characteristics (Bernard et al. 2003).

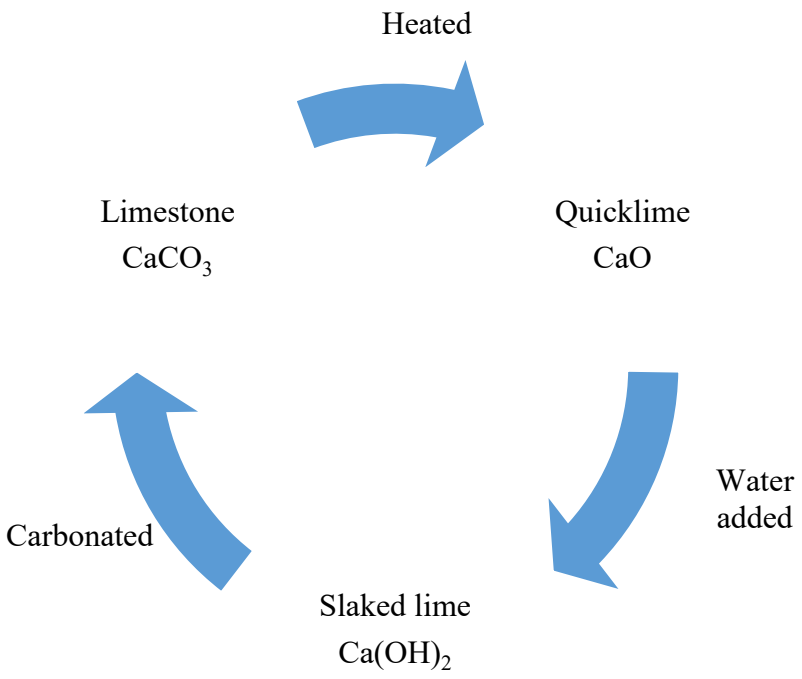

Figure 6.1 The lime cycle

During the setting and hardening processes of a mortar, various physical and chemical phenomena take place depending on the binder composition:

i) In lime-based mortars the loss of the kneading water takes place accompanied by a certain degree of shrinkage (Lanas and Alvarez-Galindo 2003). The carbonation process starts when the water content of the mortar does not hinder the diffusion of the air through the material (Van Balen and Van Gemert 1994). The reaction between CO_2 and $Ca(OH)_2$ in an aqueous medium i.e., the carbonation, results in the formation of $CaCO_3$. $CaCO_3$ crystallizes as three polymorphs, calcite, aragonite, and valerite, depending on the reaction conditions (i.e., pH,

temperature, and supersaturation), and the presence of additives (Lippmann 1973; Rodriguez-Navarro et al. 2007). Calcite is the most stable phase at ambient temperature and pressure. Whereas Aragonite, which typically appears as prisms or needle-like crystals, and Valerite, which tends to form polycrystalline spherulites, are metastable phases and, especially the latter, may play a role as a precursor in calcite formation. Apart from these three polymorphs, metastable amorphous calcium carbonate (ACC) appears as a hydrated transient phase during the initial stages of carbonation at high reactant concentrations (Cizer et al. 2012). This amorphous phase, which typically appears as small spheres less than 1 μm in diameter, transforms into calcite as the reaction progresses (Cizer et al. 2012) .

ii) In cement-based mortars, the setting is a consequence of the hydration of the calcium silicates, which starts quickly owing to the hydration of the C_3S and continues more slowly because of the hydration of the C_2S. The hydration of both compounds gives strength to the mortar (Lea 1970). The carbonation process also takes place slowly. In cement-based composites, the carbonation is a reaction of the basic compounds of hydrated cement (essentially $Ca(OH)_2$ and CSH) with carbonic acid.

X-ray fluorescence (XRF) and X-ray diffraction (XRD) are two widely used techniques to study the composition if cement/lime-based composites. In this study, XRF and XRD analysis were performed for Hydraulic Lime Mortar, Type N mortar, and Type O mortar to determine the oxide composition and mineralogical phase evaluation. The results from XRF are shown in Tables 6.4, 6.5, and 6.6 whereas those from XRD plots are presented in Figures 6.2, 6.3, and 6.4 for Hydraulic Lime Mortar, Type N mortar, and Type O mortar respectively. It can be observed from the XRF analysis that lime mortar contains higher amount of CaO when compared with cement-lime mortar. This is due to the fact that a certain fraction of lime was replaced by cement in cement-lime mortar. Also, the addition of cement increases the amount of SiO_2, aluminum oxide Al_2O_3, and ferric oxide Fe_2O_3 that ensure water resistance of lime mortar, an increases the mechanical strength, and a drop in hydraulicity (Gulbe et al. 2017). The XRD analysis of lime mortar and cement-lime mortars reveals that cement-lime has ettringite and gypsum whereas lime mortars do not have those products. Although Hydraulic Lime Mortar usually has belite, C_2S and alite, C_3S, but these compounds are not visible in the

XRD plot, as shown in Figure 6.2. This may be due to the fact that mass fraction of C_2S and C_3S are higher in high strength NHL mortar whereas these compounds are residual or non-existent for low strength NHL mortar, as experimentally demonstrated by Cristiano et. al. (2016).

Table 6.4 Oxide composition of HLM determined through XRF analysis

Compound	Al_2O_3	SiO_2	Y_2O_3	SO_3	K_2O	CaO	TiO_2	Cr_2O_3	Fe_2O_3	SrO
% by mass	1.71	23.55	2.7	0.87	1.82	67.99	0.33	0.10	0.78	0.17

Table 6.5 Oxide composition of Type N mortar determined through XRF analysis

Compound	Al_2O_3	SiO_2	Y_2O_3	SO_3	K_2O	CaO	TiO_2	ZrO_2	Fe_2O_3	SrO
% by mass	2.41	25.87	2.78	3.30	2.02	60.83	0.31	0.10	2.25	0.15

Table 6.6 Oxide composition of Type O mortar determined through XRF analysis

Compound	Al_2O_3	SiO_2	Y_2O_3	SO_3	K_2O	CaO	TiO_2	ZrO_2	Fe_2O_3	SrO
% by mass	2.28	28.16	2.53	2.66	2.28	59.68	0.28	0.08	1.89	0.16

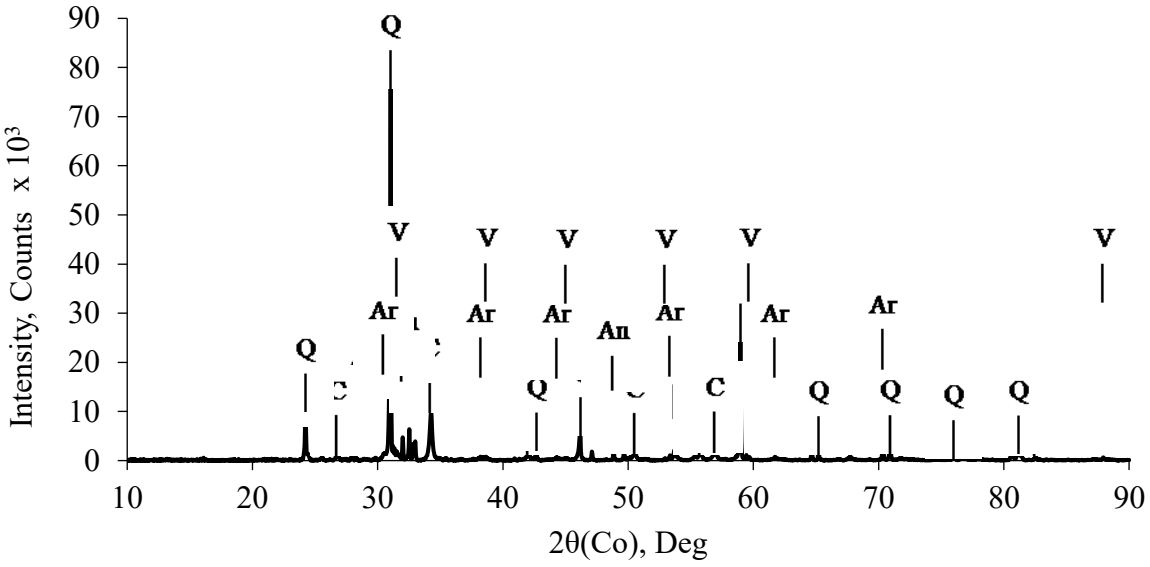

Figure 6.2 X-ray Diffraction (XRD) for HLM; Note: A ≡ Albite; C ≡ Calcite; Q ≡ Quartz; An ≡ Anorthoclase; Ar ≡ Aragonite;V ≡ Valerite

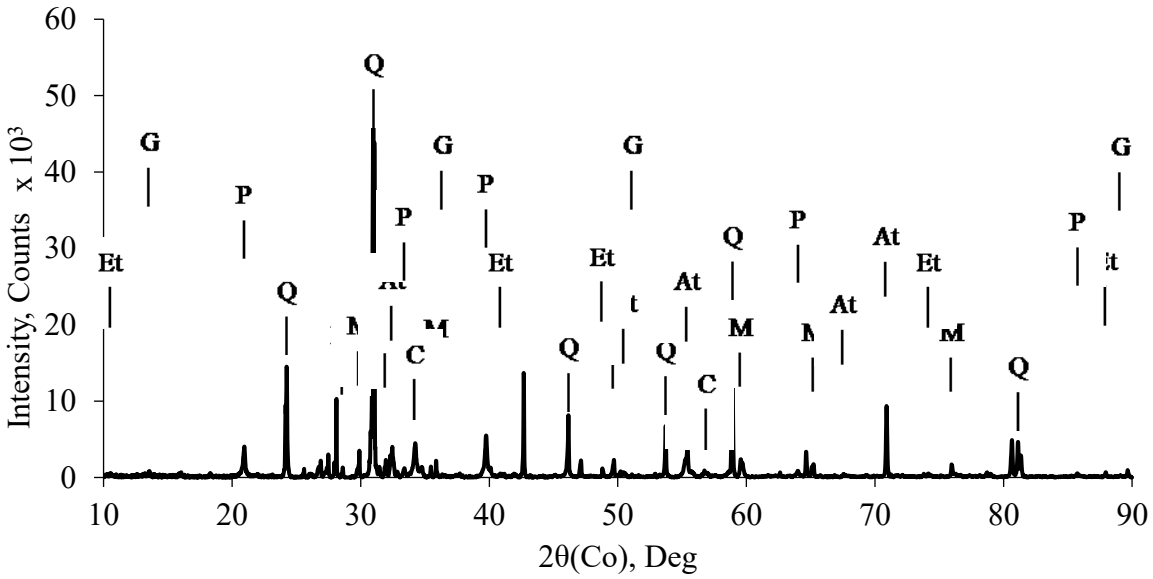

Figure 6.3 X-ray Diffraction (XRD) for Type N mortar; Note: M ≡ Microcline; C ≡ Calcite; Q ≡ Quartz; At ≡ Anorthite; Et ≡ Ettringite; G ≡ Gypsum; P ≡ Portlandite

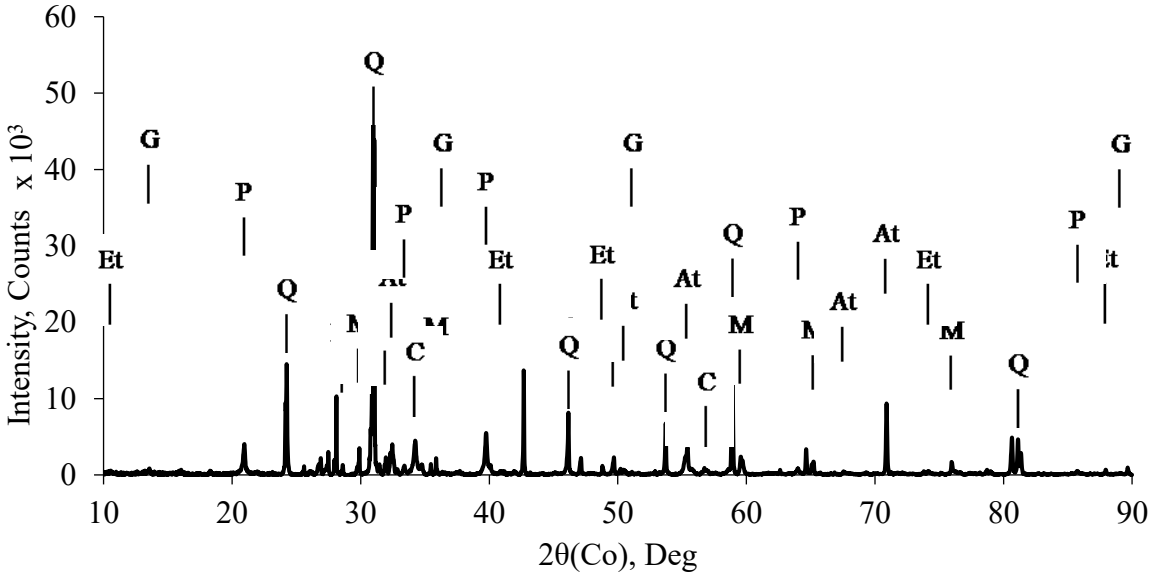

Figure 6.4 X-ray Diffraction (XRD) for Type O mortar; Note: A ≡ Albite; C ≡ Calcite; Q ≡ Quartz; Ah ≡ Anhydrite; Et ≡ Ettringite; G ≡ Gypsum; P ≡ Portlandite

6.4 Mechanical Properties Evaluation

Compressive strength is the most commonly evaluated property of concrete in routine engineering practice because of relative ease of conducting the tests. In addition, it can be used to correlate many other mechanical and durability related properties of concrete. Under compressive load, the observed stress-strain response is linear until the loading reaches a point where micro-cracks in ITZ grow in numbers and even coalesce, and thus the concrete gradually exhibits a non-linear behaviour (Mehta and Monteiro 2006; Mindess et al. 2003). After reaching the ultimate strength, due to the growth of unstable cracks, the descending branch of the stress-strain leads to the failure stage, under the combined action of primary compressive load and secondary tensile stress induced by imposed compressive load, in a generally quasi-brittle manner. Repair mortar is generally being used for all sorts of building components (e.g., load bearing walls and columns). In historic gravity dams, tensile loading is relevant since any compression failure is associated with secondary tensile stresses developed at right angles to the direction of applied compressive loading (Mindess et al. 2003), which may cause an increase in micro-cracks resulting higher permeability.

6.4.1 Materials and sample preparation

Details of material properties, mixer proportions, specimen preparation is described in Section 3.3.1.

6.4.2 Test Setup and Experiment Details

The mortar cylinders were tested in a universal testing machine with a built-in load cell of 1000 kN capacity (MTS 1000). Three replicates were tested in each case. The cylinders were instrumented as shown in Figure 6.5 to derive the compressive stress-strain response together with axial and transverse strain histories as per (ASTM C 469 2001). The loading surface was kept plane and parallel through sulphur capping.

Three linear variable displacement transducers (LVDTs) were arranged 120º apart about the longitudinal axis. The LVDTs in the lateral directions were two on opposite sides of a diameter as shown in Figure 6.7. The data acquisition system recorded the load, stroke, and LVDT measurements at 5 Hz. The test was conducted using a fixed rate of displacement at 1.25 mm/min as per ASTM C469 (2001).

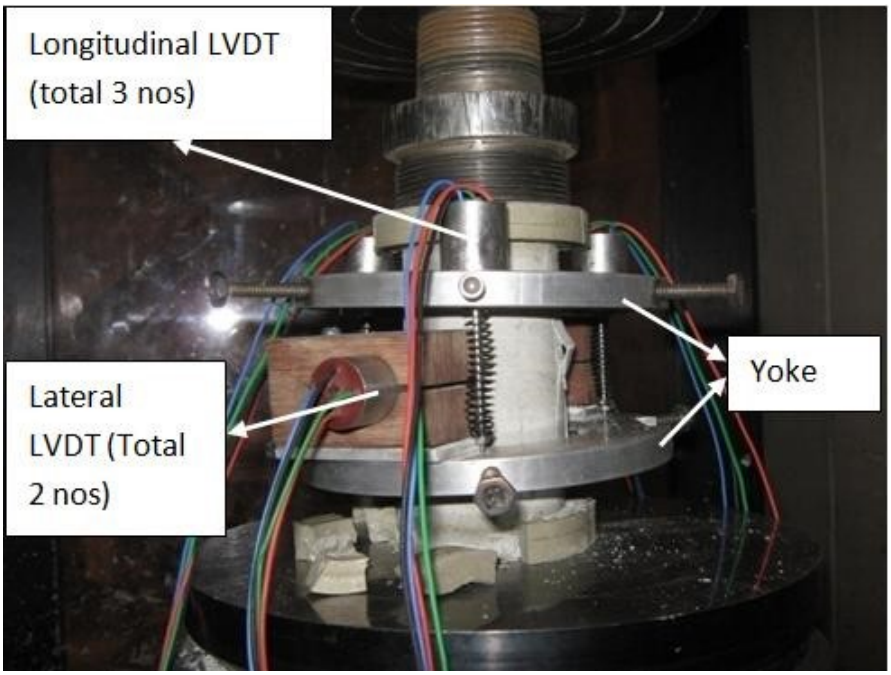

Figure 6.5 Quasi-Static Test in Progress for Compression of Mortar

6.4.3 Results and Discussion

Cement or lime-based systems are regarded as heterogeneous materials. The response of these materials depends on the loading configuration (tensile, compressive, shear, or any combination of these), degree of heterogeneity, microstructure, and the presence of any inclusions such as aggregates or fibres. An important microstructural feature of these materials is the presence of pre-existing flaws even before applying any stress. These microstructural defects may appear in the form of micro-cracks and entrained or entrapped air-voids. Micro-cracks could result due to the segregation of ingredients, shrinkage, thermal effects, dissimilar elastic modulus of cement paste and aggregates, and inefficient packing of binder particles

around any solid inclusions. On the other hand, air-voids form after the self-desiccation of capillary water due to the hydration of binder. The presence of these micro or macro defects affects the mechanical properties of the material.

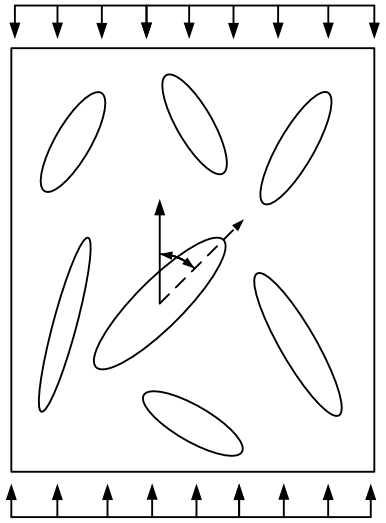

Figure 6.6 Response of cement/lime-based systems when subjected to compression

Response of cement-based systems to applied load depends on the orientation of the micro-defects with respect to the direction of applied load as shown in Figure 6.6. When the material is loaded in tension, the interfacial cracks, aligned parallel to the loading direction, have a tendency to close while those oriented perpendicular to the loading direction tend to open (Carpinteri and Ingraffea 1984). The behaviour is opposite when the loading changes from tension to compression. It is to be noted that during the application of compressive stress, the material is subjected to secondary tensile stress developed at the tip of microstructural cracks (Meschke et al. 2018; Mindess et al. 2003). According to the Griffith's theory (Griffith 1924), when the stress concentration at these cracks' tip exceeds a certain threshold, crack propagation occurs which results in the creation of new crack surfaces (Popovics 1998). Consequently, the demand for energy required to create further cracked surfaces increases. This phenomenon eventually leads to a zone of tortuous micro-cracks. Cracks continue to propagate until the largest crack in the crack cluster reaches a certain critical length (Popovics 1998). Afterwards,

the rate of change of energy will be less than that stored in the system causing a rapid crack propagation. This process initiates the failure of the specimen.

Compressive stress-strain response for Hydraulic Lime Mortar, Type N mortar, and Type O mortar are shown in Figures 6.7, 6.8, and 6.9 respectively. The effect of fibre reinforcement on compressive strength of were also evaluated. From those stress-strain response, it is apparent that compressive strength decreased with the addition of fibre. The drop in peak stress was especially noticeable for mortar having a fibre content of 0.5% across all three different types.

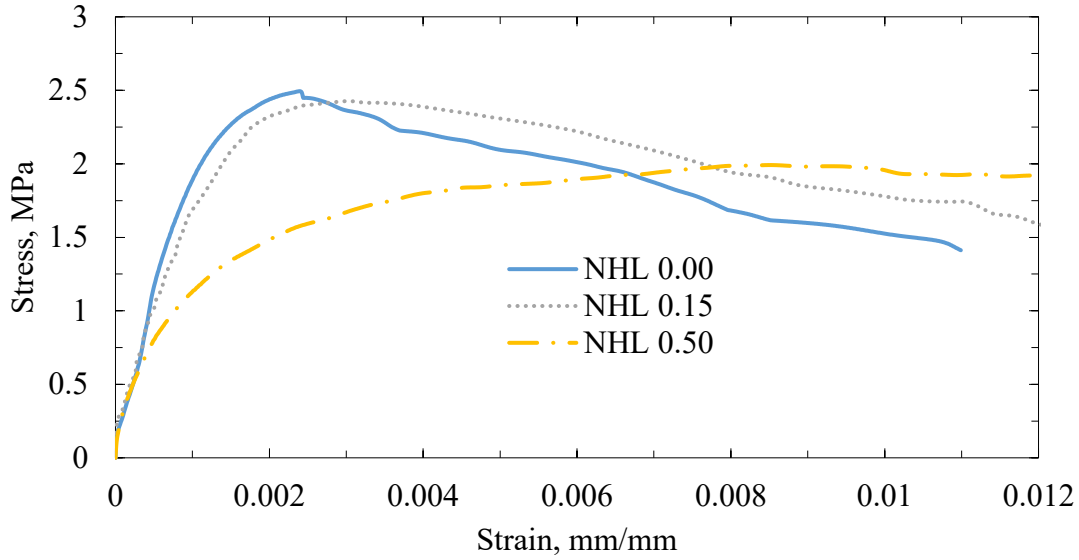

Figure 6.7 Stress-strain response of plain and fibre reinforced Hydraulic Lime Mortar

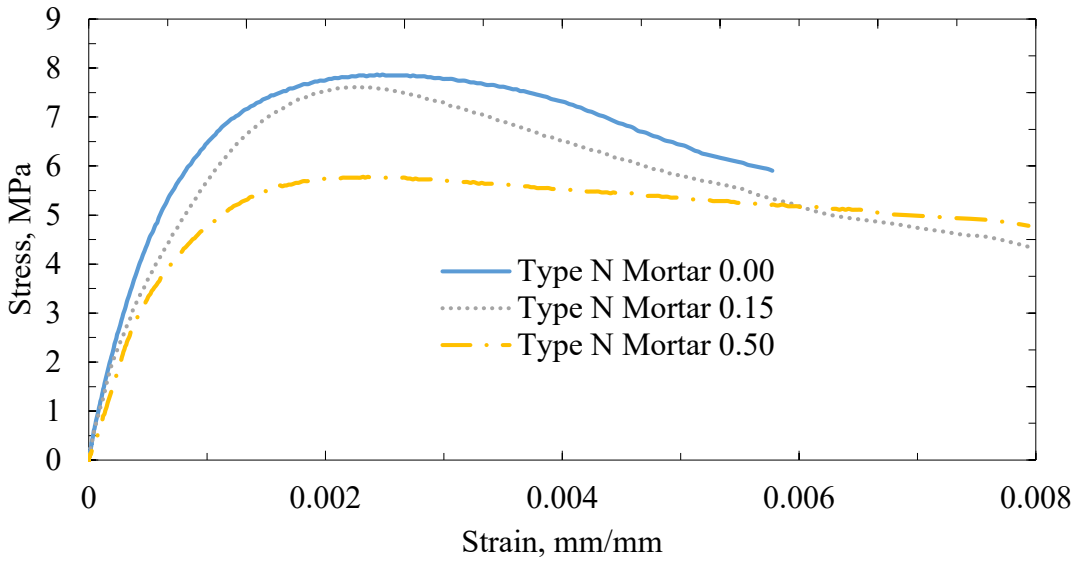

Figure 6.8 Stress-strain response of plain and fibre reinforced Type N mortar

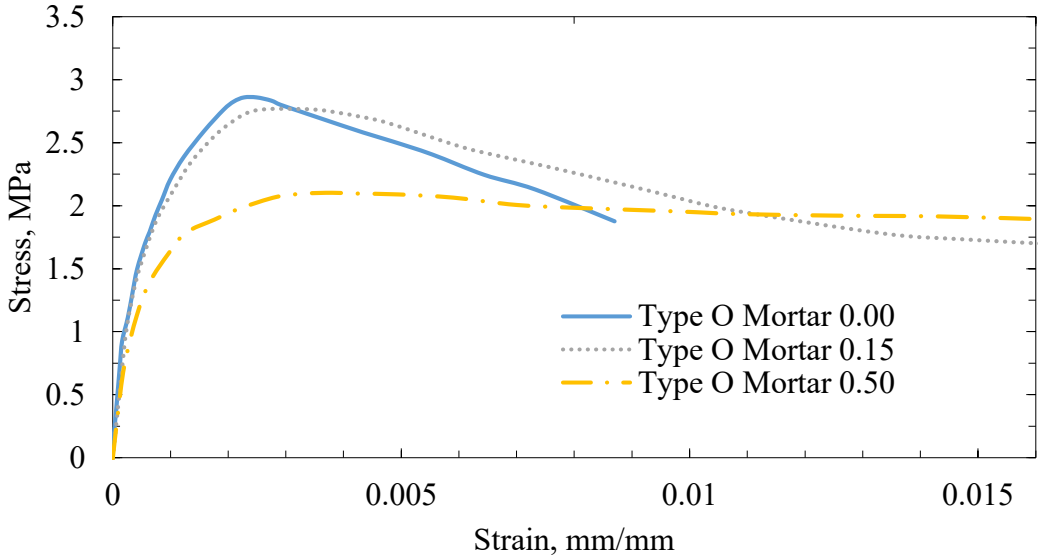

Figure 6.9 Stress-strain response of plain and fibre reinforced Type O mortar

(a)

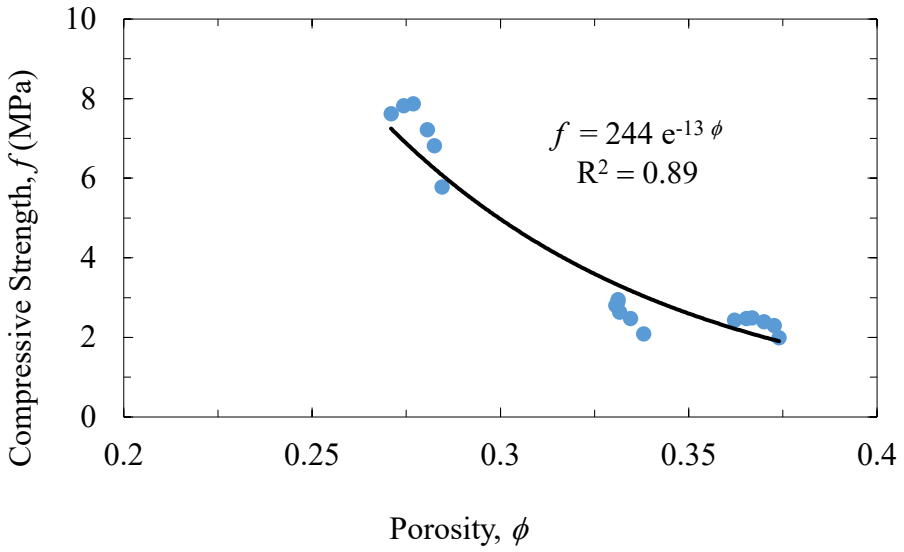

(b)

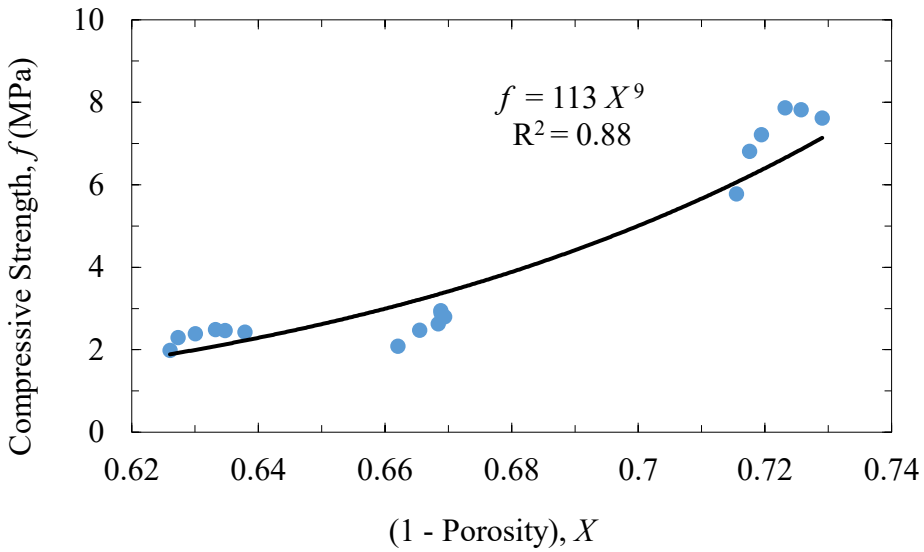

Figure 6.10 Relation between porosity and compressive strength for different plain and fibre reinforced mortars

A correlation between the mortar compressive strength and the porosity is illustrated in Figure 6.10 (a) and the corresponding correlation as a function of gel/space ratio *i.e.*, (1-porosity) is shown in Figure 6.10 (b). One will have zero strength when porosity is 100%. Although this trend is not evident in Figure 6.10 (a), but Figure 6.10 (b) clearly shows this trend by introducing parameter, X (1-porosity). Note that these porosity values were determined using a displacement-based method following the procedure of ASTM C642 (2006), as discussed in

Section 3.3.2. It can be observed that the cement-lime mortars exhibit higher compressive strength, which may be attributed to the additional strength bearing hydration products from Portland cement. Furthermore, the reduction in porosity resulted an increase in gel/space ratio, which can be expected to improve mechanical properties of the composite. Lime-based mortar generally follows the fundamental inverse relationship between strength and porosity of a solid. Since increased porosity of a heterogeneous material results a progressively weaker matrix (Mehta and Monteiro 2006), the compressive stress required for the rapid growth of interfacial as well as matrix micro-cracks—which characterizes the ultimate strength—drops considerably. It can be noticed that the compressive strength vs. gel/space ratio correlation for lime-based mortar yields an exponent of 9 which is significantly higher than that established for cement-based composites namely 3 (Mindess et al. 2003; Neville 2011).

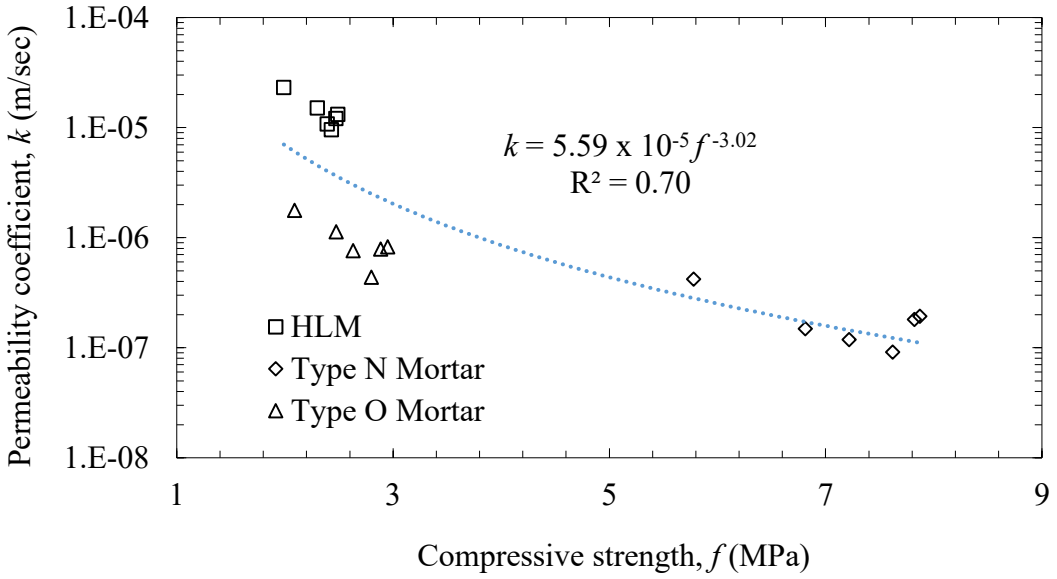

Figure 6.11 Relation between compressive strength and water permeability coefficient for different plain and fibre reinforced mortars

As discussed earlier, three different types of binder, with different amounts Portland cement as a partial replacement of lime, were used to prepare the specimens for permeability measurement. These binders led to varied microstructure having different composition of hydration products, which in turn have a direct impact on the mechanical as well as durability

characteristics. From the experimental measurement of compressive strength and permeability (Section 4.4.2), a correlation was obtained as illustrated in Figure 6.11. It is evident that the permeability drops for the mortar having a stronger matrix. This is attributed here to the presence of relatively fine hydration products such as calcium silicate hydrate (C-S-H).

6.5 Application of Nano-lime on Mortar

Understanding the flow of water through mortar and more importantly, how to control it is of great significance in many areas of its application. In this context, nano-lime application is an innovative way for better control over the water permeability of mortars. The term "nano-lime" indicates that the size of the $Ca(OH)_2$ molecules in these materials is in fact in the nano scale, so strictly speaking below 100 nm. However, the commercially obtained nano-lime for this study consists of calcium hydroxide suspended in a solution where the average diameter of the calcium hydroxide was within a range of 50 to 300 nm. Typical solvents for nano-lime could be water, or alcohol. However, water as solvent for nano-lime may not be preferable given that it may cause durability related deterioration in the material and further shrinkage cracks (Peterson 1982; Quayale 1996). The main advantage of nano-lime is that due to its small size, the particles can penetrate to a greater depth into the material, compared to the conventional calcium hydroxide, which is larger in size with on average, a diameter of 8000 nm (D'Armada and Hirst 2012). In addition, nano-lime has higher reactivity when compared to conventional lime because of higher specific surface area (kocherbitov et al. 2008) making it a superior choice of repair material for improving the durability characteristics.

Nano-lime satisfies the performance criteria for any conservation and restoration of heritage structures where it is stated that the materials used should, as far as possible, be compatible with the material being conserved and be of predictable behaviour (D'Armada and Hirst 2012). The use of nano-lime is known to improve consolidation in stonework (D'Armada and Hirst 2012). Upon treating a substrate with nano-lime, suspended calcium hydroxide is precipitated in the pores of calcareous materials as the alcohol disperse and/or evaporates. The strength and integrity of treated materials improve due to the replacement of lost binder through the

carbonation process. The carbonation of calcium hydroxide (lime) through atmospheric carbon dioxide is as follows:

$$Ca(OH)_2 + [H_2O + CO_2] = CaCO_3 + 2H_2O \quad (6.4)$$

As shown in Equation 6.4, this carbonation requires moisture in which the carbon dioxide dissolves and forms carbonic acid before engaging the lime. Note that the reaction process described in Equation 6.4 is slow. Application of nano-lime speeds up the accumulation of $CaCO_3$ (Rodriguez-Navarro et al. 2013) and the resultant products fill up the pores and eventually knit the pre-existing micro-cracks together (D'Armada and Hirst 2012). In other words, through knitting the micro-cracks together, it reduces the permeability and improves the water tightness without any undue increase in mortar strength and rigidity.

6.5.1 Materials

Natural hydraulic limes (NHL) are those hydraulic limes that are derived completely from argillaceous limestone after slaking. Hydraulic limes can be feebly, moderately, or eminently hydraulic, whereas the European Standard EN 459 (2001) classifies them by strength as listed in

Table 6.7. Natural hydraulic lime is classified as NHL2, NHL3.5, and NHL5 with compressive strengths of 2 MPa, 3.5 MPa, and 5 MPa, respectively (Maurenbrecher et al. 2007). The physical properties of hydraulic lime are described in Table 6.8, and the chemical composition of NHL2 is addressed in Table 6.9. Nano-lime that was used in this study was purchased from Germany. It was a commercially sourced nano-lime product named CaLoSiL® E 25. The producer of this nano-lime is IBZ-Salzchemie GmbH & Co., KG, Germany. The nano-lime suspension used in this study is shown in Figure 6.12 and the nano-scale structure of the material, determined using SEM, is shown Figure 6.13. Note that CaLoSiL® E 25 has a nano-lime concentration of 25 grams per one litre of ethanol solution. Other aspects of CaLoSiL® nano-products can be found in the literature (Ziegenbalg et al. 2010).

Table 6.7 Compressive Strength of Hydraulic Limes

Type of hydraulic lime	Compressive strength (MPa)	
	7 day	28 day
HL 2	-	1.5-10
HL 3.5	≥ 1.5	2.7-14
HL 5	≥ 2	4.0-20

Table 6.8 Physical Properties of Hydraulic Limes (EN 459-2 2001)

Type of hydraulic lime	Bulk density	Fineness (%)		Sound-ness	Free water content	Penetration	Air content	Setting time
	(kg/m^3)	0.09 mm	0.2 mm	(mm)	(%)	(mm)	(%)	(hour)
HL 2	400 - 800	≤ 15	≤ 5	≤ 20	≤ 2	20 and < 50	≤ 20	1 and ≤ 15
HL 3.5	400 - 800							
HL 5	400 - 800				≤ 1			

Table 6.9 Chemical Composition of NHL2 (percentages related to original dry lime) (Lanas et al. 2004)

Compound	CaO	LOI	SiO_2	MgO	Al_2O_3	SO_3	K_2O	Fe_2O_3	Na_2O
% by mass	54.26	15	12.57	7.65	5.42	2.13	1.35	1.16	0.34

Figure 6.12 Nano-lime suspension, placed in a glass jar, that was used in this study

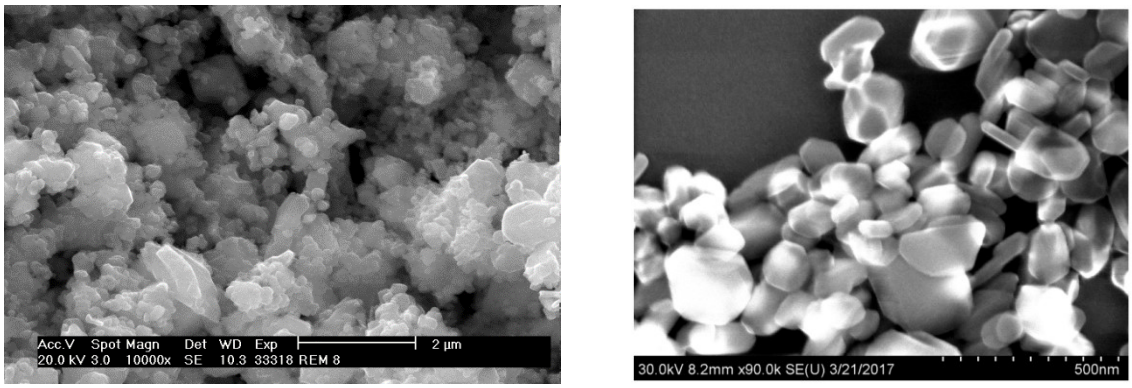

Figure 6.13 (a – left) SEM of nano-lime suspension used in this study (Source: supplier) (b – right) SEM of nano-lime suspension that was used in this study (Taken at University of Alberta)

6.5.2 Sample Preparation and Nano-lime Application

Upon preparation of base hollow cylindrical specimens, nano-lime was applied as described below. Details of material properties, mixer proportions, specimen preparation is described in Section 3.3.1.

As in earlier cases, the water permeability of the mortar was evaluated using hollow-cylindrical specimens. These were cast with an outside diameter of 100 mm, an inside diameter of 50 mm, and a height of 200 mm. The hollow core was created using a solid shaft of Teflon inserted at the time of casting. The cylinders were cured in their moulds for a sufficient amount of time to ensure adequate strength development that was enough to withstand the removal of the Teflon shaft. With HLM specimens, this period lasted 30 days. The Teflon shaft was removed using an extrusion jack. For each mix, at least three specimens were chosen for further testing. For Hydraulic Lime Mortar, the specimens were demoulded after 7 days of curing at ambient condition (18-24 ºC and 30-50% relative humidity) followed by an additional ambient curing for180 days before conducting the permeability experiments.

Figure 6.14 Hollow Cylinders Supported in a Wooden Cage

In order to evaluate the effect of nano-lime on mortars, specimens without nano-lime were first tested for water permeability. Companion series of specimens were prepared which were subsequently surface treated with nano-lime. In order to apply the nano-lime, the demolded hollow cylindrical samples were supported in a wooden case as shown in Figure 6.14 and the nano-lime was applied in layers onto the specimens' surface. Based on prior studies with nano-lime, three regimes were chosen – Using a spray-bottle, the nano-lime was applied for 10 layers in the first regime, 40 layers in the second, and 100 layers in the third regime. Subsequently, the hollow cylinders were left to cure in ambient conditions for a further 90 days. At that point,

the surface treated hollow-cylinders were tested in the permeability cell. A typical cast sample, before and after demolding is shown in Figure 6.15.

(a) (b)

Figure 6.15 (a) Preparation of hollow cylindrical specimen, (b) Extracted cylinder to be used for permeability tests Extracted cylinder to be used for permeability tests

6.5.3 Results and Discussion

After reaching a steady state, fluid flow measurements were taken for the calculation of permeability coefficients and the results are shown in Figure 6.16. It is worthwhile to recall from a prior study that in case of Portland cement mortar, the water permeability drops consistently with an increase in the fibre dosage (Hoseini 2013). However, it appears that the effect of fibre reinforcement in Hydraulic Lime Mortar is somewhat different. An optimum fibre dosage is reached at a much smaller fibre dosage than seen for Portland cement systems. A similar outcome was reported by Izaguirre et al. (2011) who studied the permeability

characteristics of fibre reinforced aerial lime. In the present study, the optimum fibre dosage was found to be 0.15% (by volume) beyond which the water permeability registered an increase.

Applying nano-lime was found to benefit Hydraulic Lime Mortar, in that it consistently reduced the water permeability. As shown in Figure 6.16, there was a drop with only 10 layers of nano-lime, and this reduction was significant at 40 layers of nano-lime. As stated earlier at the outset of Section 6.5, this drop in the observed permeability may be attributed to the smaller particle size of nano-lime that has the advantage of achieving greater penetration into the pores as well as react better with atmospheric CO_2 (Musacchi 2014). It thus creates a barrier layer upon calcite formation. Note that when a substrate is treated with nano-lime, the calcium hydroxide is precipitated in the pores of calcareous materials as the solvent (in this case, a volatile alcohol) evaporates. With time, the calcium hydroxide converts into calcium carbonate and it replaces the lost binder or matrix in natural stone and plasters, thereby knitting together fine cracks and deteriorated stone, increasing the strength and integrity. Figure 6.21 shows also that there was no perceptive lowering in the water permeability beyond 40 layers of nano-lime, as at 100 layers of spray. It implies that there is an optimal amount of nano-lime, beyond which there is little further penetration. Instead, the additional nano-lime merely formed a thicker coating at the surface. This, despite the fact that the surface that was coated with the nano-lime was also the surface with which the mortar specimen first comes into contact with water. These observations were inferred from SEM micrographs shown in Figures 6.18 and 6.19 that clearly illustrate the effect of nano-lime. Notice from Figure 6.20, which shows a magnified view, that applying nano-lime beyond 40 layers resulted in thicker layer of deposit on the surface. The portion of the specimens seen here were further examined using XRD and XRF. The subsequent analysis of these aforementioned deposits is shown in Figures 6.21 and Table 6.10. It is clear that these deposits are primarily various polymorphs of calcium carbonate, which result from the carbonation of the applied nano-lime. Preliminary XRD scan showed no definitive trend of the effect of nano-lime on the amount of $CaCO_3$ formed through carbonation. The reasons for this apparent discrepancy are: (1) difficulty encountered during sample extraction given the fact that the thickness of the applied nano-lime layer is less than

one mm; (2) Significantly high statistical variation. Note here that applying nano-lime reduces the water permeability at all dosages of polypropylene fibres. Thus, the present findings indicate that the most efficient strategy to reduce permeability in repair mortar is to include an optimum amount of polypropylene fibres, followed by repeated application of an optimum amount of nano-lime. The optimum fibre content variation with the number of nano-lime layer are shown in Figure 6.17. It can be observed that the optimum fibre content shifts towards lower fibre dosage with the increase in the number of nano-lime layers.

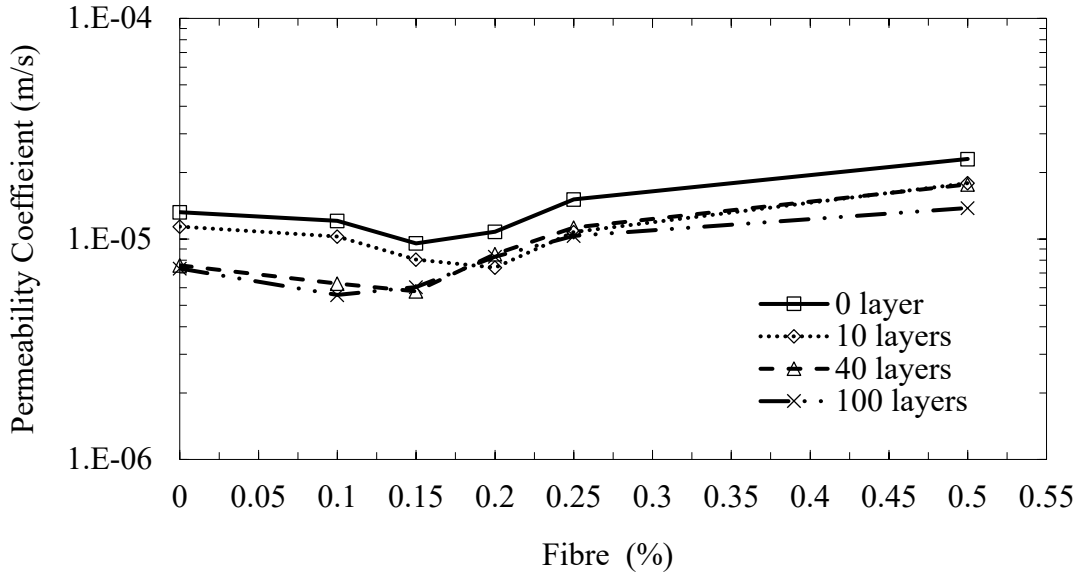

Figure 6.16 Nano-lime application on Hydraulic Lime Mortar with fibre variation

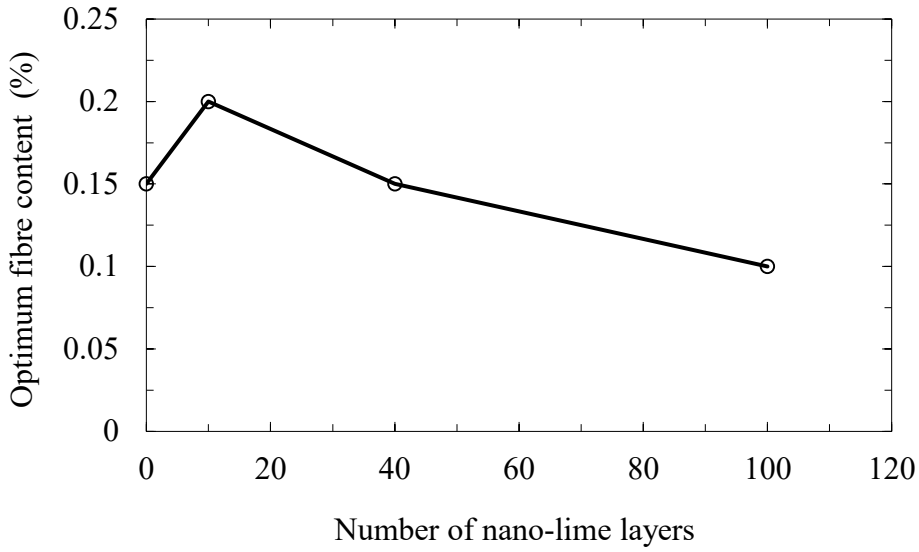

Figure 6.17 Variation of optimum fibre content with the number of nano-lime layer

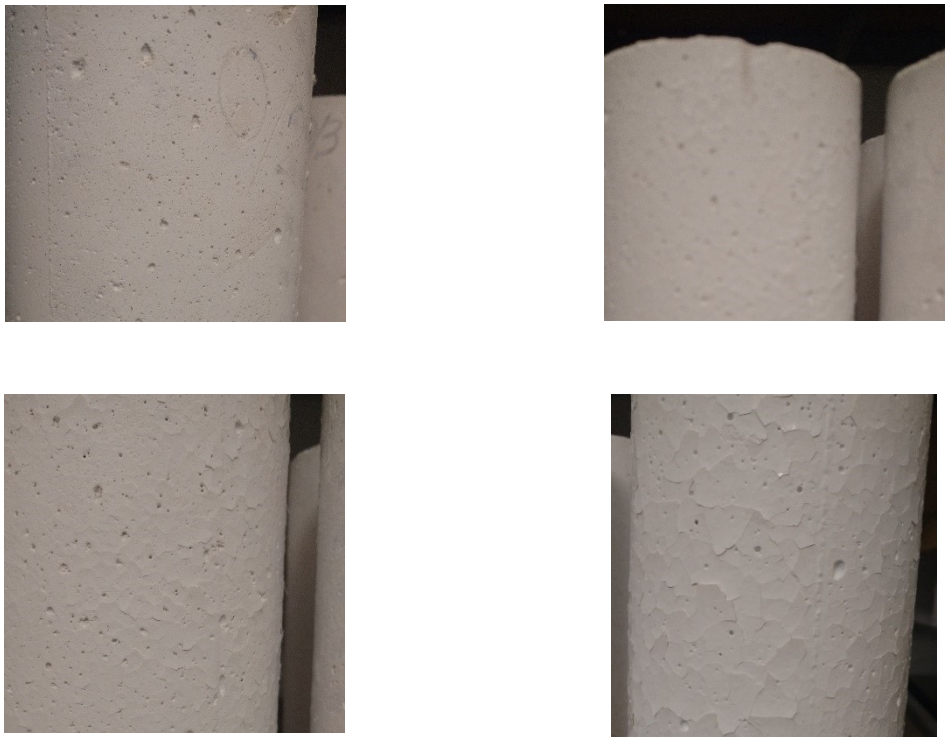

Figure 6.18 Surface deposition of nano-lime after application on outer surface of hollow cylinders casted with Hydraulic Lime Mortar (a – top left) specimen with 0 layers of nano-lime application (b – top right) specimen with 10 layers of nano-lime application (c – bottom left) specimen with 40 layers of nano-lime application (d – bottom right) specimen with 100 layers of nano-lime application

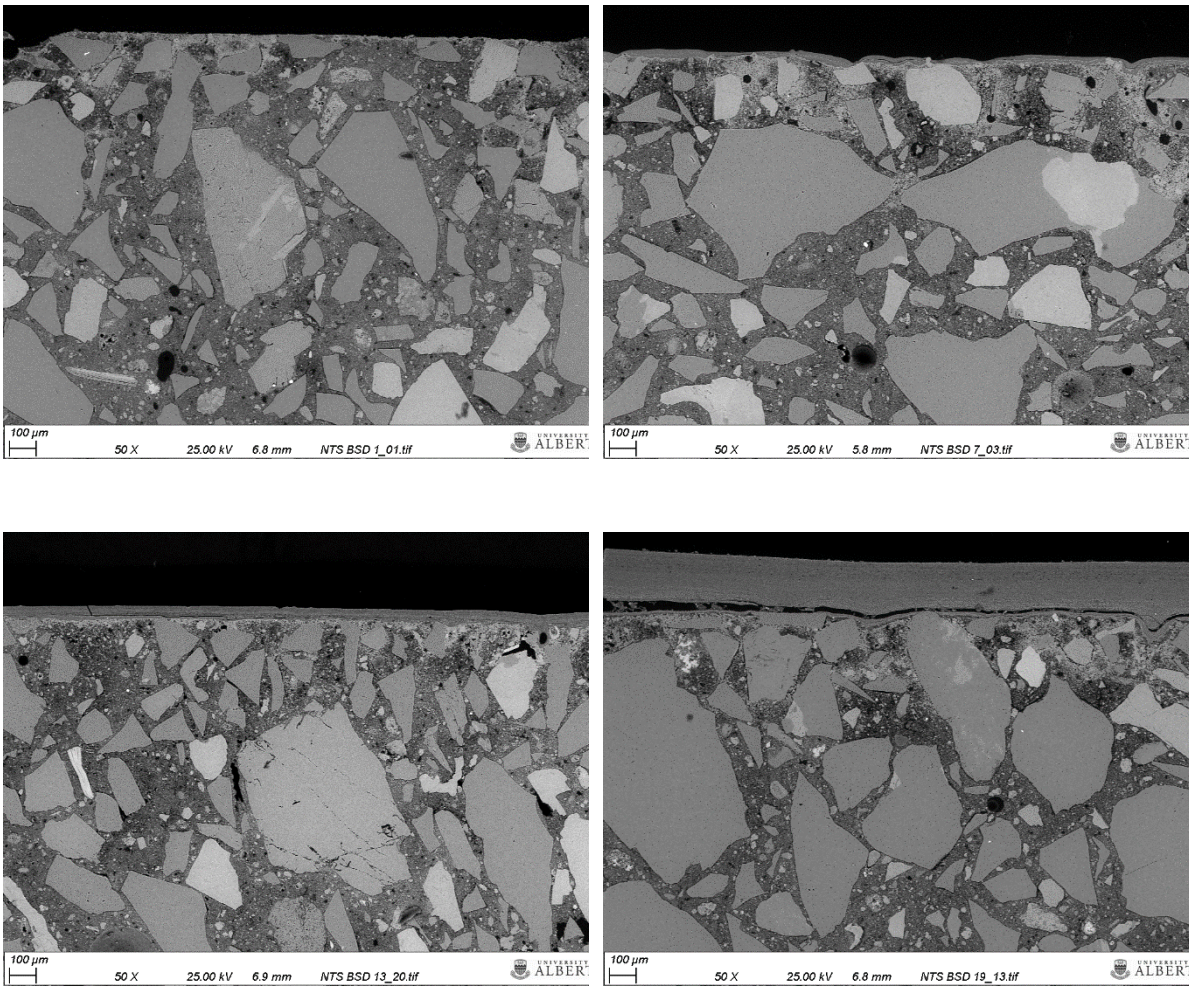

Figure 6.19 nano-lime intrusion and surface deposition of nano-lime after application on outer surface of hollow cylinders casted with Hydraulic Lime Mortar, as seen by SEM (a – top left) specimen with 0 layers of nano-lime application (b – top right) specimen with 10 layers of nano-lime application (c – bottom left) specimen with 40 layers of nano-lime application (d – bottom right) specimen with 100 layers of nano-lime application

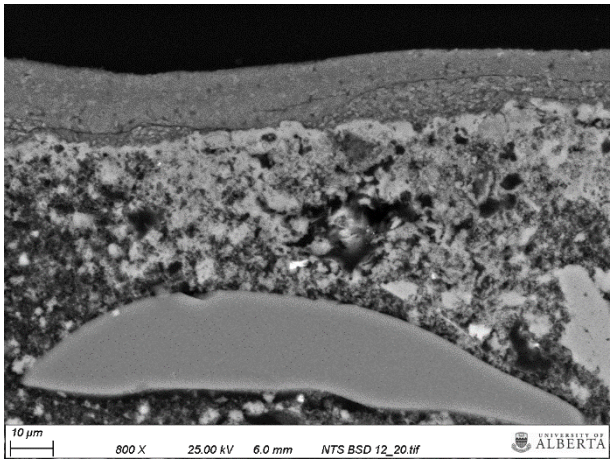

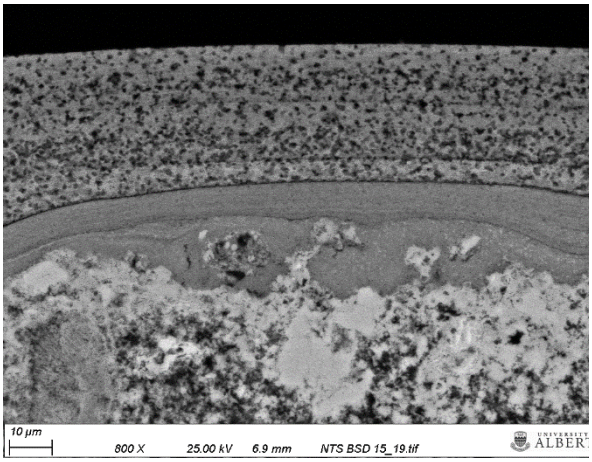

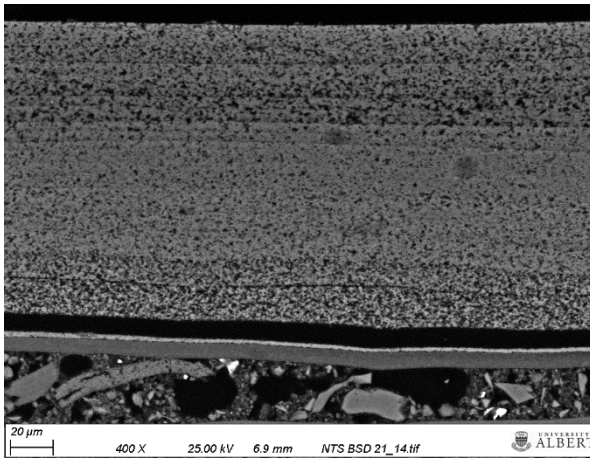

Figure 6.20 Surface deposition of nano-lime after application on outer surface of hollow cylinders casted with Hydraulic Lime Mortar, as seen by SEM (a – top) specimen with 10 layers of nano-lime application (c – bottom left) specimen with 40 layers of nano-lime application (d – bottom right) specimen with 100 layers of nano-lime application

Table 6.10 Oxide composition of deposition on hollow cylinder specimen after nano-lime application

Compound	Y_2O_3	CaO	SrO
% by mass	3.16	96.72	0.13

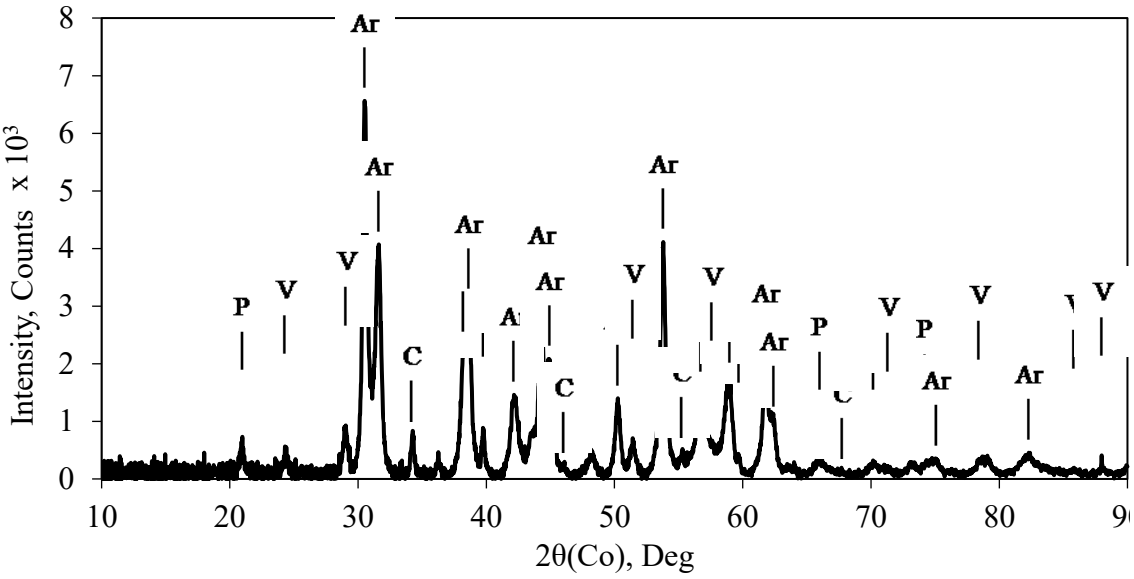

Figure 6.21 X-ray Diffraction (XRD) for deposition on hollow cylinder specimen after nano-lime application; Note: C ≡ Calcite; Ar ≡ Aragonite; V ≡ Vaterite; P ≡ Portlandite

6.6 Conclusion

Based on the outcome reported in this chapter, the following concluding remarks can be made:

- While there exists an optimal fibre content to achieve minimum water permeability, this dosage shifts to a lower value upon applying nano-lime.
- A combination of SEM, XRD and XRF reveals a build up of $CaCO_3$ at the surface of the mortar substrate. These polymorphs of $CaCO_3$ may be attributed to the carbonation of the nano-lime.
- Application of nano-lime causes a drop-in permeability for Hydraulic Lime Mortar. The optimum amount of nano-lime can be achieved by spraying the specimen for no more than 40 times.

CHAPTER 7. CONCLUSIONS AND RECOMMENDATIONS

7.1 Summary of Conclusions

In the current study, efforts have been made to evaluate and identify several microstructural features of cement-lime mortar and Hydraulic Lime Mortar. The influence of polymeric fibres on microstructural properties of mortars is also determined. It is repeatedly made clear from the present findings that there is an optimum level of fibre dosage in repair mortars, which was 0.15% by volume. Apart from that, the water permeability of plain and fibre reinforced Hydraulic Lime Mortar, Type N mortar, and Type O mortar are determined thorough laboratory experimental procedure. In addition, water permeability of these mortars is predicted by utilizing existing analytical methods such as the two-point correlation method, the Katz-Thompson model, and the fractal model. In order to understand the physics of fluid flow and transport processes through porous media such as concrete and Hydraulic Lime Mortar, one must have a detailed knowledge about the pore space geometry and their arrangement in three-dimensional space. Transport properties such as permeability depends on the porosity. In addition, the size, shape, and connectivity of the porous path strongly influence the transport properties. It is well known that microstructure of porous media is very complex in nature. Fluid passes through this porous media taking a path that is very tortuous rather than a simple straight path. Here, an image-based technique called X-ray micro computed tomography was utilized to investigate the 3D microstructure of materials under investigation. Several important parameters associated with water permeability such as quantification of porosity and pore connectivity, specific surface area, fractal number, tortuosity was measured by using X-ray micro CT method. Also, transport properties obtained by using X-ray micro CT data are compared with the results of conventional laboratory experiments. Finally, morphological characteristics of the mortars used in this study was studied through XRD and XRF analysis, the compressive response of the plain and fibre reinforced mortars and its correlation with permeability was evaluated, and the effects of nano-lime application on the permeability of NHL mortar was determined. The key findings of this thesis can be summarized as follows:

- The microstructure of mortars under investigation underwent change due to fibre addition. Porosity decreases with the fibre addition up to a volume fraction of 0.15% fibre. Beyond that level, it increases with a higher dosage fibre. At low dosage (0.15%), addition of fibre results a refinement in pores where a fraction of the larger pores transforms into smaller ones. In contrast, fibre reinforcement at high dosage causes a pore size coarsening.
- MIP underestimates the macro pores for all three types of mortar, which is evident from the comparison of pore size distribution obtained through MIP method and image analysis.
- From two-point correlation function, the monotonic nature of the asymptotic region is visible in the range of large R values implying the interconnected nature of pores in the mortar.
- The specific surface area of all three types of mortar varies with fibre addition and the variation is almost identical for all mortar types. With the addition of low fibre dosage (up to 0.15% by volume), the specific surface area decreases whereas it increases with the addition of higher dosage of fibre.
- The fractal dimension changes in a similar pattern across all types of mortar and methods of evaluation. It decreases with the addition of fibre up to a dosage of 0.15% by volume.
- Water permeability is influenced significantly by the addition of polypropylene micro-fibres. This variation occurs in an identical manner for all three types of mortars. It was discovered that an optimum fibre dosage exists, beyond which water permeability registers an increase. This optimum fibre dosage is 0.15% (by volume) and is applicable for all three types of mortar.
- At low fibre dosage, the reduction in permeability coefficients is noticeable and this coefficient increases with further fibre addition. Due to pore size refinement, a more tortuous flow path, and the reduction in pore connectivity at low fibre dosage are the main influencing factors for the observed reduction in water permeability. On the other hand, higher fibre dosage opens up to hitherto non-existent pores of a larger size. This causes an increase in pore connectivity, thus making the flow path less tortuous, which in turn causes an increase in water permeability.

- Permeability as predicted by the two-point correlation function is largely in good agreement with the experimental values across all three types of mortar. In addition, predicted permeability values from SEM images, with 50x magnification, show smaller deviation from experimental permeability coefficients when compared with that from images having a magnification of 400x. Therefore, 50x would be the recommended magnification for predicting permeability of similar types of materials using image-based approach.
- The predicted permeability coefficients by Katz-Thompson model do not agree satisfactorily with experimental values for both plain and fibre reinforced mortars of all types. This disagreement may be attributed to the inability of MIP method to identify the realistic pore size distribution of cementitious materials.
- The employed fractal model is not capable of predicting the permeability coefficients of plain and fibre reinforced mortars. The possible reason behind the apparent disagreement may be the absence of some critical parameters reflecting the pore tortuosity as well as connectivity effects. Further, the fractal model is unable to distinguish between mortars with different porosity having identical maximum pore size.
- For X-ray micro CT analysis, mortar with 0.15% fibre has the lowest amount of total segmented porosity compared to the plain mortar and the total porosity increases with further addition of fibre. In addition, the effective porosity and pore connectivity are the lowest for mortar with 0.15% fibre, whereas a higher dosage of fibre led to a reversal in trend. As well, the specific surface area decreases slightly with the addition of fibre up to 0.15% compared to the plain mix, whereas the values increase as more fibres are added.
- The tortuosity and formation factor values increase at low fibre dosage, up to 0.15% volume fraction, compared to plain mix and then decrease when fibre dosage is increased to 0.5%. On the other hand, the fractal dimension in three dimensions for plain and fibre reinforced mortars decreases with low fibre dosages (up to 0.15% by volume) in comparison to plain mortar and increases with more fibre addition.

- The predicted permeability coefficients of plain and fibre reinforced Hydraulic Lime Mortar; Type N mortar and Type O mortar by this X-ray micro CT method are in good agreement with experimental values.
- The partial replacement of lime with Portland cement increases the compressive strength and thus helps reduce the permeability of the mortar.
- Application of nano-lime causes a drop-in permeability for Hydraulic Lime Mortar. The optimum amount of nano-lime can be achieved by spraying the specimen for no more than 40 times.

7.2 Concluding Remarks

The primary objective of this study is to determine the water permeability of Hydraulic Lime Mortar, Type N mortar, and Type O mortar and find out the effects of fibre on that hydraulic property. Understanding the complex microstructure of cementitious materials is clearly necessary in order to better understand and develop a sound scientific basis for this type fluid flow. For this purpose, relevant microstructure characteristics is evaluated with the help of state-of-art method. An important step in developing this knowledge is to understand how rates of transport, characterized by values of transport coefficients such as permeability, depend on the details of the porous microstructure. A considerable amount of this knowledge generated in this research was the outcome of extensive analysis of digital images. The fair and reasonable results of any image analysis depend on some important factors including sampling process, sample extraction and preparation technique, and selection of the regions for microscopic examination. The microstructure parameters measured by SEM method depends on resolution of the image especially when they are taken by detecting the backscattered electrons rather than the secondary electrons. Further, the minimum diameter of the pores that can be detected is restricted by the maximum resolution of images. Hence, contribution of pores with a diameter smaller than the minimum resolved value is not included when analysing using SEM. In addition, it is noticeable that any image-processing algorithm may affect the results. Hence, consideration attention must be given to use consistency throughout the image capture and image analysis process.

MIP is capable of detecting a larger range of pore diameter. It, however, does not include the pores smaller than 3 nm. Besides, the MIP method is unable to include the fraction of pores contributed by the entrapped air-voids, which are relatively larger than MIP's maximum detectable size. It is important to keep in mind that both MIP and ASTM methods are unable to include the pores impermeable to mercury and water respectively.

Like other techniques, X-ray micro CT also has some inherent weakness, which much be borne in mind while using this method for microstructural analysis and evaluation of water permeability. In order to evaluate the pore structure parameter, images reconstructed from X-ray micro CT raw images need some pre-processing like cropping, adjustment of brightness and contrast, filter and binary conversion. One needs to maintain consistency while doing those processes. Several corrections including beam hardening and ring artifacts must be conducted with a trial and error to get the best quality of image output. In addition, microstructural parameters resolved by X-ray micro CT are dependent upon chosen resolution.

Permeability measurement in the laboratory often require expensive equipment and extensive amount of time. It is customary to utilize Darcy's law to determine the coefficient of water permeability in laboratory test method, assuming a steady-state unidirectional laminar flow. L Note that laboratory determination provides a direct and accurate estimation of permeability coefficient. It is also generally assumed that the material is microscopically homogeneous while evaluating permeability through laboratory experiments without compromising the accuracy of the experimental results. It is important to point out that any experimental outcomes must include the associated statistical variation of the measured properties. As laboratory permeability evaluation is often time consuming and cost prohibitive, evaluation of permeability properties through existing analytical models would be beneficial. Analytical models for permeability prediction of cementitious materials can be used which are based on microstructural properties of the material. Several parameters need to be considered when modelling properties of heterogeneous porous materials. Most of the predictive models are based on certain assumptions and many of those methods were either developed empirically or semi-empirically based on experimental outcomes. Therefore, when employing a predictive

model, it is important to justify the underlying assumptions of that particular model to estimate the permeability of porous materials such as cementitious systems.

7.3 Applications

In this thesis, a vital durability related aspect of repair mortar namely permeability was experimentally investigated. Polypropylene micro-fibre was incorporated, with different volume fraction, to evaluate its effect on the permeability. In addition, the influence of nano-lime on the permeability was studied.

The outcome of this thesis is expected to have application as described below:

- Superior quality implies enhanced durability of a material, which helps prevent ingress of deleterious agents into the material. Therefore, designing durable masonry requires low permeability mortar. To this end, the results obtained in this research work can be used as a guideline to develop optimum mixture proportion for different construction practice. It should be noted that the "optimum mixture design" refers to the determination of the proportions of various ingredients of repair mortar for the purpose of laboratory investigations, which should be modified further for field application using the guidelines of appropriate standards such as CSA A179 (2014).
- The findings of this study is also expected to assist in the repair of masonry buildings and dams.
- Utilization of nanomaterials in building construction is at the forefront of modern innovation. The information generated in this thesis regarding the effectiveness of nano-lime in improving the permeability will find its application in the development of durable building materials.
- When using the mixture designed in this study towards dam rehabilitation, the actual intended application would be on the upstream side of a dam.

7.4 Recommendations for Future Studies

An attempt is made here to systematically quantify the microstructural network and relate that to permeability in three distinct repair mortars namely, Hydraulic Lime Mortar, Type N mortar

and Type O mortar. As well, recent innovations in nanomaterials and micro-fibres are shown to effectively reduce the water permeability in such systems. Based on the findings of this research, the following recommendations are outlined here for further investigation:

- Current study was performed on plain and fibre reinforced mortars without any stressed condition while determining water permeability. It will enrich our knowledge further if the effect of stress on water permeability can be determined. Loading at different increments is also recommended for future studies. Although one may need sophisticated equipment with high sensitivity to enable such tests on low strength mortar.
- The current study was conducted to evaluate fibre effects on water permeability where polypropylene micro fibre was used. The effect of similar types of fibre such as polyester fibre on water permeability can be conducted with these types of mortars.
- In the current study, effects of fibre on porosity and other parameters were evaluated in meso scale by using nitrogen adsorption method. Cryoporometry can be used to gather more details about the influence of fibre on porosity and pore size distribution of those mortars.
- Permeability prediction was done by using a 2-D fractal-based model. It is recommended to develop an analytical model based on 2-D fractal parameters whereby parameters such as tortuosity and other relevant characteristic features which influence the water permeability, should be included. In addition, fractal geometry-based 3-D modeling may offer more accurate prediction of water permeability.
- X-ray micro CT is a convenient technique to evaluate microstructure features in three-dimension without physically destroying the sample. Nano-tomography may allow a more detailed mapping of the mortars in greater depth.
- Other non-destructive techniques such as ultrasonic pulse velocity method can be used to predict water permeability and develop a correlation with damage.
- The performance of this mortar and fibre effects can be examined in field conditions such as for a masonry wall system.
- Developing a finite element model for these types of mortars may be helpful to gather more detailed knowledge about their water permeability.

REFERENCES

Abell, A. B., Willis, K. L., and Lange, D. A. (1999). "Mercury intrusion porosimetry and image analysis of cement-based materials." *Journal of colloid and interface science*, 211(1), 39–44.

ACI 544.R1. (1996). "Report on fibre reinforced concrete." *Committee 544, American Concrete Institute, Farmington Hills, MI*, 66.

Ahmed, T. (2006). *Reservoir engineering handbook*. Gulf Professional Publishing.

Akhavan, A., Shafaatian, S.-M.-H., and Rajabipour, F. (2012). "Quantifying the effects of crack width, tortuosity, and roughness on water permeability of cracked mortars." *Cement and Concrete Research*, 42(2), 313–320.

Alexander, M., Bentur, A., Mindess, S., Bentur, A., and Mindess, S. (2017). *Durability of Concrete : Design and Construction*. CRC Press.

Aligizaki, K. (2005). *Pore Structure of Cement-Based Materials: Testing, Interpretation and Requirements*. Modern Concrete Technology, CRC Press.

Allen, T. (2013). *Particle size measurement*. Springer.

Archie, G. E. (1942). "The Electrical Resistivity Log as an Aid in Determining Some Reservoir Characteristics." *Transactions of the AIME*, 146(01), 54–62.

Armwood, C., Sorensen, A., Skourup, B., and Erdogmus, E. (2008). "Fiber reinforced mortar mixtures for the reconstruction and rehabilitation of existing masonry structures." *AEI 2008: Building Integration Solutions*, 1–10.

ASTM C 469. (2001). "Standard test method for Static Modulus of Elasticity and Poisson's Ratio of Concrete in compression." *ASTM International, West Conshohochen, PA*.

ASTM C457. (2012). "Standard Test Method for Microscopical Determination of Parameters of the Air-Void System in Hardened Concrete." *ASTM International, West Conshohochen, PA*.

ASTM C642. (2006). "Standard Test Method for Density, Absorption, and Voids in Hardened Concrete." *ASTM International, West Conshohochen, PA*.

ASTM C1437. (2007). "Standard test method for flow of hydrauluic cement mortar." *ASTM International, West Conshohochen, PA*.

Atzeni, C., Pia, G., and Sanna, U. (2010). "A geometrical fractal model for the porosity and permeability of hydraulic cement pastes." *Construction and Building Materials*, 24(10), 1843–1847.

Awoyera, P. O., Akinmusuru, J. O., Dawson, A. R., Ndambuki, J. M., and Thom, N. H. (2018). "Microstructural characteristics, porosity and strength development in ceramic-laterized concrete." *Cement and Concrete Composites*, 86, 224–237.

Balaguru, P., and Ramakrishnan, V. (1988). "Properties of Fiber Reinforced Concrete: Workability, Behavior Under Long-Term Loading, and Air-Void Characteristics." *ACI Materials Journal*, 85(3), 189–196.

Banthia, N., and Bhargava, A. (2007). "Permeability of Stressed Concrete and fiberreinforcement."

Banthia, N., Biparva, A., and Mindess, S. (2005). "Permeability of concrete under stress." *Cement and Concrete Research*, 35(9), 1651–1655.

Banthia, N., Sappakittipakorn, M., and Jiang, Z. (2012). "On permeable porosity in bio-inspired fibre reinforced cementitious composites." *International Journal of Sustainable Materials and Structural Systems*, 1(1), 29–41.

Barrett, E. P., Joyner, L. G., and Halenda, P. P. (1951). "The determination of pore volume and area distributions in porous substances. I. Computations from nitrogen isotherms." *Journal of the American Chemical society*, 73(1), 373–380.

Bear, J. (1972). *Dynamics of fluids in porous media*. Courier Corporation.

Bentur, A., and Alexander, M. G. (2000). "A review of the work of the RILEM TC 159-ETC: Engineering of the interfacial transition zone in cementitious composites." *Materials and structures*, 33(2), 82–87.

Bentur, A., and Mindess, S. (2007). *Fibre reinforced cementitious composites*. Modern concrete technology series, Taylor & Francis, London ; New York.

Bentz, D. P., and Martys, N. S. (2007). *A stokes permeability solver for three-dimensional porous media*. US Department of Commerce, Technology Administration, National Institute of Standards and Technology.

Bentz, D. P., Martys, N. S., Stutzman, P., Levenson, M. S., Garboczi, E. J., Dunsmuir, J., and Schwartz, L. M. (1994). "X-ray microtomography of an ASTM C109 mortar exposed to sulfate attack." *MRS Online Proceedings Library Archive*, 370.

Bentz, D. P., Quenard, D. A., Kunzel, H. M., Baruchel, J., Peyrin, F., Martys, N. S., and Garboczi, E. J. (2000). "Microstructure and transport properties of porous building materials. II: Three-dimensional X-ray tomographic studies." *Materials and Structures*, 33(3), 147–153.

Berg, C. F. (2014). "Permeability description by characteristic length, tortuosity, constriction and porosity." *Transport in porous media*, 103(3), 381–400.

Bernard, O., Ulm, F.-J., and Lemarchand, E. (2003). "A multiscale micromechanics-hydration model for the early-age elastic properties of cement-based materials." *Cement and Concrete Research*, 33(9), 1293–1309.

Berryman, J. G. (1985). "Measurement of spatial correlation functions using image processing techniques." *Journal of Applied Physics*, 57(7), 2374–2384.

Berryman, J. G. (1987). "Relationship between specific surface area and spatial correlation functions for anisotropic porous media." *Journal of mathematical physics*, 28(1), 244–245.

Berryman, J. G., and Blair, S. C. (1986). "Use of digital image analysis to estimate fluid permeability of porous materials: Application of two-point correlation functions." *Journal of Applied Physics*, 60(6), 1930–1938.

Berryman, J. G., and Blair, S. C. (1987). "Kozeny–Carman relations and image processing methods for estimating Darcy's constant." *Journal of Applied Physics*, 62(6), 2221–2228.

Bharatkumar, B. H., and Shah, S. P. (2004). "Impact resistance of hybrid fiber reinforced mortar." *K. Kovler K, Marchand J, Mindess S, Weiss J, editors. International RILEM symposium on concrete science and engineering: a tribute to Arnon Bentur, Evanston, IL*.

Bhargava, A. (2006). "Permeability of Fiber Reinforced Concrete under Stress." University of British Columbia.

Bhargava, A., and Banthia, N. (2008). “Permeability of concrete with fiber reinforcement and service life predictions.” *Materials and Structures*, 41(2), 363–372.

Bindiganavile, V., and Banthia, N. (2001). “Polymer and steel fiber-reinforced cementitious composites under impact loading—part 1: bond-slip response.” *Materials Journal*, 98(1), 10–16.

Bindiganavile, V., Mamun, M., Dashtestani, B., and Banthia, N. (2017). “Correlating the Permeability of Mortar under Compression with Connected Porosity and Tortuosity.” *Magazine of Concrete Research*, 1–19.

Biparva, A. (2005). “Permeability and durability of high volume fly ash concrete under an applied compressive stress.” Master’s Thesis, University of British Columbia.

Blair, S. C., Berge, P. A., and Berryman, J. G. (1993). *Two-point correlation functions to characterize microgeometry and estimate permeabilities of synthetic and natural sandstones*. Lawrence Livermore National Lab., CA (United States).

Blair, S. C., Berge, P. A., and Berryman, J. G. (1996). “Using two-point correlation functions to characterize microgeometry and estimate permeabilities of sandstones and porous glass.” *Journal of Geophysical Research: Solid Earth*, 101(B9), 20359–20375.

de Boer, J. H., Lippens, B. C., Linsen, B. G., Broekhoff, J. C. P., van den Heuvel, A., and Osinga, T. J. (1966). “Thet-curve of multimolecular N2-adsorption.” *Journal of Colloid and Interface Science*, 21(4), 405–414.

Bourdette, B., Ringot, E., and Ollivier, J. P. (1995). “Modelling of the transition zone porosity.” *Cement and concrete research*, 25(4), 741–751.

Brun, M., Lallemand, A., Quinson, J.-F., and Eyraud, C. (1977). “A new method for the simultaneous determination of the size and shape of pores: the thermoporometry.” *Thermochimica acta*, 21(1), 59–88.

Brunauer, S., Emmett, P. H., and Teller, E. (1938). “Adsorption of gases in multimolecular layers.” *Journal of the American chemical society*, 60(2), 309–319.

Carpinteri, A., and Ingraffea, A. R. (Eds.). (1984). *Fracture mechanics of concrete: Material characterization and testing: Material Characterization and Testing*. Engineering Applications of Fracture Mechanics, Springer Netherlands.

Castano, V. M., Martinez, G., Aleman, J. L., and Jimenez, A. (1990). “Fractal structure of the pore surface of hydrated portland cement pastes.” *Journal of Materials Science Letters*, 9(9), 1115–1116.

Chan, R., and Bindiganavile, V. (2010a). “Toughness of fibre reinforced hydraulic lime mortar. Part-1: Quasi-static response.” *Materials and Structures*, 43(10), 1435–1444.

Chan, R., and Bindiganavile, V. (2010b). “Toughness of fibre reinforced hydraulic lime mortar. Part-2: Dynamic response.” *Materials and Structures*, 43(10), 1445–1455.

Civan, F. (2001). “Scale effect on porosity and permeability: Kinetics, model, and correlation.” *AIChE journal*, 47(2), 271–287.

Cizer, Ö., Rodriguez-Navarro, C., Ruiz-Agudo, E., Elsen, J., Van Gemert, D., and Van Balen, K. (2012). “Phase and morphology evolution of calcium carbonate precipitated by carbonation of hydrated lime.” *Journal of Materials Science*, 47(16), 6151–6165.

Cnudde, V., Cwirzen, A., Masschaele, B., and Jacobs, P. J. S. (2009). “Porosity and microstructure characterization of building stones and concretes.” *Engineering Geology*, 103(3–4), 76–83.

Conner, W. C., Cevallos-Candau, J. F., Weist, E. L., Pajares, J., Mendioroz, S., and Cortes, A. (1986). "Characterization of pore structure: porosimetry and sorption." *Langmuir*, 2(2), 151–154.

Cook, R. A., and Hover, K. C. (1999). "Mercury porosimetry of hardened cement pastes." *Cement and Concrete research*, 29(6), 933–943.

Costa, A. (2006). "Permeability-porosity relationship: A reexamination of the Kozeny-Carman equation based on a fractal pore-space geometry assumption." *Geophysical Research Letters*, 33(2).

Cowper, A. D., Building Research Station, and Building Research Establishment. (1998). *Lime and lime mortars*. Donhead, Shaftesbury.

Cristiano, F., Mike, L., and Richard, J. B. (2016). "CHEMICAL AND PHYSICAL CHARACTERISATION OF THREE NHL 2 BINDERS AND THE RELATIONSHIP WITH THE MORTAR PROPERTIES." *REHABEND 2016 CONSTRUCTION PATHOLOGY, REHABILITATION TECHNOLOGY AND HERITAGE MANAGEMENT*, 8.

Crumbie, A. K. (2001). "SEM microstructural studies of cementitious materials: Sample preparation of polished sections and microstructural observa- tions with backscattered images—artifacts and practical considera- tions." *Proceedings of the 23rd International Conference on Cement Microscopy, Albuquerque*.

CSA A179. (2014). "Moratr and Grout for unit masonry." *Canadian Standard Association*.

CSA A179-1994. (1994). "Moratr and Grout for unit masonry." *Canadian Standard Association*.

CSA A179-2004. (2004). "Moratr and Grout for unit masonry." *Canadian Standard Association*.

CSA S 304.1. (2004). "Design of masonry structures." *Canadian Standard Association*.

CSA S304-14. (2014). "CSA S304-14 - Design of masonry structures - Third Edition." *Canadian Standard Association*.

CXI Corporate. (2014). "Accessed 20th May 2014, http://www.concreteexperts.com-/pages/Newsletter/03/03.htm." *Journal of Structural Engineering*.

Darcy, H. P. G. (1856). "Darcy, Henry (1856). Les fontaines publiques de la vile de Dijon." Victor Dalmont, Paris.

D'Armada, P., and Hirst, E. (2012). "Nano-Lime for Consolidation of Plaster and Stone." *Journal of Architectural Conservation*, 18(1), 63–80.

Därr, G. M., and Ludwig, U. (1973). "Determination of permeable porosity." *Matériaux et Construction*, 6(3), 185–190.

Davis, G. R., and Elliott, J. C. (2006). "Artefacts in X-ray microtomography of materials." *Materials Science and Technology*, 22(9), 1011–1018.

De Boever, E., Varloteaux, C., Nader, F. H., Foubert, A., Békri, S., Youssef, S., and Rosenberg, E. (2012). "Quantification and Prediction of the 3D Pore Network Evolution in Carbonate Reservoir Rocks." *Oil & Gas Science and Technology – Revue d'IFP Energies nouvelles*, 67(1), 161–178.

Defay, R., and Prigogine, I. (1966). *Surface tension and adsorption*. Wiley, New York.

Diamond, S. (2000). "Mercury porosimetry: an inappropriate method for the measurement of pore size distributions in cement-based materials." *Cement and concrete research*, 30(10), 1517–1525.

Diamond, S., and Landis, E. (2007). "Microstructural features of a mortar as seen by computed microtomography." *Materials and Structures*, 40(9), 989–993.

Doube, M., Kłosowski, M. M., Arganda-Carreras, I., Cordelières, F. P., Dougherty, R. P., Jackson, J. S., Schmid, B., Hutchinson, J. R., and Shefelbine, S. J. (2010). "BoneJ: Free and extensible bone image analysis in ImageJ." *Bone*, 47(6), 1076–1079.

Eins, S. (1996). "An improved dilation method for the measurement of fractal dimension." *Acta Stereologica*.

EN 459-2. (2001). "EN 459-2001. 2001. Building lime. Part 1: Definitions, specifications and conformity criteria. Part 2: Test methods." *European standard available from the British Standards Institution*.

Epstein, N. (1989). "On tortuosity and the tortuosity factor in flow and diffusion through porous media." *Chemical engineering science*, 44(3), 777–779.

Feldman, R. F., and Beaudoin, J. J. (1991). "Pretreatment of hardened hydrated cement pastes for mercury intrusion measurements." *Cement and Concrete Research*, 21(2–3), 297–308.

Fraunhofer. (2014). "http://www.hoki.ibp.fraunhofer.de/wufi/grundl_poros_e.html (Last access May 19, 2014)." *Journal of Structural Engineering*, <https://eprints.qut.edu.au/35997/> (Oct. 4, 2017).

Gao, Y., Jiang, J., De Schutter, G., Ye, G., and Sun, W. (2014). "Fractal and multifractal analysis on pore structure in cement paste." *Construction and Building Materials*, 69, 253–261.

Gao, Z., and Hu, Q. (2013). "Estimating permeability using median pore-throat radius obtained from mercury intrusion porosimetry." *Journal of Geophysics and Engineering*, 10(2), 025014.

Giesche, H. (2006). "Mercury Porosimetry: A General (Practical) Overview." *Particle & Particle Systems Characterization*, 23(1), 9–19.

Glinicki, M. A. (1994). "Toughness of fiber reinforced mortar at high tensile loading rates." *Materials Journal*, 91(2), 161–166.

Goldstein, I., Newbury, D., Echlin, P., Joy, D., Fiori, C., and Lifshin, E. (1981a). *Scanning Electron Microscopy and X-Ray Microanalysis*. Plenum Press, New York and London,.

Goldstein, J. I., Newbury, D. E., Echlin, P., Joy, D. C., Fiori, C., and Lifshin, E. (1981b). *Scanning Electron Microscopy and X-Ray Microanalysis*. Plenum, New York.

Gonzalez, R. C., and Woods, R. E. (2008). *Digital Image Processing*. Prentice Hall.

Goto, S., and Goto, S. (1981). "The Effect of W/C on Curing Temperature on the Permeability of Hardened Cement Paste." *Cem. Concr. Res.*, 11(4), 575–579.

Griffith, A. A. (1924). "Theory of rupture." *ResearchGate*, Delft: Technische Boekhandel and Drukkerij, 55–63.

Guéguen, Y., and Palciauskas, V. (1994). *Introduction to the Physics of Rocks*. Princeton University Press, Princeton.

Gulbe, L., Vitina, I., and Setina, J. (2017). "The Influence of Cement on Properties of Lime Mortars." *Procedia Engineering*, 172, 325–332.

Hanley, R., and Pavía, S. (2008). "A study of the workability of natural hydraulic lime mortars and its influence on strength." *Materials and Structures*, 41(2), 373–381.

Hearn, N., and Hooton, R. D. (1992). "Sample mass and dimension effects on mercury intrusion porosimetry results." *Cement and Concrete Research*, 22(5), 970–980.

Henderson, N., Brêttas, J. C., and Sacco, W. F. (2010). "A three-parameter Kozeny–Carman generalized equation for fractal porous media." *Chemical Engineering Science*, 65(15), 4432–4442.

Hendry, E. A. . (2001). "Masonry walls: materials and construction." *Construction and Building Materials*, 15(8), 323–330.

Holmes, S., and Wingate, M. (1997). "Building with lime." *London: Intermediate Technology*.

Hoseini, M. (2013). "Effect of Compressive Loading on Transport Properties of Cement-Based Materials." University of Alberta (Canada).

Hoshen, J., and Kopelman, R. (1976). "Percolation and cluster distribution. I. Cluster multiple labeling technique and critical concentration algorithm." *Physical Review B*, 14(8), 3438.

Hover, K., and Phares, R. (1996). "Impact of concrete placing method on air content, air-void system parameters, and freeze-thaw durability." *Transportation Research Record: Journal of the Transportation Research Board*, (1532), 1–8.

Hu, J. (2004). "Porosity of concrete: morphological study of model concrete." Technische Universiteit Delft, Delft.

Hughes, D. C. (1985). "Pore structure and permeability of hardened cement paste." *Magazine of Concrete Research*, 37(133), 227–233.

Ilavsky, J., Berndt, C. C., and Karthikeyan, J. (1997). "Mercury intrusion porosimetry of plasma-sprayed ceramic." *Journal of materials science*, 32(15), 3925–3932.

Ishikiriyama, K., and Todoki, M. (1995). "Pore size distribution measurements of silica gels by means of differential scanning calorimetry: II. Thermoporosimetry." *Journal of colloid and interface science*, 171(1), 103–111.

Ishikiriyama, K., Todoki, M., Min, K. H., Yonemori, S., and Noshiro, M. (1996). "Thermoporosimetry Pore size distribution measurements for microporous glass using differential scanning calorimetry." *Journal of thermal analysis*, 46(3–4), 1177–1189.

Islam, M., and Bindiganavile, V. (2014). "Dynamic Fracture Toughness of Sandstone Masonry Beams Bound with Fiber-Reinforced Mortars | Request PDF." *Materials of Civil Engg.*, 26(1), 117–224.

Iza, M., Woerly, S., Danumah, C., Kaliaguine, S., and Bousmina, M. (2000). "Determination of pore size distribution for mesoporous materials and polymeric gels by means of DSC measurements: thermoporometry." *Polymer*, 41(15), 5885–5893.

Izaguirre, A., Lanas, J., and Alvarez, J. I. (2011). "Effect of a polypropylene fibre on the behaviour of aerial lime-based mortars." *Construction and Building Materials*, 25(2), 992–1000.

Katz, A. J., and Thompson, A. H. (1986). "Quantitative prediction of permeability in porous rock." *Physical review B*, 34(11), 8179–8181.

Katz, A. J., and Thompson, A. H. (1987). "Prediction of rock electrical conductivity from mercury injection measurements." *Journal of Geophysical Research: Solid Earth*, 92(B1), 599–607.

Kaufmann, J. (2010). "Pore space analysis of cement-based materials by combined Nitrogen sorption – Wood's metal impregnation and multi-cycle mercury intrusion." *Cement and Concrete Composites*, 32(7), 514–522.

Ketcham, R. A., and Carlson, W. D. (2001). "Acquisition, optimization and interpretation of X-ray computed tomographic imagery: applications to the geosciences." *Computers & Geosciences*, 27(4), 381–400.

kocherbitov, V., Ulvenlund, S., Kober, M., Jarring, K., and Arnebrant, T. (2008). “Hydration of Microcrystalline Cellulose and Milled Cellulose Studied by Sorption Calorimetry.” 112(12), 3728–3734.

Konkol, J., and Prokopski, G. (2011). “THE USE OF FRACTAL GEOMETRY FOR THE ASSESSMENT OF THE DIVERSIFICATION OF MACRO-PORES IN CONCRETE.” *Image Analysis & Stereology*, 30(2), 89.

Korvin, G. (2016). “Permeability from Microscopy: Review of a Dream.” *Arabian Journal for Science and Engineering*, 41(6), 2045–2065.

Kumar, R., and Bhattacharjee, B. (2003). “Porosity, pore size distribution and in situ strength of concrete.” *Cement and concrete research*, 33(1), 155–164.

Lafhaj, Z., Goueygou, M., Djerbi, A., and Kaczmarek, M. (2006). “Correlation between porosity, permeability and ultrasonic parameters of mortar with variable water/cement ratio and water content.” *Cement and Concrete Research*, 36(4), 625–633.

Lanas, J., and Alvarez-Galindo, J. I. (2003). “Masonry repair lime-based mortars: factors affecting the mechanical behavior.” *Cement and Concrete Research*, 33(11), 1867–1876.

Lanas, J., Pérez Bernal, J. L., Bello, M. A., and Alvarez Galindo, J. I. (2004). “Mechanical properties of natural hydraulic lime-based mortars.” *Cement and Concrete Research*, 34(12), 2191–2201.

Landis, E. N., and Nagy, E. N. (2000). “Three-dimensional work of fracture for mortar in compression.” *Engineering Fracture Mechanics*, 65(2–3), 223–234.

Landis, E. N., Nagy, E. N., and Keane, D. T. (2003). “Microstructure and fracture in three dimensions.” *Engineering Fracture Mechanics*, 70(7), 911–925.

Landis, E. N., Nagy, E. N., Keane, D. T., and Nagy, G. (1999). “Technique to measure 3D work-of-fracture of concrete in compression.” *Journal of engineering mechanics*, 125(6), 599–605.

Landis, E. N., Zhang, T., Nagy, E. N., Nagy, G., and Franklin, W. R. (2007). “Cracking, damage and fracture in four dimensions.” *Materials and Structures*, 40(4), 357–364.

Landry, M. R. (2005). “Thermoporometry by differential scanning calorimetry: experimental considerations and applications.” *Thermochimica Acta*, 433(1–2), 27–50.

Lange, D. A., Jennings, H. M., and Shah, S. P. (1994). “Image analysis techniques for characterization of pore structure of cement-based materials.” *Cement and Concrete Research*, 24(5), 841–853.

Laskar, M. A., Kumar, R., and Bhattacharjee, B. (1997). “Some aspects of evaluation of concrete through mercury intrusion porosimetry.” *Cement and Concrete Research*, 27(1), 93–105.

Latour, L. L., Kleinberg, R. L., Mitra, P. P., and Sotak, C. H. (1995). “Pore-size distributions and tortuosity in heterogeneous porous media.” *Journal of Magnetic Resonance, Series A*, 112(1), 83–91.

Lawrence, R. M., Mays, T. J., Rigby, S. P., Walker, P., and D’Ayala, D. (2007). “Effects of carbonation on the pore structure of non-hydraulic lime mortars.” *Cement and Concrete Research*, 37(7), 1059–1069.

Lea, F. M. (1970). “THE CHEMISTRY OF CEMENT AND CONCRETE. THIRD EDITION.”

Lippmann, F. (1973). *Sedimentary Carbonate Minerals*. Minerals, Rocks and Mountains, Springer-Verlag, Berlin Heidelberg.

Mamun, M., and Bindiganavile, V. (2017). “Fractal Nature of Cementitious Systems Exposed to Sustained Elevated Temperatures.” *Procedia Engineering*, 210, 557–564.

Matyka, M., Khalili, A., and Koza, Z. (2008). “Tortuosity-porosity relation in porous media flow.” *Physical Review E*, 78(2), 026306.

Maurenbrecher, A. H. P., Trischuk, K., Rousseau, M. Z., and Subercaseaux, M. I. (2007). *Key Considerations for Repointing Mortars for Conservation of Older Masonry*. Institute for Research in Construction, National Research Council Canada.

Maurenbrecher, A. P. (2004). “Mortars for repair of traditional masonry.” *Practice periodical on structural design and construction*, 9(2), 62–65.

Mees, F., Swennen, R., Van Geet, M., and Jacobs, P. (2003). “Applications of X-ray computed tomography in the geosciences.” *Geological Society Special Publication, London*, 1–6.

Mehta, P. K., and Manmohan, D. (1980). “"Pore Size Distribution and Permeability of Hardened Cement Pastes,.” 181–185.

Mehta, P. K., and Monteiro, P. J. M. (2006). *Concrete: Microstructure, Properties, and Materials, Fourth Edition*. McGraw-Hill.

Meschke, G., Pichler, B., and Rots, J. G. (2018). *Computational Modelling of Concrete Structures: Proceedings of the Conference on Computational Modelling of Concrete and Concrete Structures (EURO-C 2018), February 26 - March 1, 2018, Bad Hofgastein, Austria*. CRC Press.

Meyer, K., Klobes, P., and Röhl-Kuhn, B. (1997). “Certification of Reference Material with Special Emphasis on Porous Solids.” *Crystal Research and Technology*, 32(1), 175–185.

Mindess, S., and Vondran, G. (1988). “Properties of concrete reinforced with fibrillated polypropylene fibres under impact loading.” *Cement and Concrete Research*, 18(1), 109–115.

Mindess, S., Young, J. F., and Darwin, D. (2003). *Concrete*. Prentice Hall, Upper Saddle River, NJ.

Mitchell, J., Webber, J., and Strange, J. (2008). “Nuclear magnetic resonance cryoporometry.” *Physics Reports*, 461(1), 1–36.

Mosquera, M. J., Benıtez, D., and Perry, S. H. (2002). “Pore structure in mortars applied on restoration Effect on properties relevant to decay of granite buildings.” *Cement and Concrete Research*, 6.

Mosquera, M. J., Silva, B., Prieto, B., and Ruiz-Herrera, E. (2006). “Addition of cement to lime-based mortars: Effect on pore structure and vapor transport.” *Cement and Concrete Research*, 36(9), 1635–1642.

Mostaghimi, P., Blunt, M. J., and Bijeljic, B. (2013). “Computations of Absolute Permeability on Micro-CT Images.” *Mathematical Geosciences*, 45(1), 103–125.

Musacchi, J. (2014). “Influence of nano-lime and nano-silica consolidants in the drying kinetics of three porous building materials.”

Naik, N. N., Jupe, A. C., Stock, S. R., Wilkinson, A. P., Lee, P. L., and Kurtis, K. E. (2006). “Sulfate attack monitored by microCT and EDXRD: Influence of cement type, water-to-cement ratio, and aggregate.” *Cement and Concrete Research*, 36(1), 144–159.

Nakashima, Y., and Kamiya, S. (2007). “Mathematica Programs for the Analysis of Three-Dimensional Pore Connectivity and Anisotropic Tortuosity of Porous Rocks using X-

ray Computed Tomography Image Data." *Journal of Nuclear Science and Technology*, 44(9), 1233–1247.

Nakashima, Y., and Nakano, T. (2011). "Accuracy of formation factors for three-dimensional pore-scale images of geo-materials estimated by renormalization technique." *Journal of Applied Geophysics*, 75(1), 31–41.

Nakashima, Y., Nakano, T., Nakamura, K., Uesugi, K., Tsuchiyama, A., and Ikeda, S. (2004). "Three-dimensional diffusion of non-sorbing species in porous sandstone: computer simulation based on X-ray microtomography using synchrotron radiation." *Journal of Contaminant Hydrology*, 74(1–4), 253–264.

Nakashima, Y., and Watanabe, Y. (2002). "Estimate of transport properties of porous media by microfocus X-ray computed tomography and random walk simulation: ESTIMATES OF TRANSPORT PROPERTIES." *Water Resources Research*, 38(12), 8-1-8–12.

Nakashima, Y., and Yamaghuci, T. (2004). "Original free Mathematica programs for the calculation of transport properties of porous media." *In: Otani, J., Obara, Y. (Eds.), X-ray CT for Geomaterials; Soils, Concrete, Rocks. A.A. Balkema, Lisse, Netherlands*, 103–110.

Nakashima, Y., and Yamaguchi, T. (2004). "DMAP. m: A Mathematica® program for three-dimensional mapping of tortuosity and porosity of porous media." *BULLETIN-GEOLOGICAL SURVEY JAPAN*, 55, 93–103.

Neithalath, N., Weiss, J., and Olek, J. (2006). "Predicting the permeability of pervious concrete (enhanced porosity concrete) from non-destructive electrical measurements." *United States: Purdue University*.

Neville, A. M. (2011). *Properties of concrete*. Pearson, Harlow, England ; New York.

Nokken, M. R., and Hooton, R. D. (2007). "Using pore parameters to estimate permeability or conductivity of concrete." *Materials and Structures*, 41(1), 1–16.

Nyame, B. K., and Illston, J. M. (1980). "Capillary Pore Structure and • Permeability of Hardened Cement Paste." 181–185.

Ohama, Y. (1995). *Handbook of Polymer-Modified Concrete and Mortars - 1st Edition*. William Andrew.

Okabe, H., and Blunt, M. J. (2004). "Predicting Permeability through 3D Pore-Space Images Reconstructed Using Multiple-Point Statistics." *International Symposium of the Society of Core Analysts, Abu Dhabi, UAE*, 5–9.

Pape, H., Clauser, C., and Iffland, J. (1999). "Permeability prediction based on fractal pore-space geometry." *Geophysics*, 64(5), 1447–1460.

Pape, H., Clauser, C., and Iffland, J. (2000). "Variation of Permeability with Porosity in Sandstone Diagenesis Interpreted with a Fractal Pore Space Model:" *Pure and Applied Geophysics*, 157(4), 603–619.

Parkinson, I. H., and Fazzalari, N. L. (2000). "Methodological principles for fractal analysis of trabecular bone." *Journal of microscopy*, 198(2), 134–142.

Paterson, M. S. (1983). "The equivalent channel model for permeability and resistivity in fluid-saturated rock—a re-appraisal." *Mechanics of Materials*, 2(4), 345–352.

Pereira de Oliveira, L. A., and Castro-Gomes, J. P. (2011). "Physical and mechanical behaviour of recycled PET fibre reinforced mortar." *Construction and Building Materials*, 25(4), 1712–1717.

Peterson, K., Carlson, J., Sutter, L., and Van Dam, T. (2009). “Methods for threshold optimization for images collected from contrast enhanced concrete surfaces for air-void system characterization.” *Materials Characterization*, 60(7), 710–715.

Peterson, S. (1982). “Lime Water Consolidation.” *Proc. Mortars, Cements and Grouts Used in the Conservation of Historic Buildings*, 53–59.

Petrov, O. V., and Furó, I. (2009). “NMR cryoporometry: Principles, applications and potential.” *Progress in Nuclear Magnetic Resonance Spectroscopy*, 54(2), 97–122.

Popovics, S. (1998). *Strength and Related Properties of Concrete: A Quantitative Approach*. John Wiley & Sons.

Promentilla, M. A. B., Cortez, S. M., Papel, R. A. D., Tablada, B. M., and Sugiyama, T. (2016a). “Evaluation of Microstructure and Transport Properties of Deteriorated Cementitious Materials from Their X-ray Computed Tomography (CT) Images.” *Materials*, 9(5), 388.

Promentilla, M. A. B., Sugiyama, T., Hitomi, T., and Takeda, N. (2009). “Quantification of tortuosity in hardened cement pastes using synchrotron-based X-ray computed microtomography.” *Cement and Concrete Research*, 39(6), 548–557.

Promentilla, M., Cortez, S., Papel, R., Tablada, B., and Sugiyama, T. (2016b). “Evaluation of Microstructure and Transport Properties of Deteriorated Cementitious Materials from Their X-ray Computed Tomography (CT) Images.” *Materials*, 9(5), 388.

Quayale, N. J. T. (1996). “The case against lime water (or, the futility of consolidating stone conservation of historic building.” *Conservation news*, 68–71.

Rodriguez-Navarro, C., Jimenez-Lopez, C., Rodriguez-Navarro, A., Gonzalez-Muñoz, M. T., and Rodriguez-Gallego, M. (2007). “Bacterially mediated mineralization of vaterite.” *Geochimica et Cosmochimica Acta*, 71(5), 1197–1213.

Rodriguez-Navarro, C., Suzuki, A., and Ruiz-Agudo, E. (2013). “Alcohol Dispersions of Calcium Hydroxide Nanoparticles for Stone Conservation.” *Langmuir*, 29(36), 11457–11470.

Rostásy, F. S., Weiβ, R., and Wiedemann, G. (1980). “Changes of pore structure of cement mortars due to temperature.” *Cement and Concrete Research*, 10(2), 157–164.

Rouquerol, F., Rouquerol, J., and Sing. (1999). *Adsorption by Powders and Porous Solids - 2nd Edition*. Academic Press, London.

Roy, D. M. (1988). “Relationships between permeability, porosity, diffusion and microstructure of cement pastes, mortar, and concrete at different temperatures.” *MRS Online Proceedings Library Archive*, 137.

Roy, D. M., Brown, P. W., Shi, D., Scheetz, B. E., and May, W. (1993). *Concrete microstructure porosity and permeability*.

Sabbioni, C. (2001). “Atmospheric deterioration of ancient and modern hydraulic mortars.” *Atmospheric Environment*, 35(3), 539–548.

Sabbioni, C., Bonazza, A., and Zappia, G. (2002). “Damage on hydraulic mortars: the Venice Arsenal.” *Journal of Cultural Heritage*, 3(1), 83–88.

Sappakittipakorn, M., Banthia, N., and Jiang, Z. (2010). “Cryoporometry based evidence of pore refinement in cementitious composites.” *Indian Concrete Journal*, 84(6), 17.

Scrivener, K. L. (1988). “The use of backscattered electron microscopy and image analysis to study the porosity of cement paste.” *MRS Online Proceedings Library Archive*, 137.

Scrivener, K. L. (2004). “Backscattered electron imaging of cementitious microstructures: understanding and quantification.” *Cement and Concrete Composites*, 26(8), 935–945.

Scrivener, K. L., and Pratt, P. L. (1984). “BACKSCATTERED ELECTRON IMAGES OF POLISHED CEMENT SECTIONS IN THE SCANNING ELECTRON MICROSCOPE.” *Proceedings of the International Conference on Cement Microscopy*, null(null), 145–155.

Scrivener, K., Snellings, R., and Lothenbach, B. (2016). *A practical guide to microstructural analysis of cementitious materials*. Crc Press.

Sébaïbi, Y., Dheilly, R. M., and Quéneudec, M. (2004). “A study of the viscosity of lime–cement paste: influence of the physico-chemical characteristics of lime.” *Construction and Building Materials*, 18(9), 653–660.

Shah, S. M., Yang, J., Crawshaw, J. P., Gharbi, O., Boek, E. S., and others. (2013). “Predicting porosity and permeability of carbonate rocks from core-scale to pore-scale using medical CT, confocal laser scanning microscopy and micro CT.” *SPE Annual Technical Conference and Exhibition*, Society of Petroleum Engineers.

Shi, D., and Winslow, D. N. (1985). “Contact angle and damage during mercury intrusion into cement paste.” *Cement and Concrete Research*, 15(4), 645–654.

Society of Petroleum Engineers. (1984). “The SI Metric System of Units and SPE Metric Standard.” *Society of Petroleum Engineers.*

Song, Y. (2014). “ANALYSIS OF AIR-VOID SYSTEM IN HARDENED CONCRETE FROM A THREE-DIMENSIONAL PERSPECTIVE.” 119.

Soroushian, P., Elzafraney, M., and Nossoni, A. (2003). “Specimen preparation and image processing and analysis techniques for automated quantification of concrete microcracks and voids.” *Cement and Concrete Research*, 33(12), 1949–1962.

Stock, S. R., Naik, N. K., Wilkinson, A. P., and Kurtis, K. E. (2002). “X-ray microtomography (microCT) of the progression of sulfate attack of cement paste.” *Cement and Concrete Research*, 32(10), 1673–1675.

Straley, C., Rossini, D., Vinegar, H., Tutunjian, P., and Morriss, C. (1997). “Core analysis by low-field NMR.” *Log Anal.*, 38(2), 84–94.

Stutzman, P. E., and Clifton, J. R. (1999). “Specimen preparation for scanning electron microscopy.” *Proceedings of the international conference on cement microscopy*, INTERNATIONAL CEMENT MICROSCOPY ASSOCIATION, 10–22.

Sugiyama, T., Ritthichauy, W., and Tsuji, T. (2003). “Simultaneous transport of chloride and calcium ions in hydrated cement systems.” *Adv. Concr. Technol.*, 1(2), 127–138.

Sugiyama, T., Ritthichauy, W., and Tsuji, T. (2008). “Experimental investigation and numerical modeling of chloride penetration and calcium dissolution in saturated concrete,.” *Cement and Concrete Research*, 38, 49–67.

Suman, R., and Ruth, D. (1993). “Formation factor and tortuosity of homogeneous porous media.” *Transport in Porous Media*, 12(2), 185–206.

Suter, G. T., Borgal, C. P., and Blades, K. (2001). “Overview of mortars for Canadian historic structures.” *Proceedings of the 9th Canadian masonry symposium. University of New Brunswick, Canada*, 4–6.

Thiéry, M., Faure, P., Morandeau, A., Platret, G., Bouteloup, J.-F., Dangla, P., and Baroghel-Bouny, V. (2011). “Effect of carbonation on the microstructure and moisture properties of cement-based materials.” *XII DBMC (12th International Conference on Building Materials and Components*, 1–8.

Thomassin, J. H., and Rassineux, F. (1992). “Ancient analogues of cement-based materials: stability of calcium silicate hydrates.” *Applied Geochemistry*, 7, 137–142.

Torabi, A., Fossen, H., and Alaei, B. (2008). "Application of spatial correlation functions in permeability estimation of deformation bands in porous rocks." *Journal of Geophysical Research*, 113(B8).

Torquato, S. (2013). *Random Heterogeneous Materials: Microstructure and Macroscopic Properties*. Springer Science & Business Media.

Van Balen, K., and Van Gemert, D. (1994). "Modelling lime mortar carbonation." *Materials and Structures*, 27(7), 393–398.

Vicat, L.-J. (2014). *A practical and scientific treatise on calcareous mortars and cements, artificial and natural*. Cambridge University Press.

Walsh, J. B., and Brace, W. F. (1984). "The effect of pressure on porosity and the transport properties of rock." *Journal of Geophysical Research: Solid Earth*, 89(B11), 9425–9431.

Wang, F. P., Reed, R. M., and others. (2009). "Pore networks and fluid flow in gas shales." *SPE annual technical conference and exhibition*, Society of Petroleum Engineers.

Washburn, E. W. (1921). "The dynamics of capillary flow." *Physical review*, 17(3), 273.

Watanabe, Y., and Nakashima, Y. (2001). "Two-dimensional random walk program for the calculation of the tortuosity of porous media." *Journal of Groundwater Hydrology*, 43(1), 13–22.

Watanabe, Y., and Nakashima, Y. (2002). "RW3D. m: three-dimensional random walk program for the calculation of the diffusivities in porous media." *Computers & geosciences*, 28(4), 583–586.

Webber, J. B. W., and Dore, J. C. (2008). "Neutron diffraction cryoporometry—a measurement technique for studying mesoporous materials and the phases of contained liquids and their crystalline forms." *Nuclear Instruments and Methods in Physics Research Section A: Accelerators, Spectrometers, Detectors and Associated Equipment*, 586(2), 356–366.

Willis, K. L., Abell, A. B., and Lange, D. A. (1998). "Image-based characterization of cement pore structure using wood's metal intrusion." *Cement and Concrete Research*, 28(12), 1695–1705.

Winslow, D. N. (1985). "The fractal nature of the surface of cement paste." *Cement and Concrete Research*, 15(5), 817–824.

Wong, H. S., Head, M. K., and Buenfeld, N. R. (2006). "Pore segmentation of cement-based materials from backscattered electron images." *Cement and Concrete Research*, 36(6), 1083–1090.

Wong, H. S., Zimmerman, R. W., and Buenfeld, N. R. (2012). "Estimating the permeability of cement pastes and mortars using image analysis and effective medium theory." *Cement and Concrete Research*, 42(2), 476–483.

Xu, P., and Yu, B. (2008). "Developing a new form of permeability and Kozeny–Carman constant for homogeneous porous media by means of fractal geometry." *Advances in Water Resources*, 31(1), 74–81.

Yun, K. K., Kim, D. H., and Kim, K. J. (2007). "Effect of micro air void system on the permeability of latex-modified concretes with ordinary Portland and very early strength cements." *Canadian Journal of Civil Engineering*, 34(8), 895–901.

Zalocha, D., and Kasperkiewicz, J. (2005). "Estimation of the structure of air entrained concrete using a flatbed scanner." *Cement and Concrete Research*, 35(10), 2041–2046.

Zhang, N., He, M., Zhang, B., Qiao, F., Sheng, H., and Hu, Q. (2016). “Pore structure characteristics and permeability of deep sedimentary rocks determined by mercury intrusion porosimetry.” *Journal of Earth Science*, 27(4), 670–676.

Zhao, H., and Darwin, D. (1990). *Quantitative Backscattered Electron Analysis Techniques for Cement-Based Materials*. University of Kansas Center for Research, Inc.

Zhou, J., Ye, G., and van Breugel, K. (2010). “Characterization of pore structure in cement-based materials using pressurization–depressurization cycling mercury intrusion porosimetry (PDC-MIP).” *Cement and Concrete Research*, 40(7), 1120–1128.

Ziegenbalg, G., Brümmer, K., and Pianski, J. (2010). “Nano-Lime - a New Material for the Consolidation and Conservation of Historic Mortars.” 9.

Zollo, R. F. (1997). “Fiber-reinforced concrete: an overview after 30 years of development.” *Cement and Concrete Composites*, 19(2), 107–122.

APPENDIX

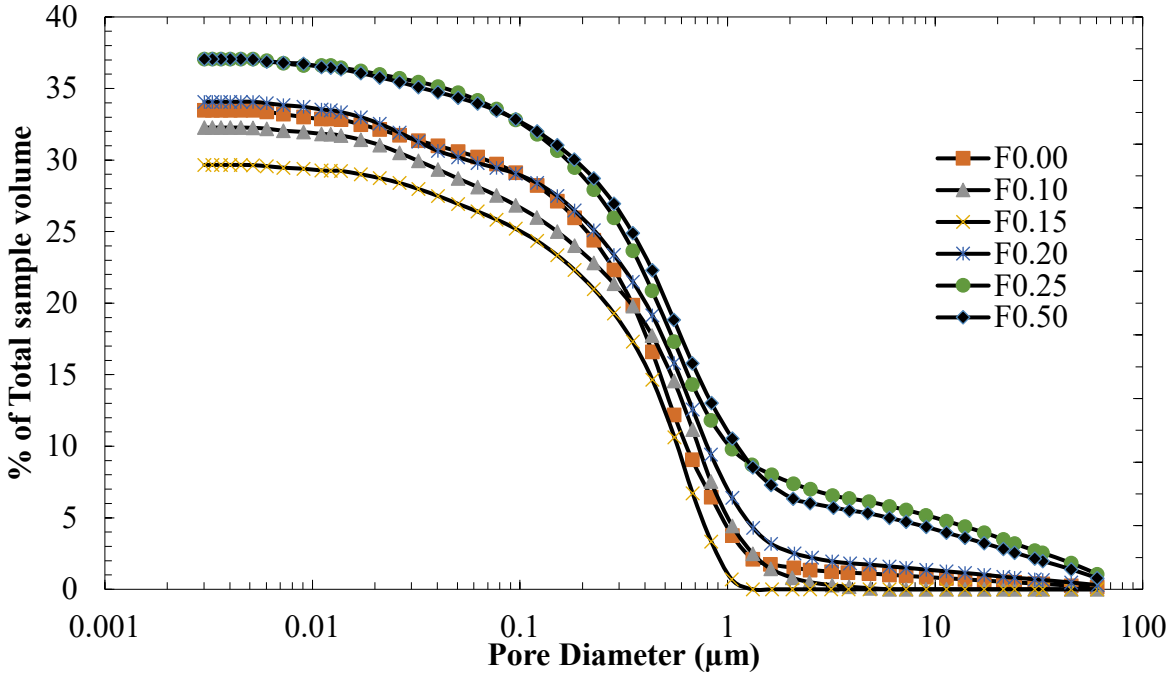

Figure A.1 Pore size distribution of Hydraulic Lime Mortar by MIP method

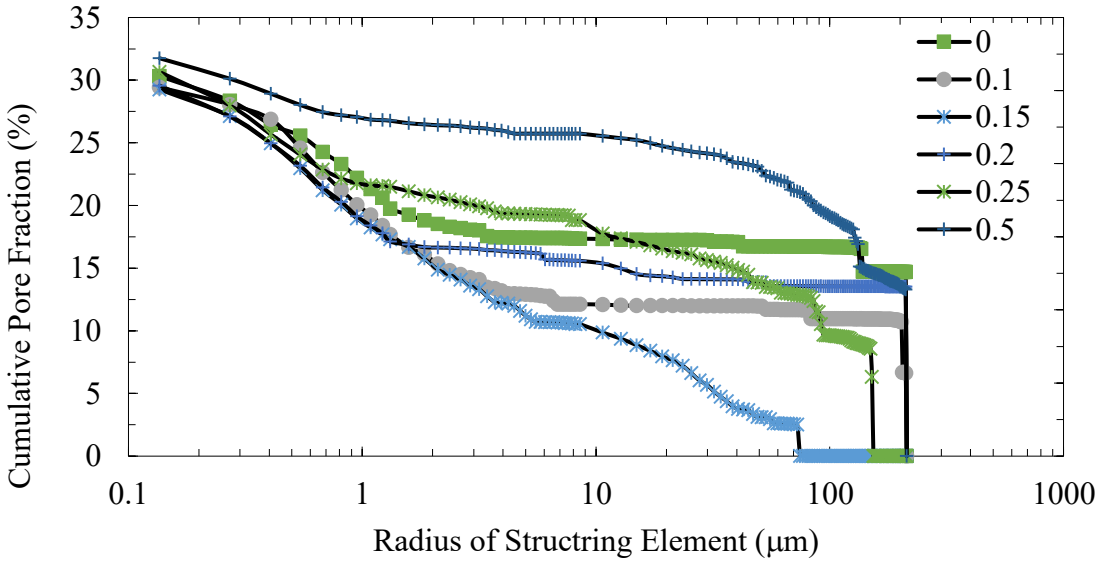

Figure A.2 Pore size distribution of Hydraulic Lime Mortar by image analysis

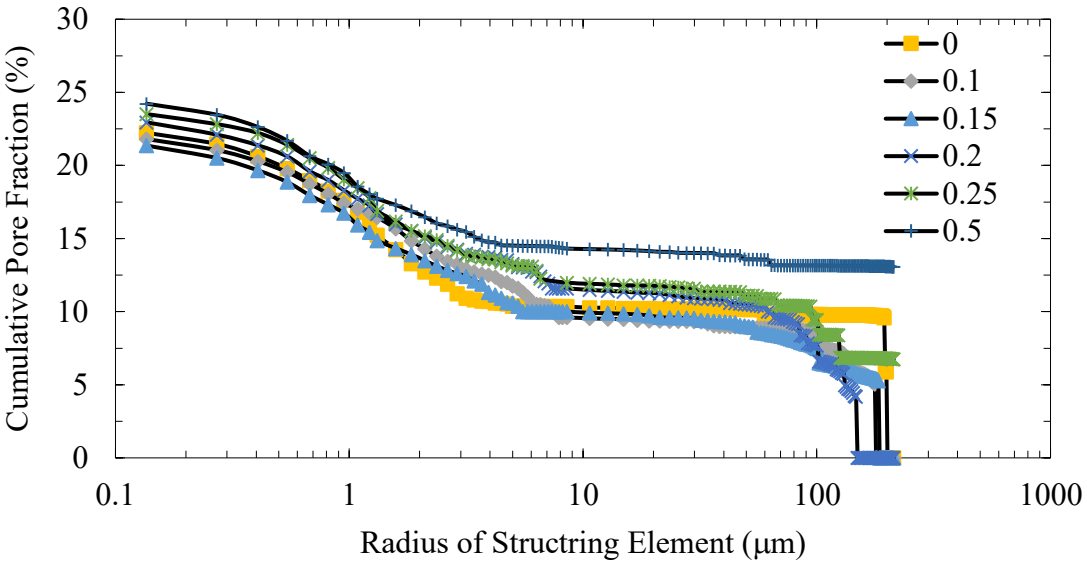

Figure A.3 Pore size distribution of Type N Mortar by image analysis

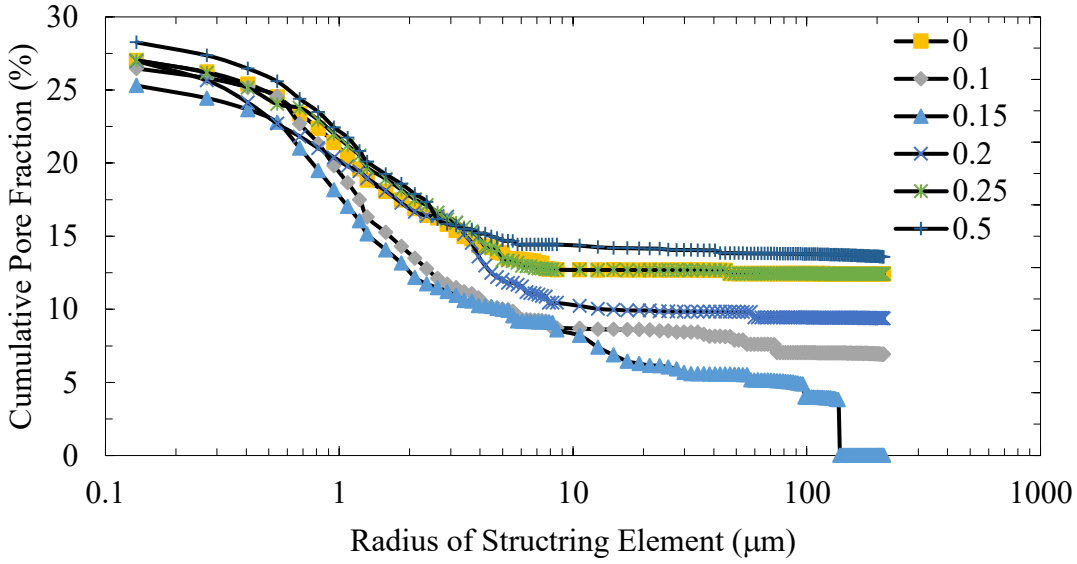

Figure A.4 Pore size distribution of Type O Mortar by image analysis

Table A1 Porosity as determined by ASTM C642 method

Hydraulic Lime Mortar			Type N mortar			Type O Mortar		
Fibre	Mean	Std. Dev.	Fibre	Mean	Std. Dev.	Fibre	Mean	Std. Dev.
0	36.68	0.24	0	27.68	0.29	0	33.12	0.22
0.10	36.53	0.29	0.10	27.43	0.31	0.10	33.11	0.41
0.15	36.21	0.19	0.15	27.10	0.15	0.15	33.06	0.16
0.20	37.00	0.39	0.20	28.06	0.19	0.20	33.16	0.22
0.25	37.27	0.36	0.25	28.24	0.35	0.25	33.45	0.31
0.50	37.40	0.23	0.50	28.45	0.28	0.50	33.80	0.27

Table A2 Porosity as determined by MIP

Hydraulic Lime Mortar			Type N mortar			Type O Mortar		
Fibre	Mean	Std. Dev.*	Fibre	Mean	Std. Dev.*	Fibre	Mean	Std. Dev.*
0	33.48	-	0	27.99	-	0	30.78	-
0.10	32.27	-	0.10	27.61	-	0.10	29.05	-
0.15	29.66	-	0.15	27.38	-	0.15	27.73	-
0.20	34.07	-	0.20	27.80	-	0.20	29.38	-
0.25	37.07	-	0.25	27.97	-	0.25	31.33	-
0.50	37.07	-	0.50	28.49	-	0.50	31.80	-

* Only one sample was tested for MIP for each category.

Table A3 Porosity as determined by Image analysis

Hydraulic Lime Mortar			Type N mortar			Type O Mortar		
Fibre	Mean	Std. Dev.	Fibre	Mean	Std. Dev.	Fibre	Mean	Std. Dev.
0	30.31	0.44	0	22.23	0.51	0	27.02	0.31
0.10	29.42	0.35	0.10	21.80	0.19	0.10	26.47	0.36
0.15	29.25	0.28	0.15	21.36	0.26	0.15	25.30	0.24
0.20	29.56	0.31	0.20	22.95	0.18	0.20	26.98	0.29
0.25	30.65	0.41	0.25	23.51	0.31	0.25	27.04	0.41
0.50	31.75	0.29	0.50	24.22	0.28	0.50	28.25	0.34

Table A4 Density (gm/cm^3) variation with fibre for Hydraulic Lime Mortar, Type N mortar, and Type O mortar as determined by ASTM C642 method

Hydraulic Lime Mortar			Type N mortar			Type O Mortar		
Fibre	Mean	Std. Dev.	Fibre	Mean	Std. Dev.	Fibre	Mean	Std. Dev.
0	1.67	0.003	0	1.76	0.007	0	1.68	0.004
0.15	1.70	0.005	0.15	1.79	0.006	0.15	1.71	0.008
0.50	1.68	0.002	0.50	1.77	0.009	0.50	1.70	0.006

Table A5 Specific surface area (μm^{-1}) of plain and fibre reinforced mortar determined using two-point correlation method

Hydraulic Lime Mortar			Type N mortar			Type O Mortar		
Fibre	Mean	Std. Dev.	Fibre	Mean	Std. Dev.	Fibre	Mean	Std. Dev.
0	0.711	0.023	0	0.313	0.014	0	0.611	0.027
0.15	0.496	0.019	0.15	0.188	0.009	0.15	0.515	0.024
0.50	0.773	0.021	0.50	0.317	0.016	0.50	0.696	0.018

Table A6 Characteristic pore radius (μm) of plain and fibre reinforced mortar determined using two-point correlation method

Hydraulic Lime Mortar			Type N mortar			Type O Mortar		
Fibre	Mean	Std. Dev.	Fibre	Mean	Std. Dev.	Fibre	Mean	Std. Dev.
0	0.789	0.0273	0	1.578	0.0156	0	1.315	0.0366
0.15	0.526	0.0331	0.15	1.131	0.0296	0.15	0.789	0.0195
0.50	1.052	0.0228	0.50	1.973	0.0315	0.50	1.7095	0.0265

Table A7 Fractal dimension of plain and fibre reinforced mortar determined using dilation method

Hydraulic Lime Mortar			Type N mortar			Type O Mortar		
Fibre	Mean	Std. Dev.	Fibre	Mean	Std. Dev.	Fibre	Mean	Std. Dev.
0	1.669	0.038	0	1.631	0.102	0	1.710	0.032
0.15	1.654	0.025	0.15	1.622	0.024	0.15	1.660	0.076
0.50	1.708	0.035	0.50	1.632	0.060	0.50	1.754	0.026

Table A8 Fractal dimension of plain and fibre reinforced mortar determined using box-counting method

Hydraulic Lime Mortar			Type N mortar			Type O Mortar		
Fibre	Mean	Std. Dev.	Fibre	Mean	Std. Dev.	Fibre	Mean	Std. Dev.
0	1.540	0.059	0	1.549	0.117	0	1.597	0.046
0.15	1.525	0.032	0.15	1.506	0.027	0.15	1.566	0.084
0.50	1.606	0.034	0.50	1.552	0.068	0.50	1.677	0.017

Table A9 Permeability coefficients (m/s) by experimental methods

Hydraulic Lime Mortar			Type N mortar			Type O Mortar		
Fibre	Mean	Std. Dev.	Fibre	Mean	Std. Dev.	Fibre	Mean	Std. Dev.
0	1.32E-05	7.02E-07	0	1.93E-07	2.47E-09	0	8.24E-07	4.58E-08
0.10	1.21E-05	2.96E-07	0.10	1.81E-07	3.42E-09	0.10	7.89E-07	3.14E-08
0.15	9.55E-06	3.69E-07	0.15	9.13E-08	3.49E-09	0.15	4.35E-07	2.09E-07
0.20	1.08E-05	4.33E-07	0.20	1.18E-07	2.63E-09	0.20	7.59E-07	2.63E-08
0.25	1.51E-05	6.59E-07	0.25	1.48E-07	1.12E-07	0.25	1.13E-06	3.54E-08
0.50	2.31E-05	6.78E-07	0.50	4.18E-07	6.49E-08	0.50	1.77E-06	3.06E-08

Table A10 Permeability coefficients prediction (m/s) by two-point correlation functions (Image resolution 50x)

Hydraulic Lime Mortar			Type N mortar			Type O Mortar		
Fibre	Mean	Std. Dev.	Fibre	Mean	Std. Dev.	Fibre	Mean	Std. Dev.
0	1.36E-06	2.78E-08	0	1.76E-08	3.65E-10	0	9.38E-08	6.65E-10
0.15	6.31E-07	7.39E-09	0.15	7.93E-09	1.84E-11	0.15	8.16E-08	3.21E-10
0.50	2.03E-06	5.66E-08	0.50	7.69E-08	4.72E-10	0.50	3.14E-07	4.65E-09

Table A11 Permeability coefficients prediction (m/s) by two-point correlation functions (Image resolution 400x)

Hydraulic Lime Mortar			Type N mortar			Type O Mortar		
Fibre	Mean	Std. Dev.	Fibre	Mean	Std. Dev.	Fibre	Mean	Std. Dev.
0	6.65E-07	7.83E-09	0	4.63E-09	5.32E-11	0	5.17E-09	6.36E-11
0.15	2.22E-07	1.36E-09	0.15	6.44E-10	6.36E-12	0.15	1.45E-09	1.92E-11
0.50	1.64E-06	3.25E-08	0.50	3.11E-09	4.33E-11	0.50	2.25E-08	3.22E-10

Table A12 Permeability coefficients prediction (m/s) by Katz Thopmson with F calculated from micro CT

Hydraulic Lime Mortar			Type N mortar			Type O Mortar		
Fibre	Mean	Std. Dev.*	Fibre	Mean	Std. Dev.*	Fibre	Mean	Std. Dev.*
0	1.36E-09	-	0	1.89E-10	-	0	9.82E-10	-
0.15	2.97E-10	-	0.15	2.69E-11	-	0.15	1.94E-10	-
0.50	3.57E-09	-	0.50	2.83E-10	-	0.50	1.02E-09	-

* Only one sample was tested for MIP for each category.

Table A13 Permeability coefficients prediction (m/s) by Katz Thopmson with F calculated as per equation 4.3

Hydraulic Lime Mortar			Type N mortar			Type O Mortar		
Fibre	Mean	Std. Dev.*	Fibre	Mean	Std. Dev.*	Fibre	Mean	Std. Dev.*
0	2.31E-09	-	0	3.27E-09	-	0	6.46E-09	-
0.15	2.07E-09	-	0.15	1.03E-09	-	0.15	4.61E-09	-
0.50	5.70E-09	-	0.50	4.62E-09	-	0.50	6.95E-09	-

* Only one sample was tested for MIP for each category.

Table A14 Permeability coefficients prediction (m/s) by Katz Thopmson with F calculated as per equation 4.6

Hydraulic Lime Mortar			Type N mortar			Type O Mortar		
Fibre	Mean	Std. Dev.*	Fibre	Mean	Std. Dev.*	Fibre	Mean	Std. Dev.*
0	2.99E-09	-	0	2.63E-09	-	0	6.19E-09	-
0.15	1.61E-09	-	0.15	1.09E-09	-	0.15	3.95E-09	-
0.50	5.76E-09	-	0.50	4.45E-09	-	0.50	6.67E-09	-

* Only one sample was tested for MIP for each category.

Table A15 Permeability coefficients prediction (m/s) by fractal model developed by Xu and Yu (2008) (Image resolution 50x)

Hydraulic Lime Mortar			Type N mortar			Type O Mortar		
Fibre	Mean	Std. Dev.	Fibre	Mean	Std. Dev.	Fibre	Mean	Std. Dev.
0	3.51E-05	4.36E-08	0	4.22E-05	5.69E-08	0	9.33E-06	8.64E-08
0.15	1.84E-05	2.66E-08	0.15	2.20E-05	3.84E-08	0.15	1.51E-05	2.59E-08
0.50	4.06E-05	1.37E-08	0.50	3.50E-05	5.38E-08	0.50	6.18E-05	7.25E-08

Table A16 Permeability coefficients prediction (m/s) by fractal model developed by Xu and Yu (2008) (Image resolution 400x)

Hydraulic Lime Mortar			Type N mortar			Type O Mortar		
Fibre	Mean	Std. Dev.	Fibre	Mean	Std. Dev.	Fibre	Mean	Std. Dev.
0	4.52E-08	6.25E-11	0	1.71E-07	2.59E-10	0	5.84E-08	4.59E-11
0.15	4.81E-08	3.56E-11	0.15	2.82E-08	3.91E-11	0.15	7.56E-08	5.68E-11
0.50	9.54E-08	8.57E-11	0.50	1.24E-07	1.84E-10	0.50	1.84E-07	2.47E-10

Table A17 Segmented total porosity of plain and fibre reinforced mortar

Hydraulic Lime Mortar			Type N mortar			Type O Mortar		
Fibre	Mean	Std. Dev.	Fibre	Mean	Std. Dev.	Fibre	Mean	Std. Dev.
0	0.211	0.031	0	0.114	0.019	0	0.117	0.021
0.15	0.184	0.025	0.15	0.099	0.0152	0.15	0.110	0.018
0.50	0.221	0.034	0.50	0.118	0.215	0.50	0.130	0.023

Table A18 Effective porosity of plain and fibre reinforced mortar

Hydraulic Lime Mortar			Type N mortar			Type O Mortar		
Fibre	Mean	Std. Dev.	Fibre	Mean	Std. Dev.	Fibre	Mean	Std. Dev.
0	0.207	0.029	0	0.057	0.012	0	0.108	0.019
0.15	0.180	0.021	0.15	0.049	0.009	0.15	0.089	0.012
0.50	0.218	0.032	0.50	0.061	0.014	0.50	0.114	0.021

Table A19 Pore connectivity of plain and fibre reinforced mortar

Hydraulic Lime Mortar			Type N mortar			Type O Mortar		
Fibre	Mean	Std. Dev.	Fibre	Mean	Std. Dev.	Fibre	Mean	Std. Dev.
0	0.983	0.012	0	0.501	0.012	0	0.827	0.0094
0.15	0.978	0.011	0.15	0.495	0.017	0.15	0.806	0.0091
0.50	0.988	0.013	0.50	0.513	0.013	0.50	0.873	0.0110

Table A20 Specific surface area (μm^{-1}) of plain and fibre reinforced mortar

Hydraulic Lime Mortar			Type N mortar			Type O Mortar		
Fibre	Mean	Std. Dev.	Fibre	Mean	Std. Dev.	Fibre	Mean	Std. Dev.
0	0.0935	0.0025	0	0.3249	0.0156	0	0.1889	0.0265
0.15	0.0838	0.0031	0.15	0.2785	0.0213	0.15	0.1665	0.0156
0.50	0.0946	0.0024	0.50	0.3160	0.0421	0.50	0.1874	0.0235

Table A21 Diffusive tortuosity of plain and fibre reinforced mortar

Hydraulic Lime Mortar			Type N mortar			Type O Mortar		
Fibre	Mean	Std. Dev.	Fibre	Mean	Std. Dev.	Fibre	Mean	Std. Dev.
0	6.60	0.48	0	18.90	0.58	0	12.43	0.81
0.15	14.88	0.56	0.15	54.30	0.67	0.15	34.57	0.56
0.50	4.64	0.86	0.50	24.39	0.95	0.50	12.51	1.10

Table A22 Formation factor of plain and fibre reinforced mortar

Hydraulic Lime Mortar			Type N mortar			Type O Mortar		
Fibre	Mean	Std. Dev.	Fibre	Mean	Std. Dev.	Fibre	Mean	Std. Dev.
0	32.42	2.23	0	329.73	6.33	0	114.61	3.56
0.15	82.51	3.25	0.15	1109.95	8.22	0.15	388.61	4.29
0.50	21.26	4.21	0.50	401.85	6.97	0.50	110.02	8.26

Table A23 Permeability (m/s) evaluation of plain and fibre reinforced mortar determined using X-ray micro CT method

Hydraulic Lime Mortar			Type N mortar			Type O Mortar		
Fibre	Mean	Std. Dev.	Fibre	Mean	Std. Dev.	Fibre	Mean	Std. Dev.
0	7.82E-06	6.36E-08	0	6.25E-08	7.45E-10	0	5.32E-07	6.25E-09
0.15	3.76E-06	2.65E-08	0.15	2.53E-08	1.94E-11	0.15	2.02E-07	1.56E-09
0.50	1.14E-05	1.09E-07	0.50	5.42E-08	6.23E-10	0.50	5.63E-07	6.23E-09

Table A24 Pore space fractality of plain and fibre reinforced mortar

Hydraulic Lime Mortar			Type N mortar			Type O Mortar		
Fibre	Mean	Std. Dev.	Fibre	Mean	Std. Dev.	Fibre	Mean	Std. Dev.
0	2.793	0.125	0	2.448	0.127	0	2.751	0.091
0.15	2.766	0.215	0.15	2.350	0.159	0.15	2.622	0.156
0.50	2.781	0.267	0.50	2.608	0.217	0.50	2.674	0.265

Table A25 Compressive strength (MPA) of plain and fibre reinforced mortar

Hydraulic Lime Mortar			Type N mortar			Type O Mortar		
Fibre	Mean	Std. Dev.	Fibre	Mean	Std. Dev.	Fibre	Mean	Std. Dev.
0	2.49	0.04	0	7.87	0.45	0	2.95	0.14
0.10	2.47	0.12	0.10	7.82	0.55	0.10	2.89	0.17
0.15	2.43	0.17	0.15	7.62	0.64	0.15	2.80	0.15
0.20	2.39	0.21	0.20	7.22	0.71	0.20	2.63	0.22
0.25	2.30	0.23	0.25	6.81	0.31	0.25	2.47	0.24
0.50	1.99	0.19	0.50	5.78	0.40	0.50	2.09	0.21

Table A26 Permeability coefficients (m/s) with different layers of nano-lime application

10 layer nano-lime application			40 layer nano-lime application			100 layer nano-lime application		
Fibre	Mean	Std. Dev.	Fibre	Mean	Std. Dev.	Fibre	Mean	Std. Dev.
0	1.14E-05	4.88E-07	0	7.59E-06	3.75E-07	0	7.35E-06	3.42E-07
0.10	1.03E-05	3.60E-07	0.10	6.28E-06	3.14E-07	0.10	5.57E-06	2.63E-07
0.15	8.06E-06	3.54E-07	0.15	5.79E-06	3.15E-07	0.15	6.05E-06	4.15E-07
0.20	7.41E-06	3.91E-07	0.20	8.54E-06	4.15E-07	0.20	8.30E-06	4.26E-07
0.25	1.07E-05	4.87E-07	0.25	1.13E-05	3.75E-07	0.25	1.03E-05	2.63E-07
0.50	1.79E-05	4.64E-07	0.50	1.77E-05	7.01E-07	0.50	1.38E-05	4.06E-07